International Journal of

Thermodynamics

International Centre for Applied Thermodynamics

Publishing Editor

Asst. Prof. Dr. Abdussamet SUBAŞI   Dr. Mustafa Yasin GÖKASLAN

Res. Assist. Ali Murat BİNARK

Language Editor

Asst. Prof. Dr. Abdussamet SUBAŞI

Journal Contacts

Editor-in-Chief

Prof. Dr. Lütfullah Kuddusi
ISTANBUL TECHNICAL UNIVERSITY
kuddusi@itu.edu.tr
+902122931300/2452
Department of Mechanical Engineering
Istanbul Technical University
Gumussuyu, 34437 Istanbul Turkey

Fractional Order Transient Thermoelastic Stress Analysis of a Thin Circular Sector Disk

Kishor R. Gaikwad*[1] and Satish G. Khavale[1]

[1] P.G. Department of Mathematics, N.E.S. Science College, Nanded-431602, (M.S.), India.
E-mail: [1]drkr.gaikwad@yahoo.in, [2]khavalesatish8@gmail.com

Abstract

Analysis of transient thermoelastic stress distribution of a thin circular sector disk with a time-fractional derivative of order α is proposed. The Neumann types of boundary conditions are used and the integral transform method and Caputo fractional derivative are used to obtain the analytical solutions of the temperature, displacement, and stresses. Numerical values of temperature, displacement, and stresses are computed for an Aluminum (pure) material and presented graphically with help of Mathcad software.

Keywords: Circular sector disk; thermal stresses; fractional order derivative; heat conduction.

1. Introduction

Lord et al. [1] introduced the generalized thermoelastic theory of dynamical system with one relaxation time, for the isotropic body. Green et al. [2] proposed the behavior of thermoelastic material without energy dissipation with linear and nonlinear theories. Ootao et. al. [3] solved the 3D problem for anon-homogeneous hollow circular cylinder with moving heat sources in the axial direction and it's transient thermal stresses. Ishihara et al. [4] presented the theoretical approach of thermoelastic deformation for a circular plate with a partially distributed heat supply. Sherief et. al. [5] studied the two-dimensional problem for a half-space whose surface is traction-free and subjected to the effects of heat sources is considered within the context of the theory of thermoelasticity with two relaxation times. Podlubny [6] presented the geometrical and physical interpretation of fractional integration and fractional differentiation. Povstenko [7] proposed the stresses corresponding to the fundamental solutions of a Cauchy problem for the fractional heat conduction equation in one-dimensional and two dimensional cases using the Caputo fractional derivative. Sherief et. al. [8] discussed the problem of a thermoelastic half-space with a permeating substance in contact with the bounding plane in the context of the theory of generalized thermoelastic diffusion with one relaxation time. Povstenko [9] discussed the heat conduction with time and space fractional derivatives and on the theory of thermal stresses based on this equation. Sherief et. al. [10] derived the new theory of thermoelasticity using the methodology of fractional calculus and the theories of coupled thermoelasticity and of generalized thermoelasticity with one relaxation time discussed.

Gaikwad et. al. [11] studied the quasi-static thermoelastic mathematical model for infinitely long circular cylinder by using the integral transform technique. El-Karamany et. al. [12] introduced the two general models of fractional heat conduction for non-homogeneous anisotropic elastic solids and the constitutive equations for thermoelasticity theory are obtained, uniqueness and reciprocal theorems are proved and the convolution variational principle is established and used to prove a uniqueness theorem with no restriction on the elasticity or thermal conductivity tensors except for symmetry conditions. Sur et. al. [13] proposed a new theory of two-temperature generalized thermoelasticity is constructed in the context of a new consideration of heat conduction with fractional orders. Gaikwad et. al. [14] studied the non-homogeneous heat conduction problem and its thermal deflection due to internal heat generation in a thin hollow circular disk. Gaikwad [15] analyzed the thermoelastic deformation of a thin hollow circular disk due to a partially distributed heat supply. Sur et. al. [16] proposed a new mathematical model of thermoelasticity theory in the context of a new consideration of heat conduction with fractional-order theory. A functionally graded isotropic unbounded medium is considered subjected to a periodically varying heat source in the context of space-time non-local generalization of three-phase-lag thermoelastic model and Green-Naghdi models. Raslan [17] studied the fractional order theory of thermoelasticity to a 1D problem of an infinitely long cylindrical cavity. Raslan [18] introduced the fractional-order theory of thermoelasticity to the two-dimensional problem of a thick plate whose lower and upper surfaces are traction-free and subjected to the given axi-symmetric temperature distribution. Gaikwad [19] studied the mathematical modeling of thermoelastic problem in a circular sector disk subject to heat generation. Gaikwad [20] proposed the two-dimensional study-state temperature distribution of a thin circular plate due to uniform internal energy generation. Gaikwad [21] discussed the axi-symmetric thermoelastic stress analysis of a thin circular plate due to heat generation. Gaikwad [22] studied the time-fractional heat conduction problem in a thin hollow circular disk and its thermal deflection.

In this work, the analysis of transient thermoelastic stress distribution of a thin circular sector disk with a time-fractional derivative of order α is proposed. The Neumann types of boundary conditions are used and the integral transform method and Caputo fractional derivative are used to obtain the analytical solutions of the temperature, displacement, and stresses. Numerical values of temperature, displacement, and stresses are computed for an Aluminum (pure) material and presented graphically with help of Mathcad software. It is believed that this particular problem has not been considered by anyone. This is a new and novel contribution to the field of thermoelasticity. The results presented here will be more useful in engineering problems particularly, in the determination of the state of strain in a thin circular disk constituting foundations of containers for hot gases or liquids, in the foundations for furnaces, etc.

2. Formulation of the Problem

Consider a 2D problem for a circular sector disk occupying the space $0 \leq r \leq a$, $0 \leq \varphi \leq \varphi_0 \leq 2\pi$, $0 \leq z \leq h$. A mathematical model is prepared considering nonlocal Caputo type time fractional heat conduction equation of order α for a thin circular disk.

"The definition of Caputo type fractional derivative given by [23]

$$D^\alpha f(t) = \begin{cases} \dfrac{1}{\overline{|n-\alpha}} \displaystyle\int_0^t \dfrac{f^n(\tau)}{(t-\tau)^{\alpha+1-n}} d\tau, & n-1 < \alpha < n; \\ \dfrac{df(t)}{dt}, & n = 1 \end{cases} \tag{1}$$

For finding the Laplace transform, the Caputo derivative requires information of the initial values of the function $f(t)$ and its integer derivative of the order $k = 1, 2, ..., n – 1$

$$L\{D^\alpha f(t); s\} = s^\alpha F(s) - \sum_{k=0}^{n-1} s^{\alpha-k-1} f^{(k)}(0), \qquad n-1 < \alpha < n \tag{2}$$

Also, the definition of Riemann-Liouville fractional derivative given by [23]

$$_aD_t^\alpha = \left(\dfrac{d}{dt}\right)^n \int_a^t (t-\tau)^{n-\alpha} f(\tau)d\tau, \qquad n-1 < \alpha < n\text{''} \tag{3}$$

The temperature of the circular sector disk $T(r, \varphi, z, t)$ at time t satisfying the time fractional differential equation,

$$\frac{\partial^2 T}{\partial r^2} + \frac{1}{r}\frac{\partial T}{\partial r} + \frac{1}{r^2}\frac{\partial^2 T}{\partial \varphi^2} + \frac{\partial^2 T}{\partial z^2} = \frac{1}{c}\frac{\partial^\alpha T}{\partial t^\alpha} \tag{4}$$

in $0 \leq r \leq a$, $0 \leq \varphi \leq \varphi_0 \leq 2\pi$, $0 \leq z \leq h$, for t > 0,
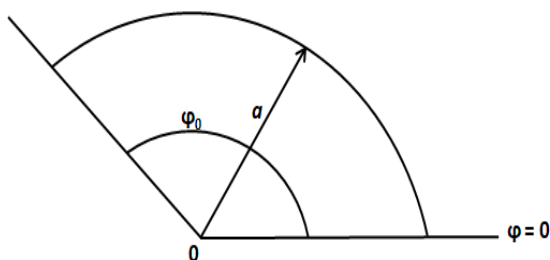
Figure 1. Geometrical representation of the problem.

with the boundary conditions,

$$kD_{RL}^{I-\alpha} \frac{\partial T}{\partial r} = f_1(\varphi, z, t), \qquad \text{at } r=a, \text{ for } t > 0 \tag{5}$$

$$kD_{RL}^{I-\alpha} \frac{\partial T}{\partial r} = f_2(r, z, t), \qquad \text{at } \varphi=0, \text{ for } t > 0 \tag{6}$$

$$kD_{RL}^{I-\alpha} \frac{\partial T}{\partial r} = f_3(r, z, t), \qquad \text{at } \varphi=\varphi_0, \text{ for } t > 0 \tag{7}$$

$$kD_{RL}^{I-\alpha} \frac{\partial T}{\partial r} = f_4(r, \varphi, t), \qquad \text{at } z=0, \text{ for } t > 0 \tag{8}$$

$$kD_{RL}^{I-\alpha} \frac{\partial T}{\partial r} = f_5(r, \varphi, t), \qquad \text{at } z=h, \text{ for } t > 0 \tag{9}$$

where, k is the thermal conductivity, and $D_{RL}^\alpha T(r, \varphi, z, t)$ for α>0 is the Riemann-Liouville fractional integral $I^\alpha T(r, \varphi, z, t)$ and initial conditions,

$$T = 0, \qquad \text{at } t=0, \ 0 < \alpha < 1, \tag{10}$$

$$\frac{\partial T}{\partial t} = 0, \qquad \text{at } t=0, \ 1 < \alpha < 2, \tag{11}$$

Following Gaikwad [20], we assumed that for small thickness h the circular disk is in a plane state of stress. In fact, "the smaller the thickness of the hollow disk compared to its diameter, the nearer to a plane state of stress is the actual state". The displacement equations:

$$U_{i,kk} + \left(\frac{1+\nu}{1-\nu}\right)e_{,i} = 2\left(\frac{1+\nu}{1-\nu}\right)a_t T_{,i}, \quad e = U_{k,k;} \ k,i = 1,2 \tag{12}$$

Introducing
$$U_i = \psi_{,i}, \ i = 1, 2, \tag{13}$$

we have
$$\nabla^2 \psi = (1+\nu)a_t T \tag{14}$$

$$\nabla^2 = \frac{\partial^2}{\partial x^2} + \frac{\partial^2}{\partial y^2} \tag{15}$$

$$\sigma_{ij} = 2\mu(\psi_{,ij} - \delta_{ij}\psi_{,kk}), \qquad i, j, k = 1, 2 \tag{16}$$

The displacement potential function $\psi(r, \varphi, z, t)$ is expressed as:

$$\frac{\partial^2 \psi}{\partial r^2} + \frac{1}{r}\frac{\partial^2 \psi}{\partial y^2} = (1+\nu)a_t T \tag{17}$$

with $\dfrac{\partial \psi}{\partial r} = 0$ at $r = a$ for all time t.

Initially $T = \psi = 0$ at $t = 0$ \tag{18}

The stresses function σ_{rr} and $\sigma_{\theta\theta}$ are:

$$\sigma_{rr} = \frac{-2\mu}{r}\frac{\partial \psi}{\partial r} \tag{19}$$

$$\sigma_{\theta\theta} = -2\mu \frac{\partial^2 \psi}{\partial r^2} \tag{20}$$

The traction-free boundary conditions as:

$$\sigma_{rr} = \sigma_{r\varphi} = 0 \ \text{ for } r=a,\, 0 \le \varphi < \varphi_0,\ t > 0 \tag{21}$$

$$\sigma_{\varphi\varphi} = \sigma_{r\varphi} = 0 \ \text{ for } 0 \le r < a,\, \varphi=0,\ t > 0 \tag{22}$$

$$\sigma_{\varphi\varphi} = \sigma_{r\varphi} = 0 \ \text{ for } 0 \le r < a,\, \varphi=\varphi_0,\ t > 0 \tag{23}$$

Equations (4) to (23) constitute the problem formulation under consideration.

3. Solution of the Heat Conduction Problem

To obtain the expression for temperature function $T(r,\varphi,z,t)$; firstly we define the finite Fourier transform and its inverse transform over the variable z in the range $0 \le z \le h$ defined in [24] as

$$\bar{T}(r,\varphi,\eta_p,t) = \int_{z'=0}^{h} K(\eta_p,z')T(r,\varphi,z',t)dz' \tag{24}$$

$$T(r,\varphi,z,t) = \sum_{n=1}^{\infty} K(\eta_p,z)\bar{T}(r,\varphi,\eta_p,t) \tag{25}$$

where

$$K(\eta_p,z) = \sqrt{\frac{2}{h}}\cos(\eta_p z) \tag{26}$$

and $\eta_1,\eta_2...$ are the positive roots of the transcendental equation

$$\sin(\eta_p h) = 0, \qquad p=1, 2, 3... \tag{27}$$

i.e. $\eta_p = \frac{p\pi}{h}, \qquad p=1, 2, 3...$

Applying the finite Fourier transform to equation (4) defined in equation (24) and using the conditions (5)-(11), we get

$$\frac{\partial^2 \bar{T}}{\partial r^2} + \frac{1}{r}\frac{\partial \bar{T}}{\partial r} + \frac{1}{r^2}\frac{\partial^2 \bar{T}}{\partial \varphi^2} - \eta_p^2 \bar{T} = \frac{1}{c}\frac{\partial^\alpha \bar{T}}{\partial t^\alpha} \tag{28}$$

the boundary conditions

$$kD_{RL}^{1-\alpha}\frac{\partial \bar{T}}{\partial r} = \bar{f}_1(\varphi,\eta_p,t), \quad \text{at } r=a, \quad t > 0 \tag{29}$$

$$kD_{RL}^{1-\alpha}\frac{\partial \bar{T}}{\partial r} = \bar{f}_2(\varphi,\eta_p,t), \quad \text{at } \varphi=0, \quad t > 0 \tag{30}$$

$$kD_{RL}^{1-\alpha}\frac{\partial \bar{T}}{\partial r} = \bar{f}_3(\varphi,\eta_p,t), \quad \text{at } \varphi=\varphi_0, \quad t > 0 \tag{31}$$

with

$$\bar{T} = 0, \qquad \text{at } t=0, \quad 0 < \alpha < 1, \tag{32}$$

$$\frac{\partial \bar{T}}{\partial t} = 0, \qquad \text{at } t=0, \quad 1 < \alpha < 2, \tag{33}$$

Secondly, we define finite Fourier transform and its inverse transform over the variable φ in the range $0 \le \varphi \le \varphi_0$ as defined in [25] as

$$\bar{\bar{T}}(r,\nu,\eta_p,t) = \int_{\varphi'=0}^{\varphi_0} K_0(\nu,\varphi')\bar{T}(r,\varphi',\eta_p,t)d\varphi' \tag{34}$$

$$\bar{T}(r,\varphi,\eta_p,t) = \sum_{\nu} K_0(\nu,\varphi)\bar{\bar{T}}(r,\nu,\eta_p,t) \tag{35}$$

where

$$K_0(\nu,\varphi) = \sqrt{\frac{2}{\varphi_0}}\cos(\nu\varphi) \tag{36}$$

where ν are the positive roots of $\sin(\nu\varphi_0) = 0$ \qquad (37)

i.e. $\nu = \frac{n\pi}{\varphi_0}, \quad n=1, 2, 3...$

Applying the finite Fourier transform to equation (28) defined in equation (34) and using the conditions (29)-(33), we get

$$\frac{\partial^2 \bar{\bar{T}}}{\partial r^2} + \frac{1}{r}\frac{\partial \bar{\bar{T}}}{\partial r} - \frac{\nu^2}{r^2}\bar{\bar{T}} - \eta_p^2 \bar{\bar{T}} = \frac{1}{c}\frac{\partial^\alpha \bar{\bar{T}}}{\partial t^\alpha} \tag{38}$$

with

$$kD_{RL}^{1-\alpha}\frac{\partial \bar{\bar{T}}}{\partial r} = \bar{\bar{f}}_1(\nu,\eta_p,t), \quad \text{at } r=a, \quad t > 0 \tag{39}$$

$$\bar{\bar{T}} = 0, \qquad \text{at } t=0, \quad 0 < \alpha < 1, \tag{40}$$

$$\frac{\partial \bar{\bar{T}}}{\partial t} = 0, \qquad \text{at } t=0, \quad 1 < \alpha < 2, \tag{41}$$

Lastly, we define finite Hankel transform and its inverse over the variable r in the range $0 \le r < a$ as defined in [25] respectively as,

$$\bar{\bar{\bar{T}}}(\beta_m,\nu,\eta_p,t) = \int_{r'=0}^{a} r'K_1(\beta_m,r')\bar{\bar{T}}(r',\nu,\eta_p,t)dr' \tag{42}$$

$$\bar{\bar{T}}(r,\nu,\eta_p,t) = \sum_{m=1}^{\infty} K_1(\beta_m,r)\bar{\bar{\bar{T}}}(\beta_m,\nu,\eta_p,t) \tag{43}$$

where

$$K_1(\beta_m,r) = \frac{\sqrt{2}}{a}\frac{1}{\left[1-\dfrac{\nu^2}{\beta_m a^2}\right]^{1/2}}\frac{J_0(\beta_m r)}{J_0(\beta_m a)} \tag{44}$$

and $\beta_1, \beta_2, ...$ are the positive roots of the transcendental equation

$$J_1(\beta_m a) = 0, \quad m = 1, 2, 3 \dots \tag{45}$$

Applying the finite Hankel transform to equation (38) defined in equation (42) and using the conditions (39)–(41), we get

$$\frac{\partial^\alpha \overline{\overline{\overline{T}}}(\beta_m, v, \eta_p, t)}{\partial t^\alpha} + c\left(\beta_m^2 + \frac{v^2}{r^2} + \eta_p^2\right)\overline{\overline{\overline{T}}}(\beta_m, v, \eta_p, t) = A(\beta_m, v, \eta_p, t) \tag{46}$$

with

$$\overline{\overline{\overline{T}}}(\beta_m, v, \eta_p, t) = 0, \qquad \text{for } t=0, \quad 0 < \alpha < 1, \tag{47}$$

$$\frac{\partial \overline{\overline{\overline{T}}}(\beta_m, v, \eta_p, t)}{\partial t} = 0, \quad \text{for } t=0, \quad 1 < \alpha < 2, \tag{48}$$

where

$$A(\beta_m, v, \eta_p, t) = caK_1(\beta_m, a)\overline{\overline{f}}_1(v, \eta_p, t)$$

$$\left\{ a\frac{dK_0(v, \varphi)}{d\varphi}\overline{\overline{f}}_2(\beta_m, \eta_p, t)\bigg|_{\varphi=0} - \frac{dK_0(v, \varphi)}{d\varphi}\overline{\overline{f}}_3(\beta_m, \eta_p, t)\bigg|_{\varphi=\varphi_0} \right.$$

$$\left. + \frac{dK(\eta_p, z)}{dz}\overline{\overline{f}}_4(\beta_m, v, t)\bigg|_{z=0} + \frac{dK(\eta_p, z)}{dz}\overline{\overline{f}}_5(\beta_m, v, t)\bigg|_{z=h} \right\} \tag{49}$$

Applying the Laplace transform and their inverse to equation (46), we get

$$\overline{\overline{\overline{T}}}(\beta_m, v, \eta_p, t) = \frac{A(\beta_m, v, \eta_p, t)}{c(\beta_m^2 + \eta_p^2)}\left[1 - E_\alpha\left(-k\left(\beta_m^2 + \frac{v^2}{r^2} + \eta_p^2\right)t^\alpha\right)\right] \tag{50}$$

Finally, taking the inverses defined in (43), (35) and (25) of equation (50), we obtain the required temperature as:

$$T(r, v, z, t) = \sum_{m=1}^\infty \sum_v \sum_{p=1}^\infty K_1(\beta_m, r)K_0(v, \varphi)K(\eta_p, z)\frac{1}{c\left(\beta_m^2 + \frac{v^2}{r^2} + \eta_p^2\right)}$$

$$\left[1 - E_\alpha\left(-k\left(\beta_m^2 + \frac{v^2}{r^2} + \eta_p^2\right)t^\alpha\right)\right] \times b_{mn} \tag{51}$$

where

$$b_{mn} = \left\{ c.a.K_1(\beta_m, a)\int_{\varphi'=0}^{\varphi_0}\int_{z'=0}^{h} K_0(v, \varphi')K(\eta_p, z').f_1(\varphi', z', t').d\varphi'dz' \right.$$

$$+ c.v.\sqrt{\frac{2}{\varphi_0}}\int_{r'=0}^{a}\int_{z'=0}^{h} r'K_1(\beta_m, r')K(\eta_p, z').f_2(r', z', t').dr'dz'$$

$$- c.v.\sqrt{\frac{2}{\varphi_0}}\cos(v\varphi_0)\int_{r'=0}^{a}\int_{z'=0}^{h} r'K_1(\beta_m, r')K(\eta_p, z').f_3(r', z', t').dr'dz'$$

$$+ \sqrt{\frac{2}{\pi}}c.\eta_p.\int_{r'=0}^{a}\int_{\varphi'=0}^{\varphi_0} r'K_1(\beta_m, r')K_0(v, \varphi').f_4(r', z', t').dr'd\varphi'$$

$$+ \sqrt{\frac{2}{\pi}}c.\eta_p.\cos(\eta_p h).\int_{r'=0}^{a}\int_{\varphi'=0}^{\varphi_0} r'K_1(\beta_m, r')K_0(v, \varphi').f_5(r', z', t').dr'd\varphi' \tag{52}$$

and

$$K_1(\beta_m, r) = \frac{\partial}{\partial r}\left[K_0(\beta_m, r)\right] \tag{53}$$

Using equation (51) in equation (17) the displacement function ψ, as follows:

$$\frac{\partial^2 \psi}{\partial r^2} + \frac{1}{r}\frac{\partial \psi}{\partial r} = (1+v)a_t\sum_{m=1}^\infty \sum_v \sum_{p=1}^\infty K_1(\beta_m, r)K_0(v, \varphi)K(\eta_p, z)$$

$$\frac{1}{c\left(\beta_m^2 + \frac{v^2}{r^2} + \eta_p^2\right)}\left[1 - E_\alpha\left(-k\left(\beta_m^2 + \frac{v^2}{r^2} + \eta_p^2\right)t^\alpha\right)\right] \times b_{mn} \tag{54}$$

Equation (54) becomes:

$$\psi = -(1+v)a_t\sum_{m=1}^\infty \sum_v \sum_{p=1}^\infty \frac{1}{\beta_m^2}K_1(\beta_m, r)K_0(v, \varphi)K(\eta_p, z)$$

$$\frac{1}{c\left(\beta_m^2 + \frac{v^2}{r^2} + \eta_p^2\right)}\left[1 - E_\alpha\left(-k\left(\beta_m^2 + \frac{v^2}{r^2} + \eta_p^2\right)t^\alpha\right)\right] \times b_{mn} \tag{55}$$

Using equation (55) in equations (19)–(20) we obtain the thermal stresses as:

$$\sigma_{rr} = -2(1+v)a_t\mu\sum_{m=1}^\infty \sum_v \sum_{p=1}^\infty \frac{1}{r\beta_m}K_2(\beta_m, r)K_0(v, \varphi)K(\eta_p, z)$$

$$\frac{1}{c\left(\beta_m^2 + \frac{v^2}{r^2} + \eta_p^2\right)}\left[1 - E_\alpha\left(-k\left(\beta_m^2 + \frac{v^2}{r^2} + \eta_p^2\right)t^\alpha\right)\right] \times b_{mn} \tag{56}$$

$$\sigma_{\theta\theta} = -2(1+v)a_t\mu\sum_{m=1}^\infty \sum_v \sum_{p=1}^\infty \frac{1}{\beta_m}\left(\beta_m K_2(\beta_m, r) - \frac{K_2(\beta_m, r)}{r}\right)K_0(v, \varphi)$$

$$K(\eta_p, z)\frac{1}{c\left(\beta_m^2 + \frac{v^2}{r^2} + \eta_p^2\right)}\left[1 - E_\alpha\left(-k\left(\beta_m^2 + \frac{v^2}{r^2} + \eta_p^2\right)t^\alpha\right)\right] \times b_{mn} \tag{57}$$

where

$$K_2(\beta_m, r) = \frac{\partial}{\partial r}\left[K_1(\beta_m, r)\right] \tag{58}$$

4. Numerical Results and Discussion

Setting

$$f_1(\varphi, z, t) = (\varphi^2 - \varphi_0^2)^2(z^2 - h^2)^2 e^{-At}$$

$$f_2(\varphi, z, t) = (r^2 - a^2)^2(z^2 - h^2)^2 e^{-At}$$

$$f_3(\varphi, z, t) = (r^2 - a^2)^2(z^2 - h^2)^2 e^{-At} \tag{59}$$

$$f_4(\varphi, z, t) = (r^2 - a^2)^2(\varphi^2 - \varphi_0^2)^2 e^{-At}$$

$$f_5(\varphi, z, t) = (r^2 - a^2)^2(\varphi^2 - \varphi_0^2)^2 e^{-At}$$

where r is the radius and $A > 0$.

4.1 Dimension

Radius of a circular sector disk $a = 1$ m,
Thickness of circular sector disk $h = 0.1$ m,
Portion of circular sector disk $\varphi_0 = 270^0$,

Central circular path of disk in radial and axial directions: $r_1 = 1$ m, and $z_1 = 0.05$ m and $\varphi_0 = 135^0$.

The first five positive root of the transcendental equation $J_1(\beta_m a) = 0$ as defined in [25] are $\beta_1 = 3.8317$, $\beta_2 = 7.0156$, $\beta_3 = 10.1735$, $\beta_4 = 13.3237$, $\beta_5 = 16.470$. The pure aluminum material was chosen for purposes of numerical evaluations and the constants of the problem were taken as following table 1.

Table 1. Material Constants.

Physical constants	Value
Thermal diffusivity (c)	84.18 m²/s
Thermal conductivity (k)	204 W/(m. K)
Young's modulus (E)	70 GPa
Coefficient of thermal expansion(a_t)	22.2×10^{-6} K^{-1}
Specific heat (c_p)	896 J/(kg. K)
Lame's constants (μ)	26.67 GPa
Poisson's ratio (ν)	0.35
Density (ρ)	2707 kg/m³

The numerical calculation and graphs have been carried out with help of computational mathematical software [26] PTC Mathcad Prime-6.0. Figure 2-5 shows the variation of temperature, displacement, stresses in radial distance r at instants α = 0.50 for time parameter t = 0.25, 0.50, 0.75, 1. From figure 2. The temperature profile increases within the region $0 \le r \le 0.4$, $0.7 \le r \le 1$ and decreases within the region $0.4 \le r \le 0.7$ in the radial direction. Figure 3. indicates the variation of displacement along the radial direction, it is clear that displacement decreases within the region $0 \le r \le 0.4$, $0.7 \le r \le 1$ and increases within the region $0.4 \le r \le 0.7$ with increasing the radius. Figure 4. Shows the radial stress distribution, it is observed that stress distribution decreases within the region $0 \le r \le 0.5$, $0.8 \le r \le 1$ and increases within the region $0.5 \le r \le 0.8$ with increasing the radius. Figure 5. indicates the circumferential stress distribution in the radial direction, it is observed that it will decrease in the region $0 \le r \le 0.2$, $0.5 \le r \le 0.8$ and increase within the region $0.2 \le r \le 0.5$, $0.8 \le r \le 1$.

Figure 6-9, depicts the temperature, displacement, and stresses in radial direction at time t = 0.50 for different values of α = 0.5, 1, 1.5, 2. From Figure 6. We can see that temperature distribution increases in the region $0 \le r \le 0.4$, $0.7 \le r \le 1$ and decreases within the region $0.4 \le r \le 0.7$ with the value of α increase with increasing the radial distance. Figure 7. indicates the displacement in the radial direction with different fractional-order parameters, it is clear that it will decrease in the region $0 \le r \le 0.4$, $0.7 \le r \le 1$ and increase within the region $0.4 \le r \le 0.7$ with the value of α increase. From Figure 8. the radial stress distribution decreases with increasing the value of α in the region $0 \le r \le 0.5$, $0.8 \le r \le 1$ and increases within the region $0.5 \le r \le 0.8$ with increasing the radius. Figure 9. indicates the circumferential stress distribution, it will decrease with increasing the α in the region $0 \le r \le 0.2$, $0.5 \le r \le 0.8$ and increase in the region $0.2 \le r \le 0.5$, $0.8 \le r \le 1$ in the radial direction.
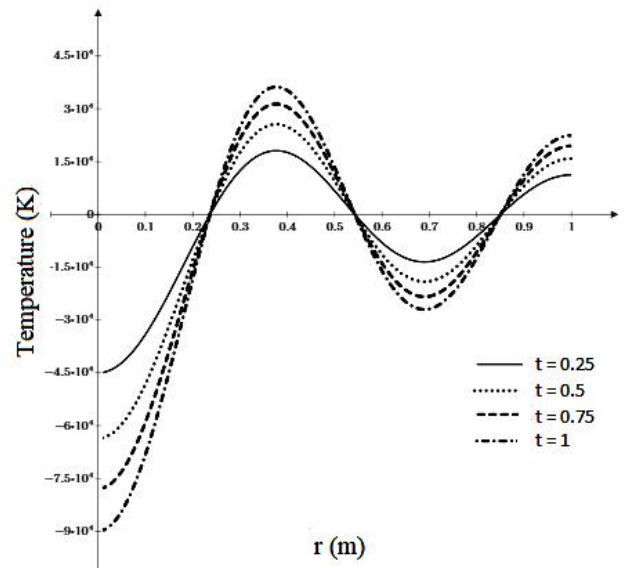
Figure 2. Temperature distribution at α = 0.5 and different values of t.
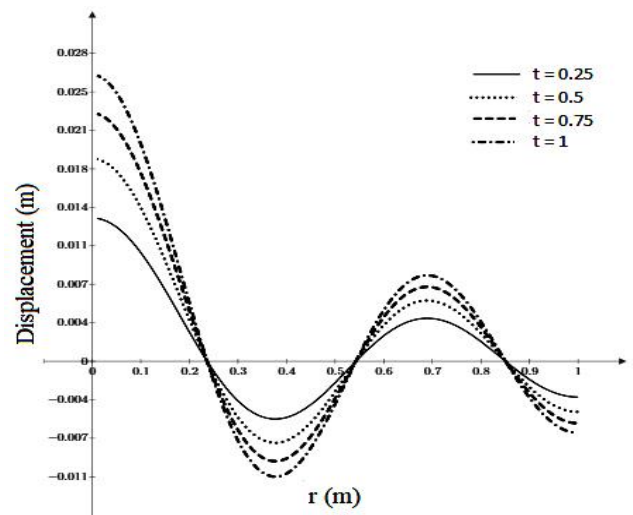
Figure 3. Displacement distribution at α = 0.5 and different values of t.
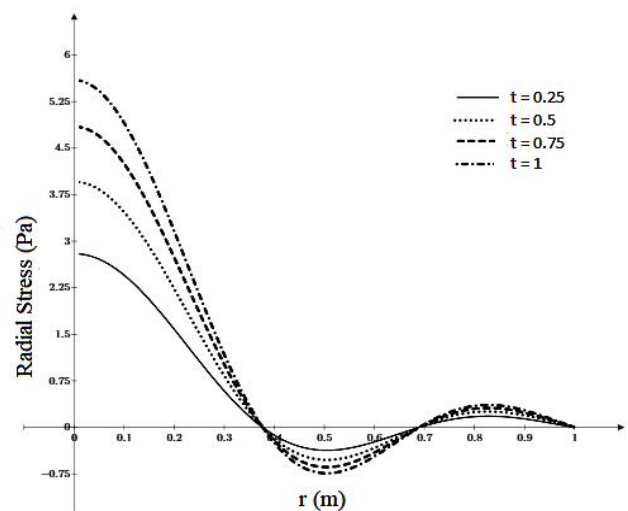
Figure 4. Radial stress distribution at α = 0.5 and different values of t.
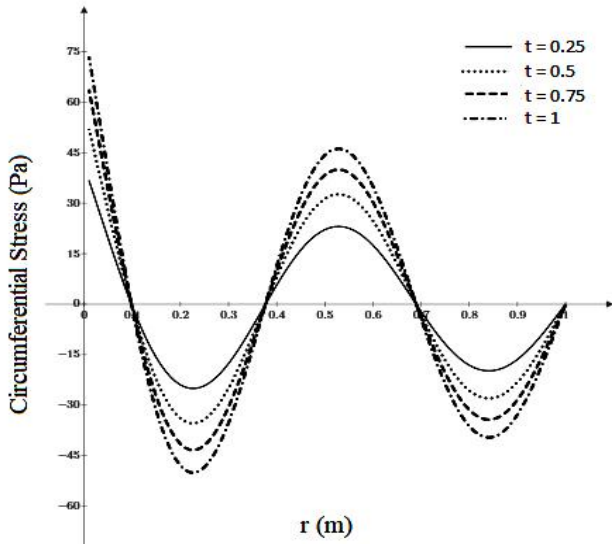
Figure 5. Circumferential stress distribution at α = 0.5 and different values of t.

Figure 6. Temperature distribution at t =0.5 and different values of α.

Figure 7. Displacement distribution at t =0.5 and different values of α.

Figure 8. Radial stress distribution at t =0.5 and different values of α.

Figure 9. Circumferential stress distribution at t =0.5 and different values of α.

5. Conclusion

This article analyzed the temperature, displacement, and thermal stresses for a circular sector disk occupying the space $0 \leq r \leq a$, $0 \leq \varphi \leq \varphi_0 \leq 2\pi$, $0 \leq z \leq h$. The general solution obtained from finite Hankel, Fourier, and Laplace transform and its inverses. Figure 2-5, shows the temperature, displacement, and thermal stresses at α = 0.5 for times $t = 0.25, 0.50, 0.75, 1$.

1. From the figures of temperature and displacement, we observed that the direction of heat flow and direction of body displacement are opposite and they are inversely proportionally to each other.
2. From the figures of radial and circumferential stresses, it develops the tensile and compressive stresses in the radial direction.
3. The fractional-order parameter $0 < \alpha < 1$, $1 < \alpha < 2$ and $\alpha = 1$ indicates the weak, strong, and normal conductivity respectively.
4. From figures 6-9, we see that the time-fractional derivatives play a significant role in all quantities in the given field and changes in

the values of the parameter α. This work may prove useful in material science, designers, real-life engineering problems, physicists, and those working to further develop the theory of fractional-order thermoelasticity.

Nomenclature (List of Symbols):

a_t linear coefficient of thermal expansion (K^{-1})

c thermal diffusivity ($m^2.s^{-1}$)

c_p specific heat at constant strain (J/Kg.K)

E cubical dilation (K^{-1})

k thermal conductivity (W/m.K)

T absolute temperature (K)

U_i Components of displacement vector (m)

Greek symbols

μ   Lame's constants (GPa)

ν   Poisson's ratio

ρ   density (kg/m^3)

ψ   displacement potential function

δ_{ij} Kronecker's delta tensor

σ_{ij} components of stress tensor

σ_{rr} radial stress (Pa)

$\sigma_{\theta\theta}$ circumferential stress (Pa)

Abbreviations

1D   one-dimensional (m)

2D   two-dimensional (m)

3D   three-dimensional (m)

References:

[1] H. W. Lord, Y. Shulman, "A Generalized Dynamical Theory of Thermoelasticity," *J. Mech. Phys. Solids.,* 15, 299-307, 1967.

[2] A. Green, P. Naghdi, "Thermoelasticity Without Energy Dissipation," *J. Elasticity., 31*, 189-208, 1993.

[3] Y. Ootao, T. Akai, Y. Tanigawa, "Three Dimentional Transient Thermal Stress Analysis of a Nonhomogeneous Hollow Circular Cylinder Due to a Moving Heat Source in the Axial Direction," *Journal of Thermal Stresses., 18*, 497-512, 1995.

[4] M. Ishihrar, N. Noda, "Theoretical Analysis of Thermoelastoplastic Deformation of a Circular Plate Due to a Partially Distributed Heat Supply," *Journal of Thermal stresses., 20*, 203-225, 1997.

[5] H. Sherief, F. Megahed, "A Two-Dimensional Thermoelasticity Problem for a Half-Space Subjected to Heat Sources," *Int. J. Solids Structures., 36*, 1369-1382, 1999.

[6] I .Podlubny, "Geometric and Physical Interpretation of Fractional Integration and Fractional Differentiation," *Fractional Calculus and Applied Analysis., 4*, 367-386, 2002.

[7] Y. Z. Povstenko, "Fractional Heat Conduction Equation and Associated Thermal Stress," *Journal of Thermal Stresses., 28*, 83-102, 2005.

[8] H. H.Sherief, H .A. Saleh, "A Half-Space Problem in the Theory of Generalized Thermoelastic Diffusion," *Int. J. Solids. Struct., 42*, 4484 - 4494, 2005.

[9] Y. Z. Povstenko, "Thermoelasticity that uses Fractional Heat Conduction Equation," *J. Math. Sci., 162*, 296-305, 2009.

[10] H. H.Sherief, A.El-Said, A. Abd El-Latief, "Fractional order Theory of Thermoelasticity," *International Journal of Solids and Structures., 47*, 269-275, 2010.

[11] K. R. Gaikwad, K. P. Ghadle, "Quasi-Static Thermoelastic Problem of an Infinitely Long Circular Cylinder," *Journal of the Korean Society for Industrial and Applied Mathematics., 14*, 141-149, 2010.

[12] A. S. El-Karamany, M. A. Ezzat, "On Fractional Thermoelasticity," *Mathematics and Mechanics of Solids., 16*, 334-346, 2011.

[13] A. Sur, M. Kanoria, "Fractional order Two-Temperature Thermoelasticity with Wave Speed," *Acta Mechanica., 223*, 2685-2701, 2012.

[14] K. R. Gaikwad, K.. P. Ghadle, "Nonhomogeneous Heat Conduction Problem and its Thermal Deflection Due to Internal Heat Generation in a Thin Hollow Circular Disk," *Journal of Thermal stresses., 35*, 485-498, 2012.

[15] K. R. Gaikwad, K. P. Ghadle, "On a Certain Thermoelastic Problem of Temperature and Thermal Stresses in a Thick Circular Plate," *Australian Journal of Basic and Applied Sciences., 6*, 34-48, 2012.

[16] A. Sur, M. Kanoria, "Fractional order Generalized Thermoelastic Functionally Graded Solid with Variable Material Properties," *Journal of Solid Mechanics., 6*, 54-69, 2014.

[17] W. Raslan, "Application of Fractional order Theory of Thermoelasticity To A 1D Problem For A Cylindrical Cavity," *Arch. Mech., 66*, 257-267, 2014.

[18] W. Raslan, "Application of Fractional order Theory of Thermoelasticity in a Thick Plate Under Axisymmetric Temperature Distribution," *Journal of Thermal Stresses., 38*, 733-743, 2015.

[19] K. R. Gaikwad, "Mathematical Modelling of Thermoelastic Problem in a Circular Sector Disk Subject to Heat Generation," *International Journal of Advances in Applied Mathematics and Mechanics., 3*, 183-195, 2015.

[20] K. R. Gaikwad, "Two-Dimensional Study-State Temperature Distribution of a Thin Circular Plate Due to Uniform Internal Energy Generation," *Cogent Mathematics, Taylor and Francis Group, 3*, 1-10, 2016.

[21] K. R. Gaikwad, "Axi-Symmetric Thermoelastic Stress Analysis of a Thin Circular Plate Due to Heat Generation," *International Journal of Dynamical Systems and Differential Equations., 9,* 187-202, 2019.

[22] K. R. Gaikwad, S. G. Khavale, "Time Fractional Heat Conduction Problem of a Thin Hollow Circular Disk And It'S Thermal Deflection," *Easy Chair Preprint., 1672,* 1-11, 2019.

[23] I. Podlubny, *Fractional Differential Equation*, Academic Press, San Diego, 1999.

[24] I. N. Sneddon, *The use of Integral Transform*, McGraw Hill, New York, 1972.

[25] N. M. Ozisik, *Boundary Value Problem of Heat Conduction*, International Textbook Company, Scranton, Pennsylvania, 84–101, 1968.

[26] PTC Mathcad Prime-6.0.0.0, [Online]. Available: https://support.ptc.com/help/mathcad/r6.0/en/ (accessed Nov. 1, 2020).

Theoretical High Pressure Study of Phonon Density of State and Debye Temperature of Solid C₆₀: Grüneisen Approximation Approach

Adnan M. Al Sheikh*[1], Sirwan K. Jalal[2], Salar A. Mawlood[3]

[1]Department of Physics, University of Mosul, Iraq
[2]Department of General Science, Charmo University, Iraq
[3]Department of Physics - Salahaddin University, Iraq
E-mail: [1]dr.adnan@uomosul.edu.iq

Abstract

A nanomaterial equation of state has been combined with Grüneisen approximation in present work to investigate the influence of high pressure on phonon density of state function of C_{60} through evaluating variations of lattice vibration frequencies and variation of mode density. Furthermore, the effect of high pressure on Debye temperature has been determined by using a formula of volume dependence of Debye temperature. Volume compression ratio in C_{60} has been computed, using a nanomaterial equation of state. Expressions of pressure dependence of phonon density of state and Debye temperature have been combined with volume compression ratio value. The evaluated result of volume compression ratio and phonon density of state have been compared with the experimental observations and good agreement can be seen.

Keywords: C_{60}, *high pressure; Grüneisen approximation; phonon density of state; Debye temperature.*

1. Introduction

A new structural form of solid carbon is C_{60}. Carbon nanotubes as integrate future of C_{60} have potential applications in the engineering industry and medical areas due to its unusual elastic properties. C_{60} has got intensive attention by researchers to describe its advantageous properties. The external mode spectrum of solid carbon under hydrostatic pressure up to 9Gpa using elastic neutron scattering has been investigated [1].

An X-ray diffraction experiment has been established on C_{60} using diamond anvil cell and up to pressure 28(Gpa) [2]. The pressure dependence lattice parameter and volume compression ratio were observed. A tight-binding molecular dynamics method used, for investigating phonon dispersions and density of states for solid C_{60}[3]. Equation of state of C_{60} has been found experimentally up to pressure of about 10Gpa [4], and theoretically using different equations of state [5,6]. Volume compression ratio, bulk modulus and spinodal pressure of C_{60} have been calculated by using various EOSs [7]. Moreover, in an intensive study, the validity of some equations of state of carbon nanotubes investigated [8].

In order to find solutions to a variety of problems in condensed phase of physics, equations of state that accurately predict solids behavior at high pressure and temperature are required. The study of C_{60} with varying pressure can help us to study many crystal forms of solid materials. This work is an attempt for investigating the effect of pressure on phonon density of state of C_{60} and Debye temperature, using a nanomaterial equation of state (EOS) [9]. In present work, pressure corresponding to volume compression ratio was evaluated by means of the EOS.

Debye temperature is an important quantity for determining various properties of solids at high pressure and high temperature. Numerous efforts have been taken for describing Debye temperature of different materials at high pressure condition [10].

The values of Grüneisen parameter and Debye temperature at ambient condition, used in the present study were calculated in literature [11]. Three body force shell model have been used to evaluate Debye temperature and Grüneisen parameter of C_{60} at atmospheric pressure and room temperature [11].

As Grüneisen parameter describes the effect of changing volume of solid phase on vibrational motions of atoms, therefore, the effect of decreasing volume of the lattice by applying high pressure, will result in changing the phonon density of state.

2. Theoretical analysis
2.1 Equations of state

The relationship between thermo dynamical variables; pressure (P), volume (V) and temperature (T) known as equation of state, with the help of EOSs, one can describe various properties of solid under varying conditions of pressures or temperatures. Based on different assumptions, many equations of state have been derived in literature. The equations of state are classified in to Thermal- pressure equation of state (Th-P EOS) and isothermal EOS.

Thermal- pressure (Th-P EOS):

At a given volume V and temperature T, the pressure P is descried as by the summation of two parameters:

$$P(V,T) = P_{initial}(V,T_0) + \Delta P_{th}(V,T) \tag{1}$$

Where $P_{initial}$ represents pressure required for compressing the sample material from initial volume (V_0) at ambient state ($P = 0$ and T_0) to another volume V at constant temperature T_0.

ΔP_{th} is the change in thermal pressure.

Thermal pressure arises due to the variation in temperature from T_0 to T at a constant volume.

If the final volume $V = V_0$ at pressure P and temperature T at the initial conditions, therefore, to obtain this final volume V no pressure is required i. e $P_{initial} = 0$, in this case $P(V,T_0) = \Delta P_{th}$ as illustrated in Fig.1 (black line).
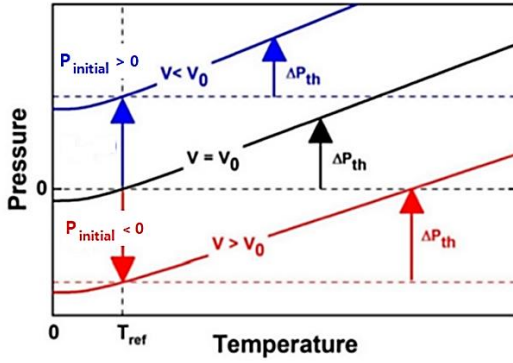
Figure 1. The description of different pressures and variables used in Th-P EOS, showing three various volumes [12].

Compression at the initial state is necessary to reach the final volume V, so that $P_{initial} = 0$. In this case, the total pressure is ΔP_{th} (black line) in the above figure. Under a positive pressure $P_{initial}$ above isochoric pressure the volume V is smaller than V_0. On the other hand, for pressure P and temperature T conditions under the isochoric pressure the V $> V_0$, the material expands at T_0 to reach the required V. This pressure is called spinodal pressure where $P_{initial} < 0$ (red in Fig. 1).

Mie-Grüneisen-Debye (MGD) EOS:

Thermal-pressure in solid crystal generate from the excitation of its vibrational modes. Thermal-Pressure EOS depends on several assumptions. Therefore, calculating the thermal-pressure and hence its variation (ΔP_{th}) from the initial temperature is used to distinguish diverse thermal-pressure EOSs. The statistical mechanics of the vibrational motion of atoms (phonons) of crystalline solids as a quasi-harmonic approximation QHA, leads to the derivation of MGD EOS.

QHA assumes that the atoms of the material are vibrating independently, without any interaction, and that their wave vectors are only dependent upon the molar volume.

phonon-mode Grüneisen parameter describes the phonon frequency dependent of the volume of the crystalline solids.

$$\gamma_i = \frac{V}{\omega_i} \frac{\partial \omega}{\partial V} \qquad (2)$$

To represent a single Grüneisen parameter γ, we assume that all of the phonon frequencies have the same volume dependence. Now, the Grüneisen parameter γ is assumed to be volume dependent by the MGD EOS $\gamma = \gamma_0 \left(\frac{V_P}{V_0}\right)^q$,

where, q is the second Grüneisen parameter, Thus two

Grüneisen parameter are associated to the vibrational frequencies, q is larger than zero and its influence is to increase the value of first Grüneisen parameter γ at high temperatures. Moreover, the value of second Grüneisen parameter q determines how fast the value of γ is changed, especially at large volumes.

In quantum-statistical framework, the vibration-rotational and intramolecular contributions of crystalline molecules, as isotropic quantum oscillators are associated with two Grüneisen parameters, i.e. γ and q [13].

The thermal pressure becomes $P_{th} = \frac{\gamma}{V} E_{th}$, V indicates molar volume, and E_{th} is the energy of the vibrational modes which indicated the thermal energy.

E_{th} is derived from a phonon density of states, which can be represented by a Debye temperature θ_D. Further assumption E_{th} is represented by the Debye function [14]. Therefore, if a finite temperature is considered for T_0, the change in P_{th} from T_0 becomes:

$$\Delta P_{th} = -\frac{3nR\gamma}{V}\left[T \times D\left[\frac{\theta_D}{T}\right] - T_{ref} \times D\left[\frac{\theta_D}{T_0}\right]\right] \qquad (3)$$

$D\left[\frac{\theta_D}{T}\right]$, is the Debye function, R represents the gas constant, n is the number of atoms and T_{ref} is the reference temperature.

Isothermal EOS:

The Pressure dependence of the volume of a material at constant temperature T_0 is characterized by isothermal equation of state. Based on different assumptions, various isothermal EOSs have been developed. In this study, an isothermal EOS is derived for Nano-size materials in terms of pressure P, as expressed in the following [9]:

$$P = B_0(1-\eta) + \frac{1}{2}B_0(B_0'+1)\left(1-\eta\right)^2 \qquad (4)$$

where,
P is the pressure

$\eta = \dfrac{V_p}{V_0}$ = volume compression ratio

V_0 and V_p are volume at ambient and high pressure respectively.
B_0: Bulk modulus at atmospheric pressure.
B_0': First pressure derivatives of bulk modulus.

2.2. Phonon Frequency Spectrum (PFS)

Atoms of crystalline solid phase vibrate around their equilibrium position in the same manner as harmonic oscillators. Thus, the vibrational motion of all atoms represents an elastic wave which is quantized and named phonons. According to Debye approximation, the vibration of each atom corresponds to a normal mode (phonon). Thus, there are a wide range of vibrational modes present in the crystal. The number of vibrational modes in the range of frequency ω to $\omega + d\omega$ is termed as density of state $D(\omega)$ or phonon frequency spectrum. One of the most outstanding investigations relating to C_{60} is its phonon frequency spectrum which has been taken considerable in this study. The phonon density of state of C_{60} at atmospheric pressure

was found by [15]and plotted in Fig. 3, as will be shown in section 3.2 in present work.

2.3. Pressure dependence of vibrational modes

From the definition of Grüneisen parameter, phonon frequencies ω_i are volume dependent and, that is described by the mode Grüneisen parameters [16,17].

$$\gamma_i = -\frac{\partial \ln \omega_i}{\partial \ln V} \tag{5}$$

The effect of pressure on the vibrational spectrum of a crystalline solid at constant temperature is described by the isothermal mode Grüneisen parameter, by the following relations. The isothermal bulk modulus B_T is

$$B_T = -V\frac{\partial P}{\partial V} \quad \rightarrow \quad \frac{\partial V}{V} = -\frac{\partial P}{B_T} \tag{6a}$$

$$\partial \ln \omega_i = \frac{\partial \omega_i}{\omega_i} \tag{6b}$$

$$\partial \ln V = \frac{\partial V}{V} = -\frac{\partial P}{B_T} \tag{6c}$$

$$\partial \ln V = -\frac{\partial P}{B_T} \tag{6d}$$

Substituting eq. (6c) and eq. (6b) into eq. (5), it becomes to

$$\gamma_i = \frac{-\left(\partial \omega_i / \omega_i\right)}{\left(-\partial P / B_T\right)} \tag{7}$$

$$\gamma_i = \frac{B_T}{\omega_i}\left(\frac{\partial \omega_i}{\partial P}\right)_T \tag{8}$$

The theory predicts a linear dependence of vibrational frequency on pressure, but is only expected to be applicable for pressures that are small compared to the bulk modulus. The effect of pressure on lattice frequency and mode density of state as is [18].

$$\omega_P = \omega\left(\frac{V_P}{V_0}\right)^{-\gamma} \tag{9}$$

$$D_P(\omega_P, V_P) = D(\omega, V_0)\left(\frac{V_P}{V_0}\right)^{\gamma} \tag{10}$$

where

ω_P, is the lattice frequency at pressure P

ω, Lattice vibration at atmospheric pressure

$D_P(\omega_P, V_P)$ and $D(\omega, V_o)$ are density of state at pressure P and atmospheric pressure respectively.

2.4. Debye temperature (θ_D)

Debye temperature (θ_D) or Debye characteristic temperature is the characteristic of each substance appearing in Debye theory of specific heats and given by:

$$\theta_D = \frac{\hbar \omega_D}{k_B} \tag{11}$$

Where θ_D - is the Debye temperature at atmospheric pressure k_B -Boltzmann constant

ω_D - Debye frequency at atmospheric pressure.

In the Debye model a solid is consider as an elastic continuum, which has a band of frequencies and the total number of vibrational modes is equal to the total number of degrees of freedom. As vibrational frequencies depend on equilibrium position which is change with pressure as a result of V_p/V_0 variation with the pressure. Pressure dependence of Debye temperature is expressed as [8,19]:

$$\theta_P = \theta_D\left(\frac{V_P}{V_0}\right)^{-\gamma} \tag{12}$$

Where θ_P: Debye temperature under high pressure.

3. Calculation and Results
3.1. Evaluation of V_p/V_0 of C_{60}

Table 1. Values of the input parameters of C_{60}, at ambient pressure and room temperature.

Parameters	Value
Bo	18.1Gpa [4]
B_0'	15.7 [4]
γ	2.899 [11]
θ_D	182.76 K[11]

Table 2: Calculated Values of V_p/V_0 versus pressure

Pressure (Gpa)	V_p/V_0
0	1
0.5976	0.97
1.3043	0.94
2.4163	0.90
3.3777	0.87
4.4483	0.84
6.0454	0.80
7.3706	0.77
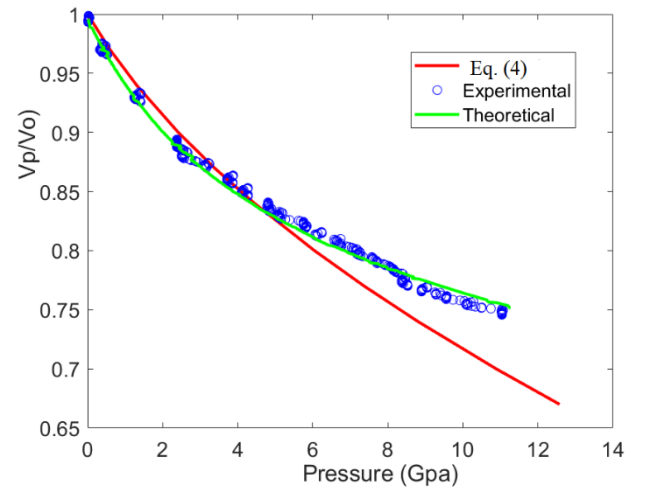
Figure 2. Variation of V_P/V_O under high pressure by using the EOS, Eq.(4), experimental data [4]and theoretical data from [5].

On substituting B_0 and B_0' values for C_{60} from Table 1 into equation 1, and choosing V_p/V_0 from 1 descending to 0.77. Variation of V_p/V_0 with high pressure for C_{60}, has been evaluated and the results are tabulated in Table 2, and shown in Fig .2. For comparison purpose, relevant experimental and theoretical data for volume compression ratio are displaced in fig.2. It is seen that our considered EOS fits the both literature results up to pressure range of 6Gpa. Then, beyond this limit, the curve expects a more dramatic decrease rather than experimental and theoretical data.

3.2 Evaluation of C_{60} Phonon Frequency Spectrum (PFS) under high pressure

The PFS of C_{60} at room temperature and atmospheric pressure is illustrated in Fig.3 [15]. Where density of state is measured in arbitrary unit.
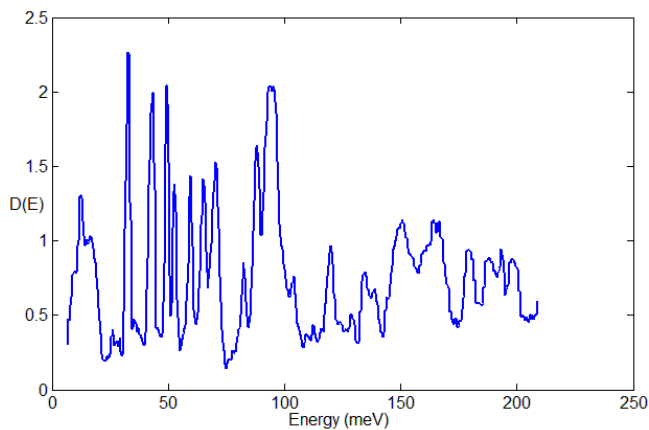
Figure 3. PFS of C_{60} at atmospheric pressure and room temperature [15].
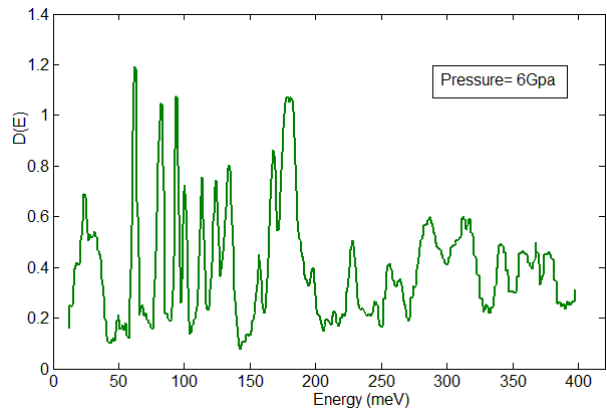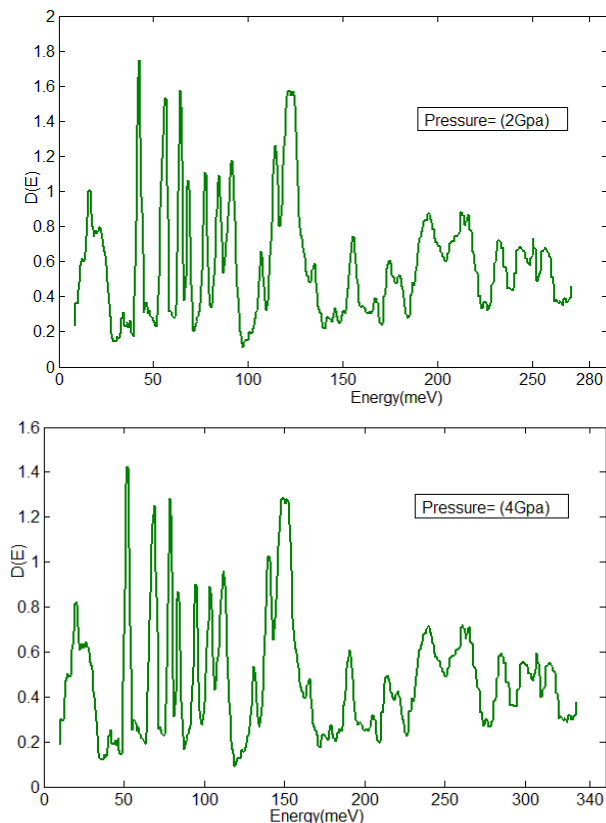
Figure 4. PFS of C_{60} at various pressure ranges and room temperature.

Equations (9 and 10), represent the pressure dependence of phonon energy (frequency) and density of state. Combining eq.4 with eqs. 9 and 10, phonon frequency spectrum of C_{60} has been computed under different high pressure values and the results are shown in Figs.4.

Figure 5. Experimantal PFS at ambient presssure and 180K[1].
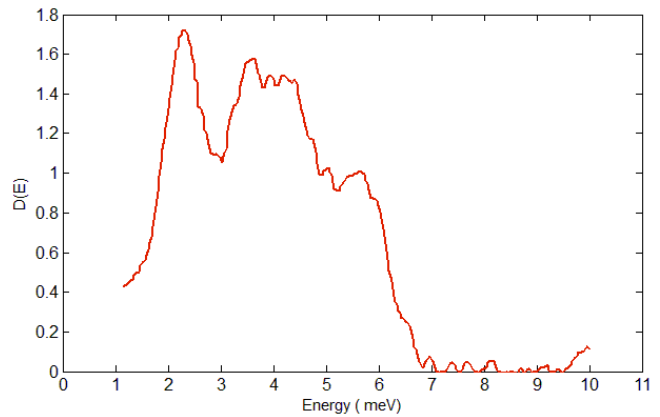
In order to support our results, Fig. 5 represents experimental PFS at ambient pressure and 180K [1] obtained by inelastic neutron scattering.
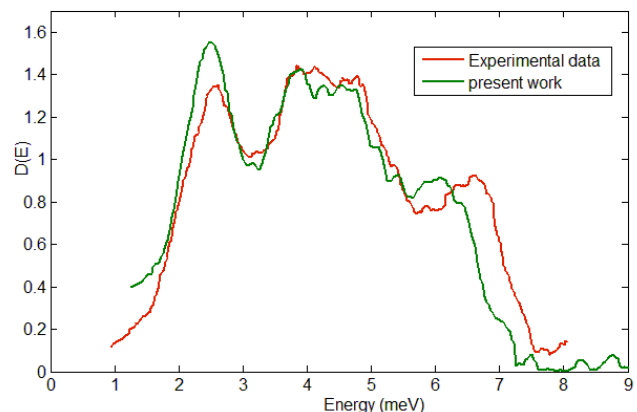
Figure 6. Experimental PFS of the external mode at P=0.5Gpa and T=290K[1], in comparison with the same spectrum evaluated in the present work.

Neglecting temperature effect and using Grüneisen approximation given in eqs.(6 and 7), Fig. 6 shows experimental data[1] for pressure dependence of the external mode spectrum of C_{60} as a function pressure at 0.5 GPa and

290K obtained by using inelastic neutron scattering in comparison with the pressure dependence of the same spectrum, evaluated theoretically in present work by applying Grünesein approximation. It is observed that a very good agreement has been achieved as the effect of temperature on the spectrum is negligible.

3.3. Evaluation of Debye Temperature (θ_P) of C$_{60}$ under high pressure

Choosing value of γ and θ_D from Table1. Then, substituting V_P/V_o values from Table 2 into eq. 12. Debye temperature under high pressure (θ_P) has been calculated and the result shown in Fig.7. It is seen that the θ_D variation rises linearly as the pressure increases.
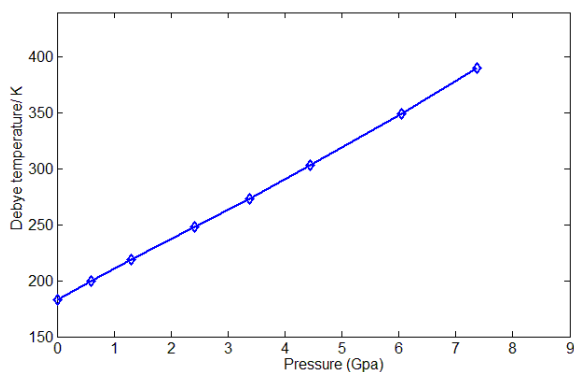
Fig.7. Pressure dependence of Debye temperature (θ_P) of C$_{60}$ using the EOS.

4. Discussion

The results of density of states D(E) and phonon energy under three different values of pressure are shown in Fig. 4. It is observed from Figs.4 that the phonon energy shifted towards higher energies with increasing pressure, while the density of states D(E) has dropped down, thus under high pressure more inactive modes become oscillating. This in line with theoretical predictions [20] that the frequencies of phonon frequency spectrum of solid materials shift towards higher frequencies, and some inactive modes become active. These results can be interpreted that as the pressure applied to a crystalline solid, lattice spacing parameter gets decreased, thus the wave number space is expanded.

The experimental results in Fig.6 supports what was obtained in Figs.4 by comparing the results obtained by applying Grüneisen approximation on spectrum of Fig.5 with experimental spectrum under high pressure [1]. For, as well as a good agreement between both experimental data and present theoretical in Fig.6. Both show frequencies shift towards higher energies and the mode density decreases and becomes wider.

Further interesting study, is the computation of Debye temperature of C$_{60}$ under strong compression. The pressure corresponding to V_P/V_0 values calculated by the EOS given in eq. 4 and reported in Table 1. Equation (12) has been used to compute Debye temperature θ_D under high pressure. The variation of Debye temperature at high pressure is shown in Fig. (7). It illustrates that Debye temperature increases linearly with pressure, since θ_D is directly proportional with ω_D and equation (8) implies that vibrational frequencies increase with pressure as well.

5. Conclusion

The present study analyzes the variety forms of EOSs that formulated on the basis of special assumptions and conditions. First, thermal- pressure EOS and its limitation is characterized. Second, as long as isothermal EOSs are identified, a nanomaterial isothermal EOS is used to perform a statistical understanding of effects of high pressure P on the volume V, Debye temperature and phonon frequency spectrum of Nano C$_{60}$. The combinations of the results of volume compression ratio attained with the nanomaterial EOS in fig.2 with equations (9,10 and 12) results in figures show the novelty of the entire calculation, as it agrees well with the experimental data shown in fig.6.

6. Nomenclature

C$_{60}$	Fullerene carbon
GPa	Gaga Pascal
K	Kelvin
η	eta
E_{th}	thermal energy
V	volume
P	pressure
V_P/V_0	volume compression ration
V_P	volume under high pressure
V_0	volume at ambient condition
γ	Grüneisen parameter
q	second Grüneisen parameter
θ_D	Debye temperature
θ_P	Debye temperature under high pressure

References:

[1] H. Schober, B. Renker, "Pressure dependence of the external mode spectrum of solid C$_{60}$, " *physical review* B 59 (5), 3287,1999.

[2] J. Haines, J. M. Leger, "An X-ray diffraction study 0f C$_{60}$ up to 28GPa, " Solid State Communications, 90 (6), 361,1994.

[3] J. Yu, R. K. Kalia, P. Vashishta, "Phonon dispersion and density of states of solid C$_{60}$," *Applied Physics Letters* 63(93), 3152 ,1993.

[4] T. Horikawa, T. Kinoshita, K. Suito, and A. Onodera, Solid State Commun. 114, 121 (2000).

[5] S. Sh. Rekhviashvili, "Equation of State for Fullerite C$_{60}$" Physics of the Solid State, 2017, Vol. 59, No. 4, pp. 835–837.

[6] S. Kareem Jalal, S. Ali mawlood, "Size dependent thermodynamic properties of nanoparticles, " *International Journal of Thermodynamics*, Vol. 23 (No. 4), 245-250,2020.

[7] A. M. Al-sheikh, S. K. Jalal, R. H. Al-saqa, "Equation of State and Thermo Dynamic Behaviour of C$_{60}$ under High Pressure," *Universal Journal of Mechanical Engineering* 8(1), 59,2020.

[8] R. S. Preston, S. S. Hanna, J. Helerle, " Mössbaruer effect in metallic Iron. *Phys. Rev.,* "128(5) 2207 1962.

[9] D. Sharma, M. Kumar, "Effect of pressure on nanomaterials," Physica B, 405(13), 2820,2010.

[10] S. K. Sharma, "Debye temperature of hcp Iron at extreme compression, Solid State Communications, " 149 (47), 2207,2009.

[11] P. Singh, N. K. Gaur, "Thermal and elastic properties of C_{60} in FCC phase, " Sop transactions on theoretical physics, 1(2) 68 ,2014

[12] R. J. Angel, F. Miozzi, M. Alvaro," Limits to the Validity of Thermal-Pressure Equations of State" *Minerals* 9, 562,2019.

[13] S. S. Rekhviashvili, "Equation of state for Fullerite C_{60}, *Physics of the Solid State*, " 59(4), 835, 2017.

[14] Anderson, O.L. Equations of State of Solids for Geophysics and Ceramic Science; Oxford University Press: Oxford, UK, 1995; p. 432.

[15] J. Yu, R. K. Kalia, P. Vashishta, "Phonon dispersion and density of states of solid C_{60}," *Applied Physics Letters* 63(93), 3152 ,1993.

[16] L. Burakovsky, D. L. Preston, "An analytical model of Grüneisen parameter at all densities,'' *Journal of physics and chemistry of solids*, 65 2002.

[17] S.Kareem Jalal, A. M. Al-Sheikh, R. H. Al-Saqa, " High Pressure Effects on the Phonon Frequency Spectrum of Silicon Nanoparticle," *Iran J Sci Technol Trans Sci* 45, 391–396 , 2021.

[18] J. L. Dlouha, "The influence of pressure on the Mössbauer effect, " Czech. J. Phys. B 14 (8), 57, 1964.

[19] S. Kareem Jalal, A. M Al-Sheikh, " Theoretical high pressure study for thermoelastic properties of NaCl-B1m" *Rafidain J Sci* 25:80–89, 2014.

[20] P. M. Sherwood, "Vibrational spectroscopy of solids, " *Cambridge university press,*182(1972).

Biophysics of Cryopreservation

Sharma Yashaswi[1], Sharma Mona[2*]

[1]MSc, Department of Reproductive Biology, AIIMS, New Delhi
[2*]Associate Professor, Department of Reproductive Biology, AIIMS, New Delhi
Email: dr.mona18sharma@gmail.com

Abstract

A significant credit towards today's scientific and medical advancements goes to the technique of cryopreservation. Cryopreservation refers to the maintenance of cellular life at subzero temperatures for a definite period of time in a state of suspended cellular metabolism. The technique has become an indispensable step in most scientific research and medical applications like assisted reproduction, transplantations, and cell-based therapies where-in it allows the long-term preservation of biological specimens like gametes, embryos, viruses, cells and tissues. Although already an extensively used technique, a significant proportion of the cryopreserved samples still incur notable damage. Ultimately this leads to a decreased post-thaw viability and proliferation. Moreover, it is also possible that events during the freezing process, provoke more serious disturbances in the preserved material with regard to its identity and functionality. Hence, with the need to use the technique more judiciously, additional studies are needed for optimizing the current cryopreservation methods in use. For this, a thorough understanding of the normal physiological changes that the cryopreserved sample undergoes and the physics of cryopreservation seems plausible. The review thus aims to unravel the current knowledge on the complex physico-chemical processes and reactions that occur during the standard cryopreservation techniques.

Keywords: *Cryopreservation; vitrification; freezing; thawing; biophysics.*

1. Introduction

Cryopreservation aims to store cells indefinitely by arresting their metabolism and retarding the cellular reactions by means of low subzero temperatures. Such ultralow temperatures ensure that the cells are maintained below the glass transition temperature.

2. The Underlying Biophysics of Cryopreservation
2.1. Water and its Transition to Ice

Like in the biology of all living cells, water play a central role in cryobiology too. A cell consists of around 60 to 85% water both in free and bounded forms. The bound form refers to the water hydrated to complex mixtures of cells like proteins, lipids and (Tg) of pure water and no detectable biochemical activity is possible due to lack of sufficient thermal energy. Moreover, the progressive reduction and ultimately the absence of liquid water (once completely frozen) limit all metabolic processes [1,2].

Freezing is removal of water so that it transforms the liquid water into ice either when within the cell or after it flows out of the cell and freezes externally. However, it should be noted that freezing only affects free water in cells and not the bound form [3].

The protons and the oxygens of multiple water molecules are attracted electrostatically which form numerous weak hydrogen bonds. These bonds are highly dynamic and undergo frequent breaks and re- formations especially at its interface with other molecules and on the surfaces [3]. However, on cooling water below its freezing point, it resists breaking of hydrogen bonds. Rather

molecules lock each other tightly to get organize into lattice like symmetry. This give rise to solid crystalline structures called ice which is less dense and occupy larger volume than liquid water.

2.2 It all begins with nucleation

Water in its pure form when cooled below its freezing point is undercooled or more commonly said to be super-cooled until it is disturbed. However, once the local thermal properties allow hydrogen and oxygen molecules to come together to form sufficient H-bonds, they initiate to form an 'ice embryo' [4]. This is called nucleation wherein molecules come close together and congregate in an arrangement which defines the crystal structure of the solid. The embryonic ice is thermodynamically capable to grow into a full-fledged ice as shown in Figure 1 [5].

Post nucleation, multiple water molecules complex with each other thereby forming networks that result in the exponential growth of the structure. Two types of nucleation exist depending upon the presence of a nucleation site [4]. The most common nucleation is the heterogeneous type wherein ice begins to form around a mere physical disturbance or an impurity like salt in the liquid or an irregularity in the container that act like a defined nucleation site.

Homogenous nucleation, on the other hand occurs only in pure water wherein ice forms without a predefined site of nucleation or a seed crystal [5]. Given to the rarity of pure water in biological samples, almost all nucleation is always heterogeneous. The types of nucleation are shown in Figure 2.
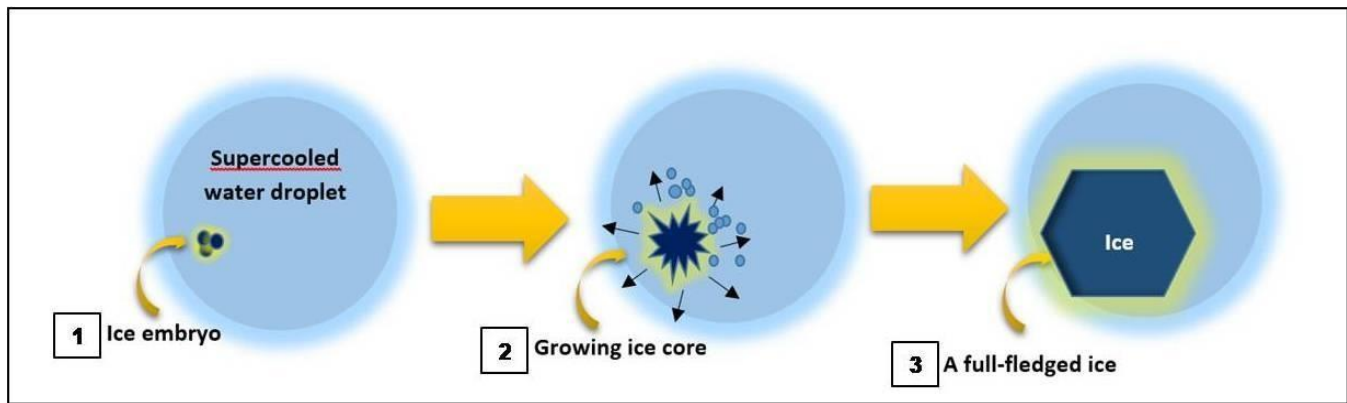
***Figure 1**. The process of nucleation. 1. Formation of a nucleation site (an ice embryo). 2. The congregation of water molecule complexes on the embryo site to form an ice core. 3. The growth of a full fledged ice crystal wit regular symmetry.*
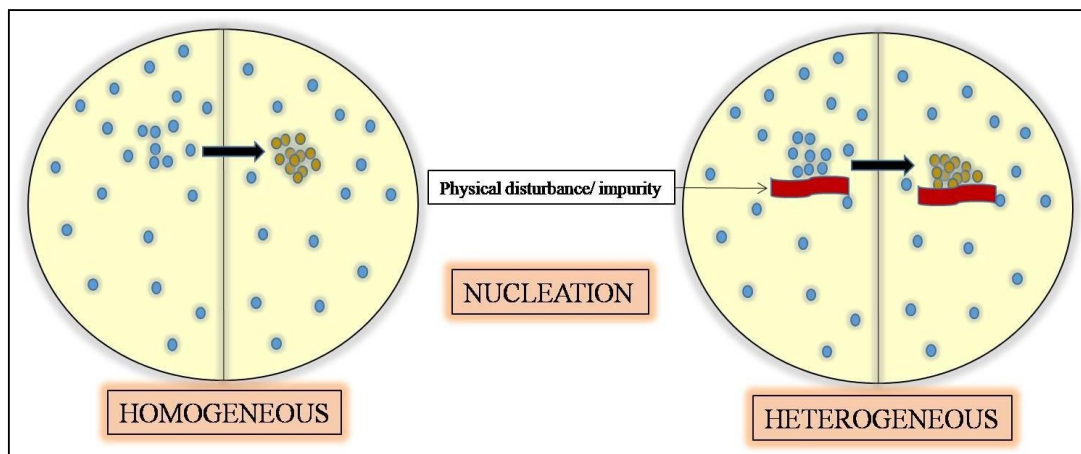
***Figure 2.** Types of nucleation: Homogenous nucleation occurs only in pure water wherein ice forms without a predefined site of nucleation or a seed crystal; heterogeneous nucleation wherein ice begins to form around a physical disturbance or an impurity or an irregularity in the container that act like a defined nucleation site.*

2.3. Osmosis follows Ice formation

Cryobiology not only concern with the state of water in the cells but also involves its movement and the factors that govern such movement of water into and out of the cells during the freezing process. The osmotic relations of the cell abides by the principle that in the absence of metabolic forces, the concentration of water and solutes in the cell is adjusted such that both are in a chemical potential equilibrium with the concentrations outside the cell [3].

Hence, the two kinetic processes occurring during the cooling of cells that is growth of ice and the loss of water from the cell, happens at a characteristic rate [3]. This is highly influenced by the cooling rate imposed on the system [6,7]. If cooling is provided at a slow constant rate (such as during conventional freezing), it allows the cell to remain close to the osmotic equilibrium and the rate of water loss from the cell will be in accordance to the rate of water loss from extracellular solution as it changes to ice. However, if a rapid cooling rate is applied, the two rates will vary significantly. The intracellular water freezes to ice at a faster rate due to the absence of a permeability barrier which the water inside of the cells need to surpass. This leads to a continuous increase in the osmolality gradient across the plasma membrane [6-8].

3. Biophysics of Conventional Slow Freezing and Rapid Freezing

Freezing usually occurs only when it is energetically and physically favorable that is when ice templates are available for it to do so [4]. With the drop in temperature associated with the cryopreservation process, ice is preferentially formed extracellularly (except when cells undergo rapid freezing). As the extracellular liquid water transitions to a solid state, the solute concentration of the system increases. This creates a deficit between the partially frozen outside of the cell and the unfrozen inside. This in turn induces the efflux from the inside of the cells to establish the osmotic equilibrium [3]. In case a controlled reduction of temperature is maintained, a sufficient osmotic pressure persists that prevents the formation of ice crystals within the cell. However, the cells continually shrink during the process due to the efflux of water [9]. During rapid freezing, there is less time for water to move in the extracellular compartment and gets supercooled very fact leading to intracellular ice formation. Therefore, an optimum cooling rate is essential. Rapid freezing leads to cell death due to intracellular ice formation. Slow freezing leads to cell exposure to hypertonic environment thereby causing water efflux and cellular dehydration. The mechanism is explained in Figure 3.
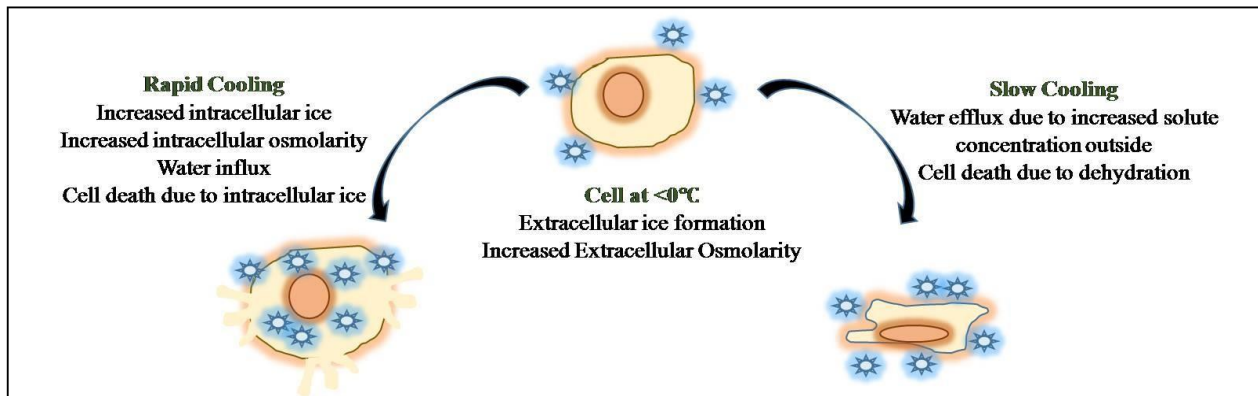
Figure 3. *The consequences of different cooling rates imposed on cells undergoing cryopreservation.*

4. Biophysics of Vitrification

Viscous liquids allow rapid cooling far below their melting temperature and undergo solidification by avoiding crystallization [10-12]. This property is utilized in the process of vitrification. The supercooled substance with the physical properties of a liquid subsequently acquires solid properties once it reaches below a particular temperature called the glass transition temperature (Tg) [10]. At this point, the molecules of the substance remain in a disordered pattern as in liquids but are locked in place and the consequent "solid-liquid" is called as the glass [11]. Since there is no crystallization event, vitrification outruns the processes of ice nucleation and growth and thus their potential adverse effects [12].

With continuous exposure to low temperatures, the energy of molecules progressively dissipates with time such that they are unable to move amongst each other. Hence the molecular motion ceases and at Tg, they are physically confined (although still disordered) and vibrate at their positions mimicking the confinement within crystals. With subsequent temperature fall, the viscosity of the system significantly increases (as cell solutes become concentrated) [11]. The increased viscosity prevents the water molecules coming together to initiate ice formation [10]. With this, the values of heat capacity, thermal expansivity, and compressibility resemble to those of a crystal and hence the substance results into an amorphous solid [11].

5. Biophysics of Thawing

The rewarming process also encompasses change in ice stability, size and structure. However, the exact magnitude and type of change depends on the type of specimen, the cooling rate and the cryoprotective additives used in the process. More significantly, the events of warming vary in terms of type of cryopreservation method employed. As the ice melts, the solute concentration in the residual phase is decreased. For cells that underwent slow freezing and thus the dehydration process, a progressive rehydration step occurs during warming [3]. This is opposed to cells frozen at high cooling rates since they are not in osmotic equilibrium during the freeze. They thus undergo further dehydration in response to the decreased extracellular solute concentration during thaw. But as more ice melts, the extracellular solution is diluted, causing the reversal of the water flux and ultimately cell rehydration [3].

A significant event during rewarming that might result in increased cell lethality is recrystallization in cells with intracellular ice. It should be noted that small ice crystals have a higher internal pressure than the larger ones due to increased interfacial curvature and ice–solution interfacial tension. Since this high pressure influences chemical potential, large ice crystals may grow while small ice crystals are melting at a given temperature causing further damage to cells [6].

6. Devitrification

Successful devitrification is a challenge. The glassy solid is extremely fragile and can revert back either to a liquid or devitrify to form ice [13]. The ice formation may be a consequence of the changes in molecular mobility of rewarmed water molecules which under sufficient energy conditions, can relax and rearrange themselves to form ice. Further the glass may simply crack or fracture causing significant damage to organelles [14,15].

Hence in practice, most vitrification protocols employ a rapid rate of warming such that ice nucleation is inhibited while passing through the temperature of glass transition [16,17]. However, utmost concern must be given since too rapid rewarming increases the possibility of stress cracks and fractures. Ideally employing a two phase procedure, in which a short slow rewarming phase lasting a mere few seconds followed by a rapid warming phase at a high temperature looks promising for successful devitrification [18].

7. Mechanism of Cryoinjuries

There may be multiple effects of ice formation such as cellular dehydration, mechanical stress by extracelluar ice, intracellular crystallization, thermal shock etc. The extent to which the cryopreservation technique will succeed depends on the immediate post-thaw survival rate and the effect of the freeze thaw process on cryopreserved cells. However, the other subtle effects on DNA, mRNA and protein function may not be observed immediately post-thaw. DNA quality and gene expression are crucial factors for cell development. Cells undergoing cryopreservation are exposed to extreme physical and chemical conditions that may alter cell integrity at molecular level.

There have been studies on molecular effects of cryopreservation targeting DNA damage and altered gene expression. Few study group showed no adverse effects of cryopreservation in the porcine and humans [19] whereas other groups showed negative effects in the ovine and human species [20,21]. The extensive work done in different cell types such as sperm, oocytes, erythrocytes and leukocytes showed that cell quality declines after the freeze-thaw process due to DNA damage and fall in mRNA levels due to addition of cryoprotectants, cryo injury, intracellular ice crystallization [20, 22,23].
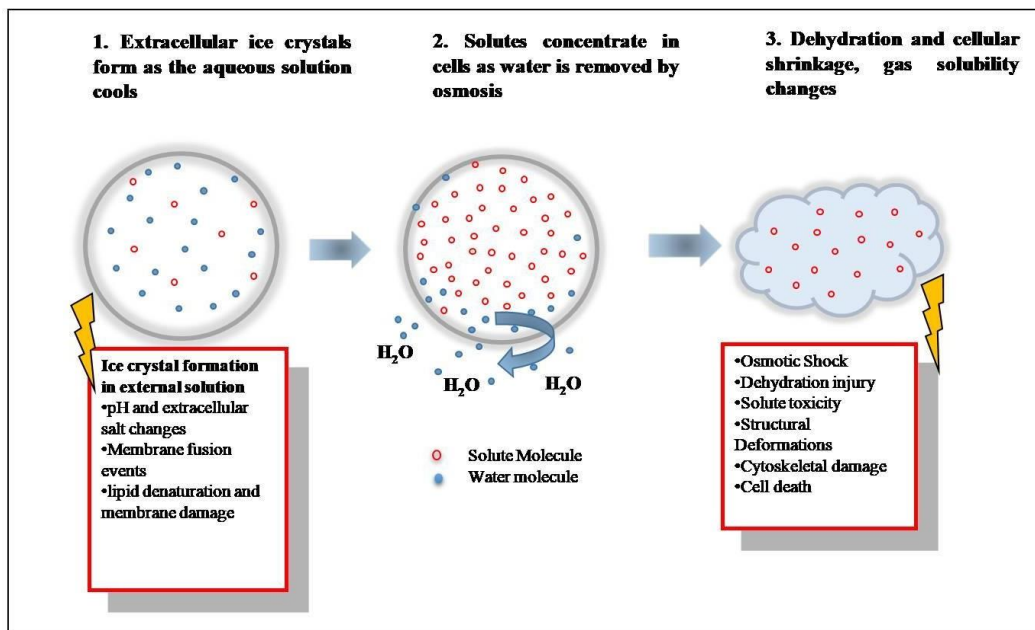
Figure 4. *The process of slow freezing of cells and its cell injury mechanisms.*

7.1 Biophysics of Slow-Freezing Injury

During slow cooling, the cell is able to sustain the osmotic equilibrium by balancing the rate of water loss from cells to the rate of extracellular ice formation [3] Although this prevents the problem of intracellular ice formation, it encompasses considerable cell dehydration. Two important mechanism of cell injury is noted during slow freezing: Solute toxicity and physical changes due to cell dehydration [7,8, 24-27]. The two major consequences of dehydration are a) increased extracellular solute concentration denaturing membrane proteins b) salt crystallization may also bring pH changes that may again denature proteins.

Solute toxicity arises due to the increased solute concentration in cells. During slow cooling process, solutes increase in concentration both extracellularly and intracellularly due to the formation of external ice and the resulting efflux of water from the cells [28]. This can lead to alterations in the chemical equilibrium of the cell through varied biophysical and biochemical changes leading to cell death. For instance, highly concentrated salt can have a lyotropic effect on the cell membrane [19]. The mechanism of cell injury in slow freezing is shown in Figure 4.

On the other hand, cell shrinkage is capable of causing structural deformations among other defects. The dehydration of the plasma membrane due to water loss may cause membrane fusion events resulting in parts of membrane being internalized as vesicles and consequently decreasing the surface area of the cell adversely affecting its housekeeping functions [27]. Besides this, there are many theories as to how cell dehydration causes damage to the cells. The minimal volume hypothesis states that once the cell reaches its minimum volume after water efflux, it fails to maintain the osmotic equilibrium and thus the gradient difference can only be minimized by salt movement from extracellular solution into the cytoplasm. On reversal to isotonic condition during thawing, the cytoplasm with higher concentration of solute would draw water in to reach equilibrium. If this expansion surpassed the yield strength of the membrane, the cell undergoes lyses [29]. A variant of the same theory suggests that once the

minimum volume is reached, the induced hydrostatic pressure gradient causes a mechanical stress on the cell resulting in injury [26].

Nevertheless, formation of large ice crystals even extracellular can have grave consequences. The expansion can cause pressure and has a shearing effect on membranes resulting in appreciable damage [9].

7.2 Biophysics of Rapid Freezing Injuries

Intracellular ice formation is the most well-known cell injury inflicted by higher rates of cooling [30]. As described earlier, during a rapid freeze protocol, a cell is unable to maintain equilibrium with the external environment since extracellular ice forms too quickly to balance by exosmosis. As a result, the cytoplasm is increasingly super-cooled which in turn increases the chance of allowing nucleation and thus intracellular ice formation. [30,31] The nucleation has been shown to result from interactions of extracellular ice with the plasma membrane. A set of hypotheses explain that the external ice with an appropriate tip radius grows through the aqueous or proteinaceous pores of plasma membrane to seed the cytoplasm for intracellular ice formation [31-33]. This results in cell injury due to the enlargement of the membrane pore on re-crystallization during warming. This is well explained under the protein-pore theory [32]. Alternatively, it could also be that membrane damage precedes intracellular ice formation (the membrane failure hypothesis) as shown through the work on unfertilized eggs of sea urchin [34]. The membrane may be damaged either by development of electrical transients created by charge separation at the interface of the growing ice and the aqueous solution or through the virtue of a critical osmotic pressure gradient across the membrane [35,36]. It has also been hypothesized that the plasma membrane could act as an effective nucleator for internal ice when acted on by extracellular ice. This is known as the surface- catalyzed nucleation theory [37].

It is widely believed that formation of intracellular ice is lethal to cells mostly due to the mechanical damage they impose via a surface-area-to-volume redistribution of the ice crystal [7,13,38]. This has been believed to damage

internal organelles of the cell. As a matter of fact, the hazardous effect of ice crystal formation is more prominently evident during the warming process. A slow thawing protocol results in the recrystallization of the ice, increasing its size. Recrystallization, however, is not the only means by which intracellular ice can be lethal. Intracellular ice formation also include non-mechanical modes of destruction such as through solution effects, thermal shock, osmotic injury, protein denaturation, and gas bubble formation [39-44]. However, the degree of lethality and damage incurred is strictly influenced by the amount, size, location and mechanism of formation of such ice crystals as described in Figure 5 [40,45,46].

8. The Role of Cryoprotectants

A range of chemical substances with high solubility that work to protect biological cells from cold shock have been employed to substantially increase the survival following freezing and thawing [47]. These substances called cryoprotective agents or cryoprotectants are either permeating or non- permeating [1] type depending upon their mode of action.

8.1 Mode of action of Permeating Cryoprotectants

Permeable cryoprotectants diffuse through the plasma membrane and equilibrate in the cytoplasm. They have a low molecular weight and are non-ionic with low cellular toxicity [9, 48]. They are most commonly employed to mitigate slow-cooling injuries and primarily work by decreasing the freezing point [48]. They lower the amount of ice that forms at a given temperature by forming H-bonds with water molecules [3]. This in turn lowers the salt concentration found normally in physiological solutions for a given temperature (below the freezing point, when ice formation causes the concentration of these salts). Besides, they also act as secondary solvent for the salt present [3]. Hence by depressing the temperature at which the cell is exposed to increased extracellular solute concentration, the magnitude of injury, and the kinetics at which damage

accumulates, is reduced. Further, it has also been seen that permeable cryoprotectants enters the cell and increases its viscosity. This helps preventing the cell reaching the minimum lethal cell volume due to dehydration [48,49].

8.2 Mode of action of Non-permeating cryoprotectants

Non-permeating cryoprotectants are bulky long-chain polymers that remain extracellular and are used mostly for rapid freeze processes [50]. They have large osmotic coefficients and use this property to dehydrate cells before freezing which then requires lesser amount of water loss from the cell to maintain osmotic equilibrium during cryopreservation [3]. As a result the cytoplasm do not supercool to the extent to initiate the formation of intracellular ice at the given cooling rate [3,9]. Figure 6 explains modes of action of permeating and non-permeating cryoprotectants.

8.3 Cryoprotectants to achieve Vitrification

Cryoprotective vitrification strategy involves the use of cryoprotectants to significantly increase the cell viscosity such that when a cell is exposed to cryogenic temperatures the nucleation event for ice formation is completely inhibited [51]. This can be achieved by the addition of cryoprotective additives at very high concentrations [49]. However, the toxicity of the cryoprotectant at the intended concentration must be taken into account [52]. In the recent years, sugars have found a utility in vitrification regimes as effective cryoprotectants especially for mammalian cells. They offer several advantages in regard to substantially increasing the cell viscosity and also protecting cells from shrinkage during the freezing process [53]. Sugars like sucrose, raffinose, trehalose etc have high molecular weights and are capable of forming hydrogen bonds with water. At high concentrations of monosaccharides and disaccharides, sugars render protection by formation of a stable glassy matrix and also by binding to sites previously stabilized by water [54- 59].
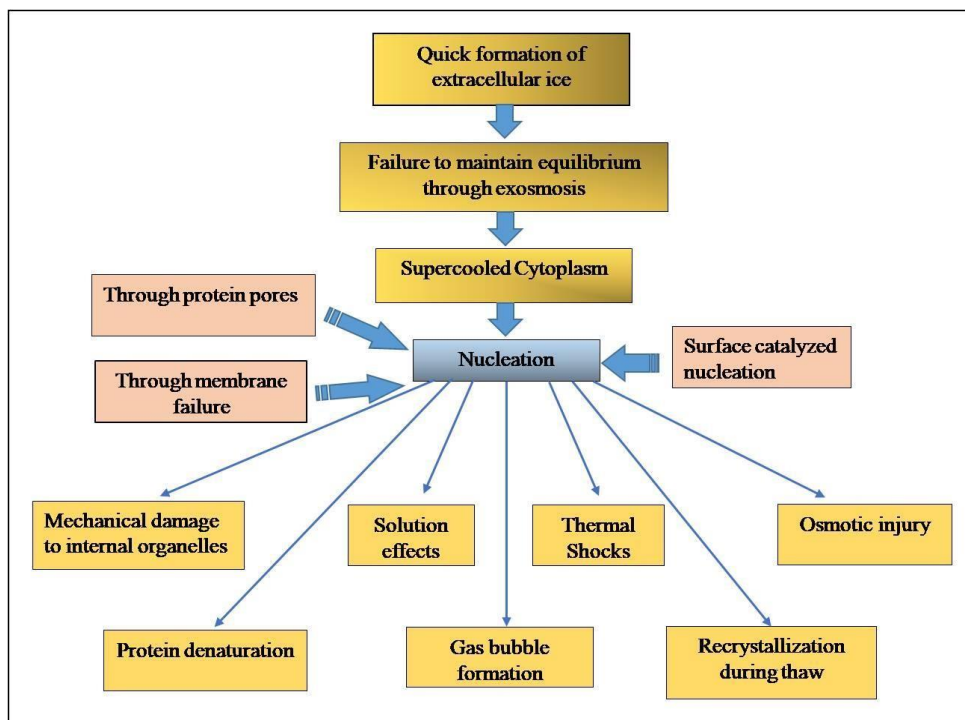
Figure 5. Physical events and possible cryoinjuries during rapid freeze.
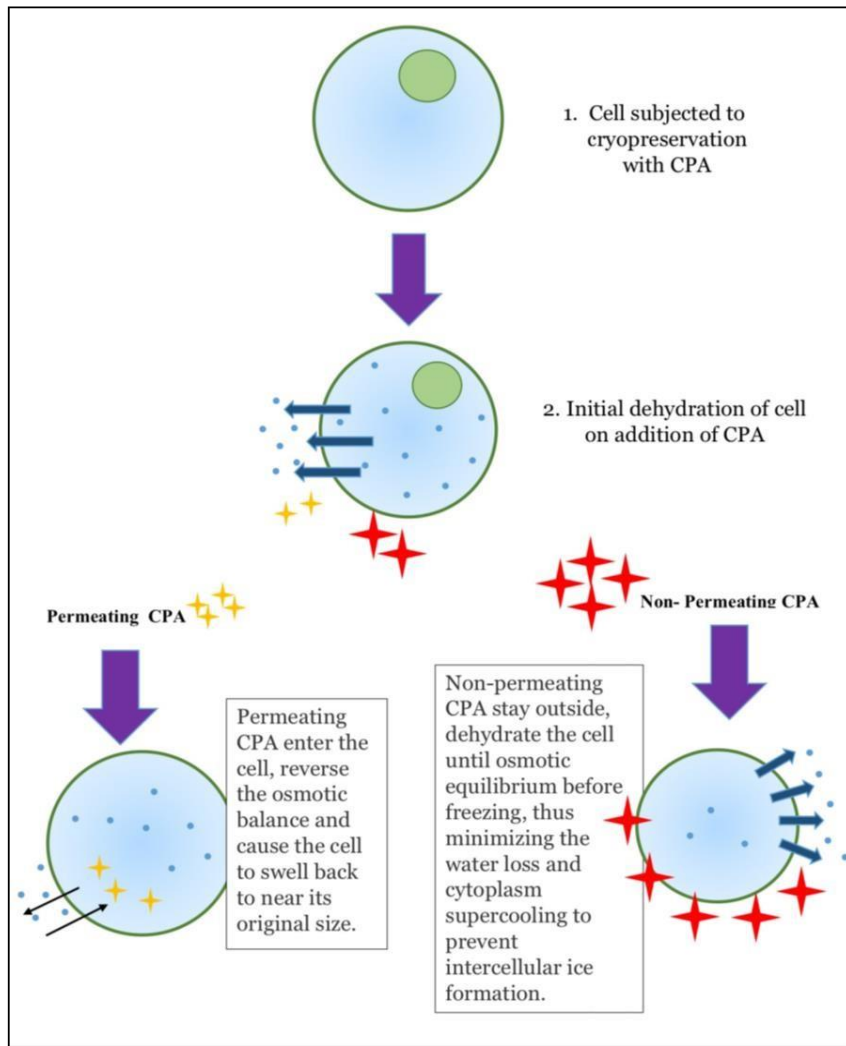
Figure 6. *Mode of action of permeating and non-permeating cryoprotectants.*

9. Applications of Biophysics Understanding
9.1 Selection of Cooling Rates

The rate of cooling imposed during the cryopreservation process greatly determines the cell survival outcome [60-62]. The effect can be explained by an underlying principle described as the inverted "U" of cryobiology (Figure 7). This is based on observations whereby graph plots of cell survival vs. cooling rate imposed on a system take the form of an inverted "U" [3]. This is because, only few cells survive when the cooling rate is very slow and even fewer survive when the rate is high. Cells remain most viable when the cooling rate is optimal which is specific for a cell type. Two opposing damaging factors account for the two arms of the inverted "U": the formation of intracellular ice crystals and dehydration injury. Formation of intracellular crystals is more likely and damaging when the cooling rate is high while dehydration damages are higher at low cooling rates [63].

The injury mechanisms that occur at both slow cooling rates and rapid cooling rates are shown. The maximal cell survival is obtained at the optimal cooling rate. When gradual cooling rates are imposed on cells, as discussed earlier, extracellular ice forms raising the solute concentration on the outside. This creates a differential water gradient and requires water from the interior of the cells to undergo exosmosis to relieve the gradient. This is the basis to the advantage of a slow controlled cooling. Since water is effluxed, the amount of water is reduced within the cell and the chance of more lethal intracellular ice crystal formation is hence minimized. Said differently, the formation of extracellular ice is advantageous since it inhibits the more lethal intracellular ice crystal formation. However, if the cooling rate is too slow, the solute concentration rises sharply causing colligative damage to the cells. Hence, an optimal cooling rate is to be chosen for best survival rates such that only a minimal water remains inside the cells to inhibit ice formation while just the right amount of it is to be removed to prevent colligative solution effects [3].

The real challenge however remains to select the optimal cooling rate since it varies with change in specimen cell type. For example, the optimum cooling rate for mouse marrow stem cells via a study may be concluded at 1°C/min for but may be over 1000°C/min for human red blood cells (RBCs) [3]. Further, the cell survival at a particular cooling rate is also largely determined by the warming and thawing procedure applied. In addition to that, the type of cryoprotectant used and the concentration it is used at further may exert a significant effect on the results.

9.2 Controlling Ice Nucleation

The most significant event in the course of conventional cryopreservation is the nucleation of ice and it has important consequences [4]. Ice nucleation is believed to affect the cell structural, osmotic and colligative properties as well as is capable of causing ruptures and mechanical injuries through same means [5].
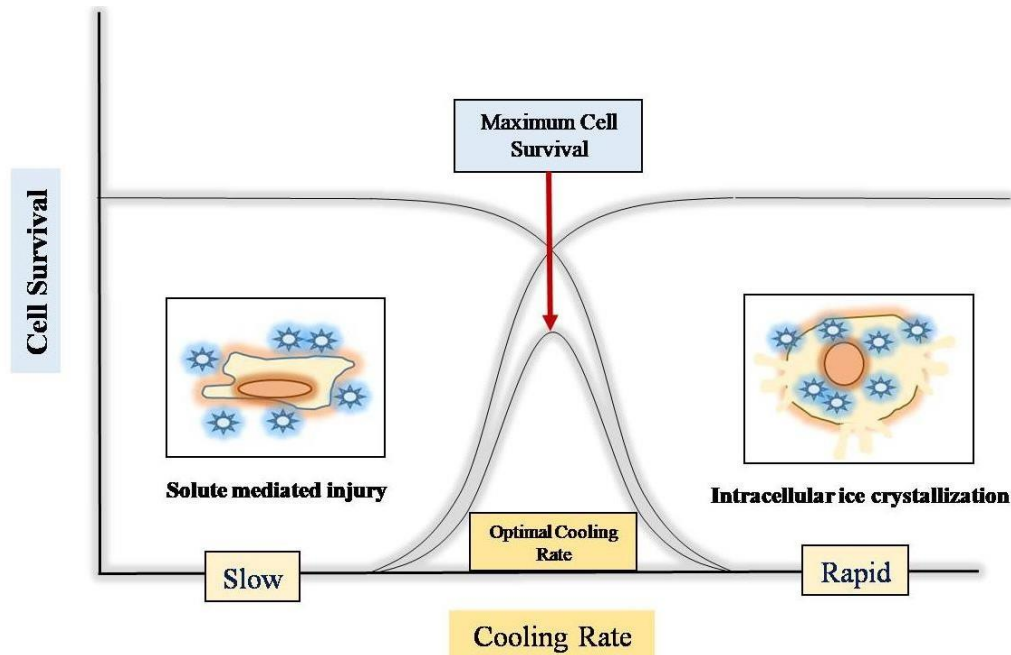
Figure 7. *Cell Survival vs. Cooling Rate Curve.*

"Seeding" refers to one such method wherein an external preformed ice crystal is deliberately introduced as a nucleator into the system at a particular temperature [7,64,65]. A cold spot is generated generally outside of the container to minimize contamination. Seeding works by preventing the supercooling of the specimen and spontaneous nucleation. If such initial transition of liquid to ice is site and time controlled, the subsequent events leading to damage is also surpassed [5]. Ice nucleators can also be formed with the use of 'chemical nucleants', added in the sample medium or by electro-freezing which utilizes a high voltage of electricity to induce crystal formation [66-69]. Alternatively, some mechanical methods exists, which involve disturbing the solution by shaking or tapping [70]. Even the use of ultrasound waves for nucleation is feasible however, the standardization is difficult [71]. Other methods include using cold shocks or pressure shifts which involves exposing the specimen to rapid changes in temperatures and pressure respectively [72,73].

9.3 Selection of Cryoprotectants

Today almost all cryopreservative regimes employ the use of some form of cryoprotective agents during the freezing process [51,52]. With the understanding of the physics of the cryoprotectants and their mode of action, a range of chemicals with one or more cryoprotective action are available. However, on understanding their working mechanism it was also clear that cryoprotectant under use must be non-toxic to the specimen being preserved [52]. This is especially true for permeating cryoprotectants. Nonetheless, non-permeating cryoprotectants also engender the risk of causing osmotic injury [51]. Cryo-conservationists have thus been increasingly exploiting and amalgamating cryoprotectant modalities.

Considering the dynamics of freezing, any cryoprotective agent rendering colligative cryoprotection will be an effective cryoprotectant. If so, it might be able to control the cooling rate and optimize the degree of cell dehydration to avoid both ice damage (caused by insufficient water loss) and colligative damage (caused by excessive water loss) [3].

It has also been shown that the use of a mixture of different cryoprotective additives is advantageous since this might help in nullifying the toxic properties of individual cryoprotectants as well as render the system with synergistic cryoprotective action [74]. The use of a mixture of permeating and non- permeating cryoprotectant is already common for many cryopreservation protocols [1].

9.4 Selection of Thawing and Rewarming Rates

As discussed earlier, the temperature and mode of thaw have as important consequences as the process of freezing employed on specimen survival and proliferation. [75,76] The method chosen however depends on the method of freezing recruited, the cooling rate imposed and the type of cryoprotectants used (Figure 8). Taking into account the biophysical relations of the cells, in general, cells frozen at supra- optimal rates give higher survival when warmed rapidly [16,17]. This is because, a slow warming may cause recrystallization of ice and/or non-uniform expansions and contractions leading to thermal, colligative and osmotic stress. On the other hand, the cells which are cooled at suboptimal rates do not follow the trend (either work oppositely or are unaffected by the warming rate) [18].

10. Increased Interest towards Vitrification

Understanding the basic biology of cryopreservation is an essential step towards achieving successful survival of cells post-thaw [77]. Since cryopreservation by vitrification completely omits ice formation and requires minimal equipment it stands as a promising alternative to conventional methods of freezing [10,11]. From the standpoint of biophysics too, vitrification is highly valuable in that it omits the drastic molecular reorganization that happens in most other freezing strategies and preserves the natural disorder of water molecules and dissolved solutes in cells [11]. This can be highly beneficial since it will allow preserving cells closer to their natural state. Hence, vitrification has gained a lot of attention in the recent years. The key to a successful vitrification regime involves exposing cells to ultralow temperatures with a very high cooling rate, and ensuring arrangements that critically

increase the cell viscosity to the point where ice formation is prevented and the water present turns into an amorphous glassy-solid [10] (Figure 8). This has been shown to be possible by either the use of cryoprotectants at very high concentrations or by the removal of water by techniques like evaporative desiccation and osmotic dehydration prior freezing; both with its own limitations [9,10].

As far as achieving highest cooling rates are concerned, studies have shown that plunging samples directly from air into a cryogenic liquid such as nitrogen, propane or ethane by virtue gives the highest cooling rates (by a factor of 20-100 over previous best practice) [78].

11. Conclusion

A robust protocol development for successful cryopreservation involves understanding the basic principles of the cryopreservation theory. Consequently, scientists can optimize their storage methods leading to enhanced long term preservation of varied specimen collections in a stable cryogenic state.
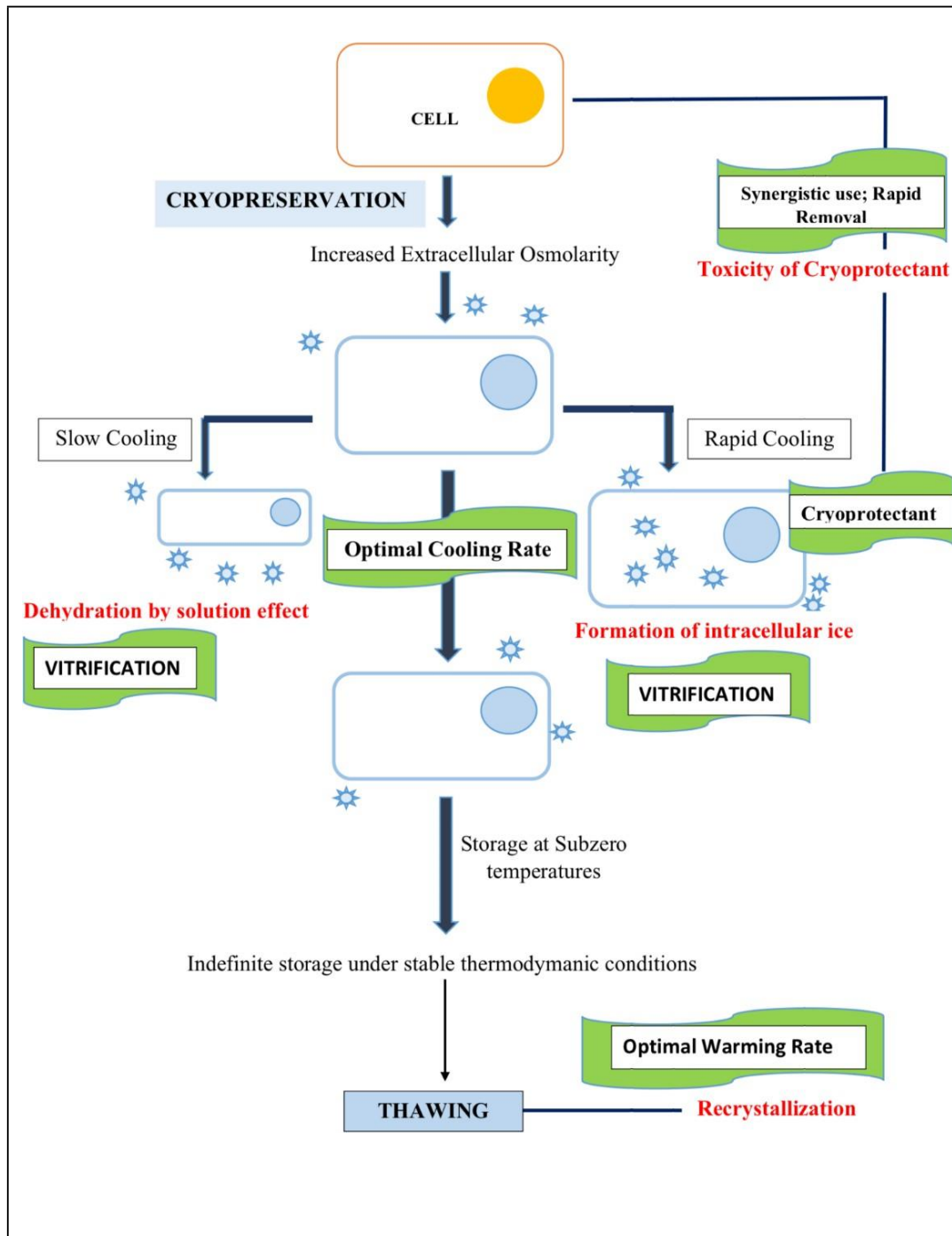
Figure 8. *Physical events, possible cryoinjuries (in red) and solution to injuries (green) during cryopreservation processes.*

References:

[1] Semen Freezing Past Present and Future. 4th Nexus E-bulletin.Indian Fertility Society & Origio India Initiative. 2017.

[2] D. E. Pegg. Principles of cryopreservation. Methods Mol Biol, 368: 39-57, 2007.

[3] P. Mazur. Principles of cryobiology. in Fuller, B.J., Lane, N.L., Benson, E.E. (Eds.), Life in the frozen state. CRC Press LLC, Boca Raton, FL, pp 3–65, 2004.

[4] The Physics of Ice: It All Begins with Nucleation. Alex Esmon 12.18.2014. Thermofisher Scientific.

[5] G. J. Morris, E. Acton. Controlled ice nucleation in cryopreservation – A review. Cryobiology, vol. 66, No. 2, pp.85-92, 2013.

[6] P. Mazur. Freezing of living cells: Mechanisms and implications, Am. J. Physiol. 247, C125–C142, 1984.

[7] P. Mazur, S. Leibo, E. Chu. A two-factor hypothesis of freezing injury. Evidence from hamster tissue-culture cells. Exp. Cell Res, vol. 71, No.2, pp. 345-355, 1972.

[8] J. E. Lovelock. The haemolysis of human red blood cells by freezing and thawing. Biochim. Biophys. Acta. Vol.10, pp. 414– 426, 1953.

[9] D.E. Pegg. Principles of cryopreservation. Methods Mol Biol. Vol. 1257, No. 3, pp.19, 2015.

[10] Principles of Cryopreservation by Vitrification Authors: Gregory M. Fahy Brian Wowk Series: Methods In Molecular Biology > Book: Cryopreservation and Freeze-Drying Protocols. 2015. Springer Protocols. Springer-Verlag New York. Humana Press. Willem F. Wolkers, Harriëtte Oldenhof (eds.).

[11] B. Wowk. Thermodynamic aspects of vitrification. Cryobiology. Vol. 60, No.1, pp. 11-22, 2010.

[12] N. Chao, I. Chiu Liao. Cryopreservation of finfish and shellfish gametes and embryos, Editor(s): Cheng-Sheng Lee, Edward M. Donaldson, Reproductive Biotechnology in Finfish Aquaculture, Elsevier, pp.161-189, 2001.

[13] G. M. Fahy. Biological Effects of Vitrification and Devitrification. In: D.E. Pegg, A.M. Karow (eds) The Biophysics of Organ Cryopreservation. NATO ASI Series (Series A: Life Sciences), Springer, Boston, MA, vol. 147, 1987.

[14] S. Seki and P. Mazur. Effect of warming rate on the survival of vitrified mouse oocytes and on the recrystallization of intracellular ice. Biology of reproduction. Vol. 79, No. 4, pp. 727–737, 2008.

[15] W. F. Rall. Factors affecting the survival of mouse embryos cryopreserved by vitrification. Cryobiology. Vol. 24, No. 5, pp.387-402, 1987.

[16] A. S. Teixeira, M. E. González-Benito, A. D. Molina-García. Measurement of cooling and warming rates in vitrification-based plant cryopreservation protocols. Biotechnol Prog. Vo. 30, No. 5, pp. 1177-84, 2014.

[17] S. Seki and P. Mazur. The dominance of warming rate over cooling rate in the survival of mouse oocytes subjected to a vitrification procedure. Cryobiology. Vol. 59, No. (1), 75–82, 2009.

[18] Reed, M. Barbara. Plant Cryopreservation: A Practical Guide. Springer Science & Business Media, Springer-Verlag New York Inc, 2008.

[19] S. Hamamah, D. Royere, J.C. Nicolle, M. Paquignon, J. Lansac. Effects of freezing- thawing on the spermatozoon nucleus: a comparative chromatin cytophotometric study in the porcine and human species. Reprod. Nutr. Dev. Vol.30, pp. 59-64, 1990.

[20] S. Succu, D. Bebbere, L. Bogliolo, et al. Vitrification of in vitro matured ovine oocytes affects in vitro preimplantation development and mRNA abundance. Mol. Reprod. Dev. Vol.75, pp. 538-546, 2008.

[21] M. Tachataki, R.M.L Winston, D.M Taylor. Quantitative RT-PCR reveals tuberous sclerosis gene, TSC2, mRNA degradation following cryopreservation in the human preimplantation embryo. Mol. Hum. Reprod. Vol. 9, pp. 593-601, 2003.

[22] T.C Fisher, S. Groner, U. Zentgraf, V. Hemleben. Evidence for nucleosomal phasing and a novel protein specifically binding to cucumber satellite DNA. Z. Naturforsch. Vol. 49, pp.79-86, 1994.

[23] S.I Peris, A. Morrier, M. Dufour, J.L Bailey. Cryopreservation of ram semen facilitates sperm DNA damage: relationship between sperm andrological parameters and the sperm chromatin structure assay. J. Androl. Vol. 25, pp. 224-233, 2004.

[24] J. E. Lovelock. The mechanism of the protective action of glycerol against haemolysis by freezing and thawing, Biochim. Biophys. Acta. Vol. 11, pp. 28–36, 1953.

[25] H. T. Meryman. The exceeding of a minimum tolerable cell volume in hypertonic suspension as a cause of freezing injury, in The Frozen Cell, Wolstenholme, G.E. and O'Connor, M., Eds., Churchill, London, pp. 51–64, 1970.

[26] H. T. Meryman. Freezing injury and its prevention in living cells, Annu. Rev. Biophys. Vol. 3, pp. 341–363, 1974.

[27] P.L. Steponkus and S.C. Wiest. Plasma membrane alterations following cold acclimation and freezing, in Plant Cold Hardiness and Freeze Stress—Mechanisms and Crop Implications, Li, P.H. and Sakai, A., Eds., Academic Press, New York, pp. 75–91, 1978.

[28] P. Mazur. Kinetics of water loss from cells at subzero temperatures and the likelihood of intracellular freezing, J. Gen. Physiol. Vol. 47, pp. 347–369, 1963.

[29] A.M.M. Zade-Oppen. Posthypertonic hemolysis in sodium chloride systems, Acta Physiol. Scand. Vol. 73, pp. 341–364, 1968.

[30] J. A. Elliott. Intracellular ice formation: the enigmatic role of cell-cell junctions. Biophys J. Vol. 105, No. 9, pp. 1935-1936, 2013.

[31] P. Mazur. The role of cell membranes in the freezing of yeast and other single cells, Ann. N.Y. Acad. Sci. Vol. 125, pp. 658–676, 1965.

[32] J.P. Acker and L.E. McGann. Membrane damage

occurs during the formation of intracellular ice, Cryo-Letters. Vol. 22, pp. 241–254, 2001.

[33] W.K. Berger and B. Uhrik. Freeze-induced shrinkage of individual cells and cell-to-cell propagation of intracellular ice in cell chains from salivary glands, Experientia. Vol. 52, pp. 843–850, 1996.

[34] E. Asahina. Frost injury in living cells. Nature. Vol. 196, pp. 445–446, 1962.

[35] P.L. Steponkus, D. Stout, J. Wolfe, R. Lovelace. Freeze-induced electrical transients and cryoinjury, Cryo-Letters. Vol. 5, pp. 343–348, 1984.

[36] K. Muldrew and L.E. McGann. Mechanisms of intracellular ice formation, Biophys. J. Vol. 57, pp. 525–532, 1990.

[37] M. Toner, E.G. Cravalho, M. Karel. Thermodynamics and kinetics of intracellular ice formation during freezing of biological cells, J. Appl. Phys. Vol. 67, pp. 1582–1593, 1990.

[38] J.O.M. Karlsson. A theoretical model of intracellular devitrification, Cryobiology. Vol. 42, pp. 154–169, 2001.

[39] J. Farrant and G.J. Morris. Thermal shock and dilution shock as the causes of freezing injury, Cryobiology. Vol. 10, pp. 134–140, 1973.

[40] J. Farrant, C.A. Walter, H. Lee, L.E. McGann. Use of two-step cooling procedures to examine factors influencing cell survival following freezing and thawing, Cryobiology. Vol. 14, pp. 273–286, 1977.

[41] J. Levitt. A sulfhydryl-disulfide hypothesis of frost injury and resistance in plants, J. Theor. Biol. Vol. 3, pp. 355–391, 1962.

[42] M.J. Ashwood-Smith, G.W Morris, R. Fowler, T.C. Appleton, R. Ashorn. Physical factors are involved in the destruction of embryos and oocytes during freezing and thawing procedures, Hum. Reprod. Vol. 3, pp.795–802, 1988.

[43] G.J. Morris and J.J. McGrath. Intracellular ice nucleation and gas bubble formation in spirogyra, CryoLetters. Vol. 2, pp. 341–352, 1981.

[44] P.L. Steponkus and M.F Dowgert. Gas bubble formation during intracellular ice formation. CryoLetters. Vol. 2, pp. 42–47, 1981.

[45] K. Shimada and E. Asahina. Visualization of intracellular ice crystals formed in very rapidly frozen cells at –27°C. Cryobiology. Vol. 12, pp. 209–218, 1975.

[46] J.C. Bischof and B. Rubinsky. Large ice crystals in the nucleus of rapidly frozen liver cells. Cryobiology. Vol. 30, pp. 597–603, 1993.

[47] T.H. Jang, S.C. Park, J.H. Yang, et al. Cryopreservation and its clinical applications. Integr Med Res. Vol. 6, No. 1, pp.12-18, 2017.

[48] H. Sieme, H. Oldenhof, W.F. Wolkers. Mode of action of cryoprotectants for sperm preservation. Anim Reprod Sci. Vol.169, pp.2-5, 2016.

[49] V. Berejnov, N. S. Husseini, O. A. Alsaied, R.E. Thorne. Effects of cryoprotectant concentration and cooling rate on vitrification of aqueous solutions. J. Appl. Cryst. Vol. 39, pp. 244-251, 2006.

[50] J. Sztein, K. Noble, J. Farley, L. Mobraaten. Comparison of Permeating and Nonpermeating Cryoprotectants for Mouse Sperm Cryopreservation. Cryobiology. Vol. 42, No. 1, pp.28-39, 2001.

[51] G. D. Elliott, S. Wang, B.J. Fuller. Cryoprotectants: A review of the actions and applications of cryoprotective solutes that modulate cell recovery from ultra-low temperatures. Cryobiology. Vol. 76, pp.74- 91, 2017.

[52] B. P. Best. Cryoprotectant Toxicity: Facts, Issues, and Questions. Rejuvenation research, 18(5), 422–436, 2015.

[53] S. Tsai, G. Chong, P. J. Meng, C. Lin. Sugars as supplemental cryoprotectants for marine organisms. Rev Aquacult. Vol. 10, pp. 703-715, 2018.

[54] J. Buitink, M.M.A.E Claessens, M.A. Hemminga, F.A Hoekstra. Influence of water content and temperature on molecular mobility and intracellular glasses in seeds and pollen, Plant Physiol. Vol. 118, pp. 531–541, 1998.

[55] J.H. Crowe, J.F. Carpenter, L.M. Crowe. The role of vitrification in anhydrobiosis, Annu. Rev. Physiol. Vol. 60, pp. 73–103, 1998.

[56] J. Wolfe, G. Bryant. Freezing, drying, and/or vitrification of membrane–solute–water systems, Cryobiology. Vol. 39, pp. 103– 129, 1999.

[57] B.P. Gaber, I. Chandrasekhar, N. Pattabiraman. The interaction of trehalose with the phospholipid bilayer: A molecular modeling study, in Membranes, Metabolism and Dry Organisms, Leopold, A.C., Ed., Cornell University Press, Ithaca, NY, pp. 231–241, 1986.

[58] J.H. Crowe, J.F. Carpenter, L.M. Crowe. Preserving dry biomaterials: The water replacement hypothesis, Part 1, Biopharm. Vol. 4, pp. 28–33, 1993.

[59] J.H. Crowe, J.F. Carpenter, L.M. Crowe. Preserving dry biomaterials: The water replacement hypothesis, Part 2, Biopharm. Vol. 5, pp. 40–43, 1993.

[60] J. M. Zhang, Y. Sheng, Y. Z Cao, H. Y Wang, Z. J Chen. Effects of cooling rates and ice-seeding temperatures on the cryopreservation of whole ovaries. Journal of assisted reproduction and genetics. Vol. 28, No.7, pp. 627–633, 2011.

[61] C.J. Hunt. Cryopreservation: Vitrification and Controlled Rate Cooling. Methods Mol Biol. Vol. 1590, pp.41-77, 2017.

[62] S. Sukumar, S.P Kar. Numerical analysis of an enhanced cooling rate cryopreservation process in a biological tissue, Journal of Thermal Biology. Vol. 81, pp. 146-153, 2019.

[63] D. Gao, J. K Critser. Mechanisms of Cryoinjury in Living Cells. ILAR Journal. Vol. 41, No. 4, pp.187–196, 2000.

[64] S.P. Leibo, J. Farrant, P. Mazur, M.G. Hanna, L.H Smith. Effects of freezing of marrow stem cell suspensions: interaction of cooling and warming rates in the presence of PVP, sucrose and Glycerol.

Cryobiology. Vol. 6, pp.315–332, 1979.

[65] D.G Whittingham. Some factors affecting embryo storage in laboratory animals, in: K. Elliot, J. Whelan (Eds.), The Freezing of Mammalian Embryos. Ciba Foundation 52, Elsevier, Amsterdam, pp. 97–127, 1977.

[66] G. Missous, B. Thammavongs, V.M. Dieuleveux, M. Guéguen, J.M Panoff. Improvement of the cryopreservation of the fungal starter Geotrichum candidum by artificial nucleation and temperature downshift control, Cryobiology. Vol. 55; pp. 66–71, 2007.

[67] Y. Sugawara, A. Ichi-Ishi. Application of ''CryoSeeds'' in the cryopreservation of cultured plant cells and tissues, Plant Tissue Cult. Lett. Vol. 9, pp. 47–50, 1992.

[68] T. Kojima, T. Soma, N. Oguri. Effect of ice nucleation by droplet of immobilized silver iodide on freezing of rabbit and bovine embryos, Theriogeneology. Vol. 30; pp. 1199–1207, 1988.

[69] A. Petersen, H. Schneider, G. Rau, B. Glasmacher. A new approach for freezing of aqueous solutions under active control of the nucleation temperature, Cryobiology. Vol. 53; pp. 248–257, 2006.

[70] P.V Hobbs. Ice Physics, Clarendon Press, Oxford, 1974.

[71] S. Passot, I.C. Trelea, M. Marin, M. Galen, G.J. Morris, F. Fonseca. Effects of controlled ice nuicleation on primary drying stage and protein receovery in vials cooled in a modified freeze-dryer, J. Biomech. Eng.

Vol. 131; pp. 1–5, 2009.

[72] R. Heidemann, M. Mered, D.Q. Wang, B. Gardner, C. Zhang, J. Michaels, H. J. Henzler, N. Abbasa, K. Konstantinov. A new seed train expansion method for recombinant mammalian cell lines, Cytotechnology. Vol 38; pp 99–108, 2002.

[73] A.K. Konstantinidis, W. Kuu, L. Otten, S.L. Nail, R.R. Sever. Controlled nucleation in freeze drying: effects of pore size in the dried product layer, mass transfer resistance, and primary drying rate, J. Pharm. Sci. Vol 100, pp. 3453–3470, 2011.

[74] G.M. Fahy. The relevance of cryoprotectant "toxicity" to cryobiology. Cryobiology. Vol. 23, No. 1, pp.1-13, 1986.

[75] G. Verheyen, I. Pletincx, A. Van Steirteghem. Effect of freezing method, thawing temperature and post-thaw dilution/washing on motility (CASA) and morphology characteristics of high-quality human sperm. Hum Reprod. Vol. 8, No.10, pp.1678-84, 1993.

[76] J.O. Nöthling, R. Shuttleworth. The effect of straw size, freezing rate and thawing rate upon post-thaw quality of dog semen. Theriogenology. Vol. 15, No.5, pp.1469-80, 2005.

[77] Y. Sharma, M. Sharma. Sperm cryopreservation: Principles and Biology. J Infertil Reprod Biol. Vol. 8, No. 3, pp. 43- 48, 2020.

[78] M. Warkentin, V. Berejnov, R.E. Thorne. Hyperquenching for Protein Crystallography. J. Appl. Cryst. Vol. 39, pp. 805-811, 2006.

Enhancing Benefits by Rectification in the Absorption Refrigeration Systems

Salek Malaine[1*], N. Ababssi[1], M. Charia[2], A. Boulal[1]

[1] Mechanical Engineering, Industrial Management and Innovation Lab (MEIMI Lab), Faculty of Science and Technology, Hassan First University of Settat, Casablanca road, Km 3.5, P.O. Box 577, Settat, Morocco, 26000
[2] Team of Thermodynamic and Energetic, Faculty of Sciences, Mohammed V University in Rabat, 4 Ibn Battouta street, P.O. Box 1014, Rabat, Morocco, 10000
E-mail: [1*]s.malaine@uhp.ac.ma

Abstract

The main objective of this article aims to enhance a single stage absorption refrigeration machine, using the ammonia-water pair as working fluid, and this from the improvement of its exergetic performances by means of a vapor rectification system. The rectifier makes it possible to emit a vapor enriched in pure fluid (ammonia) with a high flow rate; this one is thus transformed into condensate after condensation; as it also allows evacuating a liquid (water) in the form of reflux. Moreover, in order to show the role of the rectifier and to highlight its impact on the operation of the proposed installation, the methodology adopted in this work aims to develop a thermodynamic model of numerical simulation using the FORTRAN language according to two approaches. An energetic analysis approach which aims to assess, in a first time, the performance of the studied refrigeration installation. However, the exergetic approach tries to calculate the exergy efficiency, and thus to evaluate the losses of exergies of the refrigeration installation in a second time. Therefore, the obtained results showed a clear improvement in the exergetic efficiency, accompanied against by an optimization of the losses of exergies which are due to the irreversibility of the studied thermodynamic system. The novelty brought by the present study encourages the engineers and manufacturers to realize the future absorption refrigeration machines integrating rectifier systems.

Keywords: Rectifier; simulation model; exergetic efficiency; exergy loss; exergy transfer.

1. Introduction

Absorption refrigeration machines are a hot topic of research today. They arouse growing interest, thanks to their advantages such as the use of low quality heat sources and environmentally friendly working fluid pairs [1]. Among the most used couples in this topic, there are available binary mixtures for these systems, such as lithium bromide-water ($LiBr-H_2O$) and ammonia-water (NH_3-H_2O) [2]. The main problem with $LiBr-H_2O$ fluids mixture is the crystallization of the system [3], while the NH_3-H_2O couple can cause corrosion of the installation. Since, the ammonia has been used as refrigerant in absorption cooling systems for a long time [4]; the choice of the binary ammonia-water solution (H_2O-NH_3) as the working fluid of the refrigeration machine [5-6] refer to this mixture presents very interesting characteristics and advantages [7], in particular when attempting to produce cold at temperatures below zero degree Celsius [8-9]. In other words, improving a machine reverts to improving its performances. In this respect, many previous studies and research have been carried out to develop methods of improving the performance of absorption refrigeration systems, in order to make these refrigeration technologies more competitive compared with the conventional compression refrigeration systems [1]. A recently published study by Li Jianbo [10] analyzed and evaluated a new combined absorption-compression refrigeration cycle that can result in waste heat from an internal combustion engine in overloaded vehicles, ships or diesel generators. The results of the theoretical calculation

showed that the proposed cycle of the combined absorption-compression system had a higher coefficient of performance than the compression refrigeration cycle. Two other new hybrid absorption-compression refrigeration systems, using R1234yf/ionic liquid as a mixture of working fluids, have been proposed and analyzed by X. Liu et al [11] in order to improving their performance. For these last two systems, the compressors were placed respectively between the generator and the condenser on one side, and between the absorber and the evaporator on the other side, in order to study the effect of the position of the compressor on the performance of the installations. These studies showed that a greater improvement in COP related to the system with a compressor installed between the absorber and the evaporator. Massamba Thioye [12] exhibited an improvement in the performance of absorption refrigeration machines by the use of staged absorption and desorption cycles consuming energy in the form of heat with low exergetic value. J.Dardouch, M.Charia et al [13] studied energetically, the single absorption refrigeration machine with a distillation column. From this study, it emerges a high performance and optimal operation of the machine in a Moroccan climate. However, the implementation of this installation requires a further study, taking into account the economic aspect based on an exergetic analysis in order to assess the cost of profitability and investment linked to the manufacturing conditions of the refrigeration machine in question. In view of reducing the manufacturing conditions of the absorption refrigeration machine, the installation of a distillation

column was omitted by the authors M. Ahachad, M. Charia and A. Bernatchou in [14] who carried out a study of the single-stage absorption machine equipped with a bubbling system; and which can act as a distillation stage. Moreover, the study showed that the improved solar refrigeration machine could produce cooling with attractive performance while maintaining the simplicity of the machine. It should be therefore noted that the exergetic analysis was not addressed in this latest study. For this purpose, in thermodynamics, the energetic analysis according to the first law based on the laws of conservation of mass and energy alone remains insufficient to assess the efficiency of such a refrigeration system. Yet, the employment of the second law of thermodynamics, to perform an exergetic analysis of a system is extremely necessary to describe exhaustively qualitatively and quantitatively, the evaluation of the efficiency of this system. In this context, the following question arises:

How can we contribute, through this work, to improving the exergetic efficiency of the refrigeration machine with rectifier, and highlight its repercussion on its irreversibility based on the first and second laws of thermodynamics?

To answer this problem, this work was organized around three axes:

The first axis deals with a description of the proposed refrigeration installation. The second axis presents the thermodynamic analysis procedure, as well as the methodology to be adopted to initiate this study. The third axis describes and interprets the obtained results.

2. The proposed system design

The present work concerns the study of performance improvement by a rectification system of a single-stage absorption refrigeration machine illustrated in Figure 1.

2.1 Absorption frigorific installation without rectifier

The absorption refrigeration machine is composed of a boiler, a condenser, an evaporator, an absorber, two expansion valves and two heat exchangers. In this frigorific installation, we must distinguish between two circuits:

The refrigerant circuit is located between the boiler and the condenser, the evaporator and the absorber, and the circuit of the refrigerant-absorbent solution between the absorber and the boiler (Figure 1 (a)).

Like the compression machine, the absorption machine has low pressure inside the evaporator, and high pressure inside the condenser.

2.2 Absorption frigorific installation with rectifier

It is an absorption refrigeration installation, operating with the water-ammonia couple, ammonia is the refrigerant and water is the absorbent [15]. This system is composed of the same elements as the single-stage refrigeration machine, but equipped by rectifier installed at the outlet of the boiler.

In the stationary regime, the operation of the refrigeration installation (Figure 1 (b)) can be summarized as follows:

In the evaporator traversed by a water circuit, the refrigerant (here ammonia) is vaporized in a very low pressure environment. However, the amount of heat from the environment to be cooled at temperature T_F causes boiling the refrigerant (NH_3) by extracting heat from this water which is thus cooled. The produced vapors are absorbed by a poor solution in the absorber which contains the absorbent solution at ambient temperature T_M. The rich solution, before entering the boiler, is therefore sent by a pump to supply the rectifier, undergoing heating through the passage by a heat exchanger (HE 2). From the rectifier, a part of water in the form of reflux is routed to the boiler. It receives heat at the temperature T_B which causes desorption of the refrigerant. While, the vapor coming out from the boiler reverse, by putting in equilibrating, the rich solution in a rectifier which is located at temperature lower than that of the boiler, and subsequently the vapor leaving from this latter is enriched in ammonia. This system can be considered as a single stage distiller. The impoverished solution is cooled via HE 2 and returns to the absorber through an expansion valve (EV 2). Finally, the vapors leaving the high pressure rectifier are sent to the condenser, and the liquid leaving the latter is thus sent to the evaporator through an expansion valve (EV 1) undergoing cooling via the passage through a heat exchanger (HE 1) to start again, a new thermodynamic cycle.
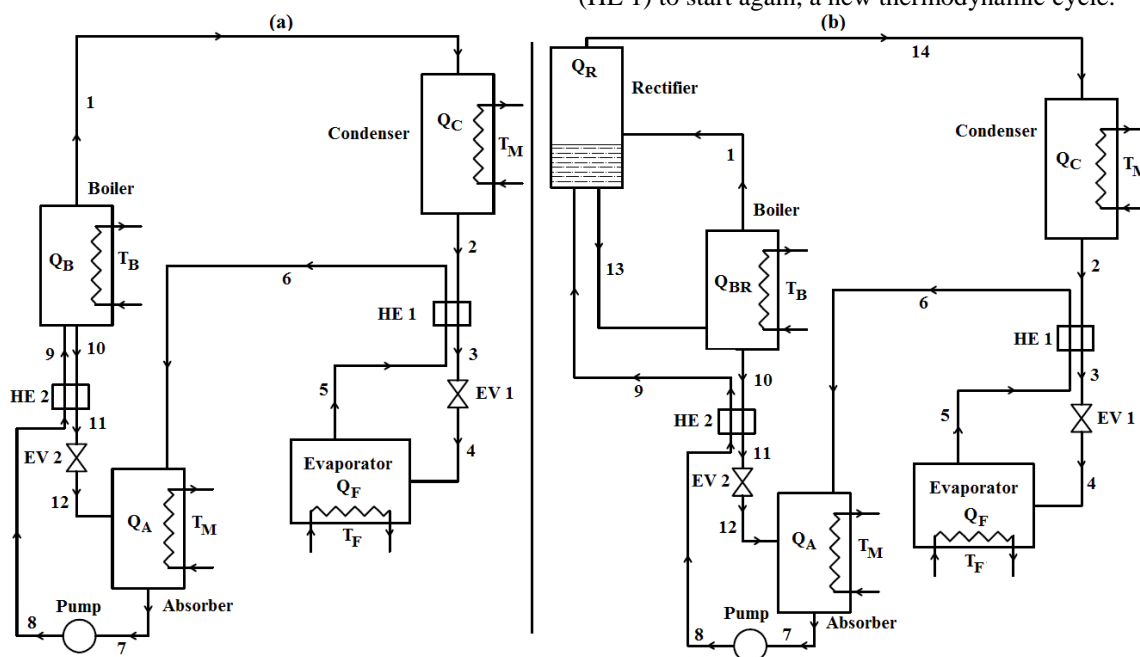
Figure 1. Schematic diagram of a single-stage absorption refrigeration machine: without rectifier (a); with rectifier (b)

3. Thermodynamic analysis methodology
3.1 Energetic analysis approach
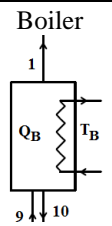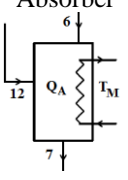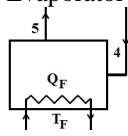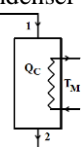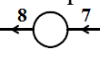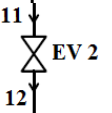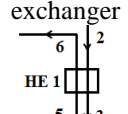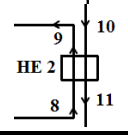
According to the first principle of thermodynamics, the energetic analysis of the refrigeration system is based on the establishment of the mass and energy balances of the various elements of the refrigeration machine [16], from the application of the following equations [17]:

$$\sum \dot{m}_{in} = \sum \dot{m}_{out} \tag{1}$$

$$\sum_i Q_i + W = \sum_{out} \dot{m}_{out}.h_{out} - \sum_{in} \dot{m}_{in}.h_{in} \tag{2}$$

Table 1. Modeling of mass and energetic balances of the simple absorption refrigeration machine without rectifier.
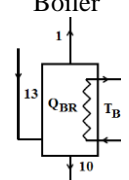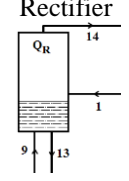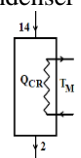
Components	Mass balances; mass concentration; energetic balances
Boiler	$\dot{m}_1 + \dot{m}_{10} = \dot{m}_9$ (3) $\dot{m}_1.Y_1 + \dot{m}_{10}.X_{10} = \dot{m}_9.X_9$ (4) $Q_B = \dot{m}_1 h_1 + \dot{m}_{10} h_{10} - \dot{m}_9 h_9$ (5)
Absorber	$\dot{m}_7 = \dot{m}_6 + \dot{m}_{12}$ (6) $\dot{m}_7.X_7 = \dot{m}_6.Y_6 + \dot{m}_{12}.X_{12}$ (7) $Q_A = \dot{m}_7.h_7 - \dot{m}_6.h_6 - \dot{m}_{12}.h_{12}$ (8)
Evaporator	$\dot{m}_4 = \dot{m}_5 = \dot{m}_1$ (9) $Q_F = \dot{m}_1.(h_5 - h_4)$ (10)
Condenser	$\dot{m}_1 = \dot{m}_2$ (11) $Q_C = \dot{m}_1.(h_2 - h_1)$ (12)
Pump	$\dot{m}_7 = \dot{m}_8$ (13) $\dot{W}_P = \dot{m}_7.(h_7 - h_8)$ (14)
Expansion valve	$\dot{m}_3 = \dot{m}_4$ (15) $h_3 = h_4$ (16) $\dot{m}_{11} = \dot{m}_{12}$ (17) $h_{11} = h_{12}$ (18)
Heat exchanger	$\dot{m}_2 = \dot{m}_3$ (19) $\dot{m}_5 = \dot{m}_6$ (20) $\dot{m}_6.(h_6 - h_5) = \dot{m}_2.(h_2 - h_3)$ (21) $\dot{m}_8 = \dot{m}_9$ (22) $\dot{m}_{10} = \dot{m}_{11}$ (23) $\dot{m}_9.(h_9 - h_8) = \dot{m}_{10}.(h_{10} - h_{11})$ (24)

With: $\dot{m}, Q_i, W$ and h represent the mass flow rate (kg/sec), heat transfer rate (kW), mechanical power (kW) and enthalpy (kJ/kg), respectively. The abbreviations in and out denote the input and output of the system.

By applying the two equations 1 and 2, the model thus established makes it possible to calculate the quantities of heat exchanged at the level of each component of the refrigeration machine.

Table 1 illustrates the mathematical modeling of the mass and energetic balances of the various components of the simple absorption refrigeration machine without rectifier. The configuration shown in table 1 remains applicable even for the configuration of the machine with rectifier, but with adoption of the new modification shown in table 2 relating to figure 1 (b). Then, table 2 represents the mathematical modeling of the mass and energetic balances of the various components of the refrigeration machine with rectifier.

Table 2. Modeling of mass and energetic balances of the simple absorption refrigeration machine with rectifier.

Components	Mass balances; mass concentration; energetic balances
Boiler	$\dot{m}_1 + \dot{m}_{10} = \dot{m}_{13}$ (25) $\dot{m}_1.Y_1 + \dot{m}_{10}.X_{10} = \dot{m}_{13}.X_{13}$ (26) $Q_{BB} = \dot{m}_1.h_1 + \dot{m}_{10}.h_{10} - \dot{m}_1.h_{13}$ (27)
Rectifier	$\dot{m}_{14} + \dot{m}_{13} = \dot{m}_1 + \dot{m}_9$ (28) $\dot{m}_{14}.Y_{14} + \dot{m}_{13}.X_{13} = \dot{m}_1.Y_1 + \dot{m}_9.X_9$ (29) $Q_R = \dot{m}_{14}.h_{14} + \dot{m}_{13}.h_{13} - \dot{m}_1.h_1 - \dot{m}_9.h_9$ (30)
Condenser	$\dot{m}_{14} = \dot{m}_2$ (31) $Q_C = \dot{m}_{14}.(h_2 - h_{14})$ (32)

3.2 Exergetic analysis approach
3.2.1 Generality on the exergy concept

Before performing the exergetic mathematical modeling, it is necessary to define the concept of exergy:

Exergy is the usable part of an amount of energy [18]. It is a quantity allowing to measuring the quality of energy in a system [19-20]. Based on the fundamental principles of this concept [19], the exergy analysis methods help to analyze the irreversibility of a frigorific system [21], with a view to improving these performances by relying on the first and second laws of thermodynamics [22]. They allow energy resources to be used more efficiently [23]. The exergetic analysis is one of the methods applied in various fields of energetic engineering [24], namely cooling and refrigeration to study especially the exergy destroyed [25] in thermodynamic system [26], with a view to minimizing them and maximizing their performance [22]. Nevertheless, the exergy balance describes how much an amount of energy in a process is consumed by it [23].

In this work, the exergy analysis methods to be applied to the machine in a stationary regime, and are dependent on the analysis of the exergy balances on the one hand, and on

the evaluation of the exergy losses of the various elements of the machine on the other hand. The exergy at any point of a thermodynamic cycle of a refrigerating machine is expressed by the following equation [24, 27-28]:

$$E_x = \dot{m}[(h - h_0) - T_0(s - s_0)] \tag{33}$$

Where:
- s is the entropy (kJ/kg.K).
- T_0 is the ambient temperature.
- h_0 and s_0 are the enthalpy and the entropy under the standard conditions, respectively.

3.2.2 Formulation of exergetic balance

By application of the first and second law of thermodynamics, and based on equation (2) and the entropy balance expressed by the following equation (Eq. (34)):

$$\sum_{out} \dot{m}_{out} \cdot s_{out} = \sum_{in} \dot{m}_{in} \cdot s_{in} + \sum_i \frac{Q_i}{T_i} + \mathcal{P} \tag{34}$$

Where $\mathcal{P}$ is the entropy due to the irreversibility of system.

Multiplying Eq. (34) by T_0 a makes it possible to write:

$$\sum_{out} \dot{m}_{out} \cdot T_0 \cdot s_{out} = \sum_{in} \dot{m}_{in} \cdot T_0 \cdot s_{in} + \sum_i \frac{T_0}{T_i} Q_i + T_0 \mathcal{P} \tag{35}$$

The system of Eq. (2) and Eq. (35) becomes:

$$\sum_{out} \dot{m}_{out} \cdot T_0 \cdot s_{out} + \sum_i Q_i + W = \sum_{in} \dot{m}_{in} \cdot T_0 \cdot s_{in} + \sum_i \frac{T_0}{T_i} Q_i + T_0 \mathcal{P} + \sum_{out} \dot{m}_{out} \cdot h_{out} - \sum_{in} \dot{m}_{in} \cdot h_{in} \tag{36}$$

Eq. (36) is equivalent to:

$$T_0 \cdot \mathcal{P} = \left(\sum_{in} Ex_{in} - \sum_{out} Ex_{out}\right) + \sum_i Q_i \left(1 - \frac{T_0}{T_i}\right) + W \tag{37}$$

With:
- $T_0 \cdot \mathcal{P} = Ex_l$ is the exergy loss.
- Ex_{in}, Ex_{out} represent the exergy at the entry and exit of system, respectively.

We obtain therefore, the fundamental equation designated below Eq. (38), which establishes the exergy balance relating to the refrigeration system.

$$\Delta Ex + \mathcal{P}_{exergie} = \sum_i Q_i \left(1 - \frac{T_0}{T_i}\right) + W \tag{38}$$

It follows that, the second term to perceive adroitly from Eq. (37) represents the irreversibility of the system, thus defined by the following equation [29]:

$$I = E_{x_{D,j}} = \sum Ex_{in} - \sum Ex_{out} + \sum[Q(1 - \frac{T_0}{T})]_{in} - \sum[Q(1 - \frac{T_0}{T})]_{out} + \sum W_{in} - \sum W_{out} \tag{39}$$

Where $E_{x_{D,j}}$ is the exery destruction for the element j (kW).

In operation condition, the irreversibility of components of system was significant high when the exergy consumption is reduced [28]. The total exergy destruction (or total irreversibility) of the absorption machine is simply quantified [30] by the sum of exergy destruction in each component [3] and is given by [31]:

$$E_{x_{D,tot}} = \sum_{j=1}^{n} E_{x_{D,j}} \tag{40}$$

With: n is the number of considered components of system.

Generally, the main objective of the exergetic analysis is to determine the location of exergy losses (affecting the production of system) and the amount of exergy destruction production during the different processes of a thermodynamic cycle [32]. The concept of exergy destruction makes the obtained results by the advanced exergy analysis different well from those obtained by conventional exergy analysis [33]. During the freezing process, the local exergy destruction analysis is performed to quantify the irreversibility produced by energy dissipation and heat transfer [34], and it should be reduced consistently [35].

By applying the last two equations (Eq. (39) and Eq. (40)) and referring to the equation Eq. (37), the total the exergy losses of the system are calculated by the following equation:

$$Ex_{l,tot} = Q_B \left(1 - \frac{T_0}{T_B}\right) + Q_F \left(1 - \frac{T_0}{T_F}\right) + \dot{W}_P \tag{41}$$

The exergetic efficiency [36] which could express the degree, to which the energy of any component of the system was exploited in quality, is however defined by the following formula:

$$\eta_{ex} = \left| \frac{Q_F(1 - \frac{T_0}{T_F})}{Q_B\left(1 - \frac{T_0}{T_B}\right) + \dot{W}_P} \right| \tag{42}$$

3.3 Hypotheses

The energetic and exergetic analysis of the thermodynamic cycle of the absorption machine with and without a rectifier is carried out taking into account the thermodynamic properties of the water-ammonia fluid couple. In order to simplify the theoretical calculations for each component of the refrigeration machine cycle and thus to facilitate modeling, the following assumptions are considered:

- Operation in stationary conditions [40,31].
- The pump is considered isentropic [41].
- Expansion valves are considered isentropic.
- Heat exchangers are considered ideal [42].
- The exergy losses in the heat exchangers are negligible on the side of the heat transfer fluids.
- Kinetic energy and potential energy are negligible [16, 37].

3.4 Methodology

The simulation model developed in this work is based on establishing the mass, energetic and exergetic balances of the various elements of the single-stage refrigeration machine with and without a rectifier, assumed to be in stationary operating. Firstly, this program allows the determination of the thermodynamic state of physical parameters (pressure, temperature, liquid and vapor phase titer, mass flow rate) at different points of the refrigeration machine cycle. Secondly, the enthalpy at any point of the thermodynamic cycle of refrigerating machines is calculated from the analytical expressions of Gibbs free energy given by B. Ziegler and Ch. Treep [18,43,44] by differentiation method. This makes it possible then, to calculate the quantities of heat exchanged at the level of the various parts of the machine. After that, the
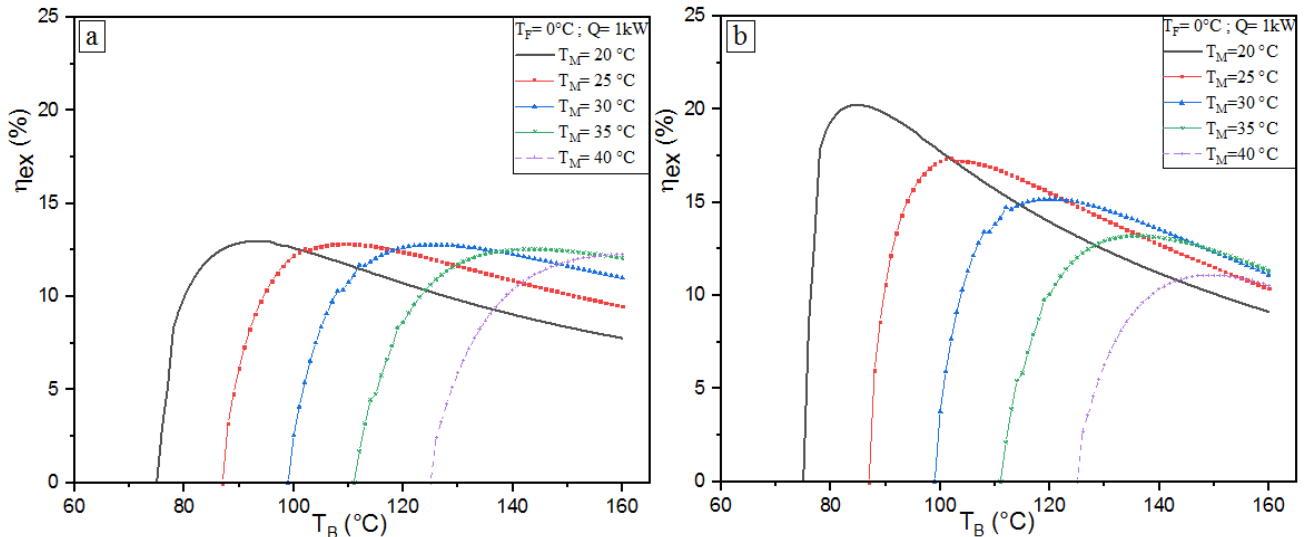
Figure 2. Evolution of the η_{ex} as a function of the temperature of the hot source T_B for different values of the average temperature T_M of the single-stage refrigeration machine: without rectifier (a); with rectifier (b)

established simulation program describes the actual process of the operation of the absorption refrigeration machine. Consequently, the calculation of all other physical quantities is done by using the thermodynamic analysis methods according to the aforementioned energy and exergy approaches.

4. Results and discussions

This section details the results of the numerical simulation with a focus on the effect of the rectification process on the exergy efficiency and exergy losses in an absorption refrigeration system.

From different values of the average source temperature T_M, and for an evaporation temperature $T_F = 0$ °C and cooling load $Q = 1kW$, figure 2 illustrates a comparison of the evolution of the exergy efficiency η_{ex} of two types of a single-stage refrigeration machines with rectifier (Figure 2 (b)) and without rectifier (Figure 2 (a)), as a function of the temperature of the hot source T_B. For this two figures, the exergy efficiency η_{ex} reaches its maximum value, respectively, around 12.98 % for the machine without a rectification system and 20.25 % for the machine equipped with a rectifier under the conditions relating to temperatures $T_M = 20$ °C, $T_F = 0$ °C. For the other values of T_M, the η_{ex} reaches its minimum values. However, when the temperature T_M increases, the exergetic efficiency η_{ex} decreases with the increasing of temperature T_B.

According to these two figures, we have shown that the operating threshold temperatures of machine with and without rectifier decrease when T_B decreases with the decreasing in temperature T_M. So, the minimum operating conditions are those which correspond to $T_M = 20$ °C.

Figure 3 exhibits an overview on a comparison of the variation of the exergy efficiency η_{ex} of the two studied machines. In this figure, the quality index represented by the parameter η_{ex} of the thermodynamic system is plotted on y-axis and the temperature of the hot source T_B is plotted on x-axis. We notice that, the two curves in Fig. 3 have almost the same appearance and the same operating temperature with a shift towards the maximum for the representative curve of the machine using rectifier as compared to the not using it. At the temperature $T_B = 85$ °C, the maximum exergy efficiency of the absorption refrigerator with rectifier is equal to 20.25%. However, the maximum exergy efficiency of the

refrigerator without rectifier is equal to 12.98% at the temperature $T_B = 93$ °C. We have therefore observed an improvement in the exergy efficiency of the refrigeration machine with a rectification system compared to the single-stage frigorific machine. Finally, we obtain a useful gain of exergies around 66% at $T_B = 85$ °C and about 17.35 % at $T_B = 160$ °C respectively.
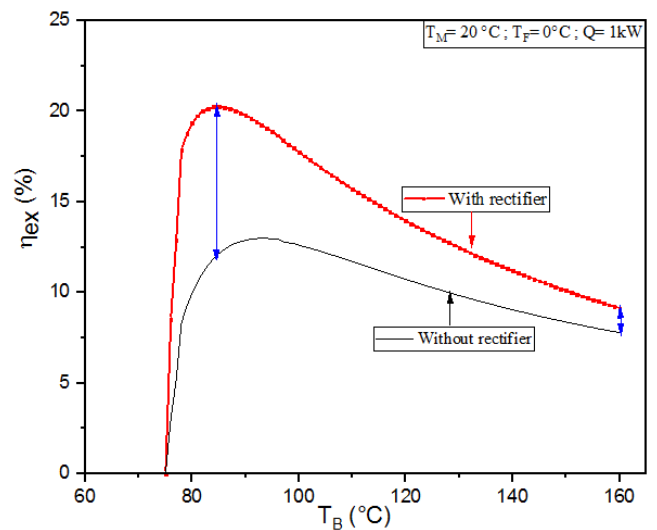
Figure 3. Variation in the exergetic efficiency of the two machines (with and without rectifier).

To evaluate the effect of rectification on the total exergy losses of the thermodynamic system, figure 4 shows the variation in the evolution of the total exergy losses as a function of the temperature of the boiler T_B and for different values of the temperature of the mean source T_M. During the evaluation of the total exergy losses relating to the two studied configurations, it appears that these losses of exergies decrease gradually when the temperature of the hot source decreases. We note therefore that the total exergy loss increase with the increasing in the values of the temperature of the mean source for the two studied configurations. From the two representations in figure 4, the minimum exergy losses are obtained for those corresponding to the temperature $T_M = 20$ °C.
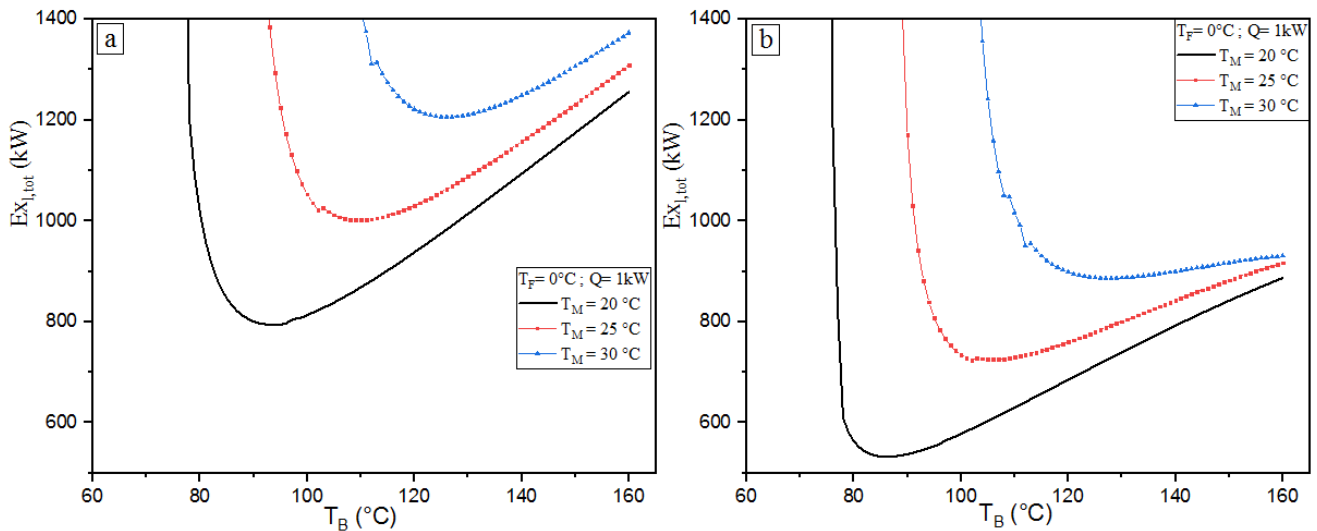
Figure 4. Evolution of the total exergy losses for different values of the average temperature T_M of the single-stage refrigeration machine: without rectifier (a); with rectifier (b).

The below Figure 5 highlights a comparison of the variation in the evolution of the total exergy losses, as a function of the temperature of the hot source T_B for the two absorption refrigeration machines (with and without rectifier). For $T_M = 20$ ° C, $T_F = 0$ ° C and Q = 1kW, we have observed a remarkable reduction in the total exergetic losses produced by the refrigeration machine using the rectifier compared to the single-stage refrigeration machine.

When we fixed the average source temperature T_M to 20 ° C, the total exergy losses of the machine with and without a rectifier have, respectively, a minimum value corresponding to 532.37 kW at $T_B = 86$ ° C and 794.25 kW at $T_B = 94$ °C.

In order to assess how the quantities of exergy losses to optimize evolve, we have chosen the following three points:
- For T_B=90 °C, we have optimized almost 263.2 kW of exergy losses.
- For T_B=120 °C, the quantity of optimized exergy losses is equal to 252.85 kW.
- For T_B=150 °C, the optimized quantity of exergetic losses exceeds the 332 kW.
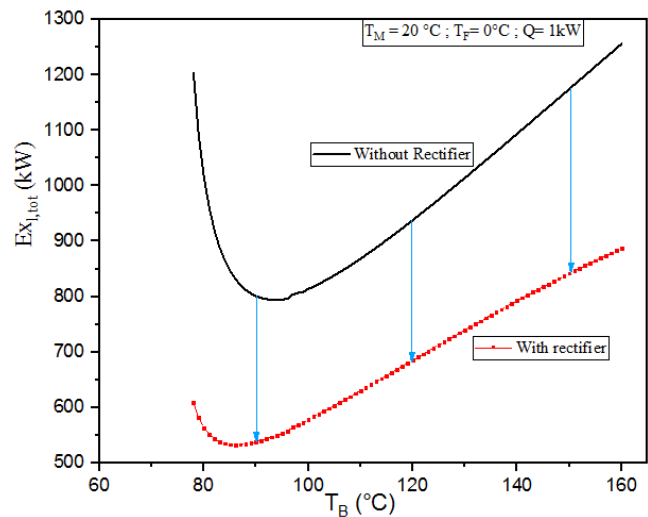
Figure 5. Evolution of the total exergy losses, as a function of the hot source temperature T_B, for the two configurations of refrigerator.
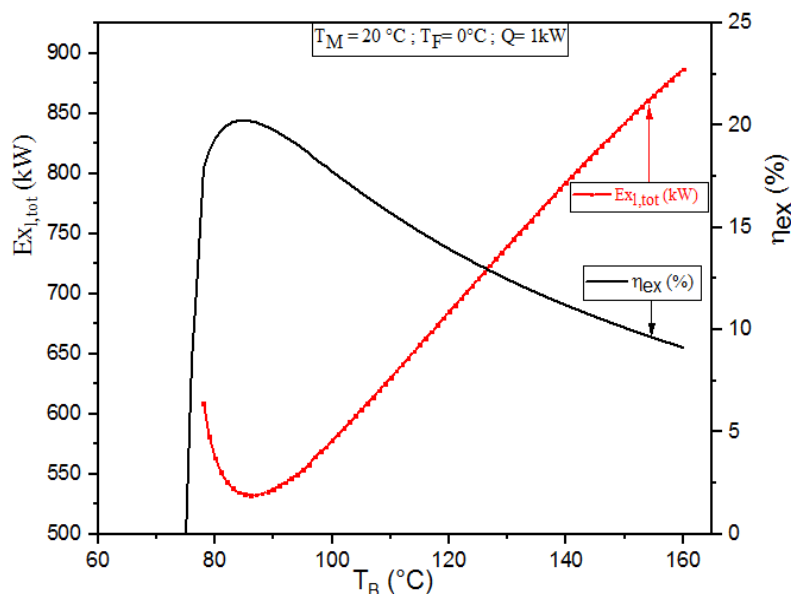
Figure 6. Comparison of the total exergy losses and the exergy efficiency for the refrigeration machine with rectifier.

This optimization deviation becomes quite large with the increasing temperature of the hot source. We have therefore highlighted the importance of the rectifier and its role in optimizing exergy losses.

In accordance with the objectives previously stated, and in order to demonstrate the relation between the different parameters evaluated in the current study, figure 6 shows the result of a comparison in the variation of the total exergy losses $Ex_{l,tot}$ with the evolution of the exergy efficiency η_{ex} of the refrigeration machine equipped with a rectifier.

According to Figure 6, we notice that when the exergy efficiency reached its maximum, the exergetic losses have becoming minimum. We have therefore observed that the exergy losses evolve in an inversely proportional way, that the exergy efficiency of the absorption refrigerator improved by the rectification system. This means that we have evaluated and verified the reliability of the simulation model established for improving exergy efficiency and optimizing exergy losses of this proposed absorption refrigerator.

4.2 General interpreting results

This section deals with a general interpretation of the results obtained by numerical simulation of the chemical-physics phenomenon of the exergy transfer of matter involved in the absorption refrigeration machine by means of the rectification process.

To close this discussion, the rectifier allows therefore, to promote the exchange of matter and energy (heat) between the gas phase (from the boiler) and the liquid phase (from the absorber), which made it possible to increase the optimum separation power of these two phases within the rectifier. The rectifier allows immediately, as a responsible mechanism to emit the vapors enriched in ammonia with a large flow rate, when they pass through a solution at a temperature below the temperature of the boiler. This ultimately resulted in an increase in the performance of the refrigeration machine, which at the same time caused a significant reduction in these exergy losses.

5. Conclusion and future recommendations

The benefit of the improvement provided by the present study lies in maximizing the purification of ammonia as refrigerant by a rectifying mechanism. Through this work, we have demonstrated clearly that the equipment of the refrigeration machine with a rectifier influences in a remarkable manner on its functioning, and therefore on its exergetic performance. The rectifier can reduce the amount of water vapor, emitted by the generator at high temperature, contained in the gas-liquid mixture which is resulting to produce an optimum flowrate of vapor enriched with a pure fluid. The obtained results showed that a considerable reduction in the exergetic losses achieved to minimum values. This is contributing to obtaining simultaneously a significant increase in the performance of the machine with rectifier compared to the simple refrigeration machine.

As a conclusion as expected objective, we succeeded to improve the single-stage refrigeration machine from the improvement of its exergetic efficiency, and consequently the contribution to reduction of the losses of exergies which are due to the irreversibility of the thermodynamic system in question.

The novelty brought by this study encourages the engineers and manufacturers specialists to realize the future absorption frigorific machines integrating rectifier systems.

As future work, we plan to determine and locate the main sources causing the loss of exergies, and searching how to minimize them. As a second step, we will try to carry out a study over the sun of the refrigeration machine with rectifier, based on real solar meteorological data relating to an appropriate Moroccan site.

Nomenclature

COP	Coefficient of performance
EV 1 & EV 2	Expansion valve number 1 & 2
HE 1 & HE 2	Heat exchanger number 1 & 2
LiBr-H2O	Lithium bromide-water mixture
NH$_3$-H$_2$O	Ammonia-Water mixture

Variables and parameters

E_x	Exergy flow rate [kW]
Ex_l	Exergy loss [kW]
$Ex_{l,tot}$	Total exergy losses [kW]
$E_{x_{D,j}}$	Exery destruction for element j [kW]
$E_{x_{D,tot}}$	Total exegy destruction [kW]
h	Specific enthalpy [kJ/kg]
I	Irreversibility [kW]
$\dot{m}$	The mass flow rate [kg/sec]
Q_A	Heat exchanged by absorber [kW]
Q_B	Heat exchanged by the boiler [kW]
Q_{BR}	Heat exchanged by the boiler (case with rectifier) [kW]
Q_C	Heat exchanged by the condenser [kW]
Q_{CR}	Heat exchanged by the condenser (case with rectifier) [kW]
Q_e	Heat flow exchanged by element e [kW]
Q_F	Heat supplied to evaporator [kW]
Q_R	Heat exchanged by the rectifier [kW]
s	Specific entropy [kJ/(kg.K)]
T	Temperature [°C]
W	Mechanical power [kW]
$\dot{W}_P$	Power pump [kW]
X	Liquid mass title
Y	Vapor mass title

Greek symbols

η_{ex}	Exergy efficiency [%]
$\mathcal{P}$	Entropy due to the irreversibility [kJ/(kg.K)]

References:

[1] Rasoul Nikbakhti et al., "Absorption cooling systems – Review of various techniques for energy performance enhancement," *Alexandria Engineering Journal*, 59, 707–738, 2020.

[2] Tuğba Kovacı and Arzu Şencan Şahin, "Energy and exergy analysis of a double-effect LiBr H$_2$O absorption refrigeration system," *International Journal of Energy and Environment*, Volume 9, Issue 1, pp.37-48, 2018.

[3] Jatin Patel et al., "Exergy Based Analysis of LiCl-H2O Absorption Cooling System," *Energy Procedia* 109, 261–269, 2017.

[4] Ana CarolinaRosa et al., "Quantitative risk analysis applied to refrigeration's industry using computational modeling," *Results in Engineering*, Volume 9, 100202, 2021.

[5] Abid Ustaoglu, "Parametric study of absorption refrigeration with vapor compression refrigeration cycle

using wet, isentropic and azeotropic working fluids: Conventional and advanced exergy approach," *Energy*, Vol. 201, 117491, 2020.

[6] Sahraoui Kherris et al., "Contribution study of the thermodynamics properties of the ammonia-water mixtures," *Thermal Science*, Vol. 17, n° 3, pp. 891-902, 2013.

[7] João M. Garcia and Armando Rosa, "Theoretical Study of an IntermittentWater-Ammonia Absorption Solar System for Small Power Ice Production," *Sustainability*, 11 (12), 3346, 2019.

[8] Mohamed Charia et al., "Machine frigorifique à absorption (eau-ammoniac) fonctionnant avec des capteurs plans sur le site de Rabat," *Rev. Int. Froid*, Vol 14, 297-303, 1991.

[9] Bahram Ghorbani and Mehdi Mehrpooya, "Concentrated solar energy system and cold thermal energy storage (process development and energy analysis)," *Sustainable Energy Technologies and Assessments,* 37, 100607, 2020.

[10] Li Jianbo et al., "A novel absorption–compression combined refrigeration cycle activated by engine waste heat," *Energy Conversion and Management*, 205, 112420, 2020.

[11] Xiangyang Liu et al., "Performance comparison of two absorption-compression hybrid refrigeration systems using R1234yf/ionic liquid as working pair," *Energy Conversion and Management*, 181, 319–330, 2019.

[12] Massamba Thioye, "Amélioration de la performance des machines frigorifiques à absorption par l'utilisation de cycles à absorption et désorption étagés," *Int J. Ref.*, Vol. 20, n° 2, pp. 136-145, 1997.

[13] J. Dardouch, M. Charia, A. Bernatchou, A. Dardouch, S. Malaine, F. Jeffali, "Study of solar absorption refrigeration Machine in the Moroccan climate," in *(ICMES 2018) Materials Today: Proceeding,* 13, 1197-1204, 2019.

[14] M. Ahachad, M. Charia and A. Bernatchou, "study of improved NH_3-H_2O solar absorption refrigerating machine in Rabat (Morocco)," *Solar Energy Materials and Solar Cells*, 28, 71-79, (1992).

[15] A. ŞENCAN et al., "Prediction of Liquid and Vapor Enthalpies of Ammonia-water Mixture," *Energy Sources, Part A*, 33:1463–1473, 2011.

[16] Gurjeet Singh, P. J. Singh, V. V. Tyagi, P. Barnwal and A. K. Pandey, "Exergy and thermoeconomic analysis of cream pasteurisation plant," *Journal of Thermal Analysis and Calorimetry (Springer)*, 137 (4), 1381-1400, 2019.

[17] MA Javadi et al., "Optimization and analysis of exergy, economic, and environmental of a combined cycle power plant," *ãdhanã* , 44 (5), 1-11, 2019.

[18] Charia Mohamed. (1990). *Contribution à l'étude des machines frigorifiques à absorption mono-étagées et biétagées* (Doctoral dissertation), FSR, Mohammed V in Rabat University.

[19] Silvio de Oliveira Junior, Exergy: Production Cost and Renewability, *1st Ed.* Springer Science & Business Media, 2013.

[20] V. Vikul and S. D. Raja, "Experimenta and Exergy Analysis of Ammonia/Water Absorption System using Ethylene Glycol [C2H4(OH)2] in the Evaporator," *Energy Procedia*, 109, 401-408, 2017.

[21] Peizhe Cui et al., "Energy, exergy, and economic (3E) analyses and multi-objective optimization of a cascade absorption refrigeration system for low-grade waste heat recovery," *Energy Conversion and Management*, 184, 249–261, 2019.

[22] Ayad Khudhair Al-Nadawi, "Irreversibility Analysis of R407C, R404A, and R134A as an Alternatives of R22 in Vapor Compression Chiller under Cycling Conditions," *International Journal of Thermodynamics*, Vol. 24, n° 1, pp. 24-29, 2021.

[23] Sandro Nizetic, Agis Papadopoulos, The Role of Exergy in Energy and the Environment, *1st Ed.* Springer International Publishing, 2018.

[24] Rupp Carriveau et al., "Transient thermodynamic modeling of an underwater compressed air energy storage plant: Conventional versus advanced exergy analysis," Sustainable Energy Technologies and Assessments 31 (2019) 146–154.

[25] Thamer Khalif Salem, Saad Sami Farhan, Israa Sami Farhan, "Energy and exergy analysis study of heat exchanger in a refrigeration system with different lengths of capillary tube," International Journal of Thermodynamics, 23 (4), 260-266, 2020.

[26] Anarghya Ananda Murthy et al., "A review on expanders and their performance in vapour compression refrigeration systems," International Journal of Refrigeration 106, 427–446, 2019.

[27] Huawei Wu et al., "Heat transfer analysis of energy and exergy improvement in water-tube boiler in steam generation process," *Journal of Thermal Analysis and Calorimetry*, 139 (4), 2791-2799, 2020.

[28] Zhihua Wang et al., "Exergy analysis of a frost-free air source heat pump system," *Journal of Mechanical Science and Technology*, 33 (5), 2439-2450, 2019.

[29] N. D. Shikalgar, S.N. Sapali, "Energy and exergy analysis of a domestic refrigerator: approaching a sustainable refrigerator," *Journal of Thermal Engineering*, Vol. 5, n° 5, pp. 469-481, 2019.

[30] Michel Wakim and Rodrigo Rivera-Tinoco, "Absorption heat transformers: Sensitivity study to answer existing discrepancies," *Renewable Energy*, 130, 881-890, 2019.

[31] Muhammad Umer Arshad et al., "Thermodynamic analysis and optimization of double effect absorption refrigeration system using genetic algorithm," *Energy Conversion and Management*, 192, 292–307, 2019.

[32] Hamed Kariman et al., "Energetic and exergetic analysis of evaporation desalination system integrated with mechanical vapor recompression circulation," *Case Studies in Thermal Engineering*, Vol. 16, 100548, 2019.

[33] Yuan Zhang et al., "Exergy destruction analysis of a low-temperature Compressed Carbon dioxide Energy Storage system based on conventional and advanced exergy methods," *Applied Thermal Engineering*, Vol. 185, 116421, 2021.

[34] Nelson O. Moraga and Diego R. Rivera, "Advantages in predicting conjugate freezing of meat in a domestic freezer by CFD with turbulence k-ε 3D model and a local exergy destruction analysis," *Int. Jour. of Refr.*, doi.org/10.1016/j.ijrefrig.2021.02.002.

[35] Chinedu F. Okwose, Muhammad Abid, Tahir A.H. Ratlamwala., "Performance analysis of compressor-assisted two-stage triple effect absorption refrigeration cycle for power and cooling," Energy Conversion and Management., *Energy Conversion and Management*, 227 , 113547, 2021.

[36] Ramen Kanti De and Aritra Ganguly., "Energy, Exergy and Economic Analysis of a Solar Hybrid Power System Integrated Double-E®ect Vapor Absorption System-Based Cold Storage," *International Journal of Air-Conditioning and Refrigeration*, Vol. 27, n° 2 1950018 (13 pages), 2019.

[37] Boris Huirem and Pradeepta Kumar Sahoo, "Thermodynamic Modeling and Performance Optimization of a Solar-Assisted Vapor Absorption Refrigeration System (SAVARS)," *International Journal of Air-Conditioning and Refrigeration*, Vol. 28, n° 1, 2050006 (18 pages), 2020.

[38] Xiao Zhang et al., "Energetic and Exergetic Investigations of Hybrid Configurations in an Absorption Refrigeration Chiller by Aspen Plus," *Processes*, 7 (9), 609, 2019.

[39] Wei Wu et al., "Comparative analysis of conventional and low-GWP refrigerants with ionic liquid used for compression-assisted absorption cooling cycles," *Applied Thermal Engineering*, 172, 115145, 2020.

[40] Manel Vallès, M Bourouis, D Boer, "Solar-driven absorption cycle for space heating and cooling," *Applied Thermal Engineering*, Vol. 168, 114836, 2020.

[41] XuPing et al., "Prediction and optimization of isentropic efficiency of vortex pump under full operating conditions in Organic Rankine Cycle waste heat recovery system based on deep learning and intelligent algorithm," *Sustainable Energy Technologies and Assessments*., Vol. 42, , 100898, December 2020.

[42] Ahmad Fakheri, "Heat Exchanger Efficiency," *Journal of heat transfer*, 129 (9):1268-1276 (9 pages), 2007, https://doi.org/10.1115/1.2739620.

[43] B. Ziegler and Ch. Trepp, "Equation of state for ammonia-water mixtures," *Int. Jour. Of Ref.*, Vol. 7, n° 2, Pages 101-106, March 1984.

[44] VijayChauhan et al., "Thermodynamic analysis of a combined cycle for cold storage and power generation using geothermal heat source," *Thermal Science and Engineering Progress*, Volume 11, Pages 19-27, June 2019.

Proposing an Ultrapure Water Unit Coupled to an Existing Reverse Osmosis Desalination Plant and its Exergy Analysis

Bashayar Al Maqbali[1], Zohreh Rahimi-Ahar[2], Hasan Mousa[3], G. Reza Vakili-Nezhaad[4*]

[1]Petroleum & Chemical Engineering Department, College of Engineering, Sultan Qaboos University, Muscat 123, Oman
[2]Chemical Engineering Department, University of Isfahan, Isfahan, Iran
[3]Department of Chemical Engineering, Jordan University of Science and Technology, Irbid, Jordan
[4]Sustainable Energy Research Center (SERC), Sultan Qaboos University, Muscat 123, Oman
[1]E-mail: Vakili@squ.edu.om

Abstract

In this study, three desalination exergy analysis models including the Cerci et al. model (Model A), Drioli et al. model (Model B) and electrolyte solution model (Model C), were developed on an existing reverse osmosis (RO) desalination plant in Oman (Plant ALG). A modified ultrapure water (UPW) unit fed by Plant ALG has also been proposed (Plant A) based on the technology used in a UPW unit operated under the climate of Europe and fed by European river water (Plant B). The most suitable exergy model for characterizing the proposed UPW production plant was used. Model C was found to be the most proper model among its counterparts. It reflected the electrolytic behavior of the relevant streams and considered as the appropriate model. The major exergy destruction sites were also identified, and the exergy efficiency was calculated. The electro-de-ionization (EDI) and the RO unit were the highest exergy destructive components in Plant A.

Keywords: Reverse osmosis; ultrapure water; exergy destruction; exergy efficiency; electro-de-ionization.

1. Introduction

The relationship between water and energy production is extremely close and co-dependent [1]. The water demand is growing annually due to population growth and economic development [2]. In Oman, annually, the drinking water need is nearly 200 MCM (Million Cubic Meter), agriculture consumption is 1,600 MCM, and industrial plants consume around 130 MCM [3]. Some reports reveal that the population of Oman will be doubled in the next 20 years and will be resulting in several development projects, mainly in the water sector [4]. Several desalination plants were commissioned in different regions to meet the continuous growth of water demand and to decrease the reliance on groundwater resources [5]. Freshwater can be recovered from seawater via RO desalination technology [6]. The useful method toward more energy-efficient desalination technology is to shift from the thermal desalination plant to RO [7]. Though, the optimization of RO desalination systems are essential [8]. Exergy Analysis is an accepted and useful analytical approach for energy optimization of the desalination systems [9]. The analysis of the real thermodynamic inefficiencies in a process is valuable for enhancing an energy-intensive operation [10].

Many exergy analysis researches have been developed to identify the energetical inefficiencies. A comprehensive study was developed based on desalination exergy analysis approaches by Fitzsimons et al. [11]. The appropriateness of the Cerci et al., Drioli et al. and the ideal mixture models were a concern. The exergy destruction, specific exergy and exergy efficiency values for most approaches were similar.

The ideal mixture model resulted in meaningful differences in exergy efficiency.

Exergy analysis of an RO plant was developed using actual operation data of the plant. The primary membrane units and the throttling valves were the main exergy destructive components in the system. The overall exergy efficiency of 4.3% was calculated which could be increased to 4.9% by adding a pressure exchanger with two throttling valves [12]. A desalination plant in California including RO, nanofiltration (NF), and electrodialysis reversal (EDR) units were analyzed exergetically by Kahraman et al. [13]. The analysis showed that the motor/pump used in EDR, RO, and NF was the most to least exergy destructive components, respectively. A hybrid organic Rankine cycle (ORC) coupled with the RO system was studied by Shekari Namin et al. [14]. Low condensing pressure in proposed system caused the requirement of a large volume turbine. Using the cascade ORC or KC (Kalina cycle) as a power supply source could solve this problem. A KC cycle was coupled to an RO system to provide drinking water, power, heating and cooling [15]. The first and second condensers, flashing device, second HEX and RO systems were high exergy destructive components. The overall exergy efficiency of 38.1% was obtained in the proposed process.

A poly-generation system including RO unit, photovoltaic panels, ORC, waste heat recovery section and homogeneous charge compression ignition engine was analyzed thermodynamically by Islam et al. [16]. Coupling the Pelton turbine to the RO plant recovered 24.3% of the input power. Exergy efficiencies of system excluding and including Pelton turbine were 44.1% and 45.01%,

respectively. A waste heat-driven hybrid system containing Rankine cycle for power generation, thermochemical copper-chlorine cycle for hydrogen and RO for water production was analyzed by Ishaq et al. [17]. The maximum irreversibility took place in pump B4 and the highest exergy efficiency associated with the third compressor. Bouzayani et al. modeled three water/power-producing systems [18]. The exergy loss in the power plant was ten times more than that in the RO unit. A dynamic RO plant model was developed by Naseri et al. [19] to produce different permeate rates. Modification of the storage tank capacity minimized its temperature fluctuation, led to minimization of the exergy destruction. Ameri and Seyd Eshaghi modeled an RO plant coupled to humidification-dehumidification (HDH) system [20] by solution–diffusion method. The results indicated that the RO-HDH system increased the exergy efficiency to 20.60%, while HDH and RO exergy efficiencies were 12.66% and 0.72%, respectively.

Desalination plants that remove impurity from water are crucial in the UPW production process. The ion exchange, ultrafiltration (UF), RO, and electro-deionization processes are proposed to produce UPW [21]. A comprehensive review of the rising role of RO to satisfy the technical requirements in the UPW sector, with an emphasis on electronic industrial applications was carried out by Lee et al. [22]. Studies on synergetic effects with other purification technologies were proposed as an in urgent demand. Zhan et al. [23] proposed a RO unit using the modified fouling index to support the stable operation of UPW plant applications. An intimate correlation between the modified fouling index and RO performance was revealed via electrochemical deionization concentrate. Jin et al. [24] used ultraviolet radiation to RO pretreatment to produce UPW. It was also revealed that the use of UPW is essential in increasing the energy efficiency of the cogeneration plants [25].

Three exergy analysis approaches using real operational data were applied to characterize ALG Plant (the main desalination plant in Oman) and the best approach could be selected. A modified UPW unit fed by ALG Plant was designed (Plant A) based on the technology used in an UPW unit operated under the climate of Europe and fed by European river water (Plant B). Exergy analysis of an integrated RO-UPW unit could provide an energy-efficient plant that has not been paid attention. Plant A was proposed to produce high-purity water which is useful in many advanced high-tech applications.

2. Methodology

This work investigates an existing RO plant coupled to a UPW unit exergetically. The exergy analysis process is summarized as follows:

1- Three exergy analysis models on an existing RO desalination plant are performed based on the real operation conditions. Temperature, pressure, salinity (See Table 1) are directly used in exergy equations as described in Section 2.5.

2- The best exergy analysis model is selected via comparing the models concept as well as the physical and chemical exergy contents.

3- A modified UPW unit fed by RO plant is proposed (Plant A) based on the technology used in a UPW unit operated under the climate of Europe and fed by European river water (Plant B).

4- The most suitable exergy model can be selected for characterizing RO-UPW production plant. The major exergy

destruction sites are identified followed by exergy efficiency calculations.

Proposing a UPW plant with high quality water production, introducing the most exergy destructive components in proposed plant and some recommendations for exergy efficiency improvement can pave the way for future real research in this field.

2.1 Plant description

The plant is located in Muscat and is operated based on RO technology. It is capable of producing 24,000 m3 of potable water per day to supply the domestic requirements. The flow diagram of the proposed system is illustrated in Figure 1.

2.2 Plant description

The seawater with a salinity of 38,321 ppm at a flow rate of 2,500 m^3/h was pumped by a low-pressure pump (stream 0). The incoming seawater was separated at the end into two streams. The brine with a salinity of 63,623 ppm was disposed to the sea at a flow rate of 1,500 m^3/h (stream 13) and permeate with a salinity of less than 321 ppm was pumped to the product tank at a flow rate of 1,000 m^3/h (stream 7).

2.3 Plant operating condition

Due to the high salinity of the incoming seawater to the plant, the proposed process was pretreated with multimedia filtration (MMF) followed by fine filtration (cartridge filter) and finally, RO process was used for removal of salts from the seawater, to make it suitable for human use. The plant was operated at a constant temperature of 40℃. The pressure of the incoming seawater increased from 100 kPa at the inlet to 340 kPa before it entered the MMF. It was increased up to 689 kPa before it entered the cartridge filter. A high-pressure pump increased the pressure of the incoming seawater to 6,080 kPa before introducing the seawater to the RO unit. The brine left the RO unit at 5,400 kPa. The pressure of the brine was reduced using three throttling valves to 200 kPa before disposing the brine to the sea. Permeate was left the RO unit at 100 kPa and was pumped to the chamber blending at 290 kPa. The operating conditions and the quality of each stream at each process stage are summarized in Table 1.

Table 1. Plant operating conditions.

Process Stream	P (kPa)	T (°C)	Total dissolved solid (TDS) (mg/L)	Volumetric Flowrate (m^3/h)
0	100	40.0	38,321	2,500
1	340	40.0	38,322	2,500
2	340	40.0	38,323	2,500
3	689	40.0	38,324	2,500
4	689	40.0	38,325	2,500
5	1,000	40.0	38,326	2,500
6	6,080	40.0	38,327	2,500
7	100	40.0	321	1,000
8	100	40.0	322	1,000
9	290	40.0	323	1,000
10	5,400	40.0	63,622	1,500
11	2,700	40.0	63,623	1,500
12	1,200	40.0	63,624	1,500
13	200	40.0	63,625	1,500
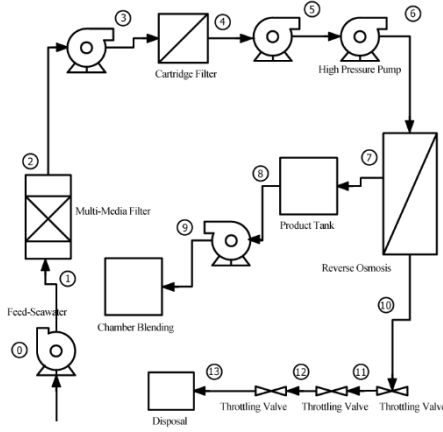
Figure 1. The flow diagram of the proposed RO desalination plant

2.4 Thermodynamic properties of seawater

In proposed process, the operating pressure was upper than 6 MPa. An accurate method was used to estimate the pressure effect on the seawater properties. The pressure-dependent correlation developed by Nayar et al. [26] was used for seawater properties calculation.

2.5 Desalination plant exergy models
2.5.1 Cerci et al. model (Model A)

In the Cerci et al. model (Model A), the system is treated as an ideal mixture of Sodium Chloride (NaCl) and water. The salinity of 3.5% is considered in Model A. Total exergy (chemical and physical) of the Cerci et al. model is calculated as [26]:

$$\dot{E} = \dot{m}\left[[(w_s h_s) + (w_w h_w)] - [(w_s h_s) + (w_w h_w)]_0 - T_0[[w_s s_s + w_w s_w] - [w_s s_s + w_w s_w]_0] + T_0[[R_{im}(x_s lnx_s + x_w lnx_w)] - [R_{im}(x_s lnx_s + x_w lnx_w)]_0]\right] \tag{1}$$

where water and salt mole fractions are calculated using Eqs. 2 and 3, respectively [1]:

$$x_w = \frac{MW_w}{MW_s\left[\frac{1}{w_s}-1\right]+MW_w} \tag{2}$$

$$x_s = \frac{MW_s}{MW_w\left[\frac{1}{w_w}-1\right]+MW_s} \tag{3}$$

NaCl is considered as an incompressible solid in the Cerci et al. model [12]. The specific entropy and specific enthalpy of the NaCl are 0.0172 kJ/kg.K and 33.472 kJ/kg, respectively. The specific enthalpy of the water is calculated at different stages using Eq. 4.

$$h_{sw}(t,S,P) = h_{sw}(t,S,P_0) + (P-P_0)\big(m_1 + m_2 t + m_3 t^2 + m_4 t^3 + s(m_{5+}m_6 t + m_7 t^2 + n_8 t^3)\big) \tag{4}$$

Where,
$$h_{sw}(t,S,P_0) = h_w(t) - S_{\frac{Kg}{Kg}}\big(n_1 + n_2 S_{kg/kg} + n_3 S_{kg/kg}{}^2 + n_4 S_{kg/kg}{}^3 + n_5 t + n_6 t^2 + n_7 t^3 + +n_8 S_{kg/kg} t + n_9 S_{kg/kg}{}^2 t + n_{10} S_{kg/kg} t^2\big) \tag{5}$$

where m_1-m_8 and n_1-n_{10} are introduced in section A.3.

$$h_w = 141.355 + 4202.07t - 0.535t^2 + 0.004t^3 \tag{6}$$

The specific entropy of the water is calculated as:

$$s_{sw}(t,S,P) = s_{sw}(t,S,P_0) + (P-P_0)\big(m_1 + m_2 t + m_3 t^2 + m_4 t^3 + S(m_5 + m_6 t + m_7 t^2 + m_8 t^3)\big) \tag{7}$$

where

$$s_{sw}(t,S,P_0) = s_w(t) - S_{\frac{kg}{kg}}\left(n_1 + n_2 S_{\frac{kg}{kg}} + n_3 S_{kg/kg}{}^2 + n_4 S_{kg/kg}{}^3 + n_5 t + n_6 t^2 + n_7 t^3 + n_8 S_{\frac{kg}{kg}} t + n_9 S_{kg/kg}{}^2 t + n_{10} S_{kg/kg} t^2\right) \tag{8}$$

where m_i and n_i are presented in Appendix A.3. The specific entropy of the salt is calculated as:

$$s_s = 0.1543 + 15.383t + 2.996 \times 10^{-2} t^2 + 8.193 \times 10^{-5} t^3 - 1.370 \times 10^{-7} t^4 \tag{9}$$

2.5.2 Drioli et al. model (Model B)

In Drioli et al. model, the system is treated as an ideal aqueous solution of ions (Cl^-, Na^+, $SO4^{-2}$, K^+). The dead state is defined as pure water at atmospheric pressure and ambient temperature. The total exergy rate is a summation of thermal, pressure and chemical exergy rates as:

$$\dot{E} = \dot{E}^{Th} + \dot{E}^P + \dot{E}^{Ch} \tag{10}$$

where the thermal, pressure and chemical exergy rate terms are calculated as:

$$\dot{E}^{Th} = \dot{m}c\,(T - T_0) \tag{10.1}$$

$$\dot{E}^P = \dot{m}\left[\frac{P-P_0}{\rho}\right] \tag{10.2}$$

$$\dot{E}^{Ch} = -\dot{m}\,N_w RT_0 \ln x_w \tag{10.3}$$

where

$$N_w = \frac{(1 - \sum \frac{C_i}{\rho})}{MW_w} \quad (11)$$

$$x_w = \frac{N_w}{\left[N_w + \sum \left(\frac{\beta_i C_i}{\rho MW_i}\right)\right]} \quad (12)$$

2.5.3 Electrolyte solution exergy analysis model (Model C)

In the electrolyte solution approach, the system is treated as a non-ideal ionic solution [11]. The activity of species is calculated as:

$$a_i = m_i \gamma_{H_i} \quad (13)$$

The activity of an electrolyte solution including seawater requires Pitzer equations [27]. For the single electrolyte of anion X and cation M, the activity coefficient is calculated as:

$$ln\, \gamma_{\pm} = -|z_m z_X| A^{\phi} \left[\frac{2}{b} ln\, ln\, (1 + b\sqrt{I}) + \right. \quad (14)$$
$$\left. \frac{\sqrt{I}}{1+b\sqrt{I}}\right] + m \frac{2 v_M v_X}{v} \left\{2\beta_{MX}^{(0)} + \frac{2\beta_{MX}^{(1)}}{\alpha^2 I}\left[1 - \left(1 + \right.\right.\right.$$
$$\left.\left.\left. \alpha\sqrt{I} - \frac{\alpha^2 I}{2}\right) e^{-\alpha^2 I}\right]\right\} + \frac{3m^2}{2}\left[\frac{2 v_M v_X^{\frac{3}{2}}}{v} C_{MX}^{\emptyset}\right]$$

where, A^{ϕ} is 0.3882, b and α are constant parameters. For a 1–1 electrolyte b and α are 1.2 and 2, respectively. $C_{MX}^{\emptyset}$, $\beta_{MX}^{(0)}$ and $\beta_{MX}^{(1)}$ are empirical parameters and their values are 0.002, 0.0714 and 0.2723, respectively. The solvent activity is calculated by the following equation.

$$ln\, a_w = -\emptyset \frac{vm}{55.51} \quad (15)$$

where, $\emptyset$ is the osmotic coefficient and is calculated as:

$$\emptyset - 1 = -|z_m z_X| A^{\phi} \frac{\sqrt{I}}{1+b\sqrt{I}} + m \frac{2 v_M v_X}{v}\left[\beta_{MX}^{(0)} + \right. \quad (16)$$
$$\left. \beta_{MX}^{(1)} e^{-\alpha^2 I}\right] + m^2 \left[\frac{2 (v_M v_X)^{\frac{3}{2}}}{v} C_{MX}^{\emptyset}\right]$$

The mole fraction of salt and water is calculated using Eqs.17 and 18, respectively.

$$x_s = \frac{\beta N_s}{\beta N_s + N_w} \quad (17)$$

$$x_w = \frac{N_s}{\beta N_s + N_w} \quad (18)$$

3. Results and discussion

Water quality parameters including chemical and physical properties were tested based on the desired specifications. Parameters that were frequently sampled for water quality include temperature, TDS, density, pressure

and composition. The exergy analysis was performed based on real data obtained from the experimented plant.

3.1 Exergy contents

As the process was isothermal, the physical exergy was achieved due to the difference in the dead state and the pressure of streams. Specific chemical and physical exergy contents calculated using three models are tabulated in Table 2.

Table 2. Specific chemical and physical exergy contents calculated using Models A, B and C.

Stream	e_{ph} Model A	e_{ph} Model B	e_{ph} Model C	e_{ch} Model A	e_{ch} Model B	e_{ch} Model C
0	0.0000	0.0000	0.0000	0.0000	3.3052	0.0000
1	0.2320	0.2351	0.2351	0.0000	3.3048	0.0000
2	0.2320	0.2351	0.2351	0.0000	3.3048	0.0000
3	0.5694	0.5770	0.5770	0.0000	3.3042	0.0000
4	0.5694	0.5770	0.5770	0.0000	3.3042	0.0000
5	0.8701	0.8817	0.8817	0.0000	3.3037	0.0000
6	5.7814	5.8581	5.8581	0.0000	3.3044	0.0000
7	0.0000	0.0000	0.0000	1.6807	0.0288	3.1349
8	0.0000	0.0000	0.0000	1.6805	0.0289	3.1345
9	0.1837	0.1861	0.1861	1.6803	0.0290	3.1341
10	5.1239	5.1920	5.1920	0.3354	5.3440	0.6173
11	2.5136	2.5470	2.5470	0.3354	5.3386	0.6174
12	1.0635	1.0776	1.0776	0.3355	5.3419	0.6174
13	0.0967	0.0980	0.0980	0.3355	5.3452	0.6175

As the process was isothermal, the physical exergy resulted due to the difference between the process pressure and the dead state pressure. For Models B and C, the similar equations were used to calculate the physical exergy rate; hence, for both models the physical exergy rates were the same. However, there was little difference in the specific physical exergy calculated using Model A and the specific physical exergy calculated using Models B and C. The difference between the specific physical exergy obtained by Model A and the specific physical exergy obtained using Models B and C did not exceed 1.3%; hence, no further investigation was required for the physical exergy term. The chemical exergy rates calculated using Models A and B were not comparable due to different salinity dead states. For Models A and C, the dead state of the solution was defined as the salinity of the incoming water; accordingly, the chemical exergy was zero in streams 0-6. It was found that Model A was an unsuitable approach as it considered an ionic solution as a mixture of water and solid salt. Accordingly, NaCl was treated as a single component in water. Furthermore, the coupling of the chemical and physical exergy equations did not provide a comprehensive understanding of chemical and physical exergy contents. The chemical exergy rates obtained using Model B were quite different from than that of the other models due to the different dead states. A negligible change in brine composition made the use of Model B an improper method for the exergy analysis of a desalination unit. Model C treated the system as a non-ideal mixture of water and NaCl and the mole fraction calculation was based on ionization of NaCl to Na^+ and Cl^-. It means even a low change in

concentration was considered. The exergy model could clarify the electrolytic behavior of the streams. On this basis, Model C was the proper model for the exergy analysis of the proposed UPW plant. In this research, seawater is assumed as a dilute solution with a typical salinity mass fraction of 3.8% [26].
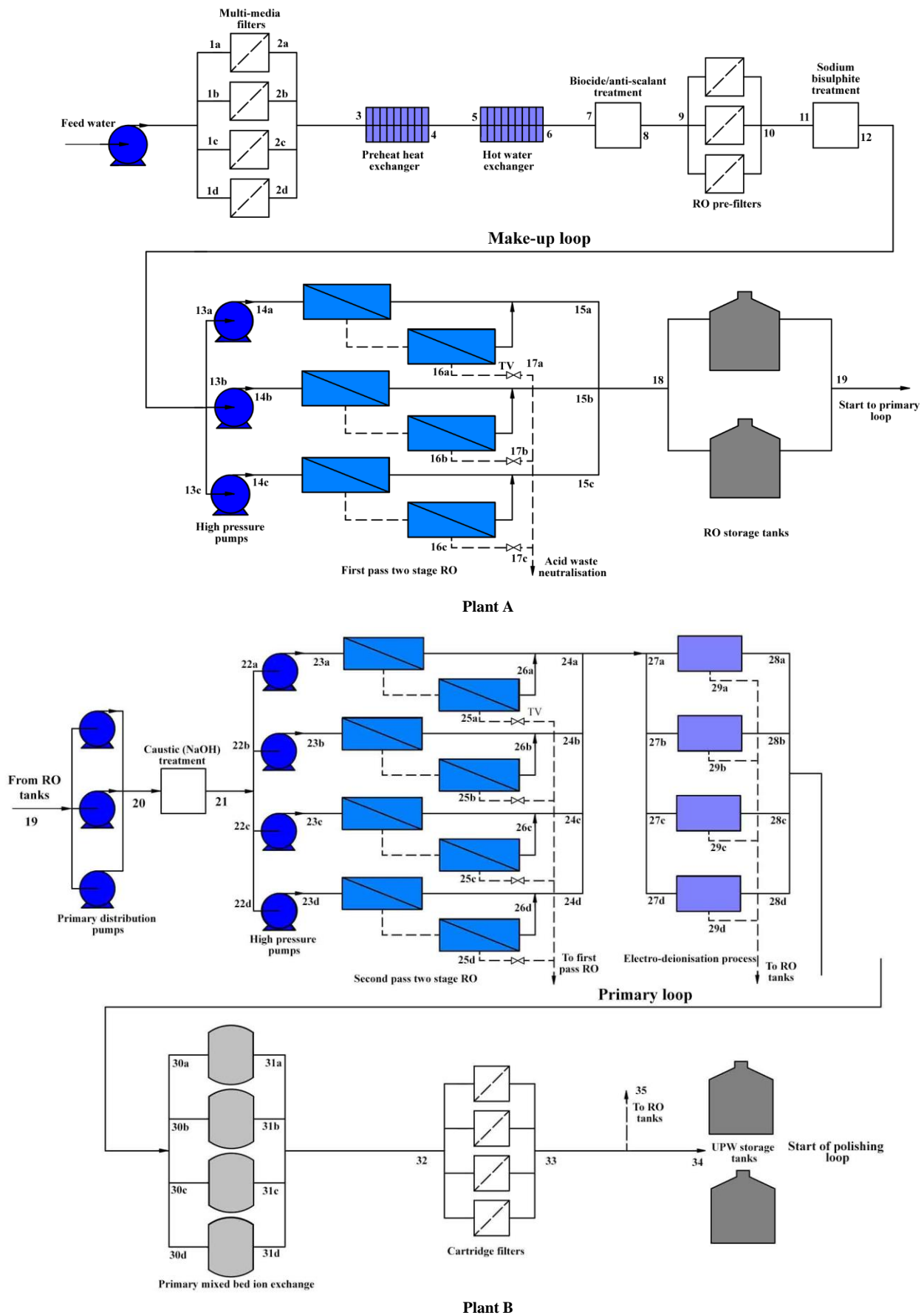
Figure 2. The process flow diagrams of the makeup and primary loops in Plants A and B.

3.2 Ultrapure water production plant analysis

Thermodynamic analysis using Model C applied for a UPW production plant operated under the climate of Oman and fed by the product of ALG Plant (Plant A). Plant A was designed using the UPW technology applied in Europe. The results were compared with the same UPW production plant operated under the climate of Europe and fed by European river water (Plant B). The process flow diagrams of the makeup and primary loops in Plants A and B are shown in Figure 2. The plant consisted of three sections; makeup, primary and polishing loops. However, in this research, only the makeup and the primary loops were analyzed. This was due to a high difference in the concentration of the incoming water. The make-up and primary loops included various levels of filtration from MMF, first and second-pass RO, ion exchange, and EDI unit. The real data used to conduct the thermodynamic analysis is detailed in Table A.2. The defined dead states of UPW production Plants A and B are tabulated in Table 3. Plants A and B differed in the temperature and the incoming water quality (TDS) due to the different climate and sources of the feedstock under which these plants were operated.

Table 3. Dead states of plants A and B.

Dead state	Parameters	Plant A	Plant B
Physical dead state	Temperature (℃)	40	16
	Pressure (bar)	1	1
Chemical dead state	TDS (ppm)	314	135

3.2.1 Exergy rates

Chemical, physical and overall exergy rates were calculated using Model C and the results for each process stream are given in Table A.3

The physical exergy for the most process stages in Plants A and B was negligible. However, there was a substantial difference in the chemical exergy between Plants A and B due to their different water properties. The high salinity of the incoming water in Plant A resulted in high chemical exergy in most of the process stages. For all process streams, physical exergy was the major source of the total exergy. The total exergy rates exceed 100 kW for both Plants A and B, and represented in Figures 3 and 4, respectively.

For both Plants A and B, the highest exergy rates were at the inlets of the hot water HEXs (Stream 5) showing the values of 640.11 kW and 686.068 kW, respectively. The outlet of the hot water HEXs (Stream 6) and the inlet of the pre-heat HEXs (Stream 3) had the next rankings in the exergy rates. Table 4 shows the first three highest exergy rates recorded for Plants A and B.

Table 4. First three highest exergy rates recorded for Plants A and B.

Process	Process Stream	Total Exergy (kW)	
		Plant A	Plant B
Pre-heat HEX	Stream 3 (Heating water-inlet)	115.98	119.455
Hot water HEX	Stream 5 (Heating water-inlet)	640.11	686.068
	Stream 6 (Heating water-outlet)	458.16	524.169

For Plant A, at the inlet of the hot water HEX, the exergy rate was higher than that of the pre-heat HEX, due to its higher temperature difference with the dead state.
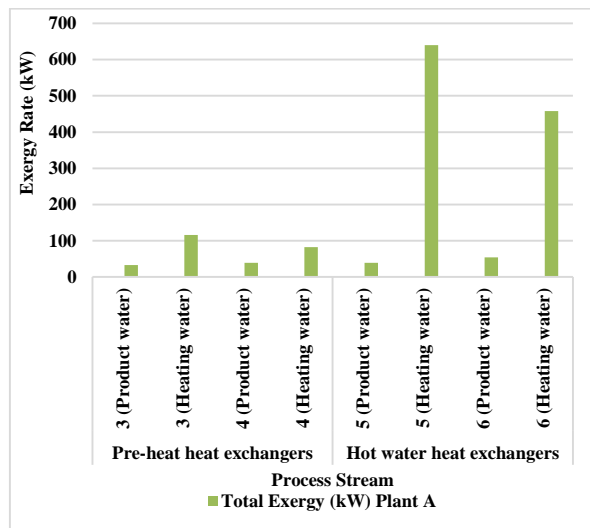
Figure 3. Total exergy rate exceeds 100 kW for UPW production Plant A.
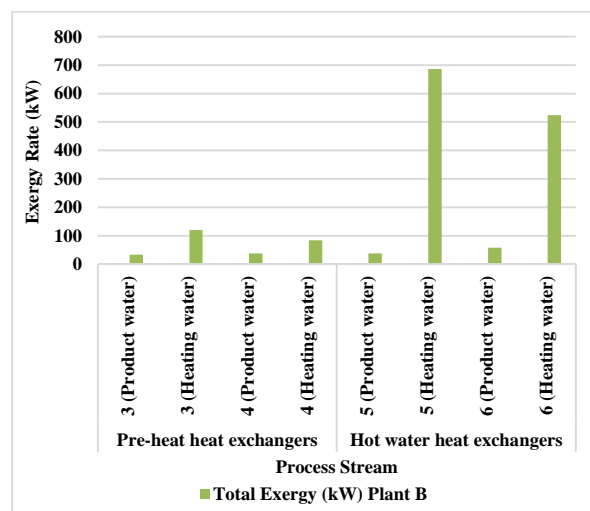
Figure 4. Total exergy rate exceeds 100 kW for UPW production Plant B.

3.2.2 Exergy destruction rates

Exergy was delivered to the UPW plant by feed water at certain values of concentration, pressure, temperature, and flow rate. The exergy was added by electrical energy input to the pumps and the EDI unit. Owing to temperature difference, throttling process, mixing and separation operations, exergy was destroyed.

The exergy destruction rates increasing due to irreversibility in the primary and make-up loops of UPW plant A showed that the key source of exergy destruction was the hot water HEX. This was supported by the results of the exergy destruction of Plant B, which are presented in Table 5.

The constant concentration during the process conducted by Plants A and B did not cause exergy destruction by chemical exergy. Hence, the differences in exergy destruction were caused by the differences in physical exergy.

The top exergy destructive components with 95% contribution in total exergy destruction within Plant A, are shown in Figure 5.

The hot water HEX, first- and second-pass RO high-pressure pumps, EDI, second and first-pass RO recorded the highest exergy destruction values. In a hot water HEX, heat transferred due to a large temperature difference; hence, an

excessive heat transfer area of finned type should be recommended. However, economical optimization is proposed for selecting the area of such an exchanger. For the first and second-pass RO high-pressure pumps, the exergy destructed due to the pressure exergy. The pressure increase from 4.7 bar to about 10 bar and from 4.3 bar to 20.9 bar for first and second-pass RO high-pressure pumps, respectively, caused exergy destruction. Coupling the variable speed drive or motor managers to pumps can be recommended to enhance the pump exergy efficiency. In the first- and second-pass RO, the temperature was constant while the increase in the pressure resulted in exergy destruction. For improving the RO process, reducing the pressure drop across the membrane can be proposed to decrease the operating pressure required to achieve acceptable permeate fluxes.

Table 5. The exergy destruction of Plants A and B.

Process	Process Stream	Exergy Destructions (kW)	
		Plant A	Plant B
MMF	b	0.45	0.50
	c	0.43	0.40
	d	0.41	0.40
Pre-heat HEXs		27.71	30.90
Hot water HEXs		166.86	140.60
Biocide/anti-scalant treatment		0.60	0.60
RO pre-filters		2.60	2.60
Sodium bisulfite treatment		0.60	0.60
First-pass RO high-pressure pumps	a	55.45	55.40
	c	55.62	55.60
First-pass RO	a	31.26	31.26
	c	23.85	23.85
Throttling valves	a	8.00	8.00
	c	4.34	4.30
RO tank		1.80	1.78
Primary distribution pumps		20.20	20.18
Caustic treatment		0.60	0.60
First-pass RO high-pressure pumps	b	34.65	34.70
	c	38.18	38.20
	d	35.18	35.20
Second-pass RO	b	30.35	30.26
	c	30.04	29.96
	d	29.23	29.16
Throttling valves	b	4.70	4.70
	c	5.28	5.20
	d	4.97	5.00
EDI process	b	38.70	38.78
	c	32.00	31.96
	d	30.90	30.87
Primary mixed bed ion exchange	b	1.14	1.07
	c	1.14	1.07
	d	1.14	1.07
One-micron cartridge filters		0.13	0.54
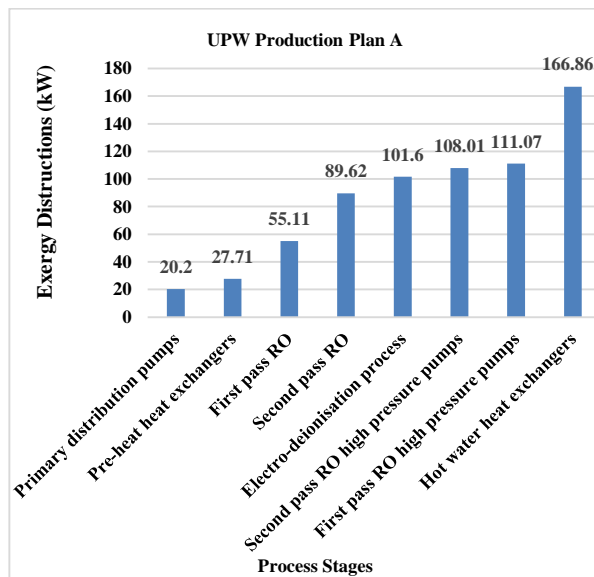
Figure 5. Top exergy destructive components in Plant A.

3.2.3 Exergy efficiency

The exergy efficiency was calculated for the first six highest exergy destructive component. The rational exergy efficiency approach was used for the exergy efficiency calculation [28,29]. The rational exergy efficiency was calculated as:

$$Efficiency_{ex} = \frac{\dot{E}_{Desired\ output}}{\dot{E}_{used}} \qquad (19)$$

The exergy efficiencies of the process streams are tabulated in Table 6.

The exergy destruction rate of the hot water HEX (166.9 kW) was higher than that of the pre-heat HEX (27.7 kW), leading to the lower exergy efficiency of the hot water HEX compared to the pre-heat HEX. To bring the exergy efficiency of the hot water HEX up to the pre-heat HEX, 7 kW could be saved. If the plant consumed 7.94 USD/kWh, the annual saving could be 2548.32 USD.

For the first-pass RO pumps, the exergy efficiency of modules (a) and (c) was 35.5% and 25.8%, respectively. The pressure in the module (c) increased from 4.7 bar to 10 bar by consuming 75 kW. While, by increasing the pressure of module (a) from 4.7 bar to about 13 bar, 86 kW was consumed. To bring the exergy efficiency of module (c) up to module (a), 3.9 kW was saved. If the plant consumed 3.9 USD/kWh, the annual saving would be 1335.21 USD.

The exergy efficiency of the RO process was significantly greater than the EDI process. The exergy efficiency of the RO process was affected by the energy consumption of the pump while the EDI exergy efficiency was affected by the energy consumption of the brine recycling pumps and rectifiers, which lowered the exergy efficiency of the EDI process, compared to the RO process.

The exergy efficiency of the first-pass RO process was ten times higher than that of the second-pass RO process. The second-pass RO modules were similar in terms of exergy efficiency. However, the exergy efficiency of module (c) in the first-pass RO was 32% more than module (a), due to different TDS and pressure drop by two modules.

The exergy efficiency of EDI module (b) was lower than modules (c) and (d). The higher energy drawn by the module (b) rectifiers caused this difference in exergy efficiency. The

lower exergy efficiency values of the EDI and the second-pass RO processes should be noted. As the purity of the water increased, the change in the chemical exergy rate decreased, lowering the exergy efficiency of the RO and EDI processes.

Table 6. The exergy efficiency of the process streams.

Component	Process stream	Exergy efficiency%
Hot water HEX		8.292
First RO high-pressure pumps	a	35.519
	c	25.835
Second RO high-pressure pumps	b	51.880
	c	50.418
	d	51.781
EDI	b	0.013
	c	0.017
	d	0.018
Second-pass RO	b	0.267
	c	0.254
	d	0.269
First-pass RO	a	3.663
	c	4.841
Pre-heat HEX		18.001
Primary distribution pumps		43.473

3. Conclusion

Exergy analysis has been made on an existing RO desalination plant (ALG) in Oman to find out the potential of energy-saving options. A modified ultrapure water (UPW) unit fed by ALG Plant was proposed [Plant A] based on the technology used in a UPW unit operated under the climate of Europe and fed by European river water [Plant B]. Three desalination exergy analysis models including the Cerci model (Model A), Drioli model (Model B) and electrolyte solution model (Model C), were developed on ALG Plant. Model C well reflected the electrolytic behavior of the process streams.

The exergy rate calculations showed the highest exergy rates were related to the inlet of the hot water heat exchangers (640.11 kW for Plant A and 686.068 kW for Plant B), followed by the outlet of the hot water heat exchangers (458.16 kW for Plant A and 524.169 kW for Plant B) and the inlet of the pre-heat heat exchangers (115.98 kW for Plant A and 119.455 kW for Plant B).

Second RO high-pressure pumps, primary distribution pumps and first RO high pressure pumps were the exergy efficient components while EDI, second-pass RO, first-pass RO, hot water HEX and pre-heat HEX with exergy efficiency of less than 20% were the most exergy destructive components.

Application of an HEX with higher contact area by consideration of economical point view, coupling the variable speed drive or motor managers to pumps and reducing the pressure drop across the membrane can be recommended to enhance the HEX, pumps and RO unit exergy efficiency, respectively.

Acknowledgements:

Nomenclature

Roman symbol

a	Activity
$A^{\emptyset}$	Pitzer model parameter
b	Pitzer model parameter
B	Debye–Huckel parameter
c	Concentration, kg/L
cp	Specific heat capacity at constant volume, kJ/kg.K
c_v	Specific heat capacity at constant volume, kJ/kg·K
$C^{\emptyset}$	Pitzer parameter
h	Specific enthalpy, kJ/kg
$\dot{E}$	Exergy rate, kW
I	Ionic strength of a solution, moles of solute/kg of solvent
$\dot{m}$	Mass flowrate, kg/s
m	molality, mole/kg
MW	Molecular weight, kg/kmol
N	Moles number
P	Pressure at the process stage under consideration, kPa
R	Universal gas constant, kJ/kmol·K
s	Specific entropy, kJ/kg.K
S	Salinity, kg/kg
t	Celsius temperature, ℃
T	Temperature, K
w	Mass fraction, kg of solvent or solute/kg of solution
x	Mole fraction, mole of solvent or solute/mole of solution
z	Valence of the ions

Greek

α	Parameter for the Debye–Huckel model
β	Number of ions of solute generated on dissociation
$\beta_{MX}^{(n)}$	Pitzer equation parameter
ρ	Density, kg/m³
$\emptyset$	Osmotic coefficient
v	Number of ions generated on the dissociation of the electrolyte
$\gamma_{\pm}$	Activity coefficient

Superscript

Ch	Chemical
P	Pressure
Th	Thermal

Subscript

0	Dead state
i	Species
H	Henry
M	Denotes to the cation
s	Salt
$soln$	Solution
w	Water
X	Denotes to the anion

Abbreviation

EDR	Electrodialysis reversal
EDI	Electro-deionization
HDH	Humidification-dehumidification

HEX   Heat exchanger

KC   Kalina cycle

MCM   Million cubic meter

MMF   Multi-media filter

NF   Nanofiltration

ORC   Organic Rankine cycle

RO   Reverse osmosis

UPW   Ultrapure water

Appendix

A.1 Water analysis

Water analysis from sampled water clarified the compositions, which are tabulated in Table A

A.2 Constants of specific enthalpy and entropy of the water

The constants of specific enthalpy of the water is evaluated by:

$m_1 = 996.7767$, $m_2 = -3.2406$, $m_3 = 0.0127$, $m_4 = -4.7723 \times 10^{-5}$, $m_5 = -1.1748$, $m_6 = 0.01169$, $m_7 = -2.6185 \times 10^{-5}$, $m_8 = 7.0661 \times 10^{-8}$

$n_1 = -2.34825 \times 10^4$, $n_2 = 3.15183 \times 10^5$, $n_3 = 2.80269 \times 10^6$, $n_4 = -1.44606 \times 10^7$, $n_5 = 7.82607 \times 10^3$, $n_6 = -4.41733 \times 10^1$,

$n_7 = 2.1394 \times 10^{-1}$, $n_8 = -1.99108 \times 10^4$, $n_9 = 2.77846 \times 10^4$, $n_{10} = 9.72801 \times 10^1$

The constants of specific entropy of the water is evaluated by:

$m_1 = = -4.4786 \times 10^{-3}$, $m_2 = -1.1654 \times 10^{-2}$, $m_3 = 6.1154 \times 10^{-5}$, $m_4 = -2.0696 \times 10^{-7}$, $m_5 = -1.5531 \times 10^{-3}$, $m_6 = 4.0054 \times 10^{-5}$, $m_7 = -1.4193 \times 10^{-7}$, $m_8 = 3.3142 \times 10^{-10}$

$n_1 = -4.231 \times 10^2$, $n_2 = 1.463 \times 10^4$, $n_3 = -9.880 \times 10^4$, $n_4 = 3.095 \times 10^5$, $n_5 = 2.562 \times 10^1$, $n_6 = -1.443 \times 10^{-1}$, $n_7 = 5.879 \times 10^{-4}$, $n_8 = -6.111 \times 10^1$, $n_9 = 8.041 \times 10^1$, $n_{10} = 3.035 \times 10^{-1}$

A.3 The process data of Plants A and B

The real data used to conduct the thermodynamic analysis is detailed in Table A.2

A.4 The calculated physical, chemical and total exergy rates using Model C at each process stream

Chemical, physical and overall exergy rates were calculated using Model C and the results for each process stream are given in Table A.3.

Table A.1. Compositions (mg/L) of experimented water.

Process Stream	Ca	Mg	Na	K	CO₃	HCO₃	SO₄	Cl	NO₃	B	SiO₂	CO₂
0	473	1400	11713	493	40	103	2861	21223	7	5	3	0
1	473	1400	11713	493	40	103	2861	21223	7	5	3	0
2	473	1400	11713	493	40	103	2861	21223	7	5	3	0
3	473	1400	11713	493	40	103	2861	21223	7	5	3	0
4	473	1400	11713	493	40	103	2861	21223	7	5	3	0
5	473	1400	11713	493	40	103	2861	21223	7	5	3	0
6	473	1400	11713	493	40	103	2861	21223	7	5	3	0
7	1	3	113	6	0	1	6	183	0	0	0	0
8	1	3	113	6	0	1	6	183	0	0	0	0
9	1	3	113	6	0	1	6	183	0	0	0	0
10	788	2332	19454	818	29	155	4764	35249	11	7	5	0
11	788	2332	19454	818	29	155	4764	35249	11	7	5	0
12	788	2332	19454	818	29	155	4764	35249	11	7	5	0
13	788	2332	19454	818	29	155	4764	35249	11	7	5	0

Process	Process stream	Q (m³/h)	T (°C) Plant A	T (°C) Plant B	P (bar)	TDS (ppm) Plant A	TDS (ppm) Plant B	Power (kW)
MMF	1b	81.4	40	16	6.2	314.00	318.01	
	1c	78.2	40	16	6.2	314.00	318.01	
	1d	74.6	40	16	6.2	314.00	318.01	
	2b	81.4	40	16	6	314.00	318.01	
	2c	78.2	40	16	6	314.00	318.01	
	2d	74.6	40	16	6	314.00	318.01	
Pre-heat HEXs	3 (Product water)	234.2	40	16	6	314.00	318.01	
	3 (Heating water)	507	46	22	6.9	314.00	318.01	
	4 (Product water)	234.2	45	21	5.3	314.00	318.01	
	4 (Heating water)	507	44	20	5.8	314.00	318.01	
Hot water HEXs	5 (Product water)	234.2	45	21	5.3	314.00	318.01	
	5 (Heating water)	78	112	88	7.3	314.00	318.01	
	6 (Product water)	234.2	48	24	5.1	314.00	318.01	
	6 (Heating water)	78	100	76	6.2	314.00	318.01	
Biocide/anti-scalant treatment	7	234.2	48	24	5.1	314.00	318.01	0.6
	8	234.2	48	24	5.1	314.00	318.01	
RO pre-filters	9	234.2	48	24	5.1	314.00	318.01	
	10	234.2	48	24	4.7	314.00	318.01	
Sodium bisulfite treatment	11	234.2	48	24	4.7	314.00	318.01	0.6
	12	234.2	48	24	4.7	314.00	318.01	
First-pass RO high-pressure pumps	13a	130.9	48	24	4.7	297.67	301.47	86
	13c	131.6	48	24	4.7	297.67	301.47	75
	14a	130.9	48	24	13.1	297.67	301.47	
	14c	131.6	48	24	10	297.67	301.47	
First-pass RO	15a	95.8	48	24	2.2	5.42	5.49	
	15c	97.6	48	24	2.2	7.56	7.65	
	16a	35.1	48	24	10.2	1095.34	1109.33	
	16c	34	48	24	6.6	1130.45	1144.89	
	17a	35.1	48	24	2	1095.34	1109.33	
	17c	34	48	24	2	1130.45	1144.89	
RO tank inlet	18	242.9	48	24	2	6.26	6.34	
RO tank outlet (Pumps inlet)	19	242.9	48	24	2	6.26	6.34	35.7
Primary pumps out (Caustic inlet)	20	242.9	48	24	4.3	6.26	6.34	0.6

Caustic treatment outlet	21	242.9	48	24	4.3	22.82	23.11	
Second-pass RO high-pressure pumps	22b	81	48	24	4.3	22.82	23.11	72
	22c	79.4	48	24	4.3	22.82	23.11	77
	22d	82.5	48	24	4.3	22.82	23.11	73
	23b	81	48	24	20.9	22.82	23.11	
	23c	79.4	48	24	21.9	22.82	23.11	
	23d	82.5	48	24	20.8	22.82	23.11	
Second-pass RO	24b	70.8	48	24	5.8	1.30	1.31	
	24c	68.6	48	24	6.5	1.30	1.31	
	24d	71.1	48	24	6.5	1.30	1.31	
	25b	10.2	48	24	18.6	172.19	174.39	
	25c	10.8	48	24	19.6	159.52	161.56	
	25d	11.4	48	24	17.7	157.08	159.08	
	26b	10.2	48	24	2	172.19	174.39	
	26c	10.8	48	24	2	159.52	161.56	
	26d	11.4	48	24	2	157.08	159.08	
EDI	27b	72.8	48	24	6.2	1.30	1.31	33.9
	27c	70.1	48	24	6.1	1.30	1.31	27.6
	27d	70	48	24	6.2	1.30	1.31	26.3
	28b	65.1	48	24	4	0.05	0.05	
	28c	65.2	48	24	4	0.05	0.05	
	28d	64.8	48	24	4	0.05	0.05	
	29b	7.7	48	24	2	11.60	11.75	
	29c	4.9	48	24	2	17.63	17.86	
	29d	5.2	48	24	2	16.56	16.77	
Primary mixed bed ion exchange	30b	66.3	48	24	3.6	0.05	0.05	
	30c	63.4	48	24	3.6	0.05	0.05	
	30d	64.8	48	24	3.6	0.05	0.05	
	31b	66.3	48	24	3	0.04	0.04	
	31c	63.4	48	24	3	0.04	0.04	
	31d	63.8	48	24	3	0.04	0.04	
One-micron cartridge filters	32	194.5	48	24	2.9	0.04	0.04	
	33	194.5	48	24	2.8	0.04	0.04	
UPW tank inlet	34	162.8	48	24	2.8	0.04	0.04	
Diverted flow to RO tanks	35	31.7	48	24	2.8	0.04	0.04	

Table A.3. The calculated physical, chemical and total exergy rates using Model C at each process stream

Process	Process stream	Physical exergy (kW)		Chemical exergy (kW)		Overall exergy (kW)	
		Plant A	Plant B	Plant A	Plant B	Plant A	Plant B
MMF	1b	11.728	11.800	0.000	0.074	11.73	11.874
	1c	11.267	11.300	0.000	0.071	11.27	11.371
	1d	10.748	10.800	0.000	0.067	10.75	10.867
	2b	11.276	11.300	0.000	0.074	11.28	11.374
	2c	10.832	10.900	0.000	0.071	10.83	10.971
	2d	10.334	10.400	0.000	0.067	10.33	10.467
Pre-heat HEXs	3 (Product water)	32.442	32.500	0.000	0.212	32.44	32.712
	3 (Heating water)	115.982	119.000	0.000	0.455	115.98	119.455
	4 (Product water)	38.525	36.900	0.000	0.210	38.52	37.110
	4 (Heating water)	82.188	83.700	0.000	0.455	82.19	84.155
Hot water HEXs	5 (Product water)	38.525	36.900	0.000	0.211	38.52	37.111
	5 (Heating water)	640.113	686.000	0.000	0.068	640.11	686.068
	6 (Product water)	53.613	58.200	0.000	0.210	53.61	58.410
	6 (Heating water)	458.162	524.100	0.000	0.069	458.16	524.169
Biocide/anti-scalant treatment	7	53.613	58.200	0.000	0.209	53.61	58.409
	8	53.613	58.200	0.000	0.209	53.61	58.409
RO pre-filters	9	53.613	58.200	0.000	0.209	53.61	58.409
	10	51.010	55.600	0.000	0.209	51.01	55.809
Sodium bisulfite treatment	11	51.010	55.600	0.000	0.209	51.01	55.809
	12	51.010	55.600	0.000	0.209	51.01	55.809
First-pass RO high-pressure pumps	13a	28.511	29.800	0.001	0.098	28.51	29.898
	13c	28.663	30.000	0.001	0.099	28.66	30.099
	14a	59.057	60.400	0.001	0.098	59.06	60.498
	14c	48.039	49.400	0.001	0.099	48.04	49.499
First-pass RO	15a	14.214	15.200	0.671	0.133	14.88	15.333
	15c	14.481	15.500	0.664	0.128	15.14	15.628
	16a	13.009	13.400	0.496	0.510	13.50	13.910
	16c	9.201	9.500	0.517	0.521	9.72	10.021
	17a	5.013	5.400	0.496	0.510	5.51	5.910
	17c	4.856	5.200	0.516	0.521	5.37	5.721
RO tank inlet	18	34.689	37.100	1.682	0.329	36.37	37.429
RO tank outlet (Pumps inlet)	19	34.689	37.100	1.682	0.329	36.37	37.429
Primary pumps out (Caustic inlet)	20	50.209	52.600	1.682	0.329	51.89	52.929
Caustic treatment outlet	21	50.209	52.600	1.372	0.217	51.58	52.817
First-pass RO high-pressure pumps	22b	16.743	17.600	0.457	0.072	17.20	17.672
	22c	16.412	17.200	0.448	0.071	16.86	17.271
	22d	17.053	17.900	0.466	0.074	17.52	17.974
	23b	54.096	54.900	0.458	0.072	54.55	54.972
	23c	55.233	56.000	0.449	0.071	55.68	56.071

	23d	54.869	55.700	0.467	0.074	55.34	55.774
	24b	17.585	18.300	0.529	0.112	18.11	18.412
	24c	18.373	19.100	0.513	0.108	18.89	19.208
	24d	19.042	19.800	0.532	0.112	19.57	19.912
Second-pass RO	25b	6.160	6.300	0.010	0.000	6.17	6.300
	25c	6.823	6.900	0.012	0.000	6.83	6.900
	25d	6.600	6.700	0.013	0.000	6.61	6.700
	26b	1.457	1.600	0.009	0.000	1.47	1.600
	26c	1.542	1.700	0.012	0.000	1.55	1.700
	26d	1.628	1.700	0.013	0.000	1.64	1.700
	27b	18.891	19.600	0.544	0.115	19.44	19.715
	27c	17.995	18.700	0.524	0.111	18.52	18.811
	27d	18.164	18.900	0.523	0.110	18.69	19.010
EDI process	28b	12.914	13.600	0.500	0.108	13.41	13.708
	28c	12.934	13.600	0.500	0.108	13.43	13.708
	28d	12.854	13.500	0.497	0.108	13.35	13.608
	29b	1.100	1.200	0.050	0.009	1.15	1.209
	29c	0.700	0.700	0.029	0.005	0.73	0.705
	29d	0.743	0.800	0.032	0.005	0.77	0.805
	30b	12.415	13.100	0.509	0.110	12.92	13.210
	30c	11.872	12.500	0.487	0.105	12.36	12.605
Primary mixed bed ion exchange	30d	12.134	12.800	0.497	0.108	12.63	12.908
	31b	11.310	12.000	0.509	0.110	11.82	12.110
	31c	10.816	11.500	0.487	0.105	11.30	11.605
	31d	10.884	11.700	0.490	0.108	11.37	11.808
One-micron cartridge filters	32	32.640	34.600	1.493	0.323	34.13	34.923
	33	32.099	34.000	1.493	0.323	33.59	34.323
UPW tank inlet	34	26.868	28.500	1.249	0.270	28.12	28.770
Diverted flow to RO tanks	35	5.232	5.500	0.243	0.053	5.47	5.553

References

[1] P. Palenzuela, B. Ortega-delgado, D. Alarcón-padilla, "Comparative assessment of the annual electricity and water production by concentrating solar power and desalination plants: A case study," *Appl. Therm. Eng.*, 2020:177:15485.
https://doi.org/10.1016/j.applthermaleng.2020.115485.

[2] Z. Rahimi-Ahar, M. S. Hatamipour, "A perspective of thermal type desalination: Technology, current development and thermodynamics analysis," Encyclopedia of Life Support Systems (EOLSS). http://www.eolss.net/Eolss-sampleAllChapter.aspx, 2020.

[3] K. Yousuf, 2019. "Efforts on to meet future water demand," Available:Https://www.omanobserver.om/efforts-on-to-meet-future-water-demand/.

[4] T. M. A. Al Sajwani, "The desalination plants of Oman: past, present and future," *Desalination*, 1998:120:8–13.
https://doi.org/10.1016/S0011-9164(98)00201-X.

[5] Z. Rahimi-Ahar, M. S. Hatamipour, L. Rahimi Ahar, "Air Humidification-Dehumidification Process for Desalination: A review," *Prog. Energy Combust. Sci.*, 2020:80:100850.
https://doi.org/10.1016/j.pecs.2020.100850.

[6] O. N. Igobo, P. A. Davies, "Isothermal Organic Rankine Cycle (ORC) driving Reverse Osmosis (RO) Desalination: experimental investigation and case study using R245fa working fluid," *Appl. Therm. Eng.*, 2018:136:740–746.
https://doi.org/10.1016/j.applthermaleng.2018.02.056.

[7] M. A. Darwish, N. M. Al-najem, "Energy consumption by multi-stage flash and reverse osmosis desalters," *Appl. Therm. Eng.*, 2000:20:399–416.
https://doi.org/10.1016/S1359-4311(99)00032-0.

[8] S. Ahmadvand, B. Abbasi, B. Azarfar, M. Elhashimi, "Looking beyond energy efficiency: an applied review of

water desalination technologies and an introduction to capillary-driven desalination," *water*, 2019:11:696–726. https://doi.org/10.3390/w11040696.

[9] Z. Rahimi-Ahar, M. S. Hatamipour, Y. Ghalavand, A. Palizvan, "Comprehensive study on vacuum humidification-dehumidification (VHDH) desalination," *Appl. Therm. Eng.*, 2020:114944. https://doi.org/10.1016/j.applthermaleng.2020.114944.

[10] F. Cziesla, G. Tsatsaronis, *Exergy, energy system analysis and optimization. Strengths and limitations of exergy analysis*, *Inst. Energy Eng.*, Vol. I, Springer. 1999.

[11] F. Fitzsimons, B. Corcoran, P. Young, G. Foley, "Exergy analysis of water purification and desalination: A study of exergy model approaches," *Desalination*, 2015:359:212–224. https://doi.org/10.1016/j.desal.2014.12.033.

[12] Y. Cerci, "Exergy analysis of a reverse osmosis desalination plant in California," *Desalination*, 2002:142: 257–266. https://doi.org/10.1016/j.desal.2004.08.045.

[13] N. Kahraman, Y.A. Cengel, B. Wood, Y. Cerci, "Exergy analysis of a combined RO, NF, and EDR desalination plant," *Desalination*, 2004:171:217–232. https://doi.org/10.1016/j.desal.2004.05.006.

[14] A. Shekari Namin, H. Rostamzadeh, P. Nourani, "Thermodynamic and thermoeconomic analysis of three cascade power plants coupled with RO desalination unit, driven by a salinity-gradient solar pond," *Therm. Sci. Eng. Prog*, 18, 100562, 2020. https://doi.org/10.1016/j.tsep.2020.100562.

[15] A. Mohammadi, M. Mehrpooya, "Energy and exergy analyses of a combined desalination and CCHP system driven by geothermal energy," *Appl. Therm. Eng.*, 116, 685–694, 2017. https://doi.org/10.1016/j.applthermaleng.2017.01.114.

[16] S. Islam, I. Dincer, B.S. Yilbas, "Development of a novel solar-based integrated system for desalination with heat recovery," *Appl. Therm. Eng.*, 129, 1618–1633, 2018. https://doi.org/10.1016/j.applthermaleng.2017.09.028.

[17] H. Ishaq, I. Dincer, G. F. Naterer, "New trigeneration system integrated with desalination and industrial waste heat recovery for hydrogen production," *Appl. Therm. Eng.*, 142, 767–778, 2018. https://doi.org/10.1016/j.applthermaleng.2018.07.019.

[18] N. Bouzayani, N. Galanis, J. Orfi, "Thermodynamic analysis of combined electric power generation and water desalination plants," *Appl. Therm. Eng.*, 29, 624–633, 2009.

https://doi.org/10.1016/j.applthermaleng.2008.03.031.

[19] A. Naseri, M. Bidi, M. H. Ahmadi, "Thermodynamic and exergy analysis of a hydrogen and permeate water production process by a solar-driven transcritical CO_2 power cycle with liquefied natural gas heat sink," *Renew. Energy*, 113, 1215–1228, 2017. https://doi.org/10.1016/j.renene.2017.06.082.

[20] M. Ameri, M. Seyd Eshaghi, "A novel configuration of reverse osmosis , humidification – dehumidification and flat plate collector: Modeling and exergy analysis," *Appl. Therm. Eng*, 103, 855–873, 2016. https://doi.org/10.1016/j.applthermaleng.2016.04.047.

[21] A. Grabowski, G. Zhang, H. Strathmann, G. Eigneberger, "The production of high purity water by continuous electrodeionization with bipolar membranes: influluence of the anion-exchange membrane permselectivity," *J. Membr. Sci.*, 281, 297–306, 2006. https://doi.org/10.1016/j.memsci.2006.03.044.

[22] H. Lee, Y. Jin, S. Hong, "Recent transitions in ultrapure water (UPW) technology: Rising role of reverse osmosis (RO)," *Desalination*, 399, 185–197, 2016. https://doi.org/10.1016/j.desal.2016.09.003.

[23] M. Zhan, H. Lee, Y. Jin, S. Hong, "Application of MFI-UF on an ultrapure water production system to monitor the stable performance of RO process," *Desalination*, 491, 114565, 2020. https://doi.org/10.1016/j.desal.2020.114565.

[24] Y. Jin, H. Lee, M. Zhan, S. Hong, "UV radiation pretreatment for reverse osmosis (RO) process in ultrapure water (UPW) production," *Desalination*, 439, 138–146, 2018. https://doi.org/10.1016/j.desal.2018.04.019.[25] J. Wood, J. Gifford, J. Arba, M. Show, "Production of ultrapure water by continuous electrodeionization," *Desalination*, 250, 973–976, 2010. https://doi.org/10.1016/j.desal.2009.09.084.

[26] K. G. Nayar, M. H. Sharqawy, L. D. Banchik, J. H. Leinhard, "Thermophysical properties of seawater: A review and new correlations that include pressure dependence," *Desalination*, 390, 1–24, 2016. https://doi.org/10.1016/j.desal.2016.02.024.

[27] K. S. Pitzer, "Thermodynamics of electrolytes. I. Theoretical basis and general equations," *J. Phys. Chem.*, 77, 268−277, 1973. https://doi.org/10.1021/j100621a026.

[28] T. J. Kotas, *The exergy method of thermal plant analysis*, *1st Ed.*, Anchor Brendon Ltd. 1997. 29] H. Hassan, M. S. Yousef, "An assessment of energy, exergy and CO_2 emissions of a solar desalination system under hot climate conditions," *Process Saf. Environ. Prot.*, 145, 157-171, 2021. https://doi.org/10.1016/j.psep.2020.

Initial Stress and Modified Ohm's Law in Magneto-thermoelastic Problem Under Three Theories with Microtemperatures and Voids

L. C. Bawankar*[1], G. D. Kedar[2]

[1] Sanjivani College of Engineering, Kopargaon, Ahmednagar, India.
[2]Department of Mathematics, RTM Nagpur University, Nagpur, India.
Email: [1]latikabawankar@gmail.com

Abstract

This paper studies the generalized magneto-thermoelastic problem with microtemperatures, voids taking into account initial stress and modified Ohm's law under three theories. The analytical solution is obtained by normal modes and expressions for micro temperature, temperature distribution, displacement, components of heat flux, change in the volume fraction field as well as stress components are calculated. The effect of initial stress and thermal shock is observed on desired field variables. The results are established graphically for all physical quantities and variation is done for three theories due to the effect of modified Ohm's law coefficient.

Keywords: Magneto-thermoelasticity; microtemperatures; voids; initial stress; modified Ohm's Law.

1. Introduction

The magneto-thermoelasticity theory tells us about the thermoelastic deformations in solids due to magnetic field presence, which is helpful in geophysics, plasma physics. The study of high temperatures and temperature gradient is vital with magnetic field presence to understand its effect on seismic waves and the emissions from nuclear devices in the form of electromagnetic radiations. For linear coupled and uncoupled thermoelasticity theory, diffusion type of heat conduction equations is considered, which predict infinite heat wave propagation speed contrary to physical observations. To eradicate the principle of coupled thermoelasticity, Biot [1] proposed the contradiction found in the classical uncoupled hypothesis that elastic changes do not influence on temperature. However, the hypothesis of both heat equations is of the kind of diffusion, estimating infinite heat wave propagation rates. The Lord and Shulman [2] was initiated by introducing a relaxation constant to account for the time required to accelerate the heat flow. If the constant of relaxation is set to zero, the equations of Lord and Shulman [2] decrease to classical field equation of thermoelasticity. The hyperbolic heat equation is consistent with this theory, removing the paradox of infinite heat wave propagation. The Green and Lindsay [3] named thermoelasticity as a temperature-dependent where its rating is included with two constant variables act as a relaxation time, which was not violating the classical Fourier's law. Agarwal [4] discussed the effect on plane thermoelastic waves due to presence of electromagnetic field. Paria [5] observed elastic and thermoelastic behavior of different problems under magnetic field influence. Youssef [6] studied the variable material properties in generalized thermoelasticity problems.

The theory of microtemperature is regarded as a theory that tackles temperature, wave propagation, and the thermal properties variation at microstructure level in a rigid thermocouple. The solid nanostructures are essential as particle can contract or stretch, and in solid vessels principal thermal stresses can be related to the effects of thermal microstructure, and so a well-structured theory of rigid solids that makes the effects of microtemperature is required. Grot [7] established the theory of microstructure in thermodynamic problem with inner structure. Microelements contain microtemperature, which causes microdeformations. Riha [8] applied micromorphic continua theory to heat conduction problem with inner structure and observed the changes in materials. Casas and Quintanilla [9] constructed the exponential stability of thermoplastic materials which have inner structure. Casas and Quintanilla and Iesan [10] discussed the microstructure of microelements in thermoelastic materials. Iesan [11] discussed the micromorphic elastic solids with microtemperatures. Scavanadze [12] provide the solution of equilibrium equation, constitutive relation with microtemperature by means of elementary function theory. Othman and Abd Elaziz [13] discussed gravity and microtemperature presence in a porous medium, and comparison is made for three theories. Quintanilla [14] have studied the uniqueness theorem of porous media with microtemperature under three theories of thermoelasticity. Eringen [15] and Eringen and Suhubi [16] discussed the micromorphic elastic solids and their behavior in the classical theory of thermoelasticity. Kalkal et al. [17] discussed the thermoelastic half space problem of microtemperature with diffusion under presence of magnetic field.

The voids are small pores distributed in elastic materials. It consists of volume and if it tends to zero becomes the limiting case for the classical theory of elasticity. The practical use of voids is important for investigating various types of biological and geological materials, but the elastic theory is not sufficient. The linear and nonlinear theory of

*Corresponding Author

elastic material with voids developed by Cowin and Nunziato [18], Nunziato and Cowin [19], Iesan [20]. The asymptotic spatial behaviour of material with voids in linear theory studied by Pompei and Scalia [21] and Stan Chirita [22]. Othman et al. [23] and Iesan [24] studied initial stress effect on thermoelastic material with voids. The concept of voids in a material distributed in the form granules introduced by Goodman and Cowin [25] and Jaric [26]. Othman et al. [27] developed the mathematical model of thermoelasticity with the existence of initial stress, voids, and microtemperature. Kalkal et al. [28] discussed wave nature in initially stressed thermoelastic problem with voids and microtemperature under magnetic field influence. Othman and Abd-Elaziz [29] observed effect of hall current and initial stress in porous thermoelastic condition with microtemperature. Othman and Abd-Elaziz [30] discussed about the rotation and hall effect on plane waves with voids and microtemperature on thermoelastic materials with magnetic field.

Initial stresses arise due to many reasons such as temperature variation, quenching process, living tissue growth and development, and gravity variations, etc. The study of initial stresses in thermal and mechanical conditions is critical as the earth consists of high initial stress due to gravity and strongly affects the propagation of waves. Ames and Straughan [31] proved the thermoelastic solids has continuous dependence if it is initially pre-stressed. The initial hydrostatic stress studied by Montanaro [32] in the linear theory of thermoelasticity. Abbas and Othman [33] investigated the interaction of thermoelastic half-space with initial hydrostatic stress under the fiber-reinforced anisotropic conditions.

The modified Ohm's law relates to the temperature gradient and current density. Lorentz force arises due to the interaction of magnetic, electric field and Ohm's law useful for the current density, which describes electric field-induced due to material particle velocity which moves in a magnetic field. Ezzat and Elall [34] and Sarkar [35] explained the problems of magneto-thermoelasticity by using modified Ohm's law and shows its effect on three different theories.

The novelty of this article is the introduction of modified Ohm's law in magneto-thermoelastic problem with microtemperature and voids under initial stress and thermal shock conditions for three theories. Modification in Ohm's law is due to the addition of temperature gradient term. This modification states that the electric potential gradient is proportional to the strength of the material at each point. The strength and temperature variation in a material at each point is observed because of microtemperature theory and modified Ohm's law.

In this work, we study the effect of modified Ohm's law with voids and microtemperature in the magneto-thermoelastic problem under initial stress. The initially stressed linear, isotropic, homogeneous half-space problem under the influence of magnetic field is considered. The expressions for the desired variables are derived for Green Lindsay (GL), Lord and Shulman, and coupled theory (CT) for isothermal boundary conditions subjected to thermal shock by using normal mode analysis. Estimations have been carried out numerically and illustrated graphically for the above said theories due to the coefficient of modified Ohm's law.

2. Basic Equations

In the linear theory of thermodynamics, the governing equations for homogeneous isotropic magneto-thermoelastic material with microtemperature, voids and initial stress can be written as

$$\sigma_{ij} = 2\mu e_{ij} + (\lambda e_{rr} + \lambda_0 \phi)\delta_{ij} - \beta(1 + \tau_1 T_{,t})\delta_{ij} -$$

$$p(\delta_{ij} + \omega_{ij}) \tag{1}$$

$$h_i = \alpha\phi_{,i} - \mu_1 w_i \tag{2}$$

$$g^* = -\lambda_0 e_{rr} - \xi_1 \phi + mT - w_0 \phi_{,t} \tag{3}$$

$$q_i + \tau_0 q_{i,t} = -k_1 w_i - k^* T_{,i} \tag{4}$$

$$q_{ij} = -k_4 w_{r,r}\delta_{ij} - k_5 w_{i,j} - k_6 w_{j,i} \tag{5}$$

$$Q_i = (k^* - k_3)T_{,i} + (k_1 - k_2)w_{,i} \tag{6}$$

$$\rho\eta^* = a_0 T + \beta e_{rr} + m\phi \tag{7}$$

$$\rho\varepsilon_i = -\mu_1\phi_{,i} - bw_i \tag{8}$$

The rotation tensor and strain-displacement relation are

$$e_{ij} = \frac{1}{2}(u_{i,j} + u_{j,i}), \quad \omega_{ij} = \frac{1}{2}(u_{j,i} - u_{i,j}) \quad i,j,r = 1,2,3 \tag{9}$$

The equation of motion with Lorentz force be

$$\sigma_{ij} + F_i = \rho u_{i,tt} \tag{10}$$

$$h_{i,i} + g^* = \rho\psi\phi_{,tt} \tag{11}$$

The balance energy equation without heat source is

$$-q_{i,i} = \rho T_0 \eta_{,t}^* \tag{12}$$

The first-moment of energy is

$$\rho\varepsilon_{i,t} = -Q_i - q_i + q_{ji,j} \tag{13}$$

where constants are defined in nomenclature.
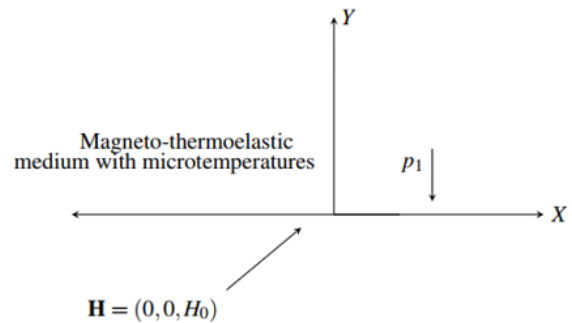
Figure 1: The geometry of the problem

3. Problem Formulation

Consider 2-D problem of isotropic, homogeneous electrically and thermally conducting thermoelastic half space ($y \geq 0$) with voids and microtemperature. For two-dimensional problem microtemperature vector is assumed as $w_i = (w_1, w_2, 0)$ and displacement vector $u_i = (u, v, 0)$. The constant magnetic field $(0,0,H_0)$ act normal to bounding plane (along positive z-direction) and applied to the medium which produces h and E as given in Figure 1. The electromagnetic field equations for a conducting

homogeneous medium which satisfy Maxwell's equations are

$$\mathbf{J} + \varepsilon_0 \dot{\mathbf{E}} = \nabla \times \mathbf{h} \tag{14}$$

$$\dot{\mathbf{B}} = \nabla \times \mathbf{E} \tag{15}$$

$$div\ \mathbf{B} = \rho_e, div\ \mathbf{D} = 0 \tag{16}$$

$$\mathbf{B} = \mu_0(\mathbf{H_0} + \mathbf{h}), \mathbf{D} = \varepsilon_0\ \mathbf{E} \tag{17}$$

In addition to this, in a finite conducting medium with modified Ohm's law is given by

$$\mathbf{J} = \sigma_0(\mathbf{E} + \mu_0 \dot{\mathbf{u}} \times \mathbf{H}) - k_0 \nabla \mathbf{T} \tag{18}$$

where constants are defined in nomenclature section. Solving equations (14) to (18) we obtain

$$h_{,x} = \sigma_0(E + \mu_0 H_0 \dot{u}) + k_0 T_{,y} - \varepsilon_0 \dot{E}_y \tag{19}$$

$$h_{,y} = \sigma_0(E + \mu_0 H_0 \dot{v}) - k_0 T_{,x} + \varepsilon_0 \dot{E}_x \tag{20}$$

$$\mu_0 \dot{h} = E_{x,y} - E_{y,x} \tag{21}$$

Lorentz force components from equation (17) and (18) are

$$F_x = \mu_0 H_0 \sigma_0 (E_y - \mu_0 H_0 \dot{u}) - k_0 T_{,y} \tag{22}$$

$$F_y = -\mu_0 H_0 \sigma_0 (E_x + \mu_0 H_0 \dot{v}) + k_0 T_{,x} \tag{23}$$

$$F_z = 0 \tag{24}$$

Using equations (1) to (9), (22) and (23) in equations (10) to (13), we obtain the linear partial differential equations with microtemperature, voids, modified Ohm's law under initial stress.
Equation of motion becomes

$$\left(\mu - \frac{p}{2}\right)\nabla^2 u + \lambda_0 \phi_{,x} + \left(\lambda + \mu + \frac{p}{2}\right)e_{,x} - \beta\left(1 + \tau_1 \frac{\partial}{\partial t}\right)T_{,x} + \mu_0 H_0 \sigma_0 (E_y - \mu_0 H_0 \dot{u}) - k_0 T_{,y} = \rho \ddot{u} \tag{25}$$

$$\left(\mu - \frac{p}{2}\right)\nabla^2 v + \lambda_0 \phi_{,y} + \left(\lambda + \mu + \frac{p}{2}\right)e_{,y} - \beta\left(1 + \tau_1 \frac{\partial}{\partial t}\right)T_{,y} - \mu_0 H_0 \sigma_0 (E_x + \mu_0 H_0 \dot{v}) + k_0 T_{,x} = \rho \ddot{v} \tag{26}$$

Volume fraction field equation is

$$\left(\alpha \nabla^2 - \xi_1 - \rho\psi \frac{\partial^2}{\partial t^2} - w_0 \frac{\partial}{\partial t}\right)\phi - \mu_1 e_1 - \lambda_0 e + m\left(1 + \tau_1 \frac{\partial}{\partial t}\right)T = 0 \tag{27}$$

$$k^* T_{,x} = \left(1 + \tau_0 \frac{\partial}{\partial t}\right)[k_6 \nabla^2 w_1 - \mu_1 \dot{\phi}_{,x} + (k_4 + k_5)e_{1,x} - bw_1 - (k^* - k_3)T_{,x} + (k_1 - k_2)w_1] - k_1 w_1 \tag{28}$$

$$k^* T_{,y} = \left(1 + \tau_0 \frac{\partial}{\partial t}\right)[k_6 \nabla^2 w_2 - \mu_1 \dot{\phi}_{,y} + (k_4 + k_5)e_{1,y} - bw_2 + (k^* - k_3)T_{,y} + (k_1 - k_2)w_2] - k_1 w_2 \tag{29}$$

Heat conduction equation is given by
$$\left[k^* \nabla^2 - a_0 T_0 \left(\frac{\partial}{\partial t} + \tau_0 \frac{\partial^2}{\partial t^2}\right)\right]T + k_1 e_1 = \left(\frac{\partial}{\partial t} + \eta_0 \tau_0 \frac{\partial^2}{\partial t^2}\right)(\beta T_0 e + m T_0 \phi) \tag{30}$$

where $e = \frac{\partial u}{\partial x} + \frac{\partial v}{\partial y}$, $e_1 = \frac{\partial w_1}{\partial x} + \frac{\partial w_2}{\partial y}$
We introduce the following nondimensional variables

$$(x_i', u_i') = \frac{\omega^*}{c_1}(x_i, u_i), \quad \phi' = \frac{\psi \omega^{*2}}{c_1^2}\phi, \quad w_i' = \frac{c_1}{\omega^*}w_i,$$

$$q_{ij}' = \frac{\omega^*}{\mu c_1^2}q_{ij}, \quad T' = \frac{1}{\mu T_0}T, \quad \sigma_{ij}' = \frac{1}{\beta T_0}\sigma_{ij},$$

$$h' = \frac{\omega^*}{\mu_0 H_0 \sigma_0}h, \quad E_i' = \frac{\omega^* c_1}{\mu_0^2 H_0 \sigma_0}E_i, \quad k_0' = \frac{\mu_0 H_0}{\beta}k_0$$

$$(t', \tau_0', \tau_1') = \omega^*(t, \tau_0, \tau_1), \quad p' = \frac{1}{\beta T_0}p,$$

$$\omega^* = \frac{a_0 T_0 c_1^2}{k^*}, c_1^2 = \frac{\lambda + 2\mu}{\rho} \tag{31}$$

4. Problem Solution

Suppose that the potential functions in dimensionless form can be consider as $q_1(x, y, t)$, $q_2(x, y, t), N_1(x, y, t)$, and $N_2(x, y, t)$

$$u = N_{1,x} + N_{2,x}, \quad v = N_{1,y} - N_{2,x}, \tag{32}$$

$$w_1 = q_{1,x} + q_{2,y}, \quad w_2 = q_{1,y} - q_{2,x}$$

To get the solution of dimensionless physical quantities, it is suitable to presume solution by using normal modes in the form

$$[N_1, N_2, q_1, q_2, \emptyset, h, T](x, y, t) =$$
$$[N_1^*, N_2^*, q_1^*, q_2^*, \emptyset^*, h^*, T^*](y)e^{i(ax - \xi t)} \tag{33}$$

Using equations (31) to (33) in equations (25) to (30) we obtained

$$(D^2 - L_1)h^* + L_2(D^2 - a^2)N_1^* = 0 \tag{34}$$

$$(D^2 - L_3)T^* + L_4(D^2 - a^2)q_1^* - L_5(D^2 - a^2)N_1^* - L_6\emptyset^* = 0 \tag{35}$$

$$(D^2 - L_7)\emptyset^* - m_{11}(D^2 - a^2)N_1^* - m_{12}(D^2 - a^2)q_1^* + L_8 T^* = 0 \tag{36}$$

$$(D^2 - L_9)N_1^* + L_{10}\emptyset^* - L_{11}T^* - L_{12}h^* = 0 \tag{37}$$

$$(D^2 - L_{13})N_2^* + m_6 T^* = 0 \tag{38}$$

$$(L_{18}D^2 - L_{14})q_1^* + L_{16}\emptyset^* - L_{15}T^* = 0 \tag{39}$$

$$(m_{15}D^2 - L_{17})q_2^* = 0 \tag{40}$$

All the constants $m_1 - m_{33}$ and $L_1 - L_{18}$ are mentioned in Appendix and $D = d/dy$. By eliminating functions $N_1^*, N_2^*, q_1^*, q_2^*, \emptyset^*, h^*, T^*$ among equations (34) to (40) yields as follows

$$(D^{12} - AD^{10} + BD^8 - CD^6 + ED^4 - FD^2 + G)(N_1^*, N_2^*, q_1^*, q_2^*, \emptyset^*, h^*, T^*) = 0 \tag{41}$$

where A, B, C, D, E, F, G are constants. Equation (41) can be classified as

$$[(D^2 - \alpha_1^2)(D^2 - \alpha_2^2)(D^2 - \alpha_3^2)(D^2 - \alpha_4^2)(D^2 - \alpha_5^2)(D^2 - \alpha_6^2)](N_1^*, N_2^*, q_1^*, q_2^*, \emptyset^*, h^*, T^*) = 0 \tag{42}$$

where α_n^2 $(n = 1,2,3,4,5,6)$ are the roots of characteristic equation. The general solution of physical quantities obtained from equation (41), bounds as $y \to \infty$ are

$$(N_1{}^*, N_2{}^*, q_1{}^*, q_2{}^*, \emptyset^*, h^*, T^*)(y) =$$

$$\sum_{n=1}^6 (1, O_{1_n}, O_{2_n}, O_{3_n}, O_{4_n}, O_{5_n}) S_n e^{-\alpha_n y + i(ax - \xi t)} \quad (43)$$

where $S_n (n = 1,2 \dots 6)$ are constants. $O_{1_{n \dots 5_n}}$ are some parameters depending on a, ξ given in appendix.
The solution of equations (34) to (40) as $y \to \infty$ can be written as

$$q_2(x, y, t) = S_7 e^{-\alpha_7 y + i(ax - \xi t)} \quad (44)$$

$$(u, v)(x, y, t) = \sum_{n=1}^6 [O_{6_n}, O_{7_n}] S_n e^{-\alpha_n y + i(ax - \xi t)} \quad (45)$$

$$(w_1, w_2)(x, y, t) = [\sum_{n=1}^6 (ia, -\alpha_n) O_{5_n} S_n e^{-\alpha_n y} -$$

$$(\alpha_7, ia) S_7 e^{-\alpha_7 y}] e^{i(ax - \xi t)} \quad (46)$$

$$(\sigma_{xx}, \sigma_{yy}, \sigma_{zz})(x, y, t) = -p +$$

$$\sum_{n=1}^6 [O_{8_n}, O_{9_n}, O_{9^*_n}] S_n e^{-\alpha_n y + i(ax - \xi t)} \quad (47)$$

$$(\sigma_{xy}, \sigma_{yx}, \sigma_{xz}, \sigma_{yz})(x, y, t) =$$

$$\sum_{n=1}^6 [O_{10_n}, O_{10^*_n}, 0, 0] S_n e^{-\alpha_n y + i(ax - \xi t)} \quad (48)$$

$$(q_{xx}, q_{yy}, q_{xy})(x, y, t) =$$

$$[\sum_{n=1}^6 [O_{11_n}, O_{12_n}, O_{13_n}] S_n e^{-\alpha_n y} +$$

$$(b_9, b_{10}, b_{11}) S_7 e^{-\alpha_7 y}] e^{i(ax - \xi t)} \quad (49)$$

where $Q(a, \xi)$ is the parameter depends on a, ξ.
Now considering the electric and magnetic field intensities h_0, E_{x0}, E_{y0} respectively. The nondimensional field equations satisfied by these variables are given by

$$h_{0,y} = \varepsilon_1 \dot{E}_{x0} \quad (50)$$

$$h_{0,x} = \varepsilon_1 \dot{E}_{y0} \quad (51)$$

$$h_0 = (E_{x0})_{,y} - (E_{y0})_{,x} \quad (52)$$

$h_0, E_{x0},$ and E_{y0} can be decompose in normal modes in the following form

$$[h_0, E_{x0}, E_{y0}](x, y, t) = [h_0{}^*, E_{x0}{}^*, E_{y0}{}^*](y) e^{i(ax - \xi t)} \quad (53)$$

Using Equation (53) to Equations (50) to (52) and after solving, the results are obtained for $y \to \infty$ as

$$h_0{}^* = Q(a, \xi) e^{-\alpha_9 y} \quad (54)$$

$$E_{x0}{}^* = \frac{\alpha_9}{(i\varepsilon_1 \xi)} Q(a, \xi) e^{-\alpha_9 y} \quad (55)$$

$$E_{y0}{}^* = \frac{\alpha_9}{(i\varepsilon_1 \xi)} Q(a, \xi) e^{-\alpha_9 y} \quad (56)$$

5. Application

To determine the parameter S_n and Q we need to consider the following boundary condition at $y = 0$

1. Thermal boundary condition: The surface $y = 0$ is exposed to time dependent thermal shock in the form

$$T(x, 0, t) = f(x, t) \quad (57)$$

2. Mechanical boundary condition:
   a. The surface of the half space is stressed by constant force p_1 i.e.

$$\sigma_{yy}(x, 0, t) = -p_1 e^{i(ax - \xi t)} - p \quad (58)$$

   b. The surface of the half space is traction free

$$\sigma_{xy}(x, 0, t) = 0 \quad (59)$$

3. Electric Boundary condition: For $y = 0$, the component of electric field intensity vector are continuous across the half surface

$$E_y(x, 0, t) = E_{y0}(x, , 0, t) \quad (60)$$

4. Magnetic Boundary condition: For $y = 0$ the component of magnetic field intensity vector are continuous across the half surface

$$h(x, 0, t) = h_0(x, , 0, t) \quad (61)$$

5. Heat flux moments Boundary condition: The heat flux moments along normal and tangential direction are free.

$$q_{xx}(x, 0, t) = q_{xy}(x, 0, t) = 0 \quad (62)$$

6. Volume fraction field boundary condition: The condition of volume fraction field change is

$$\frac{\partial \phi}{\partial y} = 0 \quad (63)$$

Substituting the desired physical quantities into the above boundary conditions and finding the value of constants by using matrix inversion method we get

$$\begin{bmatrix} S_1 \\ S_2 \\ S_3 \\ S_4 \\ S_5 \\ S_6 \\ S_7 \\ Q \end{bmatrix} = \begin{bmatrix} O_{9_1} & O_{9_2} & O_{9_3} & O_{9_4} & O_{9_5} & O_{9_6} & 0 & 0 \\ O_{10_1} & O_{10_2} & O_{10_3} & O_{10_4} & O_{10_5} & O_{10_6} & 0 & 0 \\ O_{1_1} & O_{1_2} & O_{1_3} & O_{1_4} & O_{1_5} & O_{1_6} & 0 & 0 \\ O_{4_1} & O_{4_2} & O_{4_3} & O_{4_4} & O_{4_5} & O_{4_6} & 0 & 1 \\ O_{14_1} & O_{14_2} & O_{14_3} & O_{14_4} & O_{14_5} & O_{14_6} & 0 & -L \\ O_{11_1} & O_{11_2} & O_{11_3} & O_{11_4} & O_{11_5} & O_{11_6} & b_{10} & 0 \\ O_{12_1} & O_{12_2} & O_{12_3} & O_{12_4} & O_{12_5} & O_{12_6} & b_{11} & 0 \\ \alpha_1 O_{2_1} & \alpha_2 O_{2_2} & \alpha_3 O_{2_3} & \alpha_4 O_{2_4} & \alpha_5 O_{2_5} & \alpha_6 O_{2_6} & 0 & 0 \end{bmatrix}^{-1} \begin{bmatrix} -p_1 \\ 0 \\ f^* \\ 0 \\ 0 \\ 0 \\ 0 \\ 0 \end{bmatrix} \quad (64)$$

6. Perticular and Special cases
6.1 Initially stressed thermoelastic problem with voids and microtemperature by neglecting magnetic field

By neglecting the magnetic field $H_0 = 0, k_0 = 0$ in the governing equation we obtained the equation for initially stressed thermoelastic half space problem with microtemperature and voids are given by

$$[D^2 - L_3]T^* + L_4[D^2 - a^2]q_1^* - L_5[D^2 - a^2]N_1^* - L_6\emptyset^* = 0 \quad (65)$$

$$[D^2 - L_7]\emptyset^* - m_{11}[D^2 - a^2]N_1^* - m_{12}[D^2 - a^2]q_1^* + L_8 T^* = 0 \quad (66)$$

$$[D^2 - L_9]N_1^* + L_{10}\emptyset^* - L_{11}T^* = 0 \quad (67)$$

$$[D^2 - L_{13}]N_2^* = 0 \quad (68)$$

$$[m_{20}D^2 - L_{14}]q_1^* - L_{15}T^* + L_{16}\emptyset^* = 0 \tag{69}$$

$$[m_{15}D^2 - L_{16}]q_2^* = 0 \tag{70}$$

Eliminating functions $\emptyset^*, T^*, q_1^*, N_1^*, N_2^*, q_2^*$ from equations (64) to (69) we get

$$(D^8 - A_1D^6 + A_2D^4 - A_3D^2 + A_4)\,(N_1^*, N_2^*, \emptyset^*, q_1^*, T^*) = 0 \tag{71}$$

where $A_1, A_2, A_3,$ and A_4 are constants. The general solution of physical quantities obtained from equation (70), bounds as $y \to \infty$ are

$$(T^*, \emptyset^*, N_1^*, q_1^*)(y) =$$

$$\sum_{n=1}^{4}(1,\ H_{1n},\ H_{2n},\ H_{3n})S_n^* e^{-\alpha_n^* y + i(ax - \xi t)} \tag{72}$$

The solution of equations (64) to (69) as $y \to \infty$ can be written as

$$N_2(x, y, t) = S_5^* e^{-\alpha_6 y + i(ax - \xi t)} \tag{73}$$

$$q_2(x, y, t) = S_6^* e^{-\alpha_7^* y + i(ax - \xi t)} \tag{74}$$

$$(u,v)(x, y, t) = \sum_{n=1}^{4}(ia, -\alpha_n^*)H_{2n}S_n^* e^{-\alpha_n^* y + i(ax - \xi t)} -$$

$$(\alpha_5^*, ia)S_5 e^{-\alpha_5^* y + i(ax - \xi t)} \tag{75}$$

$$(w_1, w_2)(x, y, t) = \sum_{n=1}^{4}(ia, -\alpha_n^*)H_{3n}\,S_n^* e^{-\alpha_n^* y + i(ax - \xi t)} -$$

$$(\alpha_6^*, ia)S_6^* e^{-\alpha_6^* y + i(ax - \xi t)} \tag{76}$$

$$(\sigma_{xx}, \sigma_{yy})(x, y, t) = -p +$$

$$\sum_{n=1}^{4}(H_{4n}, H_{5n})S_n^* e^{-\alpha_n^* y + i(ax - \xi t)} +$$

$$(Z_1, Z_2)S_5^* e^{-\alpha_5^* y + i(ax - \xi t)} \tag{77}$$

$$\sigma_{xy}(x, y, t) = \sum_{n=1}^{4}H_{6n}S_n^* e^{-\alpha_n^* y + i(ax - \xi t)} +$$

$$Z_3 S_5^* e^{-\alpha_5^* y + i(ax - \xi t)} \tag{78}$$

$$(q_{xx}, q_{yy})(x, y, t) = \sum_{n=1}^{4}(H_{7n}, H_{8n})S_n^* e^{-\alpha_n^* y + i(ax - \xi t)} +$$

$$(Z_4, Z_5)S_6^* e^{-\alpha_6^* y + i(ax - \xi t)} \tag{79}$$

where $\alpha_n^*, \alpha_5^*,$ and α_6^* are the roots of characteristic equation, S_n are constants.
$H_{1_{n........3n}}$ are some parameters depending on a, ξ given in Appendix. Substituting the all above physical quantities into the equations (57) to (59), (62) and (63) and finding the value of constants by using matrix inversion method we get

$$\begin{bmatrix} S_1^* \\ S_2^* \\ S_3^* \\ S_4^* \\ S_5^* \\ S_6^* \end{bmatrix} = \begin{bmatrix} H_{51} & H_{52} & H_{53} & H_{54} & Z_2 & 0 \\ H_{61} & H_{62} & H_{63} & H_{64} & Z_3 & 0 \\ 1 & 1 & 1 & 1 & 0 & 0 \\ H_{71} & H_{72} & H_{73} & H_{74} & 0 & Z_4 \\ H_{81} & H_{82} & H_{83} & H_{84} & 0 & Z_5 \\ H_{11} & H_{12} & H_{13} & H_{14} & 0 & 0 \end{bmatrix}^{-1} \begin{bmatrix} -p_1 \\ 0 \\ f^* \\ 0 \\ 0 \\ 0 \end{bmatrix} \tag{80}$$

The solution and graphical analysis match with the Othman et.al.[28]

6.2 Magneto-thermoelastic problem with modified Ohm's law by neglecting voids, initial stress and microtemperature

To study this problem we consider all parameters of voids $(\alpha = \psi = \xi_1 = \omega_0 = \lambda_0 = m = 0)$, initial stress $(p = 0)$ and microtemperature $(k_1 = k_2 = k_3 = k_4 = k_5 = k_6 = b = 0)$ as zero. After finding solution and graphical analysis this model outcomes match with those of Sarkar [35].

6.3 Initially stressed magneto-thermoelastic problem with microtemperature by neglecting voids and modified Ohm's law

To study this problem, we consider all parameters of voids are taken as zero $(\alpha = \psi = \xi_1 = \omega_0 = \lambda_0 = m = 0)$. The solution for this problem and graphical analysis are done. The outcomes of this problem coincide with those of Kalkal et al. [18] (neglecting diffusion).

7. Results and discussions

For the numerical calculations magnesium material is chosen to illustrate the analytical results. According to Othman and Abd-Elaziz [29] the material constants are as follows

$$\lambda = 9.4 \times 10^{10}\,\frac{N}{m^2}, H_0 = \frac{10^7}{4\pi}, \beta = 7.779 \times$$

$$10^{-8}\,\frac{N}{m^2},\ a_0T_0 = 1.8 \times 10^6 Jm^{-3}deg^{-1}, \mu = 4 \times$$

$$10^{10}\,\frac{N}{m^2},\ k_1 = 3.5 \times 10^{-6}\frac{N}{s}, k_2 = 4.5 \times 10^{-6}\frac{N}{s}, p =$$

$$10, b = 0.15 \times 10^{-9}N, k_3 = 5.5 \times 10^{-6}\,\frac{N}{s}, k_4 = 6.5 \times$$

$$10^{-6}\,\frac{N}{sm^2},\ k_5 = 7.6 \times 10^{-6}\,\frac{N}{sm^2}, k_6 = 9.6 \times$$

$$10^{-6}\,\frac{N}{sm^2},\mu_1 = 8.5 \times 10^{-6}N, \epsilon_0 = \frac{10^{-9}}{36\pi}, \mu_0 = 4\pi \times$$

$$10^{-7}, \sigma_0 = 9.36 \times 10^{-5}, \mu = 4 \times 10^{10}\,\frac{N}{m^2}, a = 1.6m, \chi_0 =$$

$$0.02\,\frac{rad}{s}, \eta_0 = 0.1, p_1 = 0.1K, B = 4, \tau_0 = 0,0.3, \tau_1 =$$

$$0,0.1, \varsigma = 1, \alpha_t = 7.4033 \times 10^{-7}K^{-1}, T_0 = 298\,K, k^* =$$

$$1.7 \times 10^2\,\frac{N}{sK},$$

Parameters of voids are considered from Iesan [20]

$$\alpha = 3.688 \times 10^{-5}N, \psi = 1.753 \times 10^{-15}m^2,$$

$$\xi_1 = 1.475 \times 10^{10}\,\frac{N}{m^2}, \omega_0 = 0.787 \times 10^{-3}\,\frac{N}{m^2 s},$$

$$\lambda_0 = 1.1333 \times 10^{10}\,\frac{N}{m^2}, m = 2 \times 10^6\,\frac{N}{deg\,m^2}$$

The function $f(x, t) = \theta_0 H(|B| - x)e^{-\varsigma t}$, where θ_0 is constant, $H(|B| - x)$ is the displayed Heaviside unit step function represents that around the x-axis heat is applied with 2B to keep the temperature θ_0 although it is at zero on the rest of surface.
By using equation (33) to $f(x, t)$ we obtain

$$f^* = \frac{\sqrt{2}\theta_0\ \sin(aB)(1 + ia\pi\delta(a))}{\sqrt{\pi}a(\xi + \varsigma)} \tag{81}$$

We consider $\xi = \chi_0 + i\chi_1$ but for small time $\xi = \chi_0$. The calculations are done and the results presented in graphical form. The graphs are plotted for fixed value of time and space variables $t = 0.1$ and $x = 0.1$. The physical quantities are compared for presence and absence of coefficient of Ohm's law i.e. $k_0 = 0, 0.1$ under coupled (CT), Lord Shulman (LS) (one relaxation time), Green Lindsay (GL) (two relaxation time) theory. Graphs are plotted for dimensionless field quantities. In Figures 2 to 9 the solid line represents CT theory results, the large dash line represents LS theory results and small dash line represents GL theory results. Figure 2 indicates the distribution of dimensionless temperature varies with y. Value of temperature is large for GL theory in comparison to LS and GL theory. Temperature increase in the interval $0 \le y \le 1.8$ and then decrease gradually in the interval $1.8 \le y \le 6$. Figure 3 investigates the dimensionless displacement variations of u with y values. The value of solutions for three theories is large for $k_0 = 0.1$ as compared to $k_0 = 0$. Maximum value of u appears in the range $0 \le y \le 1$ and small in the range $1.5 \le y \le 5.8$. Figure 4 shows dimensionless change in volume fraction field ϕ with the passage of distance. It shows significant change for $k_0 = 0, 0.1$ in GL theory. GL theory attains maximum value in range $0 \le y \le 1.8$ for $k_0 = 0.1$ and $0 \le y \le 1$ for $k_0 = 0$. Figure 5 depicts variation of dimensionless microtemperature with the distance y. The graph shows increasing and decreasing effect on the magnitude of w_1.

Figure 6 describes the distribution of dimensionless normal stress σ_{xx} with the y values. The value of σ_{xx} is maximum for GL theory, moderate for LS theory and minimum for CT theory. The graph is increasing for the distance $0 \le y \le 0.5$ and then gradually decreases and become constant for all three theories at $y \ge 6$. Figure 7 shows distribution of dimensionless tangential stress σ_{xy} with distance. The value decrease in the interval $0 \le y \le 1$ gradually increases for $1 \le y \le 6$. Figure 8 exhibits the distribution of dimensionless heat flux moment q_{xx} for different values of coefficient of modified Ohm's law k_0. It shows slight variations in figures for $k_0 = 0, 0.1$ in all theories. All the curves start with the zero which satisfies boundary conditions. Figure 9 represent dimensionless heat flux moment distribution of q_{xy} with distance y. Curve attains maximum value for the range $1.3 \le y \le 6$ then decreases gradually and value becomes constant for $y \ge 7$.

Figures 10 and 11 represents dimensionless temperature and displacement distribution for three different cases. Variations of graphs are observed by considering particular cases that are initially stressed thermoelastic problem with voids and microtemperature (ITVM), magneto-thermoelastic problem with modified Ohm's law (MTM) and initially stressed magneto-thermoelastic problem with microtemperature (IMTM). Figure 10 shows dimensionless temperature gradually decreases for the range $0 \le y \le 4$ and becomes finite for all three cases. Figure 11 represents dimensionless displacement decreases initially in the interval $0 \le y \le 3$ and gradually increases to become finite. The boundary condition shows the response in a bounded region of space with the finite speed of propagation. Hence the significant change is observed under three theories by using modified Ohm's law $k_0 = 0.1$ as compared to absence i.e. $k_0 = 0$.
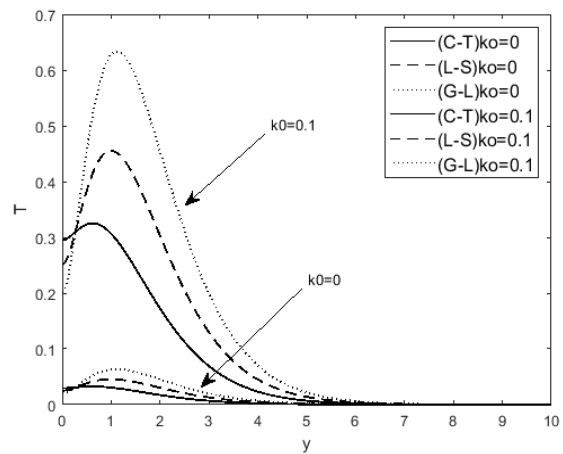
Figure 2: Temperature T variation for distinct values of k_0
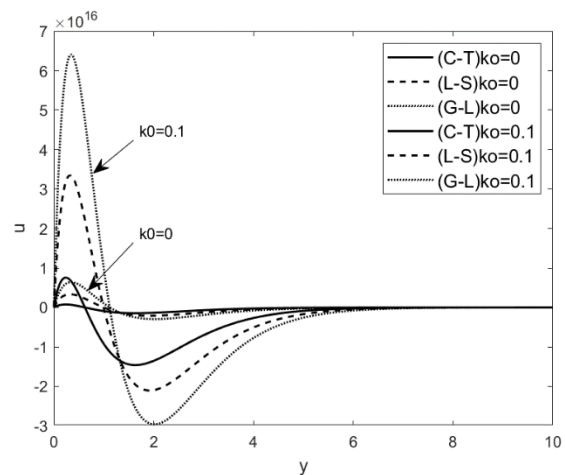
Figure 3: Displacement u variation for distinct values of k_0
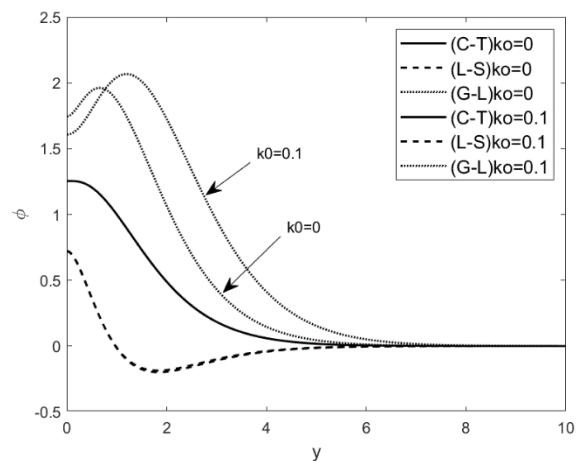
Figure 4: Change in volume field ϕ variation for distinct values of k_0

Figure 5: Microtemperature w_1 variation for distinct values of k_0

Figure 8: Heat flux moment q_{xx} variation for distinct values of k_0

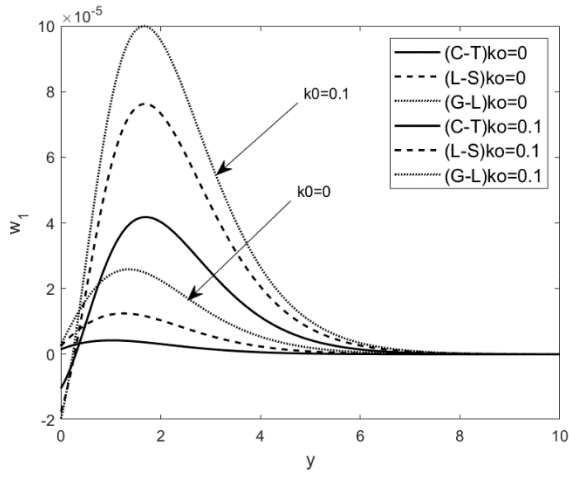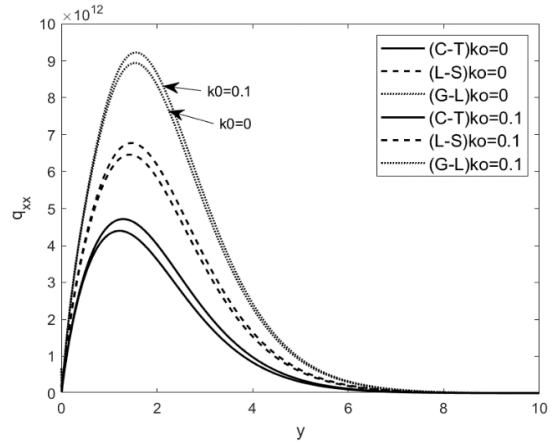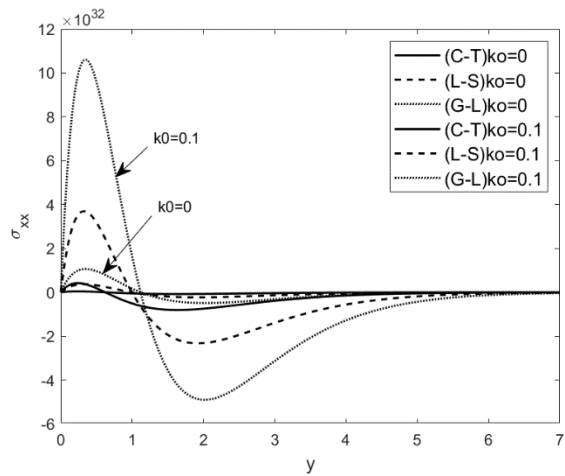Figure 6: Normal stress σ_{xx} variation for distinct values of k_0
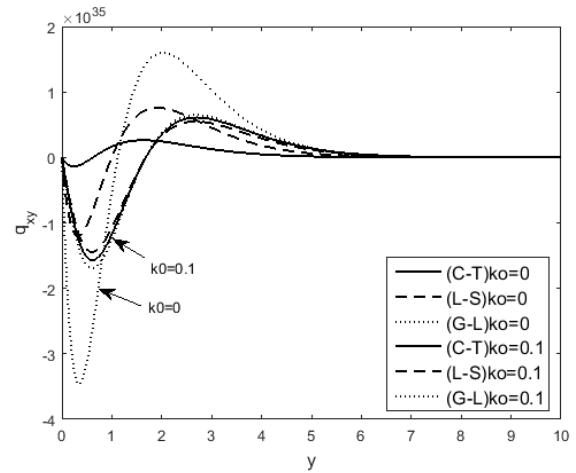

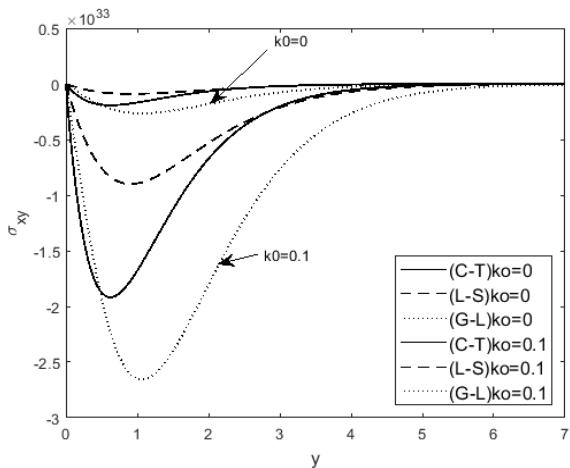Figure 9: Heat flux moment q_{xy} variation for distinct values of k_0

Figure 7: Shearing stress σ_{xy} variation for distinct values of k_0
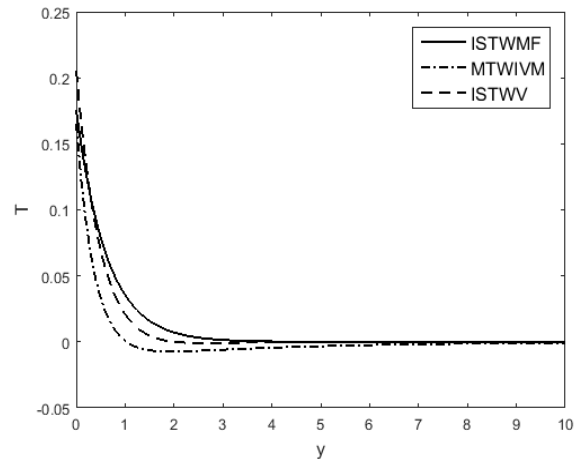

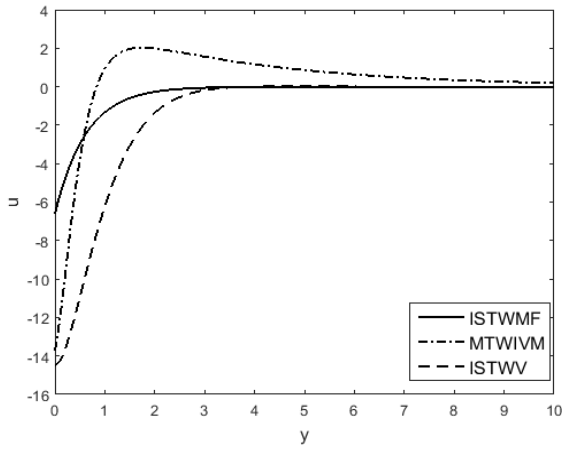Figure 10: Temperature distribution T with distance y

Figure 11: Displacement distribution u with distance y

8. Conclusion

In this article, we present a model of magneto-thermoelastic problem with modified Ohm's law, initial stress, voids, and microtemperatures in the context of GL, LS, and coupled theories. The problem is solved by using normal modes and effects of coefficient of modified Ohm's law on physical quantities are observed. The boundary conditions with thermal shock and initial stress is considered. From the graphical illustration we conclude the following facts which is useful to design new material in the development of the theory of magneto-thermoelasticity.

1. The relaxation time presence for the GL, LS leads to reduction of profile of temperature, volume fraction field, displacement, microtemperature, stresses along normal, moment of heat flux and increase in shear stresses with the change in coefficient of Ohm's law.
2. The increase in temperature values can be explained by the heat loss produced by the motion of electric current, which can be the main reason that the medium deformation tends to be normal.
3. The significant effect of modified ohm's law is observed with the change under three theories on all dimensionless field variables.
4. Finite speed of propagation is observed in all figures.

The microtemperature theory is useful to researcher's working on the area of drilling, mining tremors into the earth crust such as earthquake engineering, geophysics and seismologist. Because of the inclusion of modified Ohm's law in magneto-thermoelastic problem with microtemperature gives the new and novel contribution to this field.

Acknowledgements

Nomenclature

H_0 Component of initial magnetic field vector
Q_i Mean heat flux moment component
T Absolute temperature
T_0 Reference temperature taken as $|(T - T_0)/T_0| < 1$
$\alpha, \psi, \xi_1, m, \lambda_0, \omega_0$ Material constant for voids
α_t Coefficient of linear thermal expansion
β $= (3\lambda + 2\mu)\alpha_t$

B   Magnetic field induction vector
D   Electric displacement vector
E   Induced electric field vector
F_i   Lorentz force
H   Magnetic Intensity vector
J   Current density vector
h   Induced magnetic field vector
δ_{ij} Kronecker delta function
ϵ_0 Electric Permeability
ϵ_i First moment energy vector components
η Entropy per unit mass
λ, μ Lame's Constant
μ_0 Magnetic Permeability
ϕ Change in volume fraction field
ρ Density
σ_0 Electric conductivity
σ_{ij} Components of stress tensor
τ_0, τ_1 Relaxation times
$a_0, b, \mu_1, k_i (i = 1,2,3,4,6)$ Coefficient of constitutive relations
$c_1^2 = \frac{\lambda + 2\mu}{\rho}$ Speed of propagation of elastic waves
g^* Intrinsic equilibrated body force
h_i Equilibrated stress vector
k^* Thermal conductivity
k_0 Modified Ohm's law coefficient
p Pressure
q_i Heat flux vector components
q_{ij} First heat flux moment vector components
t Time variable
u_i Displacement vector
w_i Microtemperature vector

Appendix

$$m_1 = \frac{\left(\lambda + \mu + \frac{\beta T_0 p}{2}\right)}{\left(\mu - \frac{\beta T_0 p}{2}\right)}, m_2 = \frac{(\lambda_0 c_1^2)}{\omega^{*2} \psi \left(\mu - \frac{\beta T_0 p}{2}\right)}, \quad m_3 = \frac{(\beta T_0)}{\left(\mu - \frac{\beta T_0 p}{2}\right)},$$

$$m_4 = \frac{(\mu_0^3 \sigma_0^2 H_0^2)}{\omega^{*2}\left(\mu - \frac{\beta T_0 p}{2}\right)}, m_5 = \frac{(\sigma_0 \mu_0^2 H_0^2)}{\omega^{*2}\left(\mu - \frac{\beta T_0 p}{2}\right)},$$

$$m_6 = \frac{(\beta k_0 T_0)}{\mu_0 H_0 (\mu - \beta T_0 p/2)}, m_7 = \frac{(\rho c_1^2)}{(\mu - \beta T_0 p/2)}, m_8 = \frac{\rho c_1^2 \psi}{\alpha},$$

$$m_9 = \frac{\omega_0 c_1^2}{\alpha \omega^*}, m_{10} = \frac{\xi_1 c_1^2}{\alpha \omega^*}, m_{11} = \lambda_0 \psi / \alpha, m_{12} = \frac{\mu_1 \omega^{*2} \psi}{\alpha c_1^2},$$

$$m_{13} = \frac{(m T_0 \psi)}{\alpha}, m_{14} = k^* T_0, m_{15} = \frac{(k_6 \omega^*)}{c_1},$$

$$m_{16} = \frac{\left((k_4 + k_5)\omega^{*2}\right)}{c_1^2}, \quad m_{17} = (k_1 - k_2), \quad m_{18} = (k^* - k_3) T_0,$$

$$m_{19} = \frac{\mu_1 c_1^2}{\psi \omega^*}, m_{20} = m_{15} - m_{16}, m_{21} = \frac{k^* \omega^{*2}}{c_1^2},$$

$$m_{22} = \frac{k_1 \omega^{*2}}{T_0 c_1^2}, m_{23} = a_0 T_0 \omega^*, m_{24} = \beta \omega^*, \quad m_{25} = \frac{m c_1^2}{\psi \omega^*},$$

$$m_{26} = \frac{c_1^2}{c_0^2}, m_{27} = \frac{\sigma_0 \mu_0 c_1^2}{\omega^*}, m_{28} = \frac{(\lambda + 2\mu)\omega^{*2}}{(\beta T_0 c_1^2)}, m_{29} = \frac{(\lambda + 2\mu)}{(\beta T_0)},$$

$$m_{30} = \frac{(\lambda)}{(\beta T_0)}, m_{31} = \frac{(\lambda_0 c_1^2)}{(\beta T_0 \psi \omega^{*2})}, m_{32} = (1 - \tau_1 i \xi),$$

$$m_{33} = \frac{\mu}{(\beta T_0)}, \quad m_{34} = b \omega^*, \quad c_0^2 = \frac{1}{\mu_0 \epsilon_0}, L = \frac{(a)}{(\xi \epsilon_0)}, \quad L_1 = a^2 -$$

$$m_{26} \xi^2 - i \xi m_{27}, L_2 = i \xi c_1^2, L_3 = a^2 - \frac{m_{23}(i \xi + \tau_0 \xi^2)}{m_{21}},$$

$L_4 = \frac{m_{22}}{m_{21}}, L_5 = \frac{m_{24}(i\xi + \eta_0\tau_0\xi^2)}{m_{21}}, L_6 = \frac{m_{25}(i\xi + \eta_0\tau_0\xi^2)}{m_{21}},$

$\alpha_7 = \sqrt{\frac{L_{17}}{m_{15}}}, L_7 = a^2 - m_8\xi^2 - i\xi m_9 + m_{10},$

$L_8 = m_{13}(1 - i\xi\tau_1), L_9 = a^2 - \frac{(im_5\xi + m_7\xi^2)}{(1+m_1)}, L_{10} = \frac{(m_2)}{(1+m_1)},$

$L_{11} = \frac{m_3(1 - i\xi\tau_1)}{(1+m_1)}, \quad L_{12} = \frac{ic_1^2 m_4\xi}{a^2(1+m_1)}, \quad L_{13} = a^2 - m_7\xi^2 -$

$i\xi m_5, \quad L_{14} = \frac{m_{20}a^2 + im_{34}\xi - m_{17} + k_1}{(1+m_1)}, \quad L_{15} = m_{18} + \frac{m_{14}}{(1 - i\xi\tau_0)},$

$L_{16} = i\xi m_{19}, \quad L_{17} = \frac{k_1}{(1 - i\xi\tau_0)m_{15}}, L_{18} = a^2 - m_{17} - i\xi m_{20},$

$b_6 = \frac{\omega^{*3}}{\mu c_1^4}, \quad b_7 = k_4 b_6, \quad b_8 = (k_5 + k_6)b_6, \quad b_9 = ia(b_8 -$

$b_7)\alpha_7, b_{10} = -iab_9\alpha_7, b_{11} = b_6(\alpha_7^2 k_5 + a^2 k_6),$

$b_{12} = \frac{\alpha_7 k_0\beta T_0\omega^*}{\sigma_0\mu_0^2 H_0^2}, b_{13} = \epsilon_0\mu_0 i\xi + \frac{\sigma_0\mu_0}{\omega^*}, O_{1n} = \frac{m_6}{(L_{13} - \alpha_n^2)},$

$\alpha_9 = \sqrt{a^2 - \epsilon_0\xi^2}, \quad b_{14} = [L_5(\alpha_n^2 - a^2)(L_8(m_{20}\alpha_n^2 -$

$L_{14}) - m_{12}L_{15}(\alpha_n^2 - a^2)) + m_{11}(\alpha_n^2 - a^2)((m_{20}\alpha_n^2 -$

$L_{14})(\alpha_n^2 - L_3) + L_4 L_{15}(\alpha_n^2 - a^2))], \quad b_{15} = [L_5(\alpha_n^2 -$

$a^2)((\alpha_n^2 - L_7)(m_{20}\alpha_n^2 - L_{14}) + m_{12}L_{16}(\alpha_n^2 - a^2)) +$

$m_{11}(\alpha_n^2 - a^2)((m_{20}\alpha_n^2 - L_{14})L_6 - L_4 L_{16}(\alpha_n^2 - a^2))],$

$O_{2n} = H_{1n} = \frac{b_{14}}{b_{15}}, O_{3n} = \frac{(\alpha_n^2 - L_1)(L_{11} - L_{10}O_{2n})}{(\alpha_n^2 - L_1)(\alpha_n^2 - L_9) + L_2 L_{12}(\alpha_n^2 - a^2)},$

$O_{4n} = \frac{-L_2(\alpha_n^2 - a^2)O_{3n}}{(\alpha_n^2 - L_1)}, \quad O_{5n} = \frac{(L_{15} - L_{16}O_{2n})}{(m_{20}\alpha_n^2 - L_{14})}, \quad O_{6n} = iaO_{3n} -$

$\alpha_n, O_{7n} = -ia - \alpha_n O_{3n}, O_{8n} = iam_{29}O_{6n} - \alpha_n m_{30}O_{7n} +$

$m_{31}O_{2n} - m_{32}O_{1n}, \quad O_{9n} = iam_{30}O_{6n} - \alpha_n m_{29}O_{7n} +$

$m_{31}O_{2n} - m_{32}O_{1n}, O_{10n} = iam_{33}O_{7n} - \alpha_n m_{33}O_{6n},$

$O_{11n} = a^2 b_6 O_{5n} - \alpha_n^2 b_7 O_{5n}, \quad O_{12n} = ia(b_8 + b_9)\alpha_n O_{5n},$

$O_{13n} = \frac{O_{4n} + i\xi c_1^2 O_{6n} + b_{12}O_{1n}}{b_{13}}, H_{3n} = \frac{-L_2(\alpha_n^2 - a^2)H_{3n}}{(\alpha_n^2 - L_1)},$

$H_{2n} = \frac{(\alpha_n^2 - L_1)(L_{11} - L_{10}H_{2n})}{(\alpha_n^2 - L_1)(\alpha_n^2 - L_9) + L_2 L_{12}(\alpha_n^2 - a^2)}, H_{4n} = \frac{(L_{15} - L_{16}H_{2n})}{(m_{20}\alpha_n^2 - L_{14})}$

References:

[1] M. A. Biot, "Non-linear theory of elasticity and the linearized case for a body under initial stress," *The London, Edinburgh, and Dublin Philosophical Magazine and Journal of Science,* 27(183), 468–489, 1939.

[2] H. Lord and Y. Shulman, "A generalized dynamical theory of thermoelasticity," *Journal of the Mechanics and Physics of Solids*, 15(5), 299–309, 1967.

[3] E. Green and K. A. Lindsay, "Thermoelasticity," *Journal of Elasticity*, 1972.

[4] V. K. Agarwal, "On electromagneto-thermoelastic plane waves," *Acta Mechanica*, 34(3), 181–191, 1979.

[5] G. Paria, "Magneto-elasticity and magneto-thermoelasticity," *In Advances in Applied Mechanics. Elsevier,* 73–112, 1966.

[6] H. Youssef, "Generalized magneto-thermoelasticity in a conducting medium with variable material properties," *Applied Mathematics and Computation*, 173(2), 822–833, 2006.

[7] R. A. Grot, "Thermodynamics of a continuum with microstructure," *International Journal of Engineering Science,* 7(8), 801–814, 1969.

[8] P. Riha, "On the microcontinuum model of heat conduction in materials with inner structure," *International Journal of Engineering Science*, 14(6), 529–535, 1976.

[9] P. S. Casas and R. Quintanilla, "Exponential stability in thermoelasticity with microtemperatures," *International Journal of Engineering Science,* 43(1), 33–47, 2005.

[10] R. Quintanilla and D. Iesan, "On the theory of thermoelasticity with microtemperatures," *Journal of Thermal Stresses*, 23(3), 199–215, 2000.

[11] D. Iesan, "On a theory of micromorphic elastic solids with microtemperatures," *Journal of Thermal Stresses,* 24(8), 737–752, 2001.

[12] M. Svanadze, "Fundamental solutions of the equations of the theory of thermoelasticity with microtemperatures," *Journal of Thermal Stresses*, 27(2), 151–170, 2004.

[13] M. I. Othman and E. M. Abd-Elaziz, "Influence of gravity and microtemperatures on the thermoelastic porous medium under three theories," *International Journal of Numerical Methods for Heat & Fluid Flow*, 29(9), 3242–3262, 2019.

[14] R. Quintanilla, "Uniqueness in thermoelasticity of porous media with microtemperatures," *Archives of Mechanics*, 61(5), 371–382, 2009.

[15] C. Eringen, "Microcontinuum field theories: I. Foundations and solids," *Springer Science & Business Media,* 2012.

[16] C. Eringen and E. S. Suhubi, "Nonlinear theory of simple microelastic solids," *International Journal of Engineering Science,* 2(2), 189–203, 1964.

[17] K. K. Kalkal, R. Goyal, and S. Deswal, "Thermomechanical interactions in a magneto Thermoelastic solid with microtemperatures and diffusion," *Microsystem Technologies*, 25(10), 3747–3763, 2018.

[18] S. C. Cowin and J. W. Nunziato, "Linear elastic materials with voids," *Journal of Elasticity*, 13(2), 125–147, 1983.

[19] J. W. Nunziato and S. C. Cowin, "A nonlinear theory of elastic materials with voids," *Archive for Rational Mechanics and Analysis*, 72 (2), 175–201, 1979.

[20] D. Iesan, "A theory of thermoelastic materials with voids," *Acta Mechanica*, 60(1), 67–89, 1986.

[21] Pompei and A. Scalia, "On the asymptotic spatial behavior in linear thermoelasticity of materials with voids," *Journal of Thermal Stresses*, 25(2), 183–193, 2002.

[22] S. Chirita and A. Scalia, "On the spatial and temporal behavior in linear thermoelasticity of materials with voids," *Journal of Thermal Stresses,* 24(5), 433–455,

2001.

[23] M. I. A. Othman, M. E. Zidan, and M. I. Hilal, "Effect of magnetic field on a rotating thermoelastic medium with voids under thermal loading due to laser pulse with energy dissipation," *Canadian Journal of Physics,* 1359–1371, 2014.

[24] D. Iesan, "A theory of initially stressed thermoelastic material with voids," *An. Stiint. Univ. Ai. I. Cuza Lasi Sect. I a Mat*, 33, 167–184, 1987.

[25] M. A. Goodman and S. C. Cowin, "A continuum Theory for granular materials," *Archive for Rational Mechanics and Analysis,* 44(4), 249–266, 1972.

[26] J. Jaric, "Theory of thermoelasticity of granular materials," *Rev. Roum. Sci. Techn., Méc. Appl* 24, 793–805, 1979.

[27] M. I. A. Othman, R. S. Tantawi, and E. M. Abd-Elaziz, "Effect of initial stress on a thermoelastic medium with voids and microtemperatures," *Journal of Porous Media,* 19(2), 155–172, 2016.

[28] K. K. Kalkal, R. Kumar, A. Gunghas, and S. Deswal, "Wave propagation in an initially stressed magneto-thermoelastic medium with voids and microtemperatures," *Journal of Thermal Stresses*, 43(8), 962–980, 2020.

[29] M. I. A. Othman and E. M. Abd-Elaziz, "Effect of initial stress and hall current on a magneto-thermoelastic porous medium with microtemperatures," *Indian Journal of Physics,* 93(4), 475–485, 2018.

[30] M. I. A. Othman and E. M. Abd-Elaziz, "Plane waves in A magneto-thermoelastic solids with voids and microtemperatures due to hall current and rotation," *Results in Physics*, 7, 4253–4263, 2017.

[31] K. Ames and B. Straughan, "Continuous dependence results for initially prestressed thermoelastic bodies," *International Journal of Engineering Science,* 30(1), 7–13, 1992.

[32] Montanaro, "On singular surfaces in isotropic linear thermoelasticity with initial stress," *The Journal of the Acoustical Society of America,* 106(3), 1586–1588, 1999.

[33] Abbas and M. I. A. Othman, "Generalized thermoelastic interaction in a fiber-reinforced anisotropic half space under hydrostatic initial stress," *Journal of Vibration and Control*, 18(2), 175–182, 2011.

[34] M. A. Ezzat and M. Z. A. Elall, "Generalized magneto thermoelasticity with modified ohm's law," *Mechanics of Advanced Materials and Structures*, 17(1), 74–84, 2009.

[35] N. Sarkar, "Generalized magneto¬ thermoelasticity with modified ohm's law under three theories," *Computational Mathematics and Modeling,* 25(4), 544–564, 2014.

Mathematical Modeling of Waste Engine Oil Gasification for Synthesis Gas Production; Operating Parameters and Simulation

Mohammad Rasoul Mousazade[1], Mehdi Sedighi[2*], Mohammad Hasan Khoshgoftar Manesh[3,4], Mostafa Ghasemi[5]

[1*] Division of Thermal Sciences and Energy Systems, Department of Mechanical Engineering, Faculty of Technology & Engineering, University of Qom, Qom, Iran
[2] Department of Chemical Engineering, University of Qom, Qom, Iran
[3] Energy, Environment and Biological Systems Research Lab (EEBRlab), Division of Thermal Sciences and Energy Systems, Department of Mechanical Engineering, Faculty of Technology & Engineering, University of Qom, Qom, Iran
[4] Center of Environmental Research, University of Qom, Qom, Iran
[5] Chemical Engineering section, Sohar University, Sohar, 311, Oman
E-mail: [2]sedighi@qom.ac.ir

Abstract

The release of waste oil into the environment will have destructive effects. Gasification is an advanced and environmentally friendly process for converting waste oils into clean combustible gas products. Thermochemical equilibrium modeling has been used in this method to predict the performance of a downdraft gasifier. This model uses the thermodynamic equilibrium of gasification reactions to predict the gases produced in the gas mixture. Having the percentage of gas components produced, different characteristics of the produced gas including H_2:CO ratio, process temperature and calorific value of the produced gas, Cold gas efficiencies and carbon conversion efficiency are also obtained. The effect of equivalence ratio, oxygen enrichment and pressure on gasification properties is analyzed. The simulation results are compared with the reported experimental measurements through which the numerical model is confirmed. The results indicated that the equivalence ratio (mole of air in gasification per mole of air in combustion) between 0.4 and 0.42 had the potential to yield the highest calorific value about 10.5 $Mj.m^{-3}$. The temperature of gaseous mixture in this range will be 2000 K that can be used for other processes such as steam generation. Using pure oxygen instead of air reduces the efficiency of the gasifier from 78% to 55%. Pressure changes from 10 to 65 bar cause gas mixture temperature changes from 1684 to 1690 Kelvin. The H_2:CO ratio decreases from 1.6 to 0.6 with increasing equivalence ratio and increases from 1.2 to 1.6 with changes in oxygen enrichment.

Keywords: *Gasification; waste engine oil; chemical equilibrium; syngas production; numerical modeling.*

1. Introduction

Internal combustion engines need lubricating oils to operate. The increasing use of internal combustion engines has led to an increase in the amount of waste oil (WLO) worldwide. The production of waste lubricating oil is estimated at 24million tons annually worldwide [1]. and 45 million gallons per year in Florida alone [2]. About 60% of the lubricating oil produced is converted into waste oil [3]. Lubricating oils are used to reduce friction and wear between rotating engine components [4]. Lubricating oil is one of the distillation parts of crude oil, but joinery brands are obtained in a mixture [5]. This oil is composed of a large number of organic compounds and some heavy metals [6, 7]. Viscosity is considered as the most important property of lubricating oil [8]. Over time, lubricating oils lose their viscosity and become unsuitable for use in the engine [9]. The chemical composition of used lubricating oil varies widely and depends on the original crude oil, the refining processes, the efficiency of engine that used the oil and to the original oil, and the duration of use of engine oil. Lube oils are designed to withstand very high service temperatures in the internal combustion engines and resist thermal degradation [2].

Elemental analysis of a sample of waste engine oil indicated 13.28 wt.% hydrogen (See Table 1) content. It is twice the hydrogen available in wood biomass and about three weight percent heavier than vegetable oils. The high amount of hydrogen content in waste engine oil makes it a valuable raw material for hydrogen production. Releasing WLO into the environment poses a peril to it. The study of recycling and reuse techniques is not only an effort to recover energy but also a struggle for environmental sustainability. WLOs can also be used as raw materials for the thermochemical conversion process to produce useful products. Such processes include pyrolysis and gasification [10]. The use of lubricating oil as a raw material for hydrogen production is desirable because it is cheap and available throughout the year [2]. Used oil is available all year round without any seasonal fluctuations at a relatively low cost for example typically 10 cents/gallon delivered in Florida [2]. The gasification process is a partial thermal oxidation, Which leads to gaseous products (carbon dioxide, hydrogen, carbon monoxide, water vapor, methane and other gaseous hydrocarbons) and small amounts of coal, ash and condensable compounds [11]. The quality of gas produced

from gasification varies as a function of the gasifier agent (air, oxygen, steam, carbon dioxide or a mixture of them) and operating conditions. Installing small, low-cost, and efficient gasifier-engine systems can be an attractive alternative to direct combustion, taking into account achievable electrical efficiency and storage and transportation costs [12]. The produced gas, after cleaning and air conditioning, can be used as fuel in gas engines and turbines due to its acceptable thermochemical combustion properties (flame speed and knock tendency) [13]. Gasification is also considered as a cleaner and more efficient technology than combustion, because it enables higher electrical functions on a smaller scale and due to its very acceptable combustion properties combined with a typical Rankin cycle [14], less NO_X and SO_X emissions, And the possibility of CO_2 capture [15]. However, gasification must overcome a number of obstacles to commercialization. Important issues such as the removal of particles in the exhaust gas, issues related to the production and pre-treatment of biomass raw materials, while in the case of waste oil this cost is less. In order to optimize the gasification process, a better understanding of the effect of inlet fuel properties and parameters of gasification operation on the quality of gas produced and gasification performance is required [16]. Therefore, it is necessary to discover and understand the main mechanisms of gasification. As a result, simulation of gasification processes is required for scaling, industrial control strategies, and performance evaluation after modifying the operating conditions [17]. Compared to the direct construction of experimental units, mathematical modeling of a gasification process is a relatively quick and economical solution. Mathematical models, based on theoretical and experimental work and practical operations are used for the purpose of analyzing thermochemical processes during gasification and evaluating the effect of the main input variables on the properties of gas products (i.e., gas composition and calorific value) [17]. Different kinds of models have been developed for gasification systems, including computational fluid dynamic (CFD), artificial neural networks (ANN), thermodynamic equilibrium and kinetic models [18].

The comparison of different mathematical models showed that the thermodynamic equilibrium model, is the simplest and can be used as an effective primary tool to analyses the effect of process parameters and different fuel types on a gasification process. Thermodynamic equilibrium model, opposing to kinetic, ANN and CFD models, are characterized by a higher level of flexibility and applicability. Moreover, less computational intensity is required in a thermodynamic equilibrium model [19]. These models calculate the composition at the highest stability of the products of a reaction, a condition defined as thermodynamic equilibrium which is met at the level of the products minimum chemical potential [20]. In practice, the lack of ideal conditions along with design restrictions, e.g. retention time, prevent the output products to reach thermodynamic equilibrium [21]. In this regard, these models usually overestimate the yields of H_2 and CO, underestimate those of CO_2, and predict an outlet stream free from CH_4, tars, and charcoal. Nonetheless, thermodynamic equilibrium calculations, which are also independent of gasifier design, may provide useful insights, e.g. the influence of the most important process parameters. Further, the long residence time needed in fixed bed gasifiers suggest that the process propagate at a rather slow rate while the producer gas composition in practice ends up not too far from equilibrium [22]. For fluidized bed gasifiers, the average bed temperature can be used as the process temperature, whereas for downdraft gasifiers, the outlet temperature at the throat exit should be used [23].

Sharma et al. [24] examined how changes in humidity, pressure, equivalence ratio, and initial reactor temperature affected exhaust gas components, calorific value, temperature, and efficiency of gasification. Shen et al. [25] used Aspen Plus for biomass gasification modeling and investigated the optimal hydrogen production conditions. Mountouris et al. [26] focused on modeling Plasma gasification using constant equilibrium equations and the soot formation in the output products and investigated the effect of gasification parameters on solid waste gasification. Jarungthammachote et al. [27] used a thermodynamic equilibrium model based on the equilibrium constant to investigate the gases produced from the downdraft gasification process and investigated the effect of biomass moisture on the mole fraction of the gaseous components. Ashizawa et al. [28] studied experimentally the effect of various parameters such as an equivalence ratio, cold gas efficiency, calorific value of the produced gas and the exhaust gas mixture composition in a pilot downdraft gasifier. Beheshti et al. [29] used thermodynamic modeling to evaluate waste lubricating oil's gasification by minimizing the Gibbs free energy and these parameters in the gasification process: pressure, inlet vapor and equivalence ratio. Beheshti et al. [30] presented a mathematical equations for modeling the catalytic steam gasification of heavy oil, aiming to investigate the effect of gasification temperature, gasification pressure, steam to fuel ratio and the ratio of catalyst to fuel on the volume percentage of exhaust gas mixture's components. By using a thermodynamic equilibrium model, Khaleghi et al. [31] studied mazut gasification a heavy fuel oil with a high percentage of sulfur, assessed it's equivalence ratio and investigated the use of steam as a gasification agent. Santiago et al. [32] studied thermochemical conversion as an alternative oil sludge process and explored various gasifying agent's effects on syngas properties. The downdraft gasifier and gas engine with industrial olive oil was studied by Vera et al. [33]. Results indicated such system's ability to ensure power efficiency of 14%, the overall efficiency of 36%, and high gasification efficiency. Sanchez-Hernandez et al. [34] focused on different options to upgrade engine oils by gasification using steam and supercritical water. This method converts more than 85% of oil into valuable gases. Couto et al. [35] performed numerical and experimental modeling of municipal solid waste gasification process analysis. A two-dimensional multiphase model has been integrated with chemical reactions for the gasification process. The Computational Fluid Dynamic (CFD) Fluent framework has been used to develop the numerical model. Ruggiero and Manfrida. [36] presented a simple model for biomass gasification considering the Gibbs free energy and emphasizing the potential of using the equilibrium model. Melgar et al. [37] Modeled biomass gasification and investigated the effect of moisture content in biomass and the effect of air to fuel ratio on the adiabatic temperature of gasification, distribution of production gas components and gasification efficiency.

Prins et al. [23] investigated The gasification process with a chemical equilibrium model and showed that the equilibrium model indicates the highest gasification efficiency that can be achieved for a fuel. Altafini and

Mirandola. [38] studied coal gasification based on chemical equilibrium using Gibbs free energy minimization method. It has also studied the concentration of gases produced and the efficiency of gasification and the efficiency of carbon conversion. Their studies show that the results of chemical modeling are close to the experimental results.
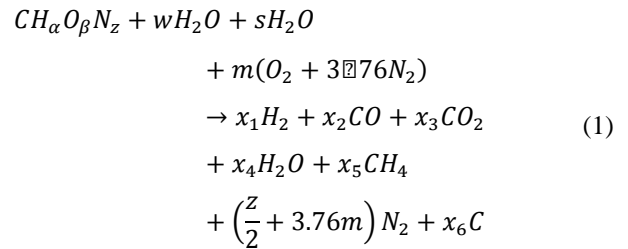
Lapuerta et al. [39] used a chemical equilibrium model to predict the concentration of gases produced in gasification as a function of fuel to air ratio. Schuster et al. [40] proposed a model for the study of biomass steam gasification in the Fluidized bed gasification. Their model includes two zones, one zone for gasification by steam and other for combustion, so that the concentration of gases produced is estimated by an equilibrium model using the Gibbs free energy minimization method. This model investigates the effect of operational parameters such as moisture in biomass, gasification temperature and gasification agent on the concentration of gases produced, their calorific value and process efficiency. Jayah et al. [41] proposed a model for two regions, gasification and pyrolysis for the downstream gasification. In the pyrolysis section, the composition of the produced gas mixture and its temperature are estimated by chemical equilibrium. The output results of the first zone will obtain the input information of the second zone. In this area, it is assumed that the carbon components do not react to the bottom of the gas generator and move vertically. This model estimates the temperature changes, the composition of the components of the produced gas mixture and carbon conversion efficiency. This model is in good agreement with the experimental data in the downstream gasifier. In this model, sensitivity analysis is performed on different biomass sizes, changes in biomass humidity, air inlet temperature, and heat loss. The result of this analysis is to obtain the optimal length of the gasifier in order to increase the efficiency of biomass to gas conversion. Di Blasi. [42] has considered a dynamic one-dimensional model in the solid phase and the gas phase for the downstream gas generator. Such things as water evaporation, pyrolysis, combustion and carbonation of carbon in biomass, gas phase combustion and heat transfer during gasification also effect of air to fuel ratio on efficiency of the gasification process and the concentration of exhaust gases and their quality. Rao et al. [43] investigated the irreversibility of a downdraft gasifier and evaluated it for various biomasses.

The novelty of the work is to apply a systematic approach using thermodynamic concepts to model and simulate the gasification process of waste engine oil using mathematical equations. The results of the simulation were compared with the experimental data with high accuracy. After validation, the results used the model to predict the gasifier's behavior in the gasification of waste oils. Furthermore, the sensitivity analysis of main parameters and operating conditions were investigated.

2. Mathematical modeling

In order to establish the chemical equilibrium, sufficient time is taken for the reactions to take place, so the effect of the velocity factor on the reactions will not be considered. gasification products will be only gaseous components and carbon components remain. Exhaust gas mixture includes hydrogen, carbon monoxide, carbon dioxide, methane, water vapor, and nitrogen. Gaseous components such as nitrogen oxides, sulfur oxides have been eliminated due to their very small amount in the experimental results.

The gasification process operates at constant pressure. The heat transfer rate from the gasification reactor is 6% of the fuel's high calorific value in the dry state. The produced gas mixture and its components are assumed to be ideal gas. The general equation of gasification is as follows:

$$
\begin{aligned}
CH_\alpha O_\beta N_z + wH_2O + sH_2O \\
+ m(O_2 + 3.76N_2) \\
\rightarrow x_1H_2 + x_2CO + x_3CO_2 \\
+ x_4H_2O + x_5CH_4 \\
+ \left(\frac{z}{2} + 3.76m\right)N_2 + x_6C
\end{aligned}
\tag{1}
$$

w, s, m, x_1 to x_5 and x_6 are mole of moisture per one mole of fuel, mole of steam, mole of air that is needed in gasification, mole number of gaseous productions and mole number of carbon respectively. Extra equations of gasification modeling are in Appendix A. The final equations will have six unknowns in the presence of carbon in the output products and five unknowns in its absence. To find all of them, chemical equilibrium constant equations are needed. To model the gasification process, five key reactions have been considered, three of which contain the carbon component and the other two contain no carbon. The equilibrium constant of these reactions and the relevant equations for finding equilibrium constants are in Appendix A.

$$C + CO_2 \leftrightarrow 2CO \tag{2}$$

$$C + H_2O \leftrightarrow H_2 + CO \tag{3}$$

$$C + 2H_2 \leftrightarrow CH_4 \tag{4}$$

$$CO + H_2O \leftrightarrow H_2 + CO_2 \tag{5}$$

$$CH_4 + H_2O \leftrightarrow CO + 3H_2 \tag{6}$$

Here are two equations of equilibrium constants for water-gas reactions and methane reforming:

$$
K_{watergas\ shift} = \exp\left(1.86\ln T - (5.4 \times 10^{-4})\frac{T}{2} + \frac{116400}{2T^2} - 18.0173 - \frac{-4.8826\times10^4}{R_uT}\right)
\tag{7}
$$

$$
K_{steam\ reforming} = \exp\left(7.9510\ln T - 0.0087\frac{T}{2} + \frac{2.1640\times10^{-6}}{6}T^2 - \frac{9700}{2T^2} - 24.7515 - \frac{1.8977\times10^5}{R_uT}\right)
\tag{8}
$$

In real gasification conditions, the reactions do not reach chemical equilibrium due to velocity constraints.

Therefore, the modeling results will deviate slightly from the experimental results. By multiplying the equilibrium constant by coefficients obtained by comparing experimental values and modeling, the amount of this deviation can be reduced by this method by other researchers such as Jurangtamachut et al. [7]. Has also been used. The energy balance equation can be used to find the gasification temperature for this purpose, the following equation will be established:
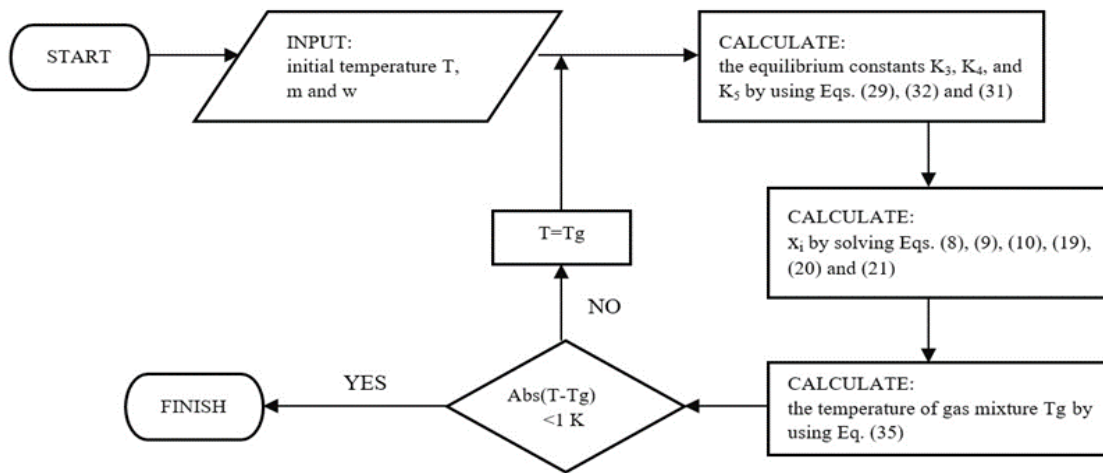
Figure 1. The calculation procedure.

$$\sum_{i=reactant} n_i\left(H_{fi}^0 + \Delta H_{Ti}^0\right) =$$
$$\sum_{j=product} n_j\left(H_{fj}^0 + \Delta H_{Tj}^0\right) \tag{9}$$

Based on the formula, the value of H_f^0 is equal to the standard enthalpy of formation for the reactant and the product. The value of ΔH_T^0 refers to the enthalpy difference between 298 K and the gasification temperature, and this value will be zero for reactant since they are at 298 K. The difference in enthalpy of the gaseous components of the product is determined by using Eq. (10)

$$\Delta h = \left(\int_{298}^{T} C_p dT\right) \tag{10}$$

T represents the outlet gasification temperature. A standard enthalpy formation of fuel is derived from this equation [44]:

$$h_{fuel}^0 = LHV_{fuel} + \frac{1}{M_{fuel}}\sum n_k h_{f.k}^0 \tag{11}$$

In the above Eq. n_k denotes the mole number of gaseous products in the complete combustion of the fuel. $h_{f.k}^0$ is the amount of enthalpy of formation of gaseous components in complete combustion. LHV_{fuel} or lower heating value of fuel can be calculated using the following equation. [27]:

$$LHV_{fuel} = HHV_{fuel} - m_h h_{fg} \tag{12}$$

m_h denotes the mass fraction of hydrogen in the dry analysis of the fuel and the value of h_{fg} denotes the enthalpy of water vaporization under standard conditions. An experimental equation has been proposed by Chaniwala et al. [44] to estimate the high calorific value of the fuel. This equation is applicable for finding higher calorific value of liquid fuel and was used by some researchers. [29, 30, 45, 46 , 47, 48]:

$$HHV_{fuel} = (0.3491)C + (1.1783)H + (0.1005)S -$$
$$(0.1034)O - (0.0151)N - (0.0211)A \tag{13}$$

The coefficients C, H, S, O, N, A represent the mass percentage of carbon, hydrogen, sulfur, oxygen, nitrogen and ash in the dry inlet fuel. These equations are a set of nonlinear polynomial equations that can be solved using the Newton-Raphson method.

This method solves the equations by the process of repetition and using the initial guess. For this purpose, the initial value for gaseous moles and gasification temperature are guessed and by calculating the equilibrium constant, the values of gaseous moles are included in the equations and new values are obtained by solving them, then these new molar values are placed in the energy balance equation For finding new temperature, if the temperature obtained is very slightly different from the initial guess temperature, the solution will be stopped and the answers will be obtained. Otherwise, the new temperature obtained will be replaced by the initial guess temperature and the solution steps will be repeated until The difference between the new temperature and the previous temperature be very small. The coding of these equations is done in MATLAB software, which is a suitable platform for solving mathematical equations. The path of the solution method can be seen as a flowchart in Figure 1.

3. Results and Discussion
3.1. Validation
This study compared simulation results with the experimental results provided by Ashizawa et al. [28] to validate the simulation. The type of fuel and the operation conditions, like the gasifier pressure and inlet temperature, will be in accordance with the reference article and after validation the type of fuel will be changed into waste engine oil. General inlet fuel information and dry fuel analysis can be found in Table 1. As the table shows, the percentage of carbon, hydrogen, oxygen and nitrogen in the waste oil is very close to its corresponding values in Orimulsion, so the waste oil fuel can be used in this mathematical modeling [29, 47]. By adding a new fuel to the model, the effective performance parameter such as pressure changes, equilibrium ratio and oxygen enrichment will be investigated.

Table 2 shows that the modeling results are very close to the experimental results, and this indicates the validity of the modeling performed in this paper. The error value is measured by the RMS error, which is shown below:

$$RMS = \sqrt[2]{\left(\frac{\sum_{i=1}^{n}(r_{iexp}-r_{imod})^2}{n}\right)} \qquad (14)$$

Table 1. Input fuel information used in the gasification process.

Proximate Analysis	Waste lube oil[49].	Orimulsion[28].
Water content	0.62 %	28.8 %
Ash	1.46 %	0.18 %
Residual carbon	-	12.84 %
Total-sulfur	-	2.81 %
HHV	53.716 MJ.kg^{-1}	29.76 MJ.kg^{-1}
Ultimate analysis (Dry)		
Ash	1.46 %	0.25 %
C	81.27 %	84.28 %
H	13.28 %	10.33 %
O	1.91 %	0.55 %
N	1.02 %	0.64 %
S	0.56 %	3.95 %
Cl	0.05 %	70 mg.kg^{-1}

In the above expression r_{imod}, r_{iexp} and n represents the molar value of gaseous components in the model, experimental results and the number of gaseous components produced, respectively. According to Jarongtamachut et al.[27], the error in the results achieved by comparing the numerical modeling to experimental results can range between 0.88 to 3.91. Therefore, the mathematical modeling of waste oil gasification has an acceptable level of error, as presented in Table 2. The waste engine oil is then used as a gasifier inlet fuel. In Table 3 gasification conditions and modeling results for gasification with waste engine oil are investigated. As can be seen, the volume percentage of hydrogen, carbon monoxide and methane gases in the gasification of waste oil is higher than the gasification of orimulsion and the calorific value of the produced gas will be higher.

Table 2. Comparison of modeling and experimental gasification results of Orimulsion [28].

Operating Condition		
Equivalence ratio		0.38
Pressure		18.75 atm
Gasification Agent		Pure Oxygen
Flue Gas Analysis		
	Experimental Results	Simulation Results
H$_2$	39.40 %	38.82 %
CO	38.70 %	40.94 %
CO$_2$	8.67 %	7.86 %
H$_2$O	11.85 %	1.25 %
CH$_4$	0.08%	10.90 %
N$_2$	0.38 %	0.16 %
HHV(MJ.kg^{-1})	9.5-10.5	10.62
RMS error		1.1942
Temperature (K)	1348	1343.6

Table 3. Results of modeling the gasification of waste engine oil.

Operating Condition	
Equivalence ratio	0.38
Pressure	18.75 atm
Gasification Agent	Pure Oxygen
Simulation Results	
H$_2$	42.55 %
CO	43.42 %
CO$_2$	4.857 %
H$_2$O	4.85 %
CH$_4$	7.713 %
N$_2$	0.26 %
HHV(MJ.kg^{-1})	11.3804
Temperature (K)	1390

To evaluate the performance of gasification, equivalence ratio, oxygen enrichment and pressure change of gasification are studied. Equivalence ratio is the ratio of oxygen or air required for gasification to the ratio of oxygen or air required for complete combustion:

$$M = \frac{\text{Oxygen gasification}}{\text{Oxygen combustion}} \qquad (15)$$

The parameters studied in the gasification process are: temperature, percentage of gas mixture components, cold gas efficiency, calorific value of the produced gas and carbon conversion efficiency. First, the effect of changing the equivalence ratio on the parameters of gasification is examined.

3.2. Equivalence ratio

In this section, the value of equivalence ratio will change from 0.3 to 0.6 and the molar changes and volume percentage of the produced gases as well as the amount of temperature changes and other gasification characteristics will be examined. Figure 2. shows the amount of change in moles of gaseous produced. The figure shows that the amount of carbon in the gasification process decreases with increasing equivalence ratio and this decrease is almost linear. This reduction in carbon moles can be explained by the equations used to model this process, as the partial combustion rate of the carbon in the fuel increases with increasing value and the production of carbon dioxide and water vapor increases and the temperature of the gas mixture increases and provides suitable conditions for the gasification process. With the increase of heat due to partial combustion of carbon and the endothermic nature of Eq. (2) and (3), these two reactions will take place and the production of carbon monoxide and hydrogen will increase. Eq. (4) is also exothermic, so a small amount of hydrogen is consumed and converted to methane. This describes the small amount of hydrogen reduction and the production of small amounts of methane in Figure 2. As can be seen from Figure 2. by increasing the equivalence ratio, in other words, by increasing the amount of oxygen input, the process will be closer to combustion in which case
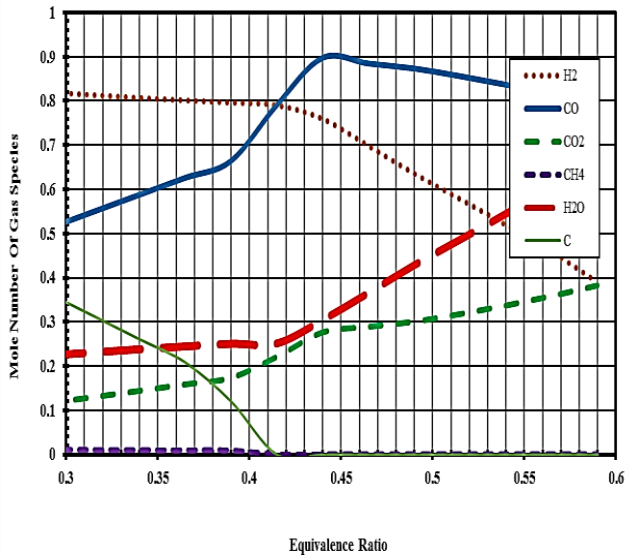
Figure 2. Changes in the number of moles of gas components produced relative to equivalence ratio (Figure is in color in the on-line version of the paper).

the molar amount of carbon dioxide and water vapor will be increased and the amount of valuable gases carbon monoxide and Hydrogen will be reduced.

Due to the fact that with increasing the equivalence ratio, the gasification process will be closer to the combustion conditions, so the temperature of the gas mixture should increase, which is quite visible in Figure 3. Also, according to this figure, it can be seen that the calorific value of the exhaust gas first decreases and then increases and decreases shortly afterwards This can be explained by the molar changes of the gaseous components that with increasing the equivalence ratio from 0.3 to 0.39, the mole's number of methane and hydrogen has decreased, which will neutralize the effect of increasing carbon monoxide on the calorific value and reduce it. But by changing the equivalence ratio from 0.39 to 0.415 and by increasing the temperature and performing Eq. (2) and (3), the amount of carbon is completely consumed and the amount of carbon monoxide production increases and will increase the calorific value of the gas mixture.

By increasing the value ratio from 0.415 to 0.6 and approaching the combustion state, the molar number of valuable gases such as hydrogen, carbon monoxide and methane is reduced and the amount of carbon dioxide and water vapor is increased and the high calorific value of the fuel is reduced.

According to Figure 3. the high calorific value of the gas mixture will increase from 10.26 MJ.m^{-3} in the equivalence ratio of 0.3 to 7.22 MJ.m^{-3} in the equivalence ratio of 0.6 and it will reach its maximum value of 10.6 MJ.m^{-3} at the ratio of 0.415.

It should also be noted that the calorific value of gas fuel required for combustion in a gas turbine is at least 6 MJ.m^{-3} [51]. The changes in cold gas efficiency and carbon conversion efficiency that are described below can be seen in Figure 4.

$$\eta_{CG} = \left(\frac{E_{pg}}{E_{feed}}\right) \times 100 \tag{16}$$

$$E_{feed} = LHV_{feed} \times M_{feed} \tag{17}$$
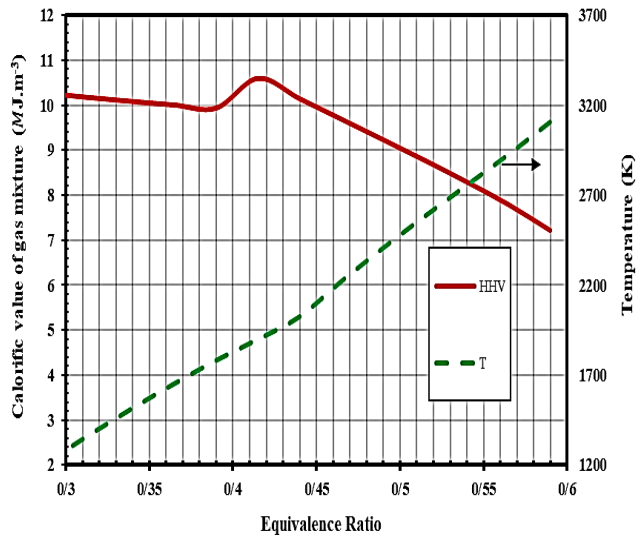
Figure 3. Changes in temperature and calorific value of the gas mixture relative to changes in equivalence ratio (Figure is in color in the on-line version of the paper).

$$E_{pg} = n_{H_2} \times \left(h^0_{H_2} - h^0_{H_2O}\right) + n_{CO} \times \left(h^0_{CO} - h^0_{CO_2}\right) + n_{CH_4} \times \left(h^0_{CH_4} - h^0_{H_2O} - h^0_{CO_2}\right) \tag{18}$$

$$\eta_{CCE} = \frac{12 \times (n_{CO} + n_{CO_2} + n_{CH_4})}{M_{fuel} \times m_c} \tag{19}$$

In the above equations, the value of n_i is equal to the molar number of produced gaseous components, m_c and M_{fuel} are the mass percentage of carbon in the dry inlet fuel and the molar mass of the fuel, respectively.

The amount of cold gas efficiency according to Equation (16) is directly dependent on the volume percentage of hydrogen, carbon monoxide and methane. According to the diagram in Figure 4. it is obvious that by changing equivalence ratio from 0.3 to 0.39, the value of this efficiency increases, although the volume percentage of hydrogen is decreasing in this period, but it should be noted that increasing the amount of carbon monoxide and presence of methane will compensate reduction in hydrogen, so an increase in cold gas efficiency is expected during this period.
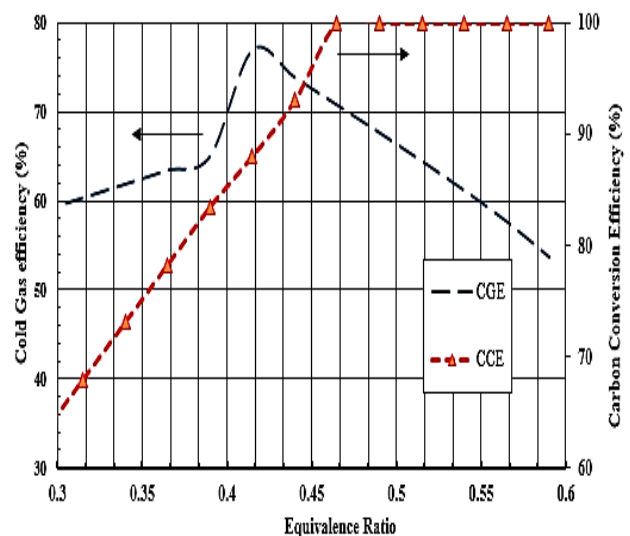
Figure 4. Changes in cold gas efficiency and carbon conversion efficiency relative to equivalence ratio (Figure is in color in the on-line version of the paper).

In the range of 0.39 to 0.415, due to the increase in the intensity of carbon-containing reactions, especially Eq. (2) the volume percentage of carbon monoxide will increase significantly which will increase the cold gas efficiency to 77%. It should be noted that with increasing the equivalence ratio, the gasification reaction tends towards combustion and the volume percentage of low value gases such as carbon dioxide and water vapor increases and the amount of carbon monoxide, methane and hydrogen gases that have high calorific value decreases. Therefore, by increasing the equivalence ratio and according to Figure 4. the cold gas efficiency will be decreased.

3.3. Oxygen enrichment

At this stage of modeling, the presence of oxygen in the inlet gasifier will change from its value in normal air (21%) to its value in pure oxygen (100%) and will cover a wide range of oxygen presence. Next with changes in oxygen enrichment, the amount of changes in gaseous production moles, changes in carbon conversion efficiency, cold gas efficiency changes, volume percentage changes of gas components, temperature changes and changes in high calorific value of the produced gas are investigated. The equivalence ratio is considered to be a constant of 0.35 to take into account the presence of carbon in the production component. The pressure of the gasifier and the temperature of the inlet components to the gasifier are set at a constant value of 18.75 atmospheres and 298 K, respectively. Figure 5. shows that the number of moles of hydrogen and carbon monoxide gases will increase with decreasing oxygen enrichment and will reach their maximum in the presence of atmospheric air. This can be explained by the equilibrium equations and the energy balance equation. Thus, as the presence of nitrogen gas in the gas mixture increases, the total mole presents in the gas chamber, n_t will increase and in the energy balance equation, due to the presence of nitrogen gas and heat consumption to change its temperature, a lower temperature will be obtained for the gasifier. Both of these factors will individually affect the chemical equilibrium constants of Eq. (2) and (3) and the molar value of the produced components.

The effect of each of these factors will be discussed with constant consideration of the other factor. In the first stage, it will be assumed that the temperature is constant and the amount of total gas moles increases with the addition of nitrogen gas, in which case the constant amount of chemical equilibrium will remain constant due to the dependence on temperature. In Eq. (2) and (3) with respect to not changing the chemical equilibrium constant and increasing n_t, molar values of carbon monoxide and hydrogen should be increased. In the second stage, the molar amount of nitrogen is considered equal to its amount in atmospheric air and as a result the total gaseous mole will not change much and the chemical equilibrium constant will change as the temperature changes. In this case, due to the presence of nitrogen on the products side in the energy balance, a lower temperature value will be obtained. This decrease in temperature will reduce the equilibrium constants of the two endothermic Eq. (2) and (3) which will affect and reduce the molar number of hydrogen and carbon monoxide gases. By looking at Figure 5. and considering the two steps simultaneously it can be concluded that as oxygen enrichment approaches its presence in atmospheric air, the amount of hydrogen and especially carbon monoxide will be increased. Equation (19), which makes the carbon
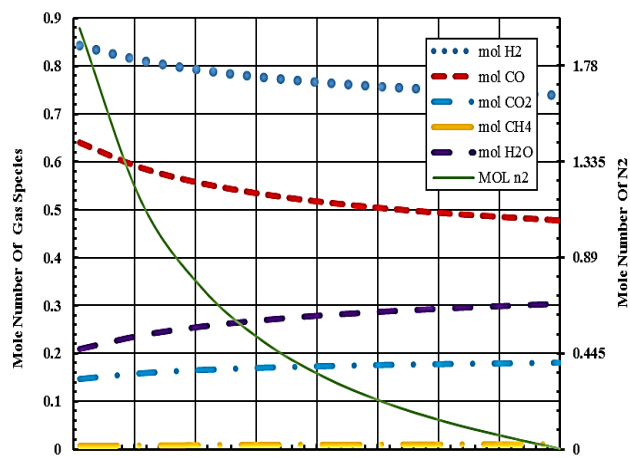
Figure 5. Changes in carbon conversion efficiency and cold gas efficiency relative to changes in input oxygen enrichment (Figure is in color in the on-line version of the paper).

conversion efficiency dependent on the carbon molecules of carbon monoxide, methane and carbon dioxide, this molar increase of carbon monoxide in the gas mixture will increase the carbon conversion efficiency, which can be seen in Figure 6.

This is incorrectly stated in the research of Vaezi et al. [28] in which the increase in carbon conversion efficiency is related to the increase in the volume percentage of carbon dioxide while it is clear that with the decrease of nitrogen in the gas mixture the volume percentage of all components will be increased due to the reduction of the total mole present in the gas chamber and slight change in amount of other gas components. However, according to Figure (5) it is quite understandable that increasing the mole number of carbon monoxide will increase the carbon conversion efficiency and increasing the volume percentage of carbon dioxide has no effect on it. In addition to the above, and according to Eq. (16) to (18), which relate cold gas efficiency to moles of methane, hydrogen and carbon monoxide, it can be expected that by decreasing the moles of these gaseous components due to the increase of oxygen enrichment, Cold gas efficiency will be decreased which can also be clearly seen from Figure 6.
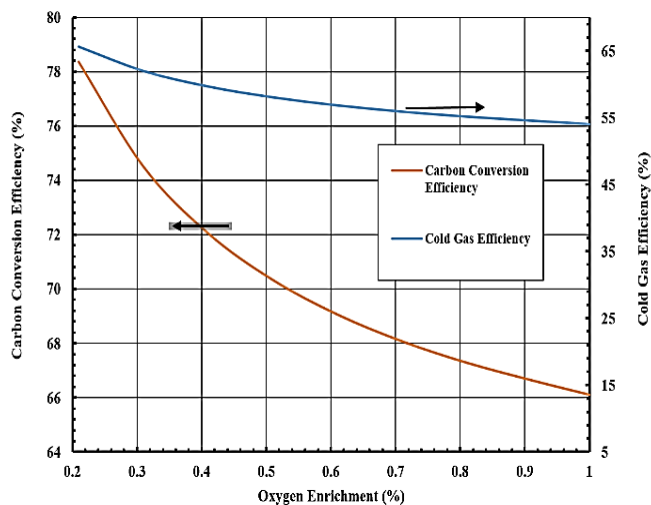
*Figure 6. Changes in the number of moles of gaseous components produced relative to changes in the oxygen enrichment of the input.*
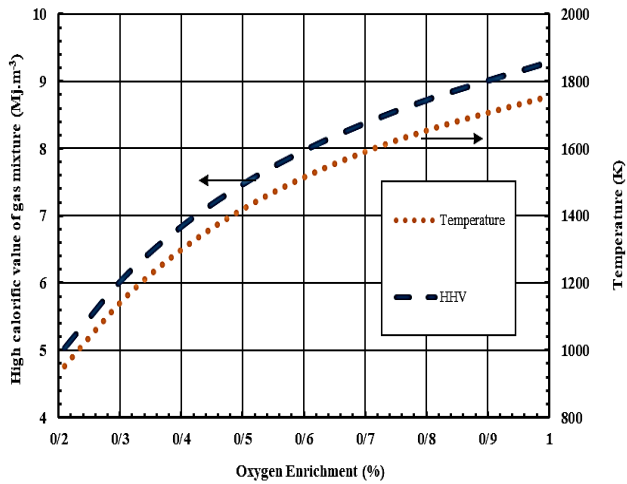
Figure 7. Changes in temperature and high calorific value of the gas mixture relative to changes in oxygen enrichment.

According to the introduction part, some amount of fuel is partially combusted to provide the necessary heat for gasification and temperature resulting from combusting with pure oxygen will be higher than with air due to the presence of nitrogen in the gas mixture which acts like a heat sink. Hence in the absence of nitrogen the temperature of gas mixture will be higher as it is shown in Figure 7.

Increasing the volume percentage of gaseous components such as hydrogen and carbon monoxide increases the high calorific value of the produced gas which according to Figure 7 its value will increase from 5 MJ.m^{-3} in air gasification to 9.28 MJ.m^{-3} in pure oxygen gasification. Figure 8 indicates that with increasing oxygen enrichment and decreasing nitrogen, the volume percentage of hydrogen and carbon monoxide are increased and there is no need to spend money for separating nitrogen from gas mixture and purify it.

This gas mixture in the combustion chamber will produce less NO$_x$, which will be beneficial to the environment and this is another advantage of increasing the presence of oxygen in the gasifier agent.
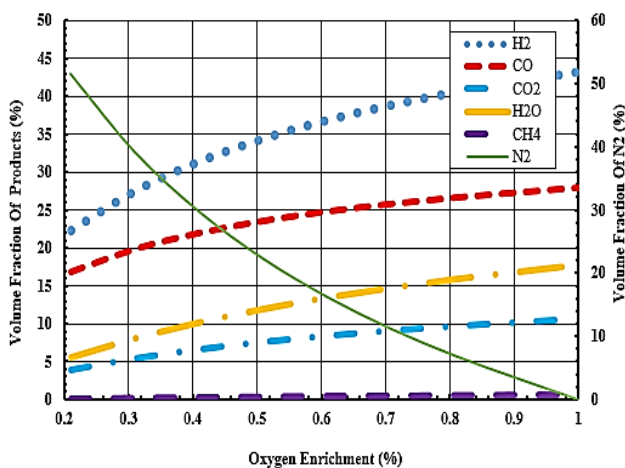
Figure 8. Changes in the volume fraction of the gas components produced relative to changes in oxygen enrichment.

3.4. Pressure change
Pressure changes in the gasification process have also been studied. For this purpose, the parameters of equivalence ratio and inlet temperature are 0.4 and 298 K and pure oxygen is gasification agent. Due to the small molar changes

in the gas mixture components compared to the pressure changes, these changes are logarithmically shown in Figure 9. for better observation. According to the diagram, the molar amount of hydrogen and carbon monoxide is slightly decreasing and the moles of methane, carbon dioxide and water vapor are increasing. This phenomenon can be expressed according to the Le Chatelier's principle that in equilibrium reactions with increasing in pressure, the reaction goes to direction that has less moles of gas to maintain the equilibrium so the methane reforming reaction is shifted to the left and subtracted from the molar amount of hydrogen and carbon monoxide and added to the amount of water vapor and methane. Also, by adding moles of water vapor to the water-gas reaction, this reaction will shift towards the consumption of the added moles of gas and the moles of carbon monoxide and water vapor will be reduced and the moles of carbon dioxide and hydrogen will be increased. In total, the effect of these two phenomena and according to the diagram, the mole number of carbon monoxide and hydrogen will decrease slightly and the mole number of carbon dioxide, water vapor and methane will increase slightly.

The amount of changes in the calorific value of the produced gas and the cold gas efficiency are plotted in Figure 10. Due to the reduction of the molar fraction of hydrogen and carbon monoxide, the calorific value of the produced gas mixture is expected to decrease, but it should be noted that increasing the molar fraction of methane will neutralize the effect of reducing hydrogen and carbon monoxide. Hence, the higher calorific value will increase slightly and changes from 10.8803 MJ.m^{-3} to 10.886 MJ.m^{-3}. The cold gas efficiency has very slight change which is due to the small changes in the moles of the produced gases.

As mentioned in pressure change, according to the Le Chatelier's principle, chemical reactions to maintain equilibrium are moved to a direction that has less gas moles, so the methane reforming reaction is shifted to the left and will be exothermic reaction, this will increase the temperature of the gas mixture, which can be seen in Figure 11.
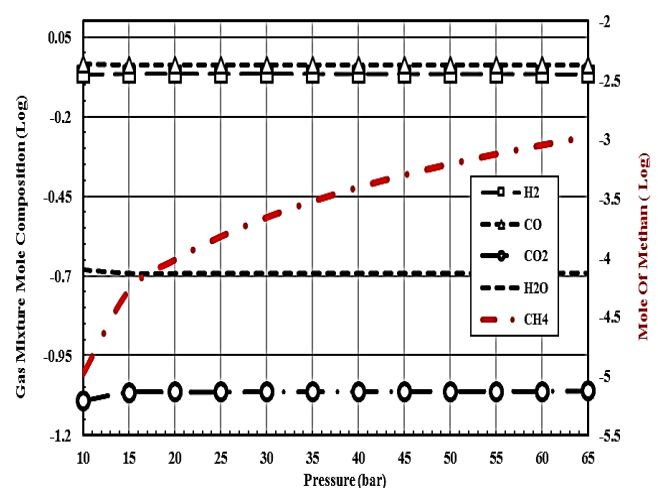
Figure 9. Changes in the volume percentage of the components of the produced gas mixture compared to the changes in pressure in the logarithmic state.

The results show that pressure changes will have negligible effect on the molar percentages of gases as well as on energy efficiency, but it should be noted that this increase

in pressure can have good economic benefits. As the exhaust gas pressure increases there will be no need for a compressor to increase the pressure. It should be noted that the gas mixture must be pressurized for use in subsequent processes such as burning in a gas turbine or participating in a chemical process and for chemical processes a minimum pressure of 10 atmospheres is required.
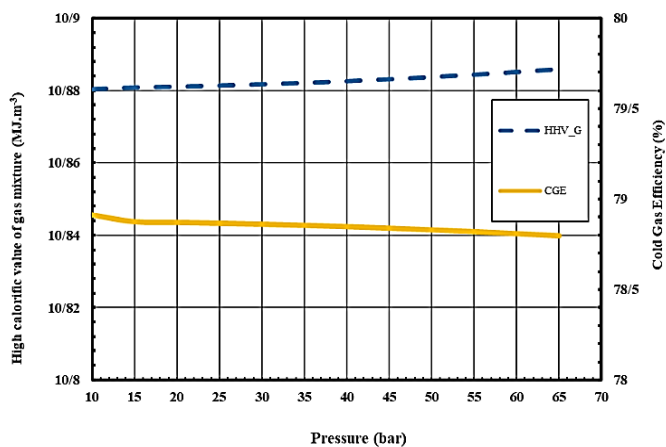
Figure 10. Changes in cold gas efficiency and calorific value of produced gas relative to pressure changes.
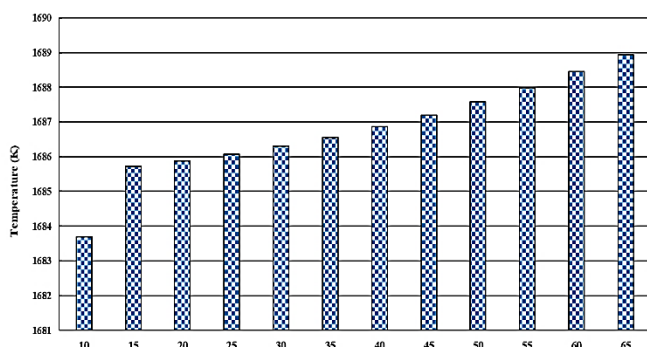
Figure 11. Changes in gas mixture temperature relative to changes in gasification pressure.

3.5. The ratio of hydrogen to carbon monoxide

In this section, changes in the ratio of hydrogen to carbon monoxide with respect to changes in the equivalence ratio, pressure and oxygen enrichment are investigated. Figure 12 shows that with changes in the equivalence ratio, the amount of H_2:CO decreases, this can be clear because by increasing the equivalence ratio, the gasification process approaches combustion and the amount of hydrogen production decreases sharply, according to Figure 2, this reduction will be much greater than the reduction of carbon monoxide therefore it is expected that the H_2:CO ratio will also decrease. By changing the oxygen enrichment the amount of carbon monoxide in the gas mixture decreases and the H_2:CO ratio will also increase. It can also be seen that with changes in pressure, the ratio of hydrogen to carbon monoxide will not change much because with increasing pressure, the volume percentage of the components of the exhaust gas mixture change slightly. The quality of the exhaust gas mixture is usually measured by the H_2:CO ratio, and high quality gas can be used in chemical processes such as methanol production.

Also, by separating hydrogen from the gas mixture, it can be used as fuel in fuel cells. The higher the quality of the gas mixture, the easier this separation will be. According to Figure 12. it can be concluded that waste engine oil

gasification will have a high potential for use in downstream chemical processes or in fuel cells. For this purpose, the value of equivalence ratio of 0.3 and 100% oxygen enrichment and arbitrary pressure will be the best values for high H_2:CO ratio.
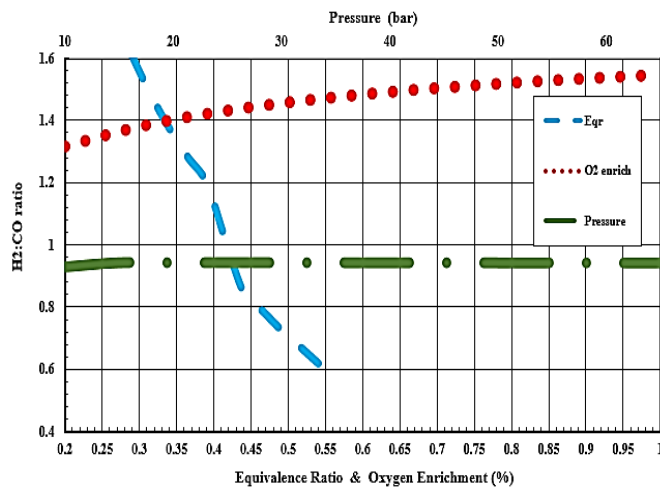
Figure 12. Changes in the ratio of H_2: CO for changes in the equivalence ratio and gasification pressure.

4. Conclusion

A numerical algorithm based on the thermochemical equilibrium approach was developed to simulate the waste oil gasification process. This model can predict the distribution of synthetic gas species produced in real gasification operating conditions. This model was confirmed by comparing numerical results with experimental results.

Through a parametric study it was shown that the gasification of waste oil with an equivalence ratio of 0.4 to 0.42 makes it possible to produce a synthesis gas with a significant calorific value of about 10 MJ.m^{-3}. Gas mixture with such a calorific value are suitable for applications such as gas turbines that consume high calorific value gases. The use of pure oxygen as a gasification agent leads to the production of a high calorific value and a hydrogen-rich gas mixture with a hydrogen content of 43% by volume and H_2:CO ratio of about 1.6. Gas mixture with such a high H_2:CO ratio can be used in the methanol synthesis process and in the production of pure hydrogen for fuel cell applications. The parametric study also showed that the gasification pressure does not have a significant effect on the gasification properties. Simulations performed during this study show that gasification of waste oil is a possible process that can be used to produce synthetic gas for various industrial applications. The developed numerical model can be used to design and optimize such gasifiers.

Nomenclature

α, β, z	numbers of atoms of hydrogen, oxygen, and nitrogen per one atom of carbon in the feedstock; respectively
w, m, s	the amounts of water, air, and steam per one kmole of feedstock, respectively
m_h	the mass fraction of hydrogen in dry fuel analyses
x_i	the mole number of species i
M_{fuel}	the molar mass of the heavy fuel oil
M_{water}	the molar mass of water
wc	the mass-based water content of the feedstock
n_t	the total number of moles of produced gas
K	equilibrium constant
R_u	the universal gas constant
η_{CG}	cold gas efficiency
η_{CCE}	the carbon conversion efficiency
P	the pressure of gas mixture (bar)
h_{fg}	the enthalpy of vaporization of water
C_p	the specific heat at constant pressure
Δh	the enthalpy difference between any given state and the reference state
m_c	the mass fraction of carbon in the dry fuel analyses

C, H, O, N, S	carbon, hydrogen, oxygen, nitrogen, sulfur, contents of feedstock, respectively
$h_{f,i}^0$	the enthalpy/heat of formation for species i
h_{fuel}^0	the enthalpy formation of fuel
Δh_f^0	the change of formation's enthalpy for a reaction
HHV	higher heating value
HHV_{fuel}	higher heating value of fuel
LHV_{fuel}	lower heating value of fuel
ΔG^0	the standard Gibbs function of formation
J	the constant of integration
I	a constant
A, B, C, and D	the coefficients for determining the specific heat
T	temperature
M	equivalence ratio
Sto	stoichiometric air for complete combustion of the fossil fuel
E_{pg}	the energy of produced gas
E_{feed}	the energy of inlet fuel

Appendix A. Gasification modeling equations

The following equations can be used to determine the fuel's chemical formula based on the mass fraction of its constituent components. α, β, z represents molar ratio of hydrogen, oxygen and nitrogen to carbon in the fuel in dry state.

$$\alpha = \frac{(m_h \times M_c)}{(m_c \times M_h)} \tag{1}$$

$$\beta = \frac{(m_o \times M_c)}{(m_c \times M_o)} \tag{2}$$

$$z = \frac{(m_N \times M_c)}{(m_c \times M_N)} \tag{3}$$

M_i and m_i are the molar mass and dry mass fraction of each element respectively. The ratio of moles of moisture to each moles of fuel is obtained by the following equation:

$$w = (M_{fuel} \times wc)/(M_{water} \times (1-wc)) \tag{4}$$

wc is the mass fraction of moisture in the fuel. M_{water} and M_{fuel} are the molecular masses of water and fuel, respectively. The amount of air required for complete combustion of a fuel with the chemical formula $CH_\alpha O_\beta N_z$ is obtained from the following equation, which is also called stoichiometric air:

$$Sto = 1 + (0.25\,\alpha) - (0.5\,\beta) \tag{5}$$

In gasification, the amount of air required is less than the amount of air needed for incomplete combustion and equal to a factor of the stoichiometric air demand (Sto). This coefficient varies between 0.3 and 0.6, which is the equivalence ratio.

$$m = eqr \times Sto \tag{6}$$

According to the mass conservation law for the three elements carbon, hydrogen and oxygen, three equations are obtained from the equations needed to find the unknown gaseous moles.

$$1 = x_2 + x_3 + x_5 + x_6 \tag{7}$$

$$\alpha + 2w + 2s = 2x_1 + 2x_4 + 4x_5 \tag{8}$$

$$\beta + w + s + 2m = x_2 + 2x_3 + x_4 \tag{9}$$

The equilibrium constant equation is defined by the following formula [13]:

$$K = \prod_i (x_i^{v_i}) \times \left(\frac{P}{n_t}\right)^{\sum_i v_i} \tag{10}$$

x_i is gas mole in the reaction, v_i stoichiometric coefficients, P total pressure gasification and n_t is total gas moles. The equilibrium constant for each reactions in this paper will be obtained as follows:

$$K_1 = \frac{x_2^2}{x_3}\left(\frac{P}{n_t}\right)^1 \tag{11}$$

$$K_2 = \frac{x_2 x_1}{x_4}\left(\frac{P}{n_t}\right)^1 \tag{12}$$

$$K_3 = \frac{x_5}{x_1^2}\left(\frac{P}{n_t}\right)^{-1} \tag{13}$$

$$K_4 = \frac{x_3 x_1}{x_2 x_4}\left(\frac{P}{n_t}\right)^0 \tag{14}$$

$$K_5 = \frac{x_2 x_1^3}{x_5 x_4}\left(\frac{P}{n_{tot}}\right)^2 \tag{15}$$

The chemical equilibrium constant of each reaction will have the following correlation with the free standard Gibbs energy:

$$\ln K = -\frac{\Delta G^0}{R_u T} \tag{16}$$

The parameter T and R_u are the outlet temperature of the gasification reactor and the universal constant of gases respectively. The dependence of Gibbs free energy on temperature is given in the following equation:

$$\frac{d\left(\frac{\Delta G^0}{R_u T}\right)}{dt} = -\frac{\Delta h_f^0}{R_u T^2} \quad (17)$$

$$\frac{d(\ln K)}{dt} = \frac{\Delta h_f^0}{R_u T^2} \quad (18)$$

Since Δh_f is a function of temperature, it can be integrated as follows:

$$\ln K = \left(\int \frac{\Delta h_f^0}{R_u T^2} dT\right) + I \quad (19)$$

"I" in the above formula is the constant of integration. The amount of enthalpy and heat capacity will be linked by the following formula:

$$h = \left(\int C_p dT\right) \quad (20)$$

Heat capacity is obtained by having the temperature by the following equation [14]:

$$C_p = R_u(A + BT + CT^2 - DT^{-2}) \quad (21)$$

The coefficients A, B, C, D are in Table A1 and the enthalpy is:

$$h = R_u\left(AT + \frac{B}{2}T^2 + \frac{C}{3}T^3 - \frac{D}{T}\right) + j \quad (22)$$

Table A1. Constants A, B, C, D for calculating heat capacity [14].

$10^{-5}D$	$10^6 C$	$10^3 B$	A	T(Kelvins)	Chemical Formula
0.083	-	0.422	3.249	298.15 to 3000	H_2
-0.031	-	0.557	3.376	298.15 to 2500	CO
-1.157	-	1.045	5.457	298.15 to 2000	CO_2
0.121	-	1.450	3.470	298.15 to 2000	H_2O
-	-2.164	9.081	1.702	298.15 to 1500	CH_4
-0.867	-	0.771	1.771	298.15 to 2000	C

The difference in enthalpies of a particular reaction is obtained as follows:

$$\Delta h = R_u\left(\Delta AT + \frac{\Delta B}{2}T^2 + \frac{\Delta C}{3}T^3 - \frac{\Delta D}{T}\right) + J \quad (23)$$

$$\ln K = \Delta A \ln T + \Delta B \frac{T}{2} + \frac{\Delta C}{6}T^2 - \frac{\Delta D}{2T^2} + I - \frac{J}{R_u T} \quad (24)$$

$$K = \exp\left(\Delta A \ln T + \Delta B \frac{T}{2} + \frac{\Delta C}{6}T^2 - \frac{\Delta D}{2T^2} + I - \frac{J}{R_u T}\right) \quad (25)$$

$$\Delta G^0 = -R_u T\left(\Delta A \ln T + \Delta B \frac{T}{2} + \frac{\Delta C}{6}T^2 - \frac{\Delta D}{2T^2} + I - \frac{J}{R_u T}\right) \quad (26)$$

Table A2. Gibbs free energy and the enthalpy of formation of each reaction at 298 K.

Gibbs Free Energy of Formation (kJ.kmol⁻¹)	Standard Enthalpy of Formation (kJ.kmol⁻¹)	Chemical Formula
0	0	H_2
-137169	-110525	CO
-394359	-393509	CO_2
-228572	-241818	H_2O
-50460	-74520	CH_4
0	0	C

I and J constants are determined by identifying the Gibbs free energy and enthalpy of formation for each reactions at 298K (Table A2).

References:

[1] M. N. Nasim, M. Sohail, B. Ravindra, V. J. J. o. M. Lotia, and C. Engineering, "Recycling waste automotive engine oil as alternative fuel for diesel engine: A review," pp. 46-50, 2014.

[2] K. K. Ramasamy and T. J. C. T. Ali, "Hydrogen production from used lubricating oils," vol. 129, no. 3-4, pp. 365-371, 2007.

[3] M. Fuentes, R. Font, M. Gómez-Rico, I. J. J. o. A. Martín-Gullón, and A. Pyrolysis, "Pyrolysis and combustion of waste lubricant oil from diesel cars: Decomposition and pollutants," vol. 79, no. 1-2, pp. 215-226, 2007.

[4] M. Rosli, F. Yee, and S. S. Tea, "Modeling and simulation of used lubricant oil re-refining process," in *2nd World Engineering Congress, Sarawak, Malaysia*, 2002.

[5] N. Selukar and S. J. I. J. o. A. C. Wagh, "Gasoline and diesel synthesis from waste lubricating oil: A kinetic approach," pp. 22-25, 2014.

[6] F. C.-Y. Wang, L. J. E. Zhang, and fuels, "Chemical composition of group II lubricant oil studied by high-resolution gas chromatography and comprehensive two-dimensional gas chromatography," vol. 21, no. 6, pp. 3477-3483, 2007.

[7] E. M. Fujita, D. E. Campbell, and B. J. F. R. Zielinska, Desert Research Institute, Reno, Nevada, USA, "Chemical analysis of lubrication oil samples from a study to characterize exhaust emissions from light-duty gasoline vehicles in the Kansas City Metropolitan Area," 2006.

[8] J. Moore, S. Cui, P. Cummings, and H. J. A. I. o. C. E. A. J. Cochran, "Lubricant characterization by molecular simulation," vol. 43, no. 12, p. 3260, 1997.

[9] J. Sharaf, B. Mishra, R. J. I. J. o. E. R. Sharma, and Applications, "Production of gasoline-like fuel obtained

from waste lubrication oil and its physicochemical properties," vol. 3, no. 3, pp. 113-118, 2013.

[10] S. S. Lam *et al.*, "Progress in waste oil to sustainable energy, with emphasis on pyrolysis techniques," vol. 53, pp. 741-753, 2016.

[11] M. Puig-Arnavat, J. C. Bruno, A. J. E. Coronas, and Fuels, "Modified thermodynamic equilibrium model for biomass gasification: a study of the influence of operating conditions," vol. 26, no. 2, pp. 1385-1394, 2012.

[12] M. Puig Arnavat, "Performance modelling and validation of biomass gasifiers for trigeneration plants," Universitat Rovira i Virgili, 2011.

[13] L. Chanphavong and Z. J. J. o. t. E. I. Zainal, "Characterization and challenge of development of producer gas fuel combustor: A review," vol. 92, no. 5, pp. 1577-1590, 2019.

[14] G. Gautam, "Parametric study of a commercial-scale biomass downdraft gasifier: experiments and equilibrium modeling," 2010.

[15] C. Higman and M. v. der Burgt, "Gasification. 2nd," 2008.

[16] A. K. J. E. C. Sharma and Management, "Modeling and simulation of a downdraft biomass gasifier 1. Model development and validation," vol. 52, no. 2, pp. 1386-1396, 2011.

[17] M. Puig-Arnavat, J. A. Hernández, J. C. Bruno, A. J. B. Coronas, and bioenergy, "Artificial neural network models for biomass gasification in fluidized bed gasifiers," vol. 49, pp. 279-289, 2013.

[18] P. Basu, *Biomass gasification and pyrolysis: practical design and theory*. Academic press, 2010.

[19] M. Puig-Arnavat, J. C. Bruno, A. J. R. Coronas, and s. e. reviews, "Review and analysis of biomass gasification models," vol. 14, no. 9, pp. 2841-2851, 2010.

[20] S. Vakalis, F. Patuzzi, and M. J. B. t. Baratieri, "Thermodynamic modeling of small scale biomass gasifiers: Development and assessment of the ''Multi-Box''approach," vol. 206, pp. 173-179, 2016.

[21] A. J. F. Bridgwater, "The technical and economic feasibility of biomass gasification for power generation," vol. 74, no. 5, pp. 631-653, 1995.

[22] M. Baratieri, P. Baggio, L. Fiori, and M. J. B. t. Grigiante, "Biomass as an energy source: thermodynamic constraints on the performance of the conversion process," vol. 99, no. 15, pp. 7063-7073, 2008.

[23] M. J. Prins, K. J. Ptasinski, and F. J. J. E. Janssen, "From coal to biomass gasification: Comparison of thermodynamic efficiency," vol. 32, no. 7, pp. 1248-1259, 2007.

[24] A. K. J. E. C. Sharma and Management, "Equilibrium modeling of global reduction reactions for a downdraft (biomass) gasifier," vol. 49, no. 4, pp. 832-842, 2008.

[25] L. Shen, Y. Gao, J. J. B. Xiao, and bioenergy, "Simulation of hydrogen production from biomass gasification in interconnected fluidized beds," vol. 32, no. 2, pp. 120-127, 2008.

[26] A. Mountouris, E. Voutsas, D. J. E. C. Tassios, and Management, "Solid waste plasma gasification: equilibrium model development and exergy analysis," vol. 47, no. 13-14, pp. 1723-1737, 2006.

[27] S. Jarungthammachote and A. Dutta, "Thermodynamic equilibrium model and second law analysis of a downdraft waste gasifier," *Energy,* vol. 32, no. 9, pp. 1660-1669, 2007.

[28] M. Ashizawa, S. Hara, K. Kidoguchi, and J. Inumaru, "Gasification characteristics of extra-heavy oil in a research-scale gasifier," *Energy,* vol. 30, no. 11-12, pp. 2194-2205, 2005.

[29] S.-M. Beheshti, H. Ghassemi, R. J. P. s. Shahsavan-Markadeh, and technology, "A comprehensive study on gasification of petroleum wastes based on a mathematical model," vol. 32, no. 22, pp. 2674-2681, 2014.

[30] S.-M. Beheshti, H. Ghassemi, R. J. P. S. Shahsavan-Markadeh, and Technology, "Modeling Steam Gasification of Orimulsion in the Presence of KOH: A Strategy for High-Yield Hydrogen Production," vol. 33, no. 2, pp. 218-225, 2015.

[31] M. S. B. Khaleghi, R. S. Markadeh, H. J. P. S. Ghassemi, and Technology, "Thermodynamic evaluation of mazut gasification for using in power generation," vol. 34, no. 6, pp. 531-538, 2016.

[32] Y. Castillo Santiago, A. Martínez González, O. J. Venturini, and D. M. Yepes Maya, "Assessment of the energy recovery potential of oil sludge through gasification aiming electricity generation," *Energy,* vol. 215, p. 119210, 2021/01/15/ 2021.

[33] D. Vera, B. de Mena, F. Jurado, and G. Schories, "Study of a downdraft gasifier and gas engine fueled with olive oil industry wastes," *Applied Thermal Engineering,* vol. 51, no. 1, pp. 119-129, 2013/03/01/ 2013.

[34] A. M. Sanchez-Hernandez, N. Martin-Sanchez, M. J. Sanchez-Montero, C. Izquierdo, and F. Salvador, "Different options to upgrade engine oils by gasification with steam and supercritical water," *The Journal of Supercritical Fluids,* vol. 164, p. 104912, 2020/10/01/ 2020.

[35] N. Couto *et al.*, "Numerical and experimental analysis of municipal solid wastes gasification process," *Applied Thermal Engineering,* vol. 78, pp. 185-195, 2015/03/05/ 2015.

[36] M. Ruggiero and G. J. R. e. Manfrida, "An equilibrium model for biomass gasification processes," vol. 16, no. 1-4, pp. 1106-1109, 1999.

[37] A. Melgar, J. F. Pérez, H. Laget, A. J. E. c. Horillo, and management, "Thermochemical equilibrium modelling of a gasifying process," vol. 48, no. 1, pp. 59-67, 2007.

[38] C. R. Altafini, P. R. Wander, R. M. J. E. C. Barreto, and Management, "Prediction of the working parameters of a wood waste gasifier through an equilibrium model," vol. 44, no. 17, pp. 2763-2777, 2003.

[39] M. Lapuerta, J. J. Hernández, F. V. Tinaut, and A. Horrillo, "Thermochemical behaviour of producer gas from gasification of lignocellulosic biomass in SI engines," SAE Technical Paper0148-7191, 2001.

[40] G. Schuster, G. Löffler, K. Weigl, and H. J. B. t. Hofbauer, "Biomass steam gasification–an extensive parametric modeling study," vol. 77, no. 1, pp. 71-79, 2001.

[41] T. Jayah, R. Fuller, L. Aye, and D. J. I. E. J. Stewart, "The potential for wood gasifiers for tea drying in Sri Lanka," vol. 2, no. 2, 2007.

[42] C. J. C. e. s. Di Blasi, "Dynamic behaviour of stratified downdraft gasifiers," vol. 55, no. 15, pp. 2931-2944, 2000.

[43] M. Rao, S. Singh, M. Sodha, A. Dubey, M. J. B. Shyam, and Bioenergy, "Stoichiometric, mass, energy and exergy balance analysis of countercurrent fixed-bed gasification of post-consumer residues," vol. 27, no. 2, pp. 155-171, 2004.

[44] S. Channiwala and P. J. F. Parikh, "A unified correlation for estimating HHV of solid, liquid and gaseous fuels," vol. 81, no. 8, pp. 1051-1063, 2002.

[45] I. P. Silva, R. M. Lima, G. F. Silva, D. S. Ruzene, D. P. J. R. Silva, and S. E. Reviews, "Thermodynamic equilibrium model based on stoichiometric method for biomass gasification: A review of model modifications," vol. 114, p. 109305, 2019.

[46] H. Ghassemi, R. J. E. C. Shahsavan-Markadeh, and Management, "Effects of various operational parameters on biomass gasification process; a modified equilibrium model," vol. 79, pp. 18-24, 2014.

[47] M. Vaezi, M. Passandideh-Fard, M. Moghiman, and M. Charmchi, "Gasification of heavy fuel oils: A thermochemical equilibrium approach," *Fuel,* vol. 90, no. 2, pp. 878-885, 2011.

[48] H. Ghassemi, S. Beheshti, and R. J. F. Shahsavan-Markadeh, "Mathematical modeling of extra-heavy oil gasification at different fuel water contents," vol. 162, pp. 258-263, 2015.

[49] K. Lin, S. Chowdhury, C. Shen, and C. Yeh, "Hydrogen generation by catalytic gasification of motor oils in an integrated fuel processor," *Catalysis Today,* vol. 136, no. 3-4, pp. 281-290, 2008.

High Pressure Effects on the Structural Properties of GaN Compound Using Equations of State

Siham J. AL-Faris[1]* , Raed H. Al-Saqa[2], Huda M. Mohmad[3] , Sirwan K. Jalal[4]

[1]*Alnoor University College Bartella ,Iraq
[2]Directorate General of Education, Iraq
[3]Alnoor University College Bartella ,Iraq
[4]G. Science Department, Charmo University, Iraq
E-mail: [1]*siham.jasim@alnoor.edu.iq

Abstract

The present study is a theoretical calculation for the effects of high pressure on thermodynamic properties on GaN up to 40Gpa at room temperature. Volume compression ratio (V_0/V_p), lattice constant (a) and elastic bulk modulus(B) have been established. Furthermore, lattice frequencies and disruptions function by analyzing phonon frequency spectrum (PFS) at (0 K). The entire calculations rely on using of two equation of state (EOS) "Birch-Murnaghan and modified Lennard-Jones" equation of state and with the integration of Grüneisen approximation theory. From the considered equations of state, formulation of bulk modulus was derived, that predicts a rising trend of bulk modulus. The large bulk modulus value of GaN has made a small fraction of change in volume (less than 15%) of the material even under an extreme pressure up to 45Gpa. It was also found that the results of phonon frequency spectrum obtained from Birch-Murnaghan equation of state in a better agreement with the experimental data than that of modified Lennard-Jones equation of state. Given that the Birch-Murnaghan equation of state developed according to Eulerian strain theory accounted as a universal equation of state. Moreover, good agreement between theoretically present calculations and experiment data of phonon frequency spectrum, reveals the validity of the equations of state used in the present study.

Keywords: Bulk modulus; volume compression ratio; lattice parameter; phonon frequency spectrum.

1. Introduction

The semiconductor materials represent today's basic building blocks of emitters and receivers in cellular, satellite, and fiberglass communications. III-nitrides, for example, are nowadays the most widely used type of semiconducting materials in the industry [1]. The III-V nitride: GaN has exhibited particular interest due to some of its attracting properties such as large energy gap, high thermal conductivity, large bulk modulus and the extreme hardness. In addition, GaN has high melting point. These, characteristics that are closely related to their strong (Ionic and covalent) bonding, they make the material very promising for optoelectronic device applications [2]. The zinc blende structured GaN has a higher saturated electron drift velocity and a somewhat lower energy gap than GaN [3]. Vibrational contribution of lattice frequencies are represented by phonon frequency spectrum, which is found to be volume or pressure dependent, then volume dependent of vibrational modes are characterized by Grüneisen parameter.

High pressure research have been an interesting field of condensed matter. Pressure induces vital structural properties within crystalline solids, for example as high pressure is applied, bulk modulus tends to increase, the Grüneisen parameter declines and also phonon frequency spectrum alters [4,5]. As high pressure alters mechanical and thermodynamic properties of solid crystalline, thus high pressure can induce new structural materials with useful characterization.

Theoretical condensed matter research has developed equations of state to predict numerically interesting properties of material, for example, thermal-pressure equation of state which demonstrates the thermally generated pressure due to lattice vibrations [6] and isothermal equation of state which is the main approach in the current study.

In the present work, the bulk modulus (B), compression volume (VP/Vo), lattice constant and phonon frequency spectrum (pfs) of a GaN compound under the influence of high pressure were calculated using the "Birch-Murnaghan and modified Lennard-Jouns" EOS. The calculated results have been compared with experimental data, which confirms the validity of the present equations of state. The Grüneisen parameter variation assumption has improved the results of phonon frequency spectrum under compression.

2. Theoretical Details

Equation of state (EOS) of crystalline materials is a straight forward mathematical expression relating high pressure P applied to compress the solid isothermally from initial volume V_0 to V. Thus, equation of state is analogue to general gas equation PV=nRT. EOSs are cost effective and time saving method, though which and without any laboratory, various outstanding properties of solid phase

can be found. Depending on various assumptions, variety of EOS have been developed in the literature. Current study focuses on using of two familiar equations that are presented in the following sections:

2.1 Birch-Murnaghan equations of state (B-M EOS)

Eulerian strain represents the strain relative to the strained state, it has widespread applications for understanding high pressure behavior of solid matter.

The Eulerian strain (f_e) is given by:

$$f_e = \frac{1}{2}\left[\left(\frac{V_0}{V_P}\right)^{2/3} - 1\right] \tag{1}$$

where V_0 is the volume at atmosphere pressure and V_p is the volume at pressure P.

The B.M EOS is obtained by expanding a series of powers of the Eulerian strain. The 2nd, 3rd and 4th order isothermal B.M EOS, they are functions of two measurable parameters, and isothermal bulk modulus (B_0) at P = 0, so that P = f(X, B_0), where X=V_0/V_p .The B-M EOS at the 2nd order when it varies as function of pressure is [7]:

$$P_{B-M} = \frac{3B_0}{2}\left(\eta^{-7/3} - \eta^{-5/3}\right)\left(1 + \frac{3}{4}(B_0' - 4)\left(\eta^{-2/3} - 1\right)\right) \tag{2}$$

where η denotes V_P/V_o.

2.2 Modified Lennard-Jones equation of state (mL-J EOS)

This equation which proposed two-parameter EOS based on the generalized Lennard-Jones (GLJ) potential which given by [8]:

$$P = \frac{B_0}{n}(V_0 / V_P)^n [(V_0 / V_P)^{(2/3)} - 1] \tag{3}$$

where, $n = \frac{1}{3}B_0'$

B_0' : First pressure derivative of bulk modulus, and

mathematically $B_0' = \left(\frac{\partial B}{\partial P}\right)_T$. Where B is bulk modulus.

ML-J EOS is just a two-parameter EOS, and the precision is higher than those for several popular EOSs.

2.3 Bulk modulus

The bulk modulus which is a physical constant of solid that indicates their properties when they are under pressure over their entire surfaces is defined as:

$$B = -\frac{\partial P}{\partial V} \tag{4}$$

From derivation of equations (2 and 3) with respect to volume and substitute them into the equation (4), expressions of pressure dependence of bulk modulus are formulated as given in eqs.5 and 6:

$$B_{B-M} = \frac{3B_o}{2}\left[\begin{array}{l}\frac{7}{3}\eta^{-7/3} - \frac{5}{3}\eta^{-5/3} - \frac{9}{4}(B_o' - 4)\eta^{-3} \\ + \frac{7}{2}(B_o' - 4)\eta^{-7/3} + \frac{5}{4}(B_o' - 4)\eta^{-5/3}\end{array}\right] \tag{5}$$

$$B_{(mL-J)} = B_o(V_o / V_P)^n[2(V_o / V_P)^n - 1] \tag{6}$$

2.4 Lattice constant

Lattice constant change with pressure was calculated using equation (7) [9,10]:

$$a_p = a_o\left(1 + B_0'\frac{P}{B_0}\right)^{-\frac{1}{3B_0'}} \tag{7}$$

where a_0, is lattice parameter at ambient condition. a_p, is lattice parameter under compression.

According to Murnaghan EOS [11] the expression

$\left(1 + B_0'\frac{P}{B_o}\right)^{-1/B_0'}$ represents $\left(\frac{V_P}{V_o}\right)$, Then eq. (7) is written as:

$$a_P = a_0\left(\frac{V_P}{V_o}\right)^{-\frac{1}{3}} \tag{8}$$

3 Calculation and Results
3.1 Evaluation of V_P/V_o of GaN

The compressibility of GaN was calculated using the B-M and mL-J equation of state (eq.2 and 3) show in Fig. 1. In which the input parameters are; B_0 and B_0', listed in Table 1. Under the application of high pressure, the material compresses and the volume of the unit cells tends to shrink as expected by the EOSs and seen in the Fig.1. Due to the high bulk modulus B_o (200Gpa) of GaN, 45Gpa of pressure is required to reduce the volume of the sample to 85% of its initial value. The V_P/V_o curves obtained with B-M EOS and ML-J EOS are inline so that no divergence is observed.
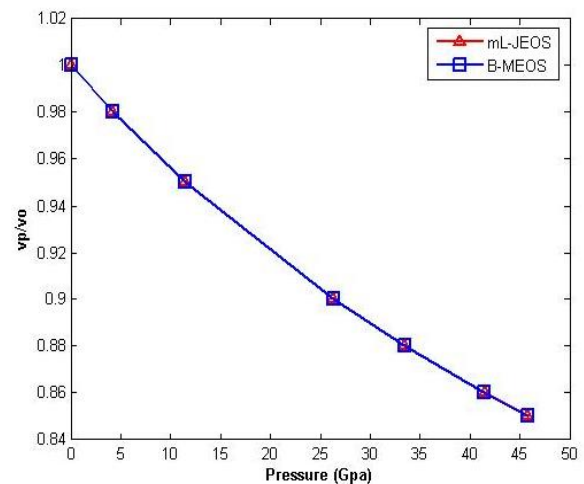
Figure 1. Variation of compressibility with pressure.

Parameters	Values	References
B_0	200Gpa	[12]
B'_0	4.4	[12]
a_0	4.5Å	[13]
γ_0	1.17	[14]

3.2 Evaluation of Bulk modulus

Equations (5 & 6) represent linear increase in bulk modulus of solid material with reducing volume. Substituting parameters in Table 1 into eqs. (5 &6) variation of bulk modulus is calculated and depicted in fig.2. Both EOSs predict that as applied pressure reaches 45Gpa or $V_p/V_o=0.85$, bulk modulus grows to an enormous value as 380Gpa.
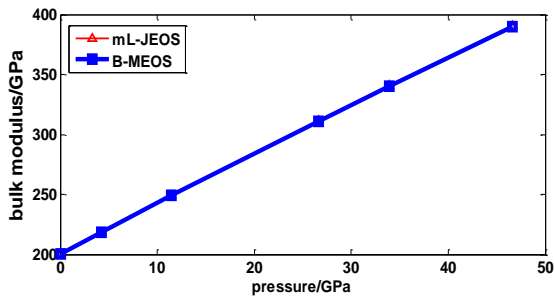
Figure 2. Variation of Bulk modulus with pressure according to the two EOSs.

Moreover, the effect of pressure on lattice parameter has been demonstrated in fig.3 with implement of equation (8), as shown in the following.
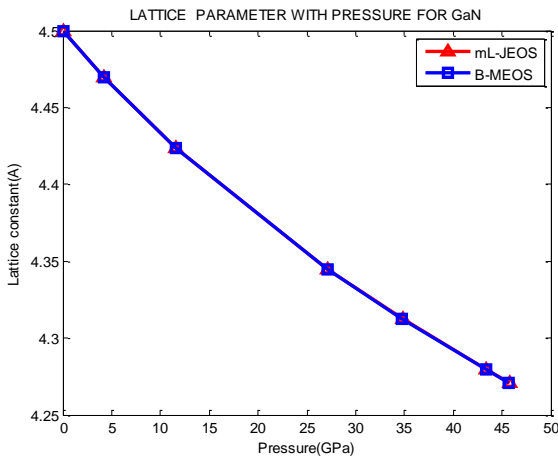
Figure 3. Variation of lattice parameter with pressure according to the two EOSs.

3.3 Phonon frequency spectrum under high pressure pfs

The high pressure produce change in (V_P/V_o) ratio, where high pressure changes the equilibrium position of lattice points and then produces the change in "pfs" as well [15], the equation that describe the "pfs" under high pressure is given by [13]:

$$v_P = v_0 \left(\frac{V_P}{V_0} \right)^{-\gamma} \tag{9}$$

$$g_P(v_P, V_P) = g_0(v_0, V_0) \left(\frac{V_P}{V_0} \right)^{-\gamma} \tag{10}$$

where v_P: frequency at pressure (P).
v_o: Frequency at atmospheric pressure.
γ_o: Grüneisen parameter at atmospheric pressure.
$G_P(v_P, V_P)$:Phonon density of state at pressure (p).
$g(v_o, V_o)$:Phonon density of state at atmospheric pressure.

3.4 Evaluation of PFS for GaN under high pressure
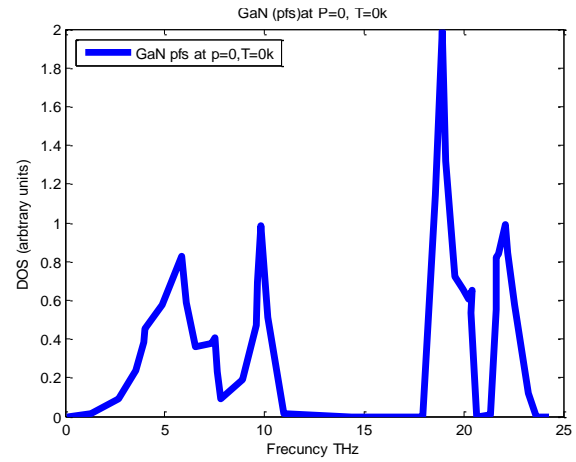
Figure 4. phonon frequency spectrum for GaN at atmospheric pressure and '0 K' [16]

(a)

(b)
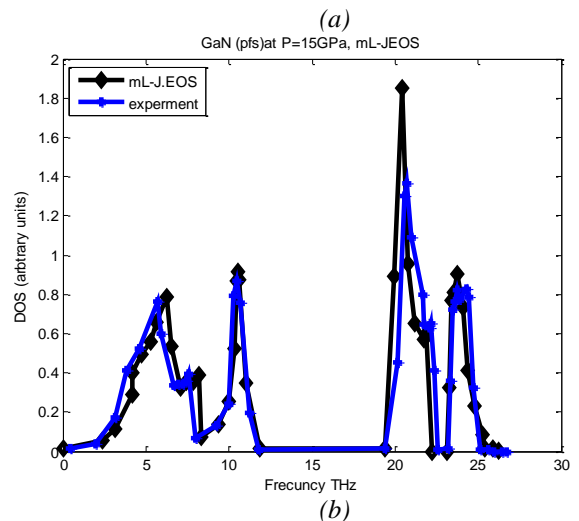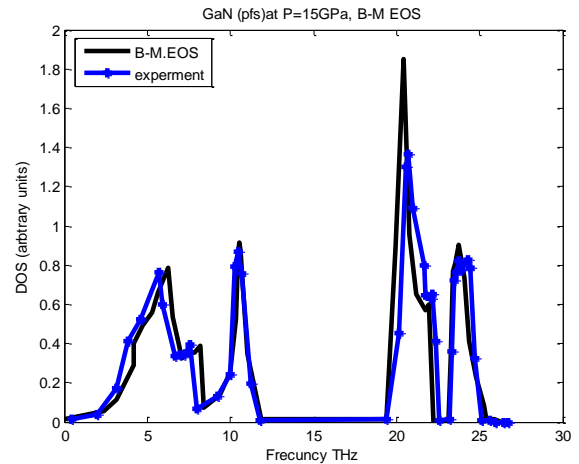
Figure 5. phonon frequency spectrum for GaN under pressure P=15 GPa using a- B-MEOS b-mL-JEOS compared with [16].

Figure (4) represents 'pfs' for GaN at atmospheric pressure and '0 K'. This section involves calculation of the effect of high pressure on pfs at different values of pressure 15Gpa and 30Gpa, using two equation of state "B-M EOS and mL-J EOS".

Given that value of (V_P/V_o) under pressures (15Gpa and 30Gpa), has already known in fig.1. Then combing the data of fig.4 with eqs. (9 and 12), the results for variation of "pfs" for GaN under high pressure using two equations" B-MEOS and mL-JEOS" has obtained and shown in figs. (5-6).

(a)

(b)
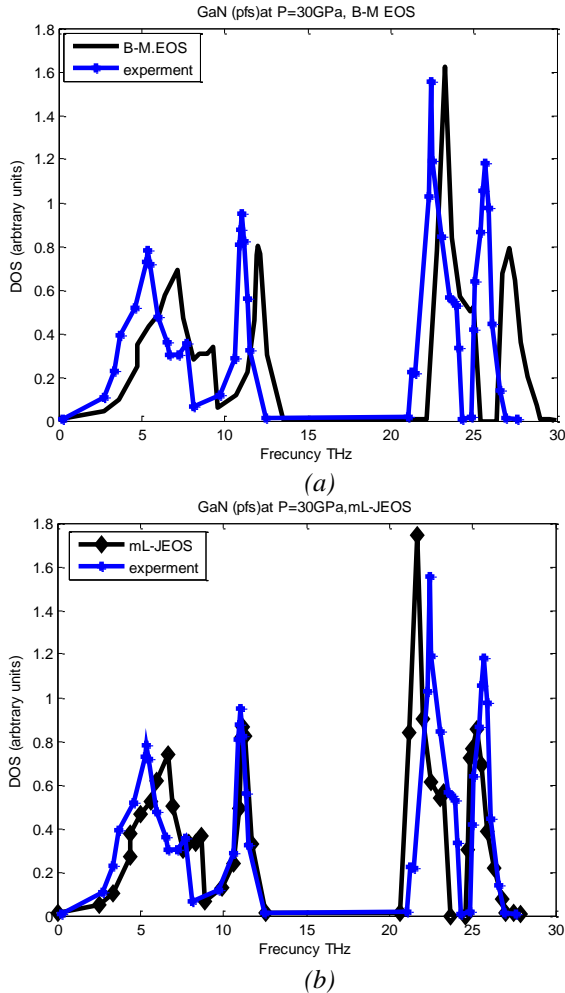
Figure 6. phonon frequency spectrum for GaN under pressure P=30GPa using (a) B-MEOS (b) mL-J EOS, compared with experimental data [16].

4. Grüneisen parameter

"The Grüneisen parameter (γ) is of considerable importance to earth scientist because it sets limitations on the thermo elastic properties of the lower core and mantle [16]. It is dimensionless and used for wide range of solid, it has an approximately constant value and varying slowly with high pressure [17]as will be seen later in fig.6.

4.1 Grüneisen parameter under high pressure

The microscopic definition of Grüneisen parameter describes the vibrational motion of atoms. As the oscillation of atoms changes with high pressure so does the Grüneisen parameter. High pressure dependence of Grüneisen parameter is expressed by the following relation [19]:

$$\gamma_P = \gamma_0 \left(\frac{V_P}{V_0} \right)^q \tag{11}$$

where γ_o : Grüneisen parameter at atmospheric pressure.
γ_P : Grüneisen parameter under high pressure.
q: Second Grüneisen parameter, q has been considered to equal unity.

Using γ_o value in table 1 and combining V_P/V_O value from fig.2 in to eq. (11), we get γ_P which declines slowly with increasing pressure. As it can be observed that even at the highest pressure (45Gpa), the Grüneisen parameter is reduced to approximately 1.
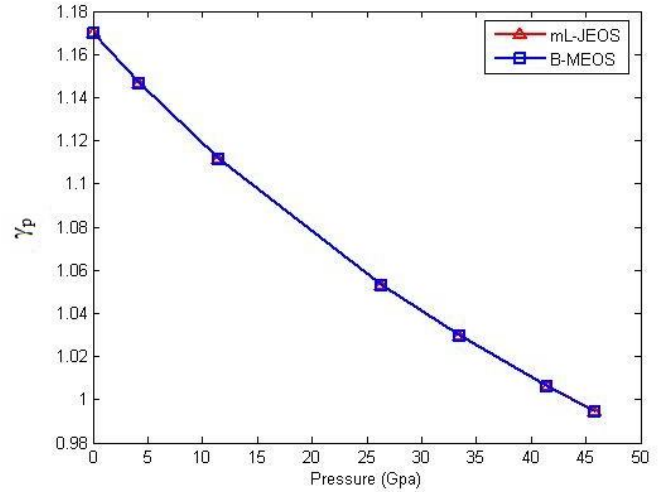
Figure 7. Variation of Grüneisen parameter with high pressure.

4.2 Calculation of pfs, using effect of pressure on Grüneisen parameter

Accounting the effect of pressure on "γ_o", we can get the theoretical results in calculating pfs, which approach to the experiment data [16] better than in the above calculation when we assumed "γ_o" is pressure independent.

Figs (5 & 6) show the different results for "pfs" under high pressure using two different equations of state "B-M EOS and mL-J EOS". Combining equations (9 and 10) with with γ_P in eq. (11) to get two new form of equations for evaluating v_P and g_P (v_P, V_P):

$$v_{P\gamma} = v_0 \left(\frac{V_P}{V_0} \right)^{-\gamma_P} \tag{12}$$

$$g_{P\gamma}(v_P, V_P) = g_0(v_0, V_0) \left(\frac{V_P}{V_0} \right)^{-\gamma_P} \tag{13}$$

Eqs.(12 and 13) are implemented to obtain improved results for analyzing pfs, under strong compression.
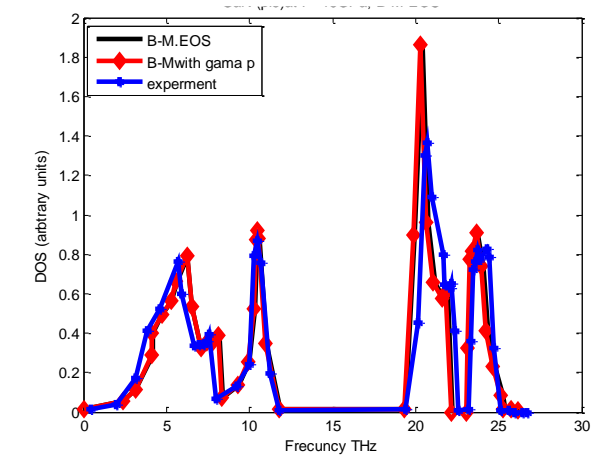
(a)
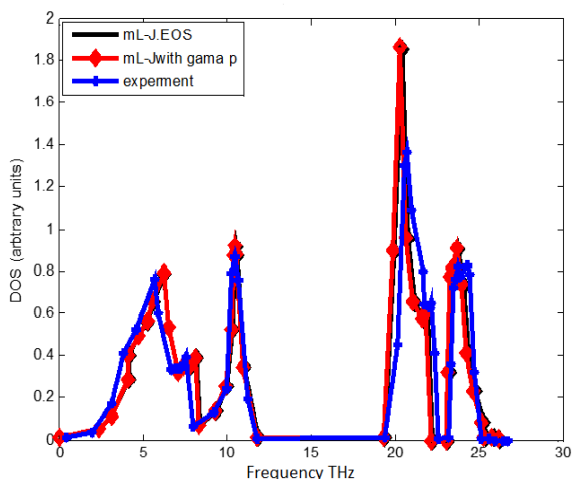
(b)

Figure 8. phonon frequency spectrum for GaN under pressure P= 15 GPa using (a) B-M EOS (b) mL-J EOS on considering the effect of pressure on γ, and compared with experimental data [16].

5. Discussion

The current study implements the use two universal EOS to describe, influence of pressure the volume compression ratio, bulk modulus and phonon frequency spectrum of GaN semiconductor. The results of V_P/V_0, Bulk modulus and γ parameter, calculated with the two EOSs are viewed to be similar and the curves are fit on each other due to very small divergence of their data, over the entire pressure range up to an enormous level 45Gpa. Accordingly, the two equations of state are seen as a two identical EOSs. However, when the result of volume compression ratio from fig.1 was combined with eq.12 and eq.13, for calculating pfs, the two EOSs have given different results as can be observed from figs.8 & 9.

It is clear that the γ pressure dependence considerations has effects on the trend of pfs variations. When γ was assumed pressure dependent, the obtained results of pfs with the EOSs indicated in figs 8-9, were improved and fitted the experimental data better than that of figs.5-6.

By comparing of the results in the present work with experimental result [16] we got an excellent agreement for evaluation "pfs" under high pressure up to 15GPa by using the above two equations, but when the pressure was exceeded to 30GPa, we got different results. Consequently, we treated this concern by assuming the effect of pressure on γ.
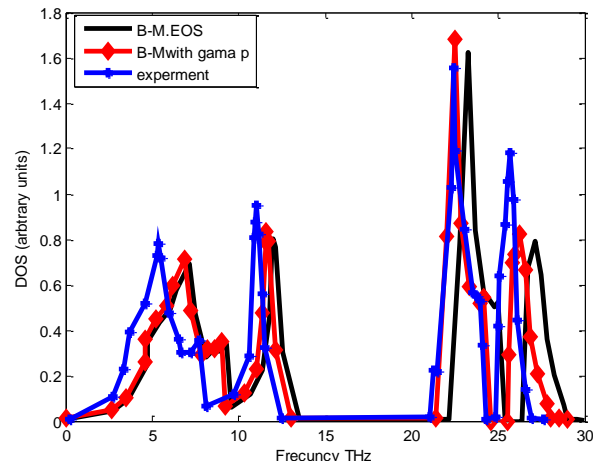
(a)
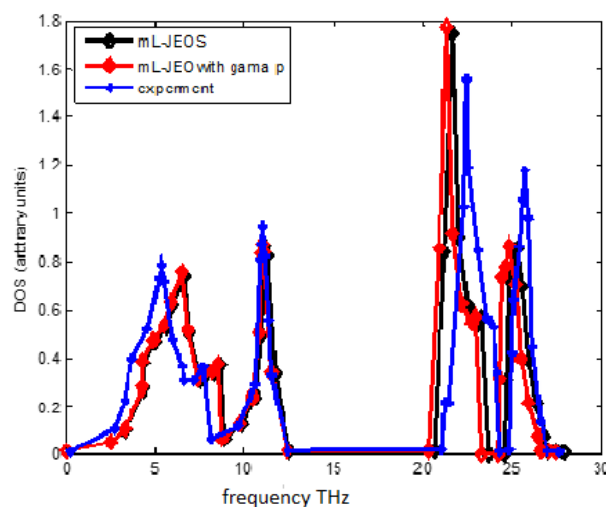
(b)

Figure 9. phonon frequency spectrum for GaN under pressure P=30GPa, using (a) B-M EOS. (b) mL-J EOS, where γ is assumed pressure dependent. Compared with experimental data represented with blue line [16].

6. Conclusion

The variation of "pfs" for GaN has been evaluated by using two equation of state for solids "B-MEOS and mL-JEOS", one time with γ without effect of pressure Figs. (4,5), and second time with effect of pressure on γ up to 30 GPa Figs. (7,8). The present work displays that BM EOS is more suitable and give very good agreement results with (Herriman et al. 2018) compared with mL-JEOS for range of pressure up to 30 GPa when using $γ_p$, Figs. (7,8), the reason of the different conclusion between results of two equations that B-M EOS based on mechanical properties of solid but mL-JEOS based on inter atomic potential.

7. Nomenclature

GaN	Gallium arsenide
V_P/V_0	Volume compression ratio
V_0	Volume at ambient condition
V_P	Volume under high pressure
EOS	Equation of state
a	Lattice parameter
$γ_o$	Grüneisen parameter
$γ_P$	Grüneisen parameter
B_o	Bulk modulus
$g_o(ν_o, V_o)$	Phonon density of state at ambient condition

gₚ(νₚ,Vₚ) — placeholder

$g_P(\nu_P, V_P)$ Phonon density of state at high pressure

pfs   phonon frequency spectrum

References

[1] K.M. Benali, "First-Principles study of structural, elastic and electronic properties of AlN and GaN semiconductors under pressure effect and magnetism in AlN:Mn and GaN:Mn systems," PhD. Thesis. Abou-bakrbelkaiduniversity – *Tlemcen faculty of sciences-Physics department*, 2004.

[2] M. Ferhat, A.Zaoui, M.Certier and B. Khelifa, " Empirical tight- binding band structure of zinc-blende nitrides GaN, AlN, and BN," *Phys. Stat. sol. (b)* 195, 415,1996.

[3] S. Berrah, H. Abid, A. Boukortt and M. Sehil, "Band gap of cubic AlN, GaNandInN compounds under pressure," *Turk J Phys.* 30, 513-518, 2006.

[4] S.K. Jalal, A.M. Al-Sheikh, R.H. Al-Saqa, " High Pressure Effects on the Phonon Frequency Spectrum of Silicon Nanoparticle,"*Iran J Sci Technol Trans Sci* 45, 391–396 , 2021.

[5] S. K. J, S. mawood, "Size dependent thermodynamic properties of nanoparticles, " *International Journal of Thermodynamics*, Vol. 23 (No. 4), 245-250,2020.

[6] R. J. Angel, F. Miozzi, M. Alvaro," Limits to the Validity of Thermal-Pressure Equations of State" *Minerals* 9, 562,2019.

[7] F. Birch, "Finite elastic strain of cubic crystals," phys. Rev. 71 ; 809 – 824,1947

[8] S. Jiuxun, " A modified Lennard-Jones type equation of state for solids strictly satisfying the spinodal condition," J. Phys.: *Condens. Matter* 17; L103-L111,2005.

[9] I. O. Radi; , M.A.Abdulsatter; M. Abdul-Lettif," Semiemperical LUC- INDO calculations on the effect of pressure on the electronic structure of diamond," *Phys. Stat. Sol.* b, 244(4), 1304-1317,2007.

[10] S. K. Jalal, A. M. Al-Sheikh, "heoretical High Pressure Study for Thermoelastic Properties of NaCl-B1. *Raf. J. Sci.*, Vol. 25, No.3, pp. 80- 89, 2014.

[11] F. D. Murnaghan, "Finite deformations of an elastic solid," *Am. J. Math.,*49. 235- 260,1937.

[12] S. Adachi, "Properties of Group IV, III-VI and II-VI semiconductors," Wiley, N. Y., chap.2,2005.

[13] N.E.Christensen and I. Gorczyca,"Optical and structural properties of III-V nitrides under pressure," *Physical Review B.* 0163-1829/94/50(7)/4397(19), 1994.

[14] Xiao-wei Sun et al, "Heat Capacity and GrÄuneisen Parameter for GaN with Zinc-Blende Structure" Chinese journal of chemical physics,(20),3,2007.

[15] A. M.AL-sheikh, R. H. AL-Saqa, "Evaluation of High Pressure Effect of Phonon Frequency Spectrum for Gold by Using Different Equations of State (EOS), " Global Proceedings Repository, *American Research Foundation*, http://proceedings.sriweb.org ISSN 2476-017X, pp 58-278, 2019.

[16] J. E. Herriman, O. Hellman, and B. Fultz, "Phonon thermo dynamics and elastic behavior of GaN at high temperatures and pressures," *physical review B* 98, 214105,2018.

[17] R. H. AL-Saqa, S. J. AL-Taie, "Theoretical Study of Mechanical, Elastic and Phonon Frequency Spectrum Properties for GaAs at High Pressure,"*Journal of Siberian Federal University. Mathematics & Physics*, 12, (**3**), 371–378,2019.

[18] D. L. Anderson,"Theory of the Earth. Blackwell Scientific Publications, " Oxford, UK,1989.

[19] R. Boehler; J.Ramakrishnan, "Experime ntal results on the pressure dependence of the Grüneisen parameter," A review. *J. Geophy. Res.,* 85 (B12), 6996-7002,1980.

Thermodynamic Analysis of a Semi-Closed Oxy-fuel Combustion Combined Cycle

R. P. Furtado[1*], R. P. Bereche[2], A. D. Rocha[3,] A. G. Gallego[4]

[1,2,3,4]Center of Engineering, Modeling and Applied Social Sciences, Federal University of ABC, Santo André, Brazil
E-mail: [1]rafaelpinho45@gmail.com, [2]reynaldo.palacios@ufabc.edu.br, [3]a.damiani@ufabc.edu.br, [4]a.gallego@ufabc.edu.br

Abstract

Semi-closed oxy-fuel combustion combined cycle (SCOC-CC) is a strong concept of carbon capture and storage (CCS) in gas-fired power plants. This technology is similar to a conventional combined cycle, however oxygen instead of air is used in fuel combustion. In the oxy-fuel combined cycle, the gas turbine flue gases consist mainly of CO_2 and H_2O. One of the problems to implement this technology is the necessity of an air separation unit (ASU) to separate the oxygen from the air, which increases the energy consumption of the power plant. Thus, a comparative thermodynamic analysis was performed between a conventional combined cycle (base case) and an oxy-fuel combined cycle. The objective is to identify each technology's pros and cons, the influence of oxygen purity in the oxy-fuel combine cycle, and the main irreversibilities of each case. The SCOC-CC optimal operating point (maximum energy efficiency) was found utilizing particle swarm optimization (PSO), which lead to the optimal ASU oxygen purity of 95.99%. It was noticed that the oxy-fuel combined cycle first law efficiency is 6.9% lower than the base case, and the second law efficiency is 6.5% lower. Despite the efficiency loss the SCOC-CC is more environmentally friendly than the conventional combined cycle since it can theoretically capture all CO_2 produced in the combustion chamber.

Keywords: Oxy-fuel; SCOC-CC; thermodynamic analysis; CCS; PSO.

1. Introduction

Global warming and greenhouse gases emissions are the most significant environmental concerns nowadays. Carbon dioxide (CO_2) represented 81% of greenhouse gas emissions in 2019 [1]. The electricity and heat production sectors will remain heavily dependent on fossil fuels for the foreseeable future. For this reason, it is a need to find ways to reduce greenhouse gas emissions in thermal power plants. Oxy-fuel combustion is a promising carbon-capture technology in fossil-fueled power plants, as it can capture up to 98% of the CO_2 produced in the combustion process, depending on the purification technique applied to remove CO_2 from the flue gas, which contains between 75 mol% and 90 mol% of CO_2 (dry basis), with nitrogen, oxygen, and argon as the major contaminants [2]. The oxy-fuel process utilizes nearly pure oxygen instead of air to burn the fuel. The combustion of a fuel with almost pure oxygen has a combustion temperature of about 3000°C, which is too high for conventional power plant materials. The combustion temperature is limited to approximately 1300-1400°C in a typical gas turbine cycle and about 1900°C in a coal-fired boiler using current technology; thus, a part of the flue gases is recycled to the combustor to control the combustion temperature [3]. An air separation unit (ASU) is required in the power plant to obtain pure oxygen for combustion. Three main technologies are used to separate oxygen from the air: cryogenic distillation, adsorption using multi-bed pressure swing units, and polymeric membranes. The adsorption system would be the most appropriate technology for oxy-fuel processes that require less than 200 tonnes of O_2 per day, while cryogenic distillation would be the most appropriate for larger applications [4]. The cryogenic distillation is the most

mature and reliable among the aforementioned technologies, as it has been in practice for over 75 years [5]. Nevertheless, the main issue in oxy-fuel power plants is the high energy consumption of the ASU and the treatment of captured CO_2. When combined, they can decrease the LHV (lower heating value) efficiency to about 10% [6].

The design of a semi-closed oxy-fuel combustion combined cycle (SCOC-CC) is very similar to a conventional combined cycle (CC), except for near-to-stoichiometric combustion with oxygen instead of air in the gas turbine. The gas turbine flue gases, consisting mainly of CO_2 and H_2O, supply energy to the heat recovery steam generator (HRSG), producing steam for the bottoming Rankine cycle. After the HRSG, the water in the flue gases is separated; then, most of the CO_2 is recycled back to the gas turbine, while the remaining CO_2 is purified and compressed for storage [7].

In this paper, a comparative analysis between a base case and an oxy-fuel combined cycle power plant is performed. The main goals of this comparison are: identifying the optimal operation point (maximal energy efficiency) of the SCOC-CC, the influence of oxygen purity on the oxy-fuel system, and identifying the main irreversibilities that occur in each case. Both cases were modeled on Engineering Equation Solver (EES) and optimized with particle swarm optimization algorithm (PSO) in Matlab.

2. Methodology

In this article, it was proposed to carry out a comparative analysis between a CC and a SCOC-CC. In the analysis, some characteristics were considered the same: a) turbine

inlet temperature (TIT); b) fuel composition and consumption; c) condenser pressure.

2.1 Thermodynamic Analysis

The thermodynamic analysis was performed through mass balance, Eq. (1); energy balance, Eq. (2); and exergy balance Eq. (3). A control volume eclosing each component is at steady-state, and kinetic and potential energy effects are negligible.

$$\left(\sum \dot{m}_i\right)_{out} = \left(\sum \dot{m}_i\right)_{in} \tag{1}$$

$$0 = \dot{Q} - \dot{W} + \left(\sum \dot{m}_i h_i\right)_{in} - \left(\sum \dot{m}_i h_i\right)_{out} \tag{2}$$

$$0 = \sum \left(1 - \frac{T_0}{T}\right) \dot{Q} - \dot{W} - \left(\sum \dot{m}_i ex_i\right)_{in} - \left(\sum \dot{m}_i ex_i\right)_{out} - \dot{I} \tag{3}$$

where $\dot{m}$ is mass flow rate (kg/s); i is state point or index i; $\dot{Q}$ is thermal energy rate (kW); $\dot{W}$ is power (kW); h is the specific enthalpy (kJ/kg); T_0 reference temperature (298K); T is temperature (K); ex is specific exergy (kJ/kg); $\dot{I}$ is the exergy destruction rate or irreversibility (kW).

The specific exergy Eq. (4) is composed of the physical exergy Eq. (5) and chemical exergy Eq. (6). The fuel exergy is calculated by Eq. (7) and the ratio of standard Chemical exergy and lower heating value of fuel by Eq. (8) [8].

$$ex = ex_f + ex_{ch} \tag{4}$$

$$ex_f = (h - h_0) - T_0(s - s_0) \tag{5}$$

$$ex_{ch} = \sum \left(x_i ex_{ch,i,0} + R_i T_0 (y_i \ln y_i)\right) \tag{6}$$

$$ex_{fuel} = \beta * LHV \tag{7}$$

$$\beta = 1.034 + 0.0183 \left(\frac{H}{C}\right) - 0.064 \left(\frac{1}{C}\right) \tag{8}$$

where ex_f is physical exergy (kJ/kg); ex_{ch} is chemical exergy (kJ/kg); h_0 is enthalpy in reference condition (kJ/kg); s_0 is entropy in reference condition (kJ/kg-K); s is entropy (kJ/kg-K); x_i is the mass fraction of each component i; y_i is the molar fraction of of each component i; $ex_{ch,i,0}$ is standard chemical exergy (kJ/kg); R_i is the gas constant of each component i; (kJ/kg-K); H is the number of hydrogen atoms in the fuel; C is the number of carbon atoms in the fuel.

The performance of each system is evaluated using energy efficiencies Eq. (9) and exergy efficiency Eq. (10), as well as the specific CO_2 production from the natural gas combustion Eq. (11).

$$\eta_I = \frac{W_{GT,net} + W_{ST,Net}}{m_{fuel} LHV} \tag{9}$$

$$\eta_{II} = 1 - \frac{I_{tot}}{m_{fuel} ex_{fuel}} \tag{10}$$

$$Em_{CO2} = \frac{m_{CO2,tot}}{W_{GT,Net} + W_{ST,Net}} \tag{11}$$

where $W_{GT,net}$ is the net power of gas turbine cycle (kW); $W_{ST,net}$ is the net power of steam cycle (kW); m_{fuel} is the fuel mass flow

(kg/s); LHV is the lower heating value of fuel (kJ/kg); Em_{CO2} specific CO_2 produced in the combustion process (g/kWh); $m_{CO2,tot}$ total CO_2 produced (g/h), I_{tot} is the total plant irreversibility (kW).

2.2 Semi-closed oxy-fuel combustion combined cycle

The SCOC-CC is presented in Figure 1. In this cycle, CO_2 (stream 1) is compressed until the combustion chamber pressure (stream 2). Then this CO_2 stream, fuel (stream 6) and oxygen provided by the ASU (stream 9) are fed in the combustion chamber. The combustion products (stream 3) are expanded in the GT turbine (stream 5), and the flue gases provide heat for a steam cycle trough an HRSG. The water present in the flue gases is then removed in the dehumidifier. Then the CO_2 (stream 13) is divided in two streams, about 90% of stream 13 mass flow is recycled to the gas turbine compressor (stream 16), and the other part is compressed (stream 14) and captured (stream 15).
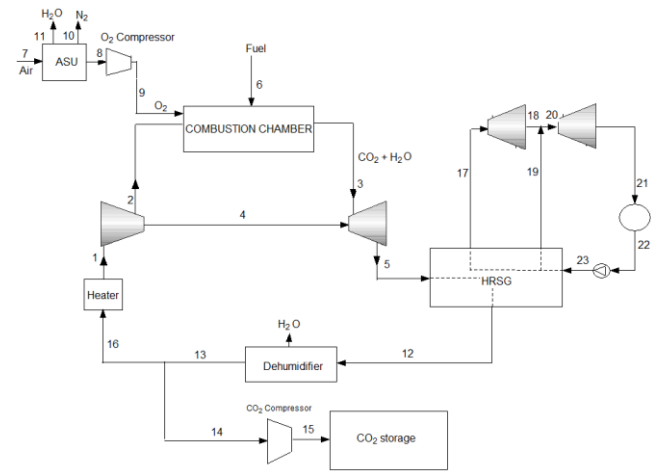
Figure 1. SCOC-CC.

The O_2 purity is an important parameter for oxy-fuel combustion power plants as purer oxygen streams increase ASU energy consumption, decreasing power plant efficiency. On the other hand, an oxygen stream with low oxygen purity will produce flue gases with more impurities, and it can result in an increase in the cost and energy consumption of the CO_2 treatment and compression unit [2]. Hu et al. [9] parameterized the specific energy consumption of ASU by cryogenic distillation as a function of oxygen purity. For oxygen purity equal or lower than 97 mol% the Eq. (12) is used, for purities greater than 97 mol% Eq. (13) is used. The molar composition of the oxygen stream supplied by the ASU is shown in Table 1 for different values of y_{O_2}. The oxygen leaves the ASU at 1.013bar and 27°C.

Table 1. Oxygen composition [9].

O_2	0.850	0.860	0.870	0.880	0.890	0.900	0.910
Ar	0.038	0.038	0.038	0.039	0.039	0.039	0.039
N_2	0.112	0.102	0.092	0.081	0.071	0.061	0.051
O_2	0.920	0.930	0.940	0.950	0.960	0.970	0.980
Ar	0.040	0.040	0.041	0.041	0.040	0.030	0.020
N_2	0.040	0.030	0.019	0.009	0	0	0

$$e_{ASU} = 92.3103 + 8.2457 \, y_{O_2} \tag{12}$$

$$e_{ASU} = 383.3773/(100 - y_{O_2})^{0.4577} + 660.0583 \tag{13}$$

where e_{ASU} is ASU specific energy consumption (kJ/kg); y_{O_2} is oxygen purity (mol%).

The isentropic and polytropic efficiencies utilized for the compressors, turbines and pumps are shown in Table 2 [11]. The isentropic efficiency is calculated by Eq. (14) for compressors and pumps and by Eq. (15) for turbines [12]. The compressions of CO_2 and O_2 are done in 3 stages with intercooling to reduce the compressors energy consumption, according to Figure 2. The fuel composition and LHV are presented in Table 3.

Table 2. Compressors and turbines efficiencies [11][12].

Equipment	$\eta_{polytropic}$	$\eta_{isentropic}$
GT Turbine	0.87	-
GT Compressor	0.87	-
Water pumps	-	0.75
CO_2/O_2 Compressors	0.85	-
High-pressure steam turbine	-	0.92
Low-pressure steam turbine	-	0.89

$$\eta_{isen} = \frac{h_{out,iso} - h_{in}}{h_{out} - h_{in}}$$
$$= \frac{\left(P_{out}/P_{in}\right)^{\frac{(\gamma-1)}{\gamma}} - 1}{\left(P_{out}/P_{in}\right)^{\frac{\eta_{pol}(\gamma-1)}{\gamma}} - 1} \quad (14)$$

$$\eta_{isen} = \frac{h_{in} - h_{out}}{h_{in} - h_{out,iso}}$$
$$= \frac{1 - \left(P_{out}/P_{in}\right)^{\frac{\eta_{pol}(\gamma-1)}{\gamma}}}{1 - \left(P_{out}/P_{in}\right)^{\frac{\gamma-1}{\gamma}}} \quad (15)$$

where h_{in} is the inlet enthalpy (kJ/kg); h_{out} is the outlet enthalpy (kJ/kg); $h_{out,iso}$ is the outlet isentropic enthalpy (kJ/kg); P_{out} is the outlet pressure (bar); P_{in} is the inlet pressure (bar); η_{pol} is the polytropic efficiency; γ is the heat capacity ratio.

The bleed air mass flow (stream 4) needed to cool the GT turbine blades has been determined by Eq. (16) [9].

$$\dot{m}_{cooling} = 4.6 \times 10^{-8}(TIT+273.15)^2 + 1.47897 \times 10^{-5}(TIT+273.15) - 0.06928 \quad (16)$$

where $\dot{m}_{cooling}$ is the bleed air mass flow (kg/s); TIT is the GT turbine inlet temperature (°C).

This study assumed that combustion is stoichiometric, and it is given by Eq (17). A pressure drop of 3% was assumed in the combustion chamber. The electric generators efficiency is 98.5% [13].

Table 3. Fuel composition and fuel LHV [8].

Fuel composition (mol %)	
CH_4	89%
C_2H_6	7%
C_3H_8	1%
C_4H_{10}	0.1%
C_6H_{14}	0.001%
CO_2	2%
N_2	0.899%
Fuel LHV (kJ/kg)	46480
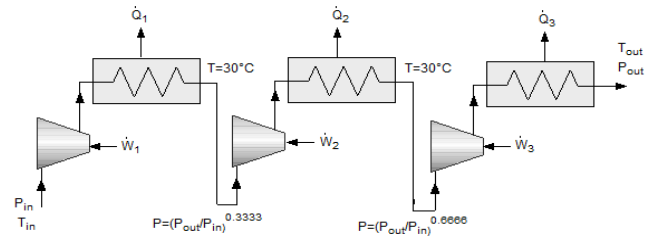
Figure 2. Compressions of CO_2 and O_2.
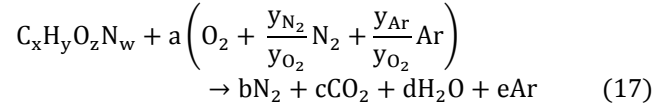
$$C_xH_yO_zN_w + a\left(O_2 + \frac{y_{N_2}}{y_{O_2}}N_2 + \frac{y_{Ar}}{y_{O_2}}Ar\right) \rightarrow bN_2 + cCO_2 + dH_2O + eAr \quad (17)$$

where x, y, z, w are, respectively, the number of atoms of carbon, hydrogen, oxygen and nitrogen in the fuel; a, b, c, d, e are stoichiometric coefficients; y_{N_2}, y_{O_2}, y_{Ar} are the molar fractions of the nitrogen, oxygen and argon provided by the ASU.

The HRSG of the SOCC-CC and the CC has two pressure levels, and it consists of three heat exchangers (economizer, evaporator and superheat) for each pressure level. It was considered that the high-pressure level water is pre-heated in the low-pressure economizer, and then it is pumped to the high-pressure economizer. A pressure loss of 40 mbar was assumed on the flue gases side of the HRSG [11]; on the water/steam side, pressures losses were neglected. For HRSG design, the pinch point is between 8-20 °C, and the approach point is between 5-12 °C [14][15]. For the HRSG design, it was considered an approach point of 12° C for low and high-pressure economizers, the pinch point of the low-pressure evaporator is 15° C, and the high-pressure evaporator is 20°C [16]. In addition to the pinch and approach point, a temperature difference of 35° C was considered between the high-pressure steam turbine inlet temperature and the gas turbine exhaust gases on the HRSG inlet. The HRSG temperature distribution is shown in Figure 3. Table 4 presents the usual nominal temperature and pressure ranges for the HRSG.
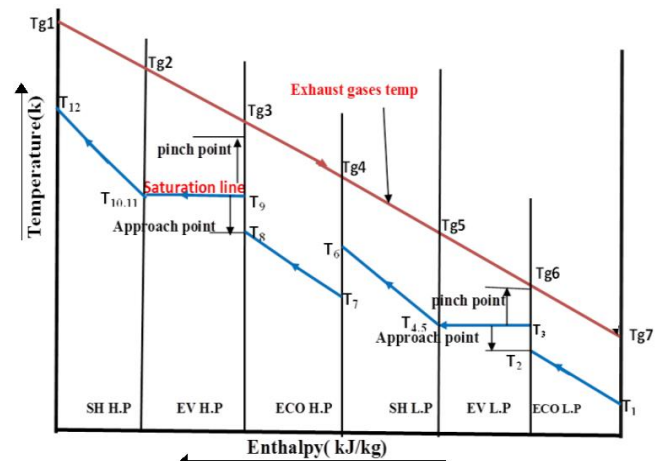
Figure 3. HRSG temperature distribution [17].

Table 4. HRSG usual operational range [18].

High-pressure level	Temperature (°C)	500-565
	Pressure (bar)	55-85
Low-pressure level	Temperature (°C)	200-260
	Pressure (bar)	3-8

Flue gas water is removed in a dehumidifier, where , a pressure loss of 10mbar was assumed. A heater before the

gas turbine compressor is needed to decrease the relative humidity of the CO_2 stream leaving the dehumidifier, this device increases the temperature by 4°C [7]. The condenser, dehumidifier and intercooler compression stages are cooled with water, which enters the equipment at ambient temperature (25 °C) and leaves at 35°C.

The first law efficiency of the SCOC-CC is calculated by Eq. (9), and it can also be determined in function of the input variables: dehumidifier outlet temperature (T_{13}), GT compressor pressure ratio (pr), GT turbine inlet temperature (T_3), fuel and oxygen temperature in the combustion chamber inlet (T_9 and T_6), ASU oxygen purity ($y_{O2_{ASU}}$), low-pressure steam turbine inlet pressure (p_{20}), high-pressure steam turbine inlet pressure (p_{17}), condenser pressure (p_{21}).

The GT compressor pressure ratio for SCOC-CC is in the range of 30-40 [16]. According to [19], the GT turbine inlet temperature can reach temperatures in the range of 1500°C for modern conventional gas turbines. The condenser pressure is 0.088bar [20]. It was considered that the dehumidifier outlet temperature should be in the range of 27-55°C, and fuel and oxygen temperature are 30°C in the combustion chamber inlet.

From the operational limits of the SCOC-CC, it is possible to formulate an optimization problem to maximize the energetic/first law efficiency:

Maximize: $\eta_I = \eta_I\big(T_{13}, pr, T_3, y_{O2_{ASU}}, p_{20}, p_{17}\big)$
Subject to:
$$\begin{cases} 27 \le T_{13} \le 55 \\ 30 \le pr \le 40 \\ 1050 \le T_3 \le 1500 \\ 0.8 \le y_{O2_{ASU}} \le 0.995 \\ 3 \le p_{20} \le 8 \\ 55 \le p_{17} \le 85 \\ 200 \le T_{20} \le 260 \\ 500 \le T_{17} \le 565 \end{cases}$$

where the temperatures and pressures are indexed accordingly to Figure 1.

2.3 Conventional combined cycle
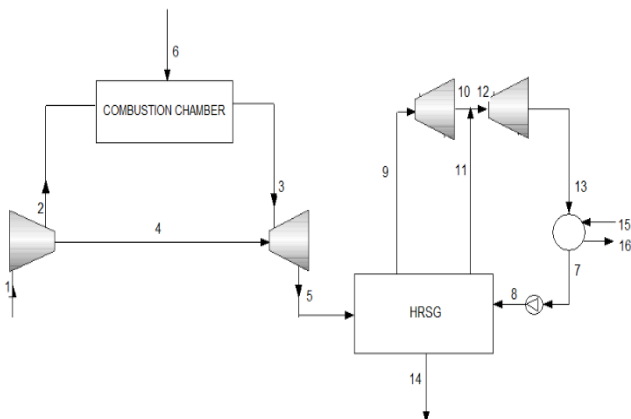
Figure 4. Combined cycle.

Figure 4 shows the conventional combined cycle. The same thermodynamic assumptions were utilized in the CC model. The gas turbine working fluid is air, which enters the GT compressor (stream 1) at 25 °C, 1.013 bar, and relative humidity of 60%, the air is compressed until the combustion chamber pressure (stream 2) and the air and fuel are fed in the combustion chamber. The combustion was also considered stoichiometric, and it is given by Eq. (18). The flue gases (stream 3) are expanded in the GT turbine (stream 5), and after the expansion, the flue gases provide heat for a steam cycle trough an HRSG and are released into the atmosphere (stream 14).
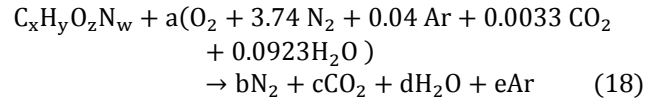
$$\begin{aligned} C_xH_yO_zN_w + a(O_2 + 3.74\,N_2 + 0.04\,Ar + 0.0033\,CO_2 \\ + 0.0923H_2O\,) \\ \to bN_2 + cCO_2 + dH_2O + eAr \end{aligned} \quad (18)$$

where x, y, z, w are, respectively, the number of atoms of carbon, hydrogen, oxygen and nitrogen in the fuel; a, b, c, d, e are stoichiometric coefficients.

For the comparative analysis, the CC GT turbine inlet temperature is the same as the SCOC-CC. The pressure ratio for conventional gas turbines is usually in the range of 5-30 [20]. The following optimization problem finds the optimal efficiency of the conventional CC:

Maximize: $\eta_I = \eta_I(pr, p_9, p_{12})$
Subject to:
$$\begin{cases} 5 \le pr \le 30 \\ 3 \le p_{12} \le 8 \\ 55 \le p_9 \le 85 \\ 200 \le T_{12} \le 260 \\ 500 \le T_9 \le 565 \end{cases}$$

where the temperatures and pressures are indexed accordingly to Figure 4.

2.4 Particle swarm optimization

The optimization problems were solved by particle swarm optimization (PSO). PSO is an optimization algorithm for the solution of nonlinear and linear functions created by [21]. It was inspired by the intelligent behaviour of groups of animals such as swarms, shoals and flocks of birds. PSO is a search technique based on the social behaviour of individuals. This behaviour initially presents a random and disordered search, but an organization in the flight is observed over time, and a search pattern is presented. When the search target is reached, all particles tend to go towards the objective [22].

The PSO population is initialized randomly, over time, the position of the particles is updated based on pre-established rules. The position and velocity of each particle *i* at the iteration *(t+1)*, respectively, are given by Eq. (19) and Eq. (20), respectively. Although there are several proposals for the weight of inertia (*w*), in this work, the weight of inertia by linear decrease is used (Eq. 21) [23].

$$x_i(t+1) = x_i(t) + v_i(t+1) \quad (19)$$

$$\begin{aligned} v_i(t+1) = wv_i(t) + c_1r_1\big(P_{best-i}(t) - x_i(t)\big) \\ + c_2r_2\big(G_{best}(t) - x_i(t)\big) \end{aligned} \quad (20)$$

$$w(t) = w_{max} - \frac{w_{max} - w_{min}}{t_{max}}t \quad (21)$$

where w is the weight of inertia, r_1 and r_2 are random independent variables between 0 and 1, P_{best-i} is the best position found by the particle i, G_{best} the best position found by the swarm, c_1 and c_2 are learning parameters, t_{max} is the maximum number of iterations, w_{max} is the maximum weight of inertia, w_{min} is the minimum weight of inertia.

Table 5 shows the PSO parameters. [24] presented the effect of the number of particles in the swarm for several optimization problems and concluded that 30 particles provide a good trade-off between robustness and speed of convergence. The other parameters of the PSO were obtained from [25] and [23].

Table 5. PSO parameters.

c_1	c_2	Maximum Velocity	Number of particles	Number of iterations	w_{max}	w_{min}
1.5	2.5	4	30	300	0.9	0.4

3. Results

The computacional models of both thermodynamic cycles were validated utilizing the same computacional assumptions as [11]. The first law efficiency obtained for the SCOC-CC in [11] is 47%, in this work, with the same computacional assumptions of [11] an efficiency of 48.28% was obtained, which represents a deviation of 2.74%. For the CC case, [11] obtained a first law efficiency of 57% and in this work an efficiency of 57.74% was obtained, representing a deviation of 1.3%. Considering that different softwares were used for the thermodynamic models development, the difference in the efficiencies obtained is acceptable. In this work, EES was used for the computacional models development and [11] developed their computacional models with SimSCI PRO/II.

Applying the PSO algorithm, the optimal operational points from Table 6 were obtained. The optimization utilizing the ASU model from [9] found that the optimal ASU oxygen purity (y_{O2ASU}) for the SCOC-CC is 95.99 mol%. The SCOC-CC optimal pressure ratio is 40, which is the maximum value from the optimization problem. The SCOC-CC pressure ratio is 3.28 times the CC pressure ratio; this big difference occurs due to the change in the working fluid. Figure 5 shows the variation of the heat capacity ratio (γ) with the temperature of the GT compressor and GT turbine working fluid of the SCOC-CC and CC. It is noticed that the heat capacity ratio is lower in the SCOC-CC compressor and turbine than in the CC case. For this reason, a higher pressure ratio is needed in the SCOC-CC to obtain a similar temperature drop as in the CC. In this way, the influence of the heat capacity ratio is the main reason for the higher-pressure ratio needed in the SCOC-CC.

Table 6. PSO optimization results.

	T_{13}	pr	T_3	y_{O2ASU}	p_{19}	p_{17}
	(°C)		(°C)	(mol%)	(bar)	(bar)
SCOC-CC	33.017	40	1223	95.99	5.71	85
	-	pr	T_3	-	p_{12}	p_9
			(°C)		(bar)	(bar)
CC	-	12.18	1223	-	5.93	85

The SCOC-CC efficiency obtained from the optimal point is 45.55%. The properties of each stream of the SCOC-CC at the optimal point and considering a fuel consumption of 1 kg/s are presented in Table 7, and the mass composition of each stream is shown in Table 8, the streams are numbered accordingly to Figure 1.

The CC efficiency obtained from the optimal point is 52.51%. The properties of each stream of the CC at the optimal point and considering a fuel consumption of 1 kg/s are presented in Table 9, and the mass composition of each stream is shown in Table 10, the streams are numbered accordingly to Figure 4.
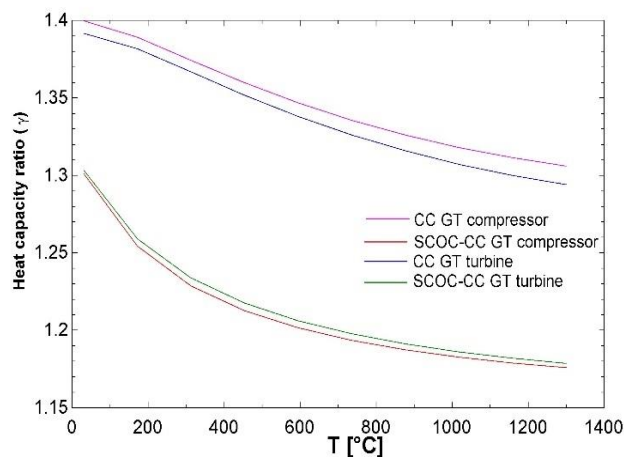
Figure 5. Heat capacity ratio in the GT turbine and GT compressor.

Table 7. SCOC-CC: Properties of each stream.

#	Mass flow (kg/s)	Pressure (bar)	Tempe-rature (°C)	Enthalpy (kJ/kg)	Entropy (kJ/kg.K)	Exergy (kJ/kg)
1	42.6	1.013	37.02	-8433	4.942	0.2004
2	40.4	40.52	450.8	-8017	5.055	382.2
3	45.35	39.71	1223	-7234	6.217	1112
4	2.196	40.52	450.8	-8017	5.055	382.2
5	47.55	1.063	600.2	-8032	6.261	287.1
6	1.00	40.52	30.0			48938
7	17.15	1.013	25.0	-158	6.745	0
8	3.945	1.013	27.0	1.789	6.288	0.00597
9	3.945	40.52	30.0	4.475	5.348	283
10	13.01	1.013	27.0	2.072	6.834	0.00790
11	0.202	1.013	27.0	113.2	0.3949	0.02794
12	47.55	1.023	95.72	-8588	5.336	0.6009
13	45.54	1.013	33.02			
14	2.943	1.013	33.02	-8436	4.931	0.0897
15	2.943	100	30.0	-8439	4.023	268.3
16	42.6	1.013	33.02	-8436	4.931	0.0897
17	6.997	85	565	3553	6.889	1503
18	6.997	5.712	205.8	2864	7.017	776.1
19	1.297	5.712	195	2840	6.968	767.4
20	8.294	5.712	204.1	2860	7.01	774.7
21	8.294	0.0888	43.51	2278	7.237	124.7
22	8.294	0.0888	43.51	182.2	0.6189	2.216
23	8.294	5.712	43.58	183	0.6195	2.795

Table 8. SCOC-CC: Mass composition of each stream.

#	x_{CO_2} (%)	x_{O_2} (%)	x_{Ar} (%)	x_{H_2O} (%)	x_{N_2} (%)
1	91.26	-	6.627	2.112	0.001
2	91.26	-	6.627	2.112	0.001
3	87.23	-	6.335	6.432	0.001
4	91.26	-	6.627	2.112	0.001
5	87.42	-	6.348	6.233	0.001
6	-	-	-	-	-
7	-	21.86	1.365	1.177	75.6
8	-	95.05	4.945	-	0.001
9	-	95.05	4.945	-	0.001
10	-	-	0.300	-	99.7
11	-	-	-	100	-
12	87.42	-	6.348	6.233	0.001
13	91.26	-	6.627	2.112	0.001
14	91.26	-	6.627	2.112	0.001
15	91.26	-	6.627	2.112	0.001
16	91.26	-	6.627	2.112	0.001
17	-	-	-	100	-
18	-	-	-	100	-
19	-	-	-	100	-
20	-	-	-	100	-
21	-	-	-	100	-
22	-	-	-	100	-
23	-	-	-	100	-

Table 9. CC: Properties of each stream.

#	Mass flow (kg/s)	Pressure (bar)	Tempe-rature (°C)	Enthalpy (kJ/kg)	Entropy (kJ/kg.K)	Exergy (kJ/kg)
1	44.01	1.013	25	-169.2	6.741	0
2	41.74	12.33	391	212.1	6.85	349
3	42.74	12.09	1223	46.28	7.959	1085
4	2.26	12.33	391	212.1	6.85	349
5	45.01	1.053	600	-675.5	7.999	290.5
6	1.00	12.33	30			48938
7	7.91	0.088	43.5	182.2	0.6189	2.216
8	7.91	5.93	43.5	183	0.6195	2.817
9	6.56	85.00	565	3553	6.889	1503
10	6.56	5.93	209.6	2871	7.016	783.8
11	1.35	5.93	198.9	2848	6.967	775.1
12	7.91	5.93	207.8	2867	7.007	782.3
13	7.91	0.088	43.5	2278	7.237	124.7
14	45.00	1.013	102	-1234	7.07	9.006

Table 10. CC: Mass composition of each stream.

#	x_{CO_2} (%)	x_{O_2} (%)	x_{Ar} (%)	x_{H_2O} (%)	x_{N_2} (%)
1	0.105	22.92	1.27	1.19	74.52
2	0.105	22.92	1.27	1.19	74.52
3	6.388	13.58	1.24	5.99	72.78
4	0.105	22.92	1.27	1.19	74.52
5	6.074	14.05	1.24	5.59	72.88
6	-	-	-	-	-
7	-	-	-	100	-
8	-	-	-	100	-
9	-	-	-	100	-
10	-	-	-	100	-
11	-	-	-	100	-
12	-	-	-	100	-
13	-	-	-	100	-
14	6.074	14.05	1.24	5.57	72.88

From Tables 7 to 10, some characteristics of the SCOC-CC and CC can be observed:

- The SCOC-CC combustion chamber needs 3.945 kg/s of oxygen (stream 9 - Figure 1) to burn 1 kg/s of fuel, corresponding to 8.5% of the GT compressor inlet mass flow (stream 1 – Figure 1).

- 94% of the SCOC-CC GT exhaust gases (stream 13-Figure 1) are recirculated to the GT compressor. In pipeline transport, CO_2 will be transported at supercritical pressure in the range of 80-150 bar [6]. The remaining 6% (stream 14 and 15 - Figure 1) are compressed to 100 bar in the CO_2 compressor in this work.

- Oxy-fuel GT turbine exhaust mass flow (stream 5-Figure 1) is 5% greater than CC GT, which results in more steam circulating in the Rankine/bottoming cycle.

- The optimal pressure ratio for both cycles corresponds to the maximum GT turbine exhaust temperature allowed (600°C). Since a temperature difference of 35°C was considered between the high-pressure (HP) steam turbine inlet temperature and the GT exhaust gases on the HRSG inlet. The maximum temperature allowed at the HP steam turbine inlet is 565 °C.

The power consumed (-) or produced (+) from each device are shown in Table 11. The SCOC-CC gross power is 45897 kW against 41982 kW of the CC cycle. The ASU, O_2 and CO_2 compressor represent together a power consumption of 13.5% from the 45897-kW of gross power; considering the equipment needed for oxy-fuel combustion, the SCOC-CC net power is 13.2% lower than the CC net power.

As mentioned before, the condensers, dehumidifier and intercooler stages are cooled with water. Table 12 shows the heat removed from each device and the quantity of water for cooling.

Table 11. Power consumption.

Equipment	SCOC-CC Power (kW)	CC Power (kW)
GT Compressor	-17706	-16778
GT Turbine	36249	32851
GT Net Power	18543	15832
LP Pump	-6.29	-6.22
LP Steam Turbine	4830	4661
HP Pump	-80.09	-74.97
HP Steam Turbine	4818	4470
Steam Cycle Net Power	9561	9050
ASU	-3314	-
O_2 Compressor	-1695	-
CO_2 Compressor	-1200	-
Global Net Power	21473	24745

Table 12. Water consumption.

SCOC-CC Equipment	Heat (kW)	Cooling Water (kg/s)
Condenser	-17381	415.5
Dehumidifier	-7588	181.5
CO_2 Compressor intercooled stages	-1208	40.26
O_2 Compressor intercooled stages	-1684	28.87
Total	-29501	666.2
CC Equipment	Heat (kW)	Cooling Water (kg/s)
Condenser	-16581	396.4
Dehumidifier	-	-
CO_2 Compressor intercooler stages	-	-
O_2 Compressor intercooler stages	-	-
Total	-16581	396.4

It is noticed that the water consumption of the SCOC-CC is much higher than the CC consumption since the SCOC-CC has more components that need cooling and more steam flows through its bottoming cycle.

For the irreversibilities of each cycle components, an exergetic analysis was performed. Table 13 shows the exergy fuel and product, irreversibility and second law efficiency of the SCOC-CC components. The second law efficiency of the components is given by Eq. 22.

$$\eta_{II} = \frac{\text{Prod}}{\text{Fuel}} \qquad (22)$$

where Prod is the exergy product (kW), Fuel is the exergy fuel (kW).

From Table 13, it is observed that the SCOC-CC second law efficiency is 45.67%. It is highlighted that the oxygen production in the ASU is very irreversible, and the ASU second law efficiency is 0.004%. Figure 6 shows the contribution of each piece of equipment to the global irreversibility of the plant. The most irreversible components of the SCOC-CC are the Combustion chamber, ASU, HRSG, GT compressor and GT turbine. The ASU, heater, dehumidifier, CO_2 and O_2 compressors combined correspond to 16.43% of the total SCOC-CC irreversibilities.

Table 14 shows the exergy fuel, exergy product, irreversibility and second law efficiency of the CC components. The CC second law efficiency is 52.2 %, which is 6.5% greater than the SCOC-CC.

Table 13. SCOC-CC: Components Irreversibility.

Equipment	Fuel (kW)	Product (kW)	Irreversibility (kW)	η_{II} (%)
GT Compressor	17706	16272	1434	91.9
Combustion Chamber	48938	33875	15063	69.2
GT Turbine	37624	36249	1375	96.3
GT Generator	18543	18265	278.1	98.5
HRSG	13620	11489	2131	84.4
HP ST	5087	4818	269.1	94.7
HP ST Generator	4818	4745	72.27	98.5
LP ST	5391	4830	560.5	89.6
LP ST Generator	4830	4758	72.45	98.5
Condenser	1016	285.1	731	28.1
LP Water pump	6.293	4.799	1.494	76.3
HP Water pump	80.09	78.05	2.035	97.5
Dehumidifier	888.4	124.6	763.8	14.1
Heater	5.626	4.716	0.9094	83.8
ASU	3314	0.132	3314	0.004
O_2 Compressor	1783	1493	290.3	83.7
CO_2 Compressor	1284	1056	227.8	82.3
Global			26,586	45.7

*HP ST= High-pressure steam turbine, LP ST= Low-pressure steam turbine
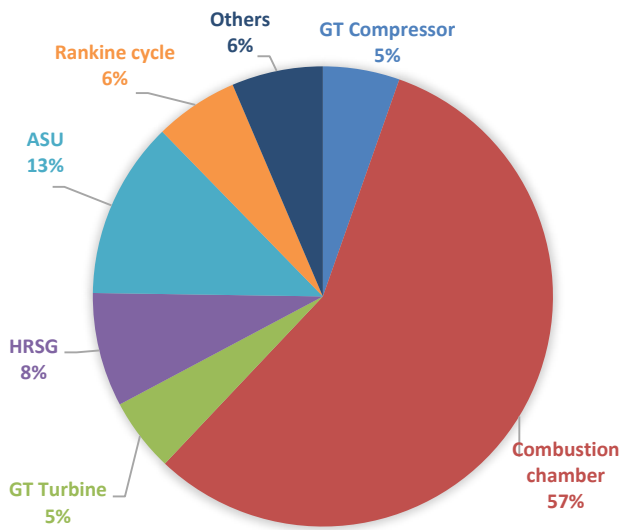
Figure 6. SCOC-CC: Irreversibilities.

Figure 7 are shown the contribution of each piece of equipment to the global irreversibility of the CC. The most irreversible components are the combustion chamber, HRSG, GT compressor and GT turbine. The global irreversibility of the SCOC-CC is 26586 kW against 23394 kW of the CC.

The GT turbine, GT compressor and steam turbines irreversibility are smaller in the CC cycle. In contrast, the combustion chamber of the CC cycle is more irreversible than the SCOC-CC combustion chamber.

Table 14. CC: Components Irreversibility.

Equipment	Fuel (kW)	Product (kW)	Irreversibility (kW)	η_{II} (%)
GT Compressor	16778	15355	1423	91.5
Combustion Chamber	48938	31811	17127	65.0
GT Turbine	34094	32851	1243	96.3
GT Generator	16073	15832	241.1	98.5
HRSG	12668	10886	1782	85.9
HP ST	4717	4470	247.1	94.8
HP ST Generator	4470	4403	67.05	98.5
LP ST	5212	4669	543.6	89.6
LP ST Generator	4669	4599	70.03	98.5
Condensator	906.9	272	634.9	29.9
LP Water pump	6.219	4.755	1.465	76.4
HP Water pump	74.97	61.69	13.28	82.3
Global			23394	52.2

*HP ST= High-pressure steam turbine, LP ST= Low-pressure steam turbine

The SCOC-CC specific CO_2 production is 450 g-CO_2/kWh, and theoretically, 100% of the produced CO_2 is captured. The CC produces 390 g-CO_2/kWh and all the CO_2 produced is emitted to the atmosphere. Ferrari et al. [26] obtained a specific CO_2 production of 416 g-CO_2/kWh and 90% of the CO_2 produced is captured. Ferrari et al. [26] reference CC emits 348 g-CO_2/kWh. The specific CO_2 productions obtained in this paper are higher mainly because [26] considered higher TIT (1352 °C), pressure ratio (45) and turbine exhaust temperature (620 °C). Although the SCOC-CC specific CO_2 production in this study and [26] is about 60-70 g-CO_2/kWh higher than the CC.
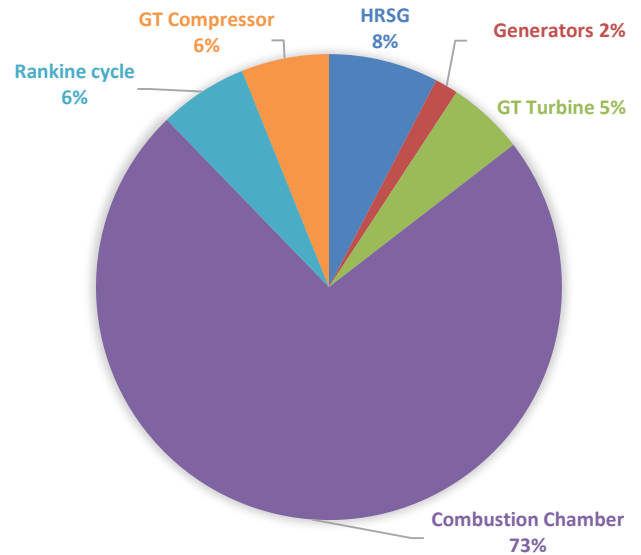
Figure 7. CC: Irreversibilities.

The captured CO_2 can be injected and stored into deep saline aquifers or depleted oil and gas reservoirs or it also be used to enchance recovery of valuable fossil fuels (oil, gas and coalbed methane) [6]. The captured CO_2 can be also used in beverage, medical and food processing industries, however low tolerances of various impurities and CO_2 purity of at least 99.9 vol% are needed in these industries. To achieve higher CO_2 purities, CO_2 purification units should be installed in the plant [2].
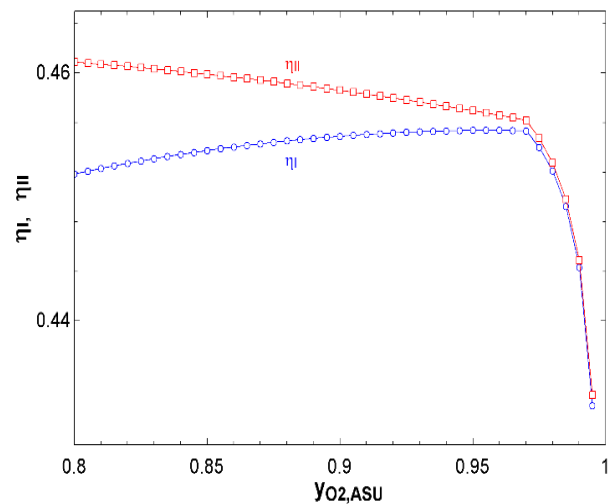
Figure 8. First and second law efficiency vs O_2 purity.

Figure 8 shows the first law efficiency, second law efficiency as a function of the ASU oxygen purity. The first law efficiency increases until the optimal oxygen purity found utilizing the PSO algorithm (95.99%), and after the optimal point ($y_{O2ASU} > 0.9599$), the first law efficiency starts to decrease. The second law efficiency decreases when the oxygen purity is increased since the ASU second law efficiency is small; thus, increasing O_2 purity also increases the ASU energy consumption and irreversibility.

4. Conclusion

The SCOC-CC first law efficiency was found through the particle swarm optimization algorithm, and its optimal first law efficiency is 45.55%, representing a first law efficiency penalty of 6.96% in comparison to CC. The ASU, CO_2 and O_2 consume 13.5% of the SCOC-CC gross power, and the optimal oxygen purity obtained is 95.99%. The SCOC-CC needs more water for cooling than the CC due to the dehumidifier, CO_2, and O_2 compressors intercooler stages. Despite the efficiency loss and higher water consumption, the SCOC-CC is more environmentally friendly since it can capture all or almost all CO_2 produced in the combustion.

Future investigations will highlight the importance of feasibility analysis of the semi-closed oxy-fuel combustion combined cycle presented in this work. It is also essential to investigate the potential usage or storage methods of the captured CO_2.

Nomenclature

Variables
C: number of carbon atoms in the fuel
c_1: learning parameter
c_2: learning parameter
Em_{CO2}: specific CO_2 produced in the combustion process (kg/kWh)
e_{ASU}: ASU specific energy consumption (kJ/kg)
Em_{CO2}: specific CO_2 production (g/kWh)
ex: exergy (kJ/kg)
ex: specific exergy (kJ/kg)
$ex_{ch,0}$: standard chemical exergy (kJ/kg)
ex_{ch}: chemical exergy (kJ/kg)
ex_f: physical exergy (kJ/kg)
G_{best}: best position found by the swarm
H: number of hydrogen atoms in the fuel
h: specific enthalpy (kJ/kg)
h_0: enthalpy in reference condition (kJ/kg)
i: state point or index i
$\dot{I}$: irreversibility (kW)
I_{tot}: total plant irreversibility (kW)
LHV: lower heating value of fuel (kJ/kg)
$\dot{m}$: mass flow rate (kg/s)
$m_{CO2,tot}$: total CO_2 produced (g/h)
m_{fuel}: fuel mass flow (kg/s);
P: pressure (bar)
P_{best-i}: best position found by the particle i
pr: pressure ratio
$\dot{Q}$: thermal energy rate (kW)
R: gas constant (kJ/kg-K);
r_1: random independent variables between 0 and 1
r_2: random independent variables between 0 and 1
s: entropy (kJ/kg-K)
s_0: entropy in reference condition (kJ/kg-K)
T: temperature (K)

t_{max}: maximum number of iterations,
w: weight of inertia
$\dot{W}$: power (kW)
$W_{GT,net}$: net power of gas turbine cycle (kW)
w_{max}: maximum weight of inertia,
w_{min}: minimum weight of inertia.
$W_{ST,net}$: net power of steam cycle (kW)
x: mass fraction
y: mass fraction
y_{O_2}: oxygen purity (mol%)

Greek letters
η_I: first law efficiency
η_{II}: second law efficiency
η_{isen}: isentropic efficiency
η_{pol}: the polytropic efficiency
β: ratio of standard chemical exergy and lower heating value of fuel
γ: heat capacity ratio

Acronyms
ASU: air separation unit
CC: conventional combined cycle
CCS: carbon capture and storage
EES: Engineering Equation Solver
GT: gas turbine
HP ST: high-pressure steam turbine
HRSG: heat recovery steam generator
LHV: lower heating value
LP ST: low-pressure steam turbine
PSO: particle swarm optimization
SCOC-CC: semi-closed oxy-fuel combustion combined cycle
TIT: turbine inlet temperature

References:

[1] The United States Environmental Protection Agency (EPA), *Overview of Greenhouse gases* [Online]. Available: https://www.epa.gov/ghgemissions/overview-greenhouse-gases (accessed May 15, 2021).

[2] L. Zheng, *Oxy-fuel combustion for power generation and carbon dioxide (CO₂) capture*. Elsevier, 2011.

[3] B. Metz et al., *Carbon dioxide and storage: special report of the intergovernmental panel on climate change*. Cambridge University Press, 2005.

[4] M. Wilkinson et al., "Oxyfuel conversion of heater and boilers for CO2 capture" in *2nd Annual Conference on Carbon Sequestration*, Virginia (USA), 2003.

[5] National Energy Technology Laboratory, *Commercial technologies for oxygen production*. Available: https://www.netl.doe.gov/research/Coal/energy-systems/gasification/gasifipedia/commercial-oxygen (accessed May 15, 2021).

[6] M. Maroto-Valer, *Developments and innovation in carbon dioxide (CO₂) capture and storage technology: carbon dioxide (CO₂) capture, transport and industrial applications*. Elsevier, 2010.

[7] S. G. Sundkvist et al., "Concept for a combustion system in oxyfuel gas turbine combined cycles," *Journal of*

engineering for gas turbines and power, v. 136, n.10, 2014.

[8] J. Szargut, D. R. Morris, F.R Steward, *Exergy analysis of thermal, chemical, and metallurgical processes.* New York: Hemisphere, 1988.

[9] Y. Hu, H. Li, J. Yan, "Integration of evaporative gas turbine with oxy-fuel combustion for carbon dioxide capture," *International Journal of Green Energy*, 7(6), 615-631, 2010.

[10] A. Ebrahimi et al., "Energetic, exergetic and economic assessment of oxygen production from two columns cryogenic air separation unit." *Energy* 90, 1298-1316, 2015.

[11] H. M. Kvamsdal, K. Jordal, O. Bolland. "A quantitative comparison of gas turbine cycles with CO2 capture." *Energy* 32.1, 10-24, 2007.

[12] A. M. Y, Razak. *Industrial gas turbines: performance and operability*. Elsevier, 2007.

[13] A. L. Sheldrake, *Handbook of electrical engineering for practitioners in the oil, gas and petrochemical industry*, John Wiley & Sons Ltd, Southern Gate, Chichester, 2003.

[14] O. Bolland, *Thermal Power Generation*, Department of Energy and Process Engineering - NTNU, 2010.

[15] R. Kehlhofer et al., *Combined-cycle gas & steam turbine power plants*. PennWell Books, LLC, 2009.

[16] A. N. Dahlqvist (2016). *Conceptual Thermodynamic Cycle and Aerodynamic Gas Turbine Design-on an Oxy-fuel Combined Cycle* (Doctoral dissertation), Lund University, Sweden.

[17] S. S. Maher, H.A Abid-Al-Rahman, *Design of Dual Pressure Heat Recovery Steam Generator for Combined Power Plants* [Online]. Available: http://conf-scoop.org/IEPEM-2013/11_Maher_IEPEM.pdf (accessed April 15, 2021).

[18] L. Bojici, C. Neaga. "Technical optimization of a two-pressure level heat recovery steam generator." *UPB Sci. Bull. Series D* 74.2, 209-216, 2012.

[19] S. C. Gülen, *Gas turbines for electric power generation*, Cambridge University Press, 2019.

[20] GTW, *Gas Turbine World: 2018 GTW Handbook (Vol. 33),* Pequot Publishing.

[21] R. C. Eberhart, J. Kennedy, "Particle swarm optimization.", *Proceedings of the IEEE international conference on neural networks*, Vol. 4, Citeseer, 1995.

[22] A. F. Silva, A. C. Lemonge, Beatriz S. Lima. "Algoritmo de Otimização com Enxame de Partículas auxiliado por Metamodelos.", *XI Simpósio de Mecânica Computacional, II Encontro Mineiro de Modelagem Computacional, SIMMEC/EMMCOMP,* 2014.

[23] Y. Shi, R. C. Eberhart, "Empirical study of particle swarm optimization.", *Proceedings of the 1999 congress on evolutionary computation-CEC99 (Cat. No. 99TH8406)*. Vol. 3. IEEE, 1999.

[24] I. C. Trelea, "The particle swarm optimization algorithm: convergence analysis and parameter selection.", *Information processing letters* 85.6 (2003): 317-325.

[25] M. Juneja, S. K. Nagar. "Particle swarm optimization algorithm and its parameters: A review.", *2016 International Conference on Control, Computing, Communication and Materials (ICCCCM)*. IEEE, 2016.

[26] N. Ferrari et al., *"IEA GHG R&D programme report: Oxy-turbine power plants"*, 2015.

Thermodynamic Properties of Fluids from Speed of Sound:
Integration Along Isentropes

M. Bijedić[1]*, E. Đidić[2]

[1]Faculty of Technology, University of Tuzla, 8 Univerzitetska Str., 75000 Tuzla, Bosnia and Herzegovina
[2]BNT – Factory of Machines and Hydraulics, 1 Mehmeda Spahe Str., 72290 Novi Travnik, Bosnia and Herzegovina
E-mail: [1]muhamed.bijedic@untz.ba [2]enver.dzidic@bnt-tmh.ba

Abstract

The equations connecting speed of sound with other thermodynamic properties of gases and liquids, suitable for numerical integration with respect to temperature, density, and pressure, along isentropes, are derived. Algorithms of their solution are given too. They are tested with several substances (e.g., Ar, N_2, O_2, CH_4, CO_2, and H_2O) in wide ranges of pressure and temperature. Average absolute deviation of thermal properties is 0.0129% in supercritical gaseous phase, 0.0308% in transcritical gaseous phase, and 0.0009% in liquid phase. Corresponding deviations of caloric properties are 0.1706%, 0.1863%, and 0.0702%, respectively.

Keywords: Thermodynamic properties; fluids; speed of sound, entropy.

1. Introduction

Thermodynamic properties of gases above their critical temperature may be derived from speed of sound if pressure and temperature, or density and temperature, are used as independent variables. In the former case, initial values of dependent variables (e.g., density and isobaric heat capacity) are specified along the lowest temperature at several pressures. In the later case, initial values of dependent variables (e.g., pressure and isochoric heat capacity) are specified along the lowest temperature at several densities. Numerical integration is performed with respect to temperature in both cases, but along isobars and isochores, respectively. When speed of sound is measured in the same pressure range at each temperature, these data are best exploited if integration is performed along isobars [1, 2]. For initial values specified in the same pressure range, integration along isochores will cover wider pressure range [3]. In this case, initial values may also be specified along the lowest density (e.g., in the limit of ideal gas) at several temperatures, and integration performed with respect to density along isotherms [4]. However, in order to retain stability of the solution, boundary values are needed along the lowest temperature(s). The same sets of initial values may be used to carry out integration below critical temperature. In this case, pressure [2] and density [3, 5] are divided by their corresponding values at saturation, at each temperature, and these quantities are used as new independent variables instead of pressure and density, respectively.

When it comes to liquid phase above critical pressure, temperature and pressure are used as independent variables. Initial values of dependent variables (e.g., density and isobaric heat capacity) are specified along the lowest pressure at several temperatures. Numerical integration is performed with respect to pressure along isotherms [6, 7]. The same set of initial values may be used to carry out integration below critical pressure. In this case integration is

performed along paths whose shapes gradually change from that of an isotherm to that of the saturation line [6]. Also, initial values may be specified along the lowest pressure at several temperatures and integration performed along the same paths in opposite direction, or along isotherms with temperature range being extended to the saturation line in each integration step [7]. However, in order to retain stability of the solution in two later approaches, boundary values are needed along the saturation line. Initial values may also be specified along the saturation line and integration performed with respect to pressure along isotherms, but with front of integration having shape of the saturation line rather than that of isobar [6].

If all derivatives appearing in equations connecting speed of sound with other thermodynamic properties (of gases and vapors) are expressed in terms of finite differences [8] or cubic splines [9], the sets of nonlinear algebraic equations are obtained. They can be solved for pressure and heat capacity in very wide ranges of temperature and density. Unlike an approach based on numerical integration, which requires initial values not only of thermal but also of caloric properties (or of thermal ones but of Neumann type), this approach requires only boundary values of thermal properties of Dirichlet type. However, they have to be imposed along overall boundary (e.g., along two isotherms and two isochores).

For initial values specified in the same pressure range, integration along isentropes in gaseous phase will cover wider pressure range than integration along isochores, as one can see from example given at Figure 1. Here, temperature and entropy are used as independent variables.

If density and entropy are used as independent variables, domain of integration could be increased even further, as one can see from example given at Figure 2.

Similarly, for initial values specified in the same temperature range, integration along isentropes in liquid phase will cover wider temperature range than integration

along isotherms, as one can see from example given at Figure 3. Also, isentrope on the left side of integration domain crosses melting line (not seen on the figure) at much higher pressure than corresponding isotherm does. Here, pressure and entropy are used as independent variables.
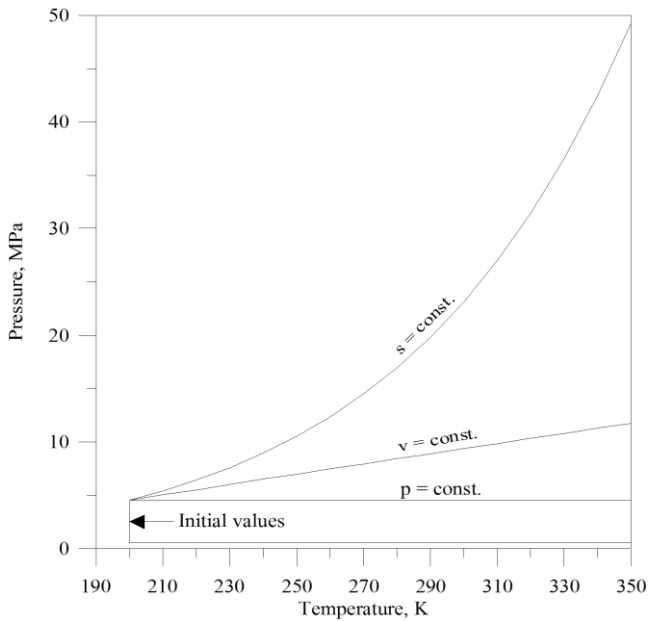
Figure 1. Integration with respect to T at p = const., v = const., and s = const., for methane in gaseous phase [22].
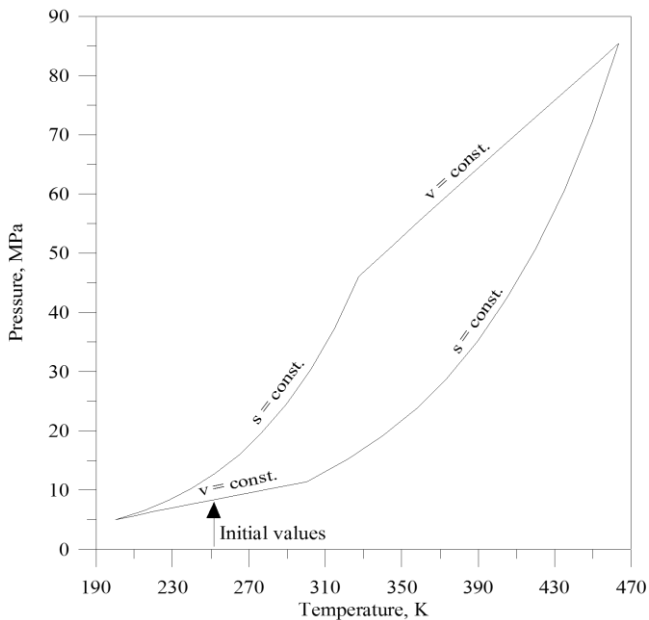
Figure 2. Integration with respect to ρ at s = const., for methane in gaseous phase [22].

Integration with respect to pressure at T = const. in supercritical gaseous phase is not recommended in general, since density increases very quickly with pressure at fixed temperature, and this becomes even more emphasized as critical point is approached. This area of thermodynamic surface could be avoided if integration is conducted at s = const., as one can see from example given at Figure 4.

While entropy is not measurable quantity, it still can be calculated from thermal properties and heat capacity along initial isochore or isobar. Also, it may be used explicitly or implicitly (e.g., in terms of other properties).
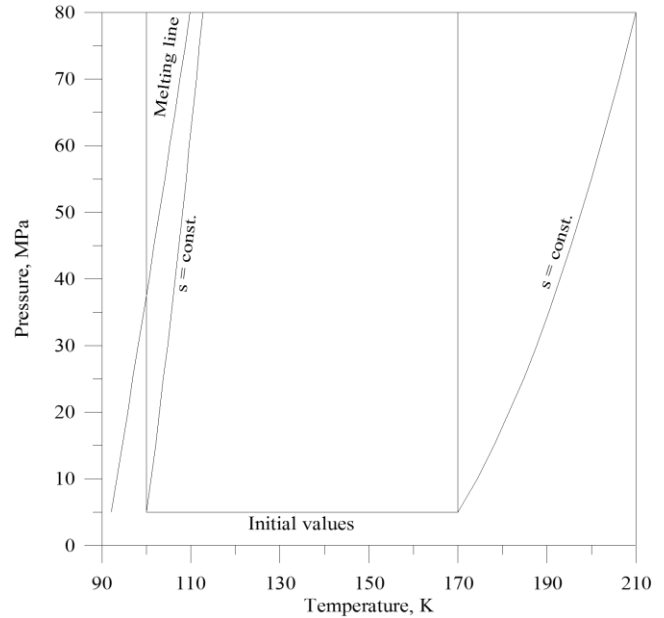
Figure 3. Integration with respect to p at T = const. and s = const., for methane in liquid phase [22].
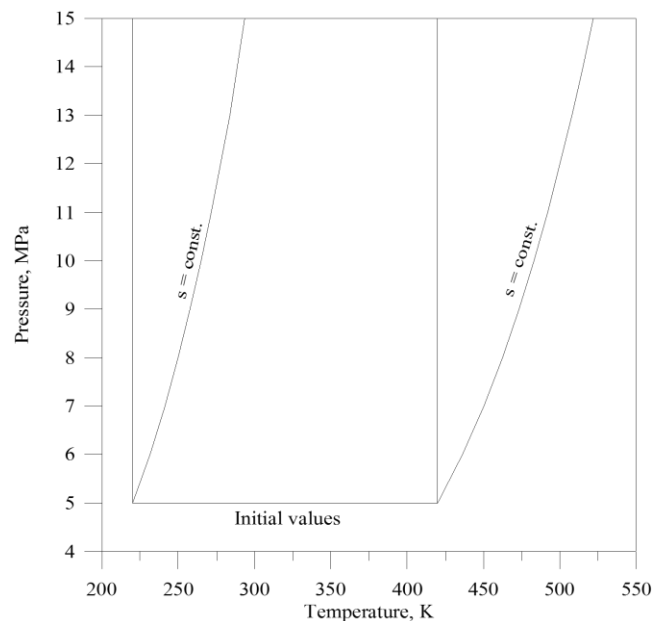
Figure 4. Integration with respect to p at T = const. and s = const., for methane in gaseous phase [22].

2. Theory

The speed of sound is an intensive property whose value depends on the state of the medium through which sound propagates. Experiments indicate that the relation between pressure and density across a sound wave is nearly isentropic. The expression for the speed of sound reads [10]

$$u^2 = \left(\frac{\partial p}{\partial \rho} \right)_s \tag{1}$$

where: u is the speed of sound, p is the pressure, ρ is the mass density, and s is the specific entropy. However, Eq. (1) may not be solved for ρ since u is not measured along isentropes but rather along isotherms. To overcome this, additional property relations have to be included.

2.1 Temperature and entropy as independent variables
2.1.1 Isothermal and isochoric derivatives
According to the following rule of differential calculus

$$\left(\frac{\partial y}{\partial x}\right)_a = \left(\frac{\partial y}{\partial x}\right)_b + \left(\frac{\partial y}{\partial b}\right)_x \left(\frac{\partial b}{\partial x}\right)_a \tag{2}$$

one can write

$$\left(\frac{\partial p}{\partial T}\right)_s = \left(\frac{\partial p}{\partial T}\right)_\rho + \left(\frac{\partial p}{\partial \rho}\right)_T \left(\frac{\partial \rho}{\partial T}\right)_s \tag{3}$$

where T is the thermodynamic temperature. According to another rule

$$\left(\frac{\partial z}{\partial x}\right)_a = \left(\frac{\partial z}{\partial y}\right)_a \left(\frac{\partial y}{\partial x}\right)_a \tag{4}$$

one can also write

$$\left(\frac{\partial p}{\partial T}\right)_s = \left(\frac{\partial p}{\partial \rho}\right)_s \left(\frac{\partial \rho}{\partial T}\right)_s \tag{5}$$

Combining (1), (3), and (5) one obtains

$$\left(\frac{\partial \rho}{\partial T}\right)_s = \left(\frac{\partial p}{\partial T}\right)_\rho \left[u^2 - \left(\frac{\partial p}{\partial \rho}\right)_T\right]^{-1} \tag{6}$$

$$\left(\frac{\partial p}{\partial T}\right)_s = u^2 \left(\frac{\partial \rho}{\partial T}\right)_s \tag{7}$$

If rule (2) is applied to the isochoric derivative in (6), it is obtained

$$\left[\frac{1}{\partial T}\left(\frac{\partial p}{\partial T}\right)_\rho\right]_s = \left(\frac{\partial^2 p}{\partial T^2}\right)_\rho + \frac{\partial^2 p}{\partial T \partial \rho}\left(\frac{\partial \rho}{\partial T}\right)_s \tag{8}$$

The second order isochoric derivative in (8) may be obtained from the following thermodynamic relation [10]

$$\left(\frac{\partial^2 p}{\partial T^2}\right)_\rho = -\frac{\rho^2}{T}\left(\frac{\partial c_v}{\partial \rho}\right)_T \tag{9}$$

where c_v is the specific heat capacity at constant volume, which may be obtained from

$$c_v = \frac{T}{\rho^2}\left(\frac{\partial p}{\partial T}\right)_\rho^2 \left[u^2 - \left(\frac{\partial p}{\partial \rho}\right)_T\right]^{-1} \tag{10}$$

and finally

$$c_p = c_v u^2 \left(\frac{\partial p}{\partial \rho}\right)_T^{-1} \tag{11}$$

where c_p is the specific heat capacity at constant pressure.

2.1.2 Isothermal and isobaric derivatives
According to the rules (2) and (4) one can also write

$$\left(\frac{\partial \rho}{\partial T}\right)_s = \left(\frac{\partial \rho}{\partial T}\right)_p + \left(\frac{\partial \rho}{\partial p}\right)_T \left(\frac{\partial p}{\partial T}\right)_s \tag{12}$$

$$\left(\frac{\partial \rho}{\partial T}\right)_s = \left(\frac{\partial \rho}{\partial p}\right)_s \left(\frac{\partial p}{\partial T}\right)_s \tag{13}$$

Combining (1), (12), and (13) one obtains

$$\left(\frac{\partial p}{\partial T}\right)_s = \left(\frac{\partial \rho}{\partial T}\right)_p \left[\frac{1}{u^2} - \left(\frac{\partial \rho}{\partial p}\right)_T\right]^{-1} \tag{14}$$

$$\left(\frac{\partial \rho}{\partial T}\right)_s = \frac{1}{u^2}\left(\frac{\partial p}{\partial T}\right)_s \tag{15}$$

If rule (2) is applied to the isobaric derivative in (14), it is obtained

$$\left[\frac{1}{\partial T}\left(\frac{\partial \rho}{\partial T}\right)_p\right]_s = \left(\frac{\partial^2 \rho}{\partial T^2}\right)_p + \frac{\partial^2 \rho}{\partial T \partial p}\left(\frac{\partial p}{\partial T}\right)_s \tag{16}$$

The second order isobaric derivative in (16) may be obtained from the following thermodynamic relation [10]

$$\left(\frac{\partial^2 \rho}{\partial T^2}\right)_p = \frac{\rho^2}{T}\left(\frac{\partial c_p}{\partial p}\right)_T + \frac{2}{\rho}\left(\frac{\partial \rho}{\partial T}\right)_p^2 \tag{17}$$

The specific heat capacity at constant pressure may be obtained from

$$c_p = \frac{T}{\rho^2}\left(\frac{\partial \rho}{\partial T}\right)_p^2 \left[\left(\frac{\partial \rho}{\partial p}\right)_T - \frac{1}{u^2}\right]^{-1} \tag{18}$$

and finally

$$c_v = \frac{c_p}{u^2}\left(\frac{\partial \rho}{\partial p}\right)_T^{-1} \tag{19}$$

2.2 Density and entropy as independent variables
2.2.1 Implicit use of entropy
In this case, one can start from the relation [10]

$$\left(\frac{\partial p}{\partial \rho}\right)_s = u^2 \tag{20}$$

and the following property relation [10]

$$\left(\frac{\partial T}{\partial \rho}\right)_s = \frac{1}{\rho^2}\left(\frac{\partial p}{\partial s}\right)_\rho \tag{21}$$

In order to eliminate s at R.H.S. of (21), one can use rule (4) to obtain

$$\left(\frac{\partial p}{\partial s}\right)_\rho = \left(\frac{\partial T}{\partial s}\right)_\rho \left(\frac{\partial p}{\partial T}\right)_\rho \qquad (22)$$

If (22) is combined with the following relation [10]

$$c_v = T\left(\frac{\partial s}{\partial T}\right)_\rho \qquad (23)$$

it becomes

$$\left(\frac{\partial p}{\partial s}\right)_\rho = \frac{T}{c_v}\left(\frac{\partial p}{\partial T}\right)_\rho \qquad (24)$$

Combining (21) and (24) one obtains

$$\left(\frac{\partial T}{\partial \rho}\right)_s = \frac{T}{\rho^2 c_v}\left(\frac{\partial p}{\partial T}\right)_\rho \qquad (25)$$

However, Eqs. (20) and (25) may not be solved for p and T since c_v is also unknown. This may be overcome by introducing the following relation [10]

$$\left(\frac{\partial c_v}{\partial \rho}\right)_T = -\frac{T}{\rho^2}\left(\frac{\partial^2 p}{\partial T^2}\right)_\rho \qquad (26)$$

Having in mind rule (2) one can write

$$\left(\frac{\partial c_v}{\partial \rho}\right)_s = \left(\frac{\partial c_v}{\partial \rho}\right)_T + \left(\frac{\partial c_v}{\partial T}\right)_\rho \left(\frac{\partial T}{\partial \rho}\right)_s \qquad (27)$$

Combining (26) and (27) one obtains

$$\left(\frac{\partial c_v}{\partial \rho}\right)_s = -\frac{T}{\rho^2}\left(\frac{\partial^2 p}{\partial T^2}\right)_\rho + \left(\frac{\partial c_v}{\partial T}\right)_\rho \left(\frac{\partial T}{\partial \rho}\right)_s \qquad (28)$$

When c_v is known, c_p may be calculated from

$$c_p = c_v u^2 \left[u^2 - \frac{T}{\rho^2 c_v}\left(\frac{\partial p}{\partial T}\right)_\rho^2\right]^{-1} \qquad (29)$$

2.2.2 Explicit use of entropy
In this case, one can also start from the relation [10]

$$\left(\frac{\partial p}{\partial \rho}\right)_s = u^2 \qquad (30)$$

and the following property relation [10]

$$\left(\frac{\partial T}{\partial \rho}\right)_s = \frac{1}{\rho^2}\left(\frac{\partial p}{\partial s}\right)_\rho \qquad (31)$$

Now, c_v is calculated from [10]

$$c_v = T\left(\frac{\partial T}{\partial s}\right)_\rho^{-1} \qquad (32)$$

According to the rule (2), one can write

$$\left(\frac{\partial p}{\partial \rho}\right)_s = \left(\frac{\partial p}{\partial \rho}\right)_T + \left(\frac{\partial p}{\partial T}\right)_\rho \left(\frac{\partial T}{\partial \rho}\right)_s \qquad (33)$$

Combining (30), (31), and (33) one obtains

$$\left(\frac{\partial p}{\partial \rho}\right)_T = u^2 - \frac{1}{\rho^2}\left(\frac{\partial p}{\partial s}\right)_\rho \left(\frac{\partial p}{\partial T}\right)_\rho \qquad (34)$$

and finally [10]

$$c_p = c_v u^2 \left(\frac{\partial p}{\partial \rho}\right)_T^{-1} \qquad (35)$$

2.3 Pressure and entropy as independent variables
In this case, one can start from the relation [10]

$$\left(\frac{\partial \rho}{\partial p}\right)_s = \frac{1}{u^2} \qquad (36)$$

and the following property relation [10]

$$\left(\frac{\partial T}{\partial p}\right)_s = -\frac{1}{\rho^2}\left(\frac{\partial \rho}{\partial s}\right)_p \qquad (37)$$

In order to eliminate s at R.H.S. of (37), one can use rule (4) to obtain

$$\left(\frac{\partial \rho}{\partial s}\right)_p = \left(\frac{\partial T}{\partial s}\right)_p \left(\frac{\partial \rho}{\partial T}\right)_p \qquad (38)$$

If (38) is combined with the following relation [10]

$$c_p = T\left(\frac{\partial s}{\partial T}\right)_p \qquad (39)$$

it becomes

$$\left(\frac{\partial \rho}{\partial s}\right)_p = \frac{T}{c_p}\left(\frac{\partial \rho}{\partial T}\right)_p \qquad (40)$$

Combining (37) and (40) one obtains

$$\left(\frac{\partial T}{\partial p}\right)_s = -\frac{T}{\rho^2 c_p}\left(\frac{\partial \rho}{\partial T}\right)_p \qquad (41)$$

However, Eqs. (36) and (41) may not be solved for ρ and T since c_p is also unknown. This may be overcome by introducing the following relation [10]

$$\left(\frac{\partial c_p}{\partial p}\right)_T = -\frac{T}{\rho^2}\left[\frac{2}{\rho}\left(\frac{\partial \rho}{\partial T}\right)_p^2 - \left(\frac{\partial^2 \rho}{\partial T^2}\right)_p\right] \qquad (42)$$

Having in mind rule (2) one can write

$$\left(\frac{\partial c_p}{\partial p}\right)_s = \left(\frac{\partial c_p}{\partial p}\right)_T + \left(\frac{\partial c_p}{\partial T}\right)_p \left(\frac{\partial T}{\partial p}\right)_s \tag{43}$$

Combining (42) and (43) one obtains

$$\left(\frac{\partial c_p}{\partial p}\right)_s = -\frac{T}{\rho^2}\left[\frac{2}{\rho}\left(\frac{\partial \rho}{\partial T}\right)_p^2 - \left(\frac{\partial^2 \rho}{\partial T^2}\right)_p\right] + \left(\frac{\partial c_p}{\partial T}\right)_p \left(\frac{\partial T}{\partial p}\right)_s \tag{44}$$

When c_p is known, c_v may be calculated from

$$c_v = \frac{c_p}{u^2}\left[\frac{1}{u^2} + \frac{T}{\rho^2 c_p}\left(\frac{\partial \rho}{\partial T}\right)_p^2\right]^{-1} \tag{45}$$

3. Algorithms of solution

In this paper it is supposed that practical speed of sound measurements are conducted in p–T domain bounded by two isentropes and two isotherms, isochores, or isobars, respectively, or in any other domain from which speed of sound data can be mapped into the former domains with negligible error. Since true isentropes are yet to be found, approximate ones are generated by a cubic equation of state (EOS). For that purpose the following relation is used

$$s_2 - s_1 = s_2^R - s_1^R + \Delta s^{ig} \tag{46}$$

where entropy change, $s_2 - s_1$, between any two states 1 and 2 is represented as a sum of residual entropy change, $s_2^R - s_1^R$, and ideal gas entropy change Δs^{ig}. The former is obtained from an EOS, while the later is given by

$$\Delta s^{ig} = \int_{T_1}^{T_2} c_p^{ig}(T)\frac{dT}{T} - R\ln\left(\frac{p_2}{p_1}\right) \tag{47}$$

where c_p^{ig} is the ideal gas heat capacity. Since along an isentrope it holds

$$s_2 - s_1 = 0 \tag{48}$$

Eqs. (47) and (48) are replaced into (46), and the resulting equation

$$s_2^R - s_1^R + \int_{T_1}^{T_2} c_p^{ig}(T)\frac{dT}{T} - R\ln\left(\frac{p_2}{p_1}\right) = 0 \tag{49}$$

is solved for p_2 or T_2, given p_1 and T_1. Since Eq. (49) is nonlinear with respect to p_2 and T_2, the solution is obtained by iteration. If u is specified along isotherms or along isochores, specific volume or temperature is iterated, respectively, and pressure is obtained from an EOS directly, since the cubic EOSs are pressure explicit. However, if u is specified along isobars, temperature is iterated in outer loop (finding zero of Eq. (49)), and specific volume in inner loop (finding zero of an EOS).

3.1 Temperature and entropy as independent variables

When it comes to gaseous phase above critical temperature, the most common way of deriving thermodynamic properties from speed of sound is the one based on numerical integration with respect to temperature, along paths of constant density. Although this approach is more demanding (e.g., computationally and experimentally) than the one conducted along paths of constant pressure, it is proved to be more stable. The main source of instability in the later approach are isobaric derivatives, which are estimated less accurately than isochoric ones in the former approach. The aim of the following two algorithms is to check out if isochoric derivatives also introduce less error than isobaric ones when entropy is used instead of density (in the former approach) or pressure (in the latter approach) as independent variable.

3.1.1 Isothermal and isochoric derivatives

1. Specify $u(p, T)$ at several isotherms, along several isentropes generated by a cubic EOS

2. Specify ρ and c_v or $(\partial p/\partial T)_\rho$ at several pressures along isotherm with lowest temperature (T_0)

3. Estimate $(\partial p/\partial \rho)_T$

4. Calculate c_v and c_p from (10) and (11), respectively

5. Estimate $\partial^2 p/\partial T\partial\rho$ and $(\partial c_v/\partial \rho)_T$

6. Calculate $(\partial \rho/\partial T)_s$, $(\partial p/\partial T)_s$, $[\partial(\partial p/\partial T)_\rho/\partial T]_s$, and $(\partial^2 p/\partial T^2)_\rho$ from (6), (7), (8), and (9), respectively

7. Calculate ρ, p, and $(\partial p/\partial T)_\rho$ at $T=T_0+\Delta T$ by numerical integration of (6), (7), and (8), respectively

8. Interpolate EOS pressures along EOS isentropes to T

9. Interpolate u along EOS isentropes to T

10. Interpolate u from EOS pressures to those from step 7

11. Repeat steps 3 to 10 until final temperature is reached

3.1.2 Isothermal and isobaric derivatives

1. Specify $u(p, T)$ at several isotherms, along several isentropes generated by a cubic EOS

2. Specify p and c_p or $(\partial \rho/\partial T)_p$ at several densities along isotherm with lowest temperature (T_0)

3. Estimate $(\partial \rho/\partial p)_T$

4. Calculate c_p and c_v from (18) and (19), respectively

5. Estimate $\partial^2 \rho/\partial T\partial p$ and $(\partial c_p/\partial p)_T$

6. Calculate $(\partial p/\partial T)_s$, $(\partial \rho/\partial T)_s$, $[\partial(\partial \rho/\partial T)_p/\partial T]_s$, and $(\partial^2 \rho/\partial T^2)_p$ from (14), (15), (16), and (17), respectively

7. Calculate p, ρ, and $(\partial \rho/\partial T)_p$ at $T=T_0+\Delta T$ by numerical integration of (14), (15), and (16), respectively

8. Interpolate EOS pressures along EOS isentropes to T

9. Interpolate u along EOS isentropes to T

10. Interpolate u from EOS pressures to those from step 7

11. Repeat steps 3 to 10 until final temperature is reached

3.2 Density and entropy as independent variables

Thermodynamic properties of gases above their critical temperature may be derived from speed of sound also if numerical integration is conducted with respect to density, along paths of constant temperature. Since this approach requires boundary values along the lowest temperature(s), the aim of the following two algorithms is to check out if the solution is stable without boundary values imposed when integration is conducted along isentropes instead of isotherms. It would be also interesting to compare algorithm which uses entropy explicitly to the one which uses entropy implicitly, because the former solves first order PDEs, while the later solves second order PDEs. Since both temperature and pressure are dependent variables here, it would be also interesting to see if fitted values of speed of sound could successfully replace interpolated ones.

3.2.1 Implicit use of entropy

1. Specify $u(p, T)$ at several isochores and several isentropes generated by a cubic EOS

2. Fit u from step 1 to a suitable function of p and T

3. Specify p and c_v at several temperatures along isochore with lowest density (ρ_0)

4. Estimate $(\partial p/\partial T)_\rho$, $(\partial^2 p/\partial T^2)_\rho$, and $(\partial c_v/\partial T)_\rho$

5. Calculate $(\partial p/\partial \rho)_s$, $(\partial T/\partial \rho)_s$, and $(\partial c_v/\partial \rho)_s$ from (20), (25), and (28), respectively

6. Calculate p, T, and c_v at $\rho=\rho_0+\Delta\rho$ by numerical integration of (20), (25), and (28), respectively

7. Calculate c_p from (29)

8. Calculate u at p and T from step 6 by a function from step 2.

9. Repeat steps 4 to 8 until final density is reached

3.2.2 Explicit use of entropy

1. Specify $u(p, T)$ at several isochores and several isentropes generated by a cubic EOS

2. Fit u from step 1 to a suitable function of p and T

3. Specify p and c_v at several temperatures along isochore with lowest density (ρ_0)

4. Calculate s from (23) along ρ_0, at temperatures from step 3, with initial value chosen arbitrarily

5. Estimate $(\partial p/\partial s)_\rho$ and $(\partial T/\partial s)_\rho$

6. Calculate $(\partial p/\partial T)_\rho = (\partial p/\partial s)_\rho / (\partial T/\partial s)_\rho$

7. Calculate c_v from (32)

8. Calculate $(\partial p/\partial \rho)_T$ from (34)

9. Calculate c_p from (35)

10. Calculate $(\partial p/\partial \rho)_s$ and $(\partial T/\partial \rho)_s$ from (30) and (31), respectively

11. Calculate p and T at $\rho=\rho_0+\Delta\rho$ by numerical integration of (30) and (31), respectively

12. Calculate u at p and T from step 11 by a function from step 2

13. Repeat steps 5 to 12 until final density is reached

3.3 Pressure and entropy as independent variables

When thermodynamic properties of liquids are derived from speed of sound, pressure is always used as a variable with respect to which the integration is performed, and the other independent variable is usually temperature. Integration domain is situated between melting line at the left and saturation line at the right, and since these two are not isotherms, significant part of the domain is left uncovered. However, it can be increased considerably if integration is performed along isentropes instead of isotherms. When it comes to gaseous phase, integration with respect to pressure is not stable, even if isothermal paths are replaced by isentropic ones. However, it would be interesting to see if isentropic paths combined with approach similar to the one tried before [9] may solve the problem, especially having in mind aggravating circumstance that boundary values may not be specified along isentrope(s).

3.3.1 Numerical integration

1. Specify $u(p, T)$ at several isobars, along several isentropes generated by a cubic EOS

2. Specify ρ and c_p at several temperatures along isobar with lowest pressure (p_0)

3. Estimate $(\partial \rho/\partial T)_p$, $(\partial^2 \rho/\partial T^2)_p$, and $(\partial c_p/\partial T)_p$

4. Calculate $(\partial \rho/\partial p)_s$, $(\partial T/\partial p)_s$, and $(\partial c_p/\partial p)_s$ from (36), (41), and (44), respectively

5. Calculate ρ, T, and c_p at $p=p_0+\Delta p$ by numerical integration of (36), (41), and (44), respectively

6. Calculate c_v from (45)

7. Interpolate u along EOS isentropes to p

8. Interpolate u from EOS temperatures to those from step 5

9. Repeat steps 3 to 8 until final pressure is reached

3.3.2 Least squares

1. Specify $u(p, T)$ at several isobars, along several isentropes generated by a cubic EOS

2. Specify ρ and c_p at several temperatures along isobar with lowest pressure (p_0)

3. Calculate s from (39) along p_0, at temperatures from step 2, with initial value chosen arbitrarily

4. Guess ρ along isentropes from step 3 at several pressures

5. Estimate $(\partial \rho / \partial p)_s$

6. Calculate u from (36)

7. Interpolate T with respect to u and p

8. Estimate $(\partial T / \partial p)_s$, $(\partial \rho / \partial s)_p$, and $(\partial T / \partial s)_p$

9. Calculate $(\partial \rho / \partial T)_p = (\partial \rho / \partial s)_p / (\partial T / \partial s)_p$

10. Calculate c_p from (39)

11. Calculate c_v from (45)

12. Calculate $f = (\partial T / \partial p)_s + (\partial \rho / \partial s)_p / \rho^2$

13. Calculate $g = (\Sigma f^2) / 2$

14. If $g > 10^{-4}$, calculate new values of ρ by a least squares method

15. Repeat steps 5 to 14 as many times as necessary to obtain $g \leq 10^{-4}$

4. Results and discussion

All interpolations are performed by polynomials [11], while derivatives are estimated by cubic splines [12] and interpolation polynomials. When both pressure and temperature are dependent variables (Algorithms 3.2.1 and 3.2.2), speed of sound data are fitted to bivariate Chebyshev polynomials (with $\ln(p)$ and $\ln(T)$ scaled between -1 and +1). The polynomials coefficients are obtained by method of linear least squares with iterative refinement of Björck [13]. Numerical integrations are performed by Runge-Kutta-Verner fifth-order and sixth-order method with adaptive step-size [14]. In Algorithm 3.3.2, densities are calculated by a modified Levenberg – Marquardt method [15 – 17]. Algorithms of solution described in Sections 3.1 and 3.2 (for gaseous phase) and 3.3 (for liquid and gaseous phase) are tested with several substances. Their list and p–ρ–T ranges covered are given in Tables 1 to 4, 16, 19, and 20. Reference properties are generated by corresponding fundamental EOSs [18 – 24]. Speed of sound data used are obtained from the same EOSs and from measurements [3]. All the results obtained as well as the coefficients of Chebyshev polynomials (see appendix) are given in separate file as a supplement to this paper.

Initial values for supercritical gaseous phase (Algorithms 3.1.1 and 3.1.2) are specified along isotherm with the lowest temperature, at 10 equally spaced pressures (see Table 5). Reference properties are specified at 16 equally spaced isotherms, along 10 isentropes passing through the points with initial values. Speed of sound data are specified at the same isotherms, but along isentropes generated by Peng-Robinson (P-R) EOS [25]. All derivatives are estimated by cubic splines. Both thermal and caloric properties are derived with AADs an order of magnitude smaller if isochoric derivatives are used instead of isobaric ones (see Tables 9 and 10). These AADs are of similar magnitude to those when temperature and density [4] or temperature and pressure [1], respectively, are used as independent variables.

Initial values for supercritical gaseous phase (Algorithms 3.2.1 and 3.2.2) are specified along isochore with the lowest density, at 11 equally spaced temperatures (see Table 6). Entropies corresponding to these temperatures are obtained from Eq. (23), with initial values chosen arbitrarily. Reference properties are specified at 11 isochores, along 11 isentropes passing through the points with initial values. Speed of sound data are specified at isochores and isentropes generated by P-R EOS [25]. Derivatives are estimated by interpolation polynomials (Algorithm 3.2.1) and cubic splines (Algorithm 3.2.2). Both thermal and caloric properties are derived with AADs about 50% smaller if entropy is used explicitly instead of implicitly (see Tables 11 and 12). The solution is stable without boundary values imposed when integration is conducted along isentropes instead of isotherms. Fitted values of speed of sound can successfully replace interpolated ones.

Initial values for transcritical gaseous phase (Algorithms 3.1.1 and 3.1.2) are specified along isotherm with the lowest temperature, at 10 equally spaced pressures (see Table 7). Reference properties are specified at 11 to 15 equally spaced isotherms, along 10 isentropes passing through the points with initial values. Speed of sound data are specified at the same isotherms, but along isentropes generated by P-R EOS [25]. All derivatives are estimated by cubic splines. Both thermal and caloric properties are derived with AADs 4 to 5 times smaller if isochoric derivatives are used instead of isobaric ones (see Tables 13 and 14). These AADs are of similar magnitude to those when temperature and ratio of density to saturated vapor density [5], or temperature and ratio of pressure to saturation pressure [2], respectively, are used as independent variables.

Initial values for liquid phase (Algorithm 3.3.1) are specified along isobar with the lowest pressure, at 7 to 10 equally spaced temperatures (see Table 8). Reference properties are specified at 9 to 11 isobars, along 7 to 10 isentropes passing through the points with initial values. Speed of sound data are specified at the same isobars, but along isentropes generated by P-R EOS [25]. All derivatives are estimated by interpolation polynomials. Both thermal and caloric properties are derived with AADs of similar magnitude to those when pressure and temperature [6, 7] are used as independent variables (see Table 15). It is confirmed that stability of solution in liquid phase, when integration is performed along isentropes, is similar to that along isotherms [26].

Initial values for supercritical gaseous phase (Algorithm 3.3.2) are specified along isobar with the lowest pressure, at 11 equally spaced temperatures (see Table 17). Entropies corresponding to these temperatures are obtained from Eq. (39), with initial values chosen arbitrarily. Reference properties are specified at 11 isobars, along 11 isentropes passing through the points with initial values. Speed of sound data are specified at the same isobars, but along isentropes generated by P-R EOS [25]. All derivatives are estimated by

interpolation polynomials. The results are the same whether guessed values of density are generated by reference EOS (with simulated error of 5%) or by P-R EOS. Both thermal and caloric properties are derived with AADs of similar magnitude to those when density and temperature [4, 9] are used as independent variables (see Table 18). The solution is obtained even without boundary values imposed, but with initial values consisting of thermal and caloric properties.

Initial values for argon in supercritical gaseous phase (Algorithm 3.1.1) are specified along isotherm with the lowest temperature, at 11 equally spaced pressures (see Table 21). Reference properties are specified at 10 isotherms, along 11 isentropes passing through the points with initial values. Speed of sound data [3, 18] are specified at the same isotherms, but along isentropes generated by P-R EOS [25]. All derivatives are estimated by cubic splines. Similar results are obtained with measured and EOS generated speed of sound values, when these later are specified in the same (p, T) points in which speed of sound measurements are conducted (see Table 23).

Initial values for carbon dioxide in transcritical gaseous phase (Algorithm 3.1.1) are specified along isotherm with the lowest temperature, at 8 equally spaced pressures (see Table 22). Reference properties are specified at 9 isotherms, along 9 isentropes passing through the points with initial values. Speed of sound data [3, 23] are specified at the same isotherms, but along isentropes generated by P-R EOS [25]. All derivatives are estimated by cubic splines. Similar results are obtained with measured and EOS generated speed of sound values, when these later are specified in the same (p, T) points in which speed of sound measurements are conducted (see Table 24).

The fact that similar results are obtained with measured and EOS generated speed of sound values, in the last two cases, is confirmation that the two sets of speed of sound have similar uncertainty. So, why AADs in Tables 9 and 23 for argon, or 13 and 24 for carbon dioxide, are an order of magnitude different? This question may be best answered if one takes a closer look at corresponding data sets for argon and carbon dioxide. From Table 1 one can see that temperature range covered for argon is 160 to 310 K and the number of isotherms used is 16, while in Table 20 the corresponding range is 156.08 to 350 K and the number of experimental isotherms is only 10. Also, from Table 3 one can see that temperature range covered for carbon dioxide is 240 to 480 K and the number of isotherms used is 13, while in Table 20 the corresponding range is 250 to 450 K and the number of experimental isotherms is only 6.

5. Conclusions

With only a few initial data, specified at single isotherm, isochore, or isobar, it is possible to derive thermal and caloric properties of real fluids from speed of sound in a wide p–T range if integration paths follow isentropes. While isentropic paths enable covering wider pressure range in gaseous phase, comparing to isochoric paths, this advantage comes at a price. Namely, quicker rise of pressure with temperature along isentropes results in higher nonlinearities, which introduces additional error during interpolation and derivation. It is especially the case when integration is conducted with respect to temperature, but somewhat less pronounced when integration is conducted with respect to density. Besides, selection of appropriate initial temperature and initial pressure range, or initial density and initial temperature range, is of crucial significance if one wants to

cover specific area of thermodynamic surface in gaseous phase. Since isentropes of liquids have similar shape to isotherms in p–T coordinates, the solution stability is similar too. However, their positive inclination with respect to isotherms enables wider temperature range to be covered. Generally, the AADs of the results obtained, with respect to corresponding reference data, are such that their uncertainties are similar to those of direct measurements.

Nomenclature
AAD   average absolute deviation (%)
c_p specific heat capacity at constant pressure (J/kgK)
c_v specific heat capacity at constant volume (J/kgK)
p pressure (Pa)
s specific entropy (J/kgK)
T thermodynamic temperature (K)
u speed of sound (m/s)
v specific volume (m³/kg)

Greek Letters
ρ mass density (kg/m³)

Superscripts
ig ideal gas
R residual

Abbreviations
EOS   equation of state
PDE   partial differential equation
P-R   Peng-Robinson

Appendix

Table 1. p–ρ–T ranges covered in supercritical gaseous phase (Algorithms 3.1.1 and 3.1.2).

	p (MPa)		ρ (kg·m⁻³)		T (K)	
	Min	Max	Min	Max	Min	Max
Ar	0.50	29.5246	15.4656	455.7321	160.0	310.0
N_2	0.35	41.5905	8.6420	381.1771	140.0	290.0
O_2	0.50	41.2324	11.6120	457.2604	170.0	320.0
CH_4	0.50	49.2063	4.9837	231.6339	200.0	350.0
CO_2	0.70	35.1821	11.9116	453.9972	320.0	470.0
H_2O	2.20	51.8782	7.4587	218.9286	660.0	810.0

Table 2. p–ρ–T ranges covered in supercritical gaseous phase (Algorithms 3.2.1 and 3.2.2).

	p (MPa)		ρ (kg·m⁻³)		T (K)	
	Min	Max	Min	Max	Min	Max
Ar	5.0	63.5603	243.2643	500.0	160.0	489.4233
N_2	3.5	76.0620	120.9870	375.0	140.0	455.4120
O_2	5.0	73.7194	162.6782	460.0	170.0	470.1185
CH_4	5.0	85.4198	87.76400	240.0	200.0	463.6393
CO_2	7.0	72.2296	178.7401	530.0	320.0	608.2809
H_2O	22.0	98.9995	141.9413	290.0	660.0	957.4060

Table 3. p–ρ–T ranges covered in transcritical gaseous phase (Algorithms 3.1.1 and 3.1.2).

	p (MPa)		ρ (kg·m^{-3})		T (K)	
	Min	Max	Min	Max	Min	Max
Ar	0.1	21.7206	4.0577	252.3890	120.0	400.0
N_2	0.1	33.2891	3.1089	306.9767	110.0	310.0
O_2	0.1	36.8089	3.1174	358.3584	125.0	365.0
CH_4	0.1	48.0311	1.2617	190.7753	155.0	415.0
CO_2	0.1	19.1436	2.2282	240.7653	240.0	480.0
H_2O	0.1	6.9887	0.4738	22.7240	460.0	720.0

Table 4. p–ρ–T ranges covered in liquid phase (Algorithm 3.3.1).

	p (MPa)		ρ (kg·m^{-3})		T (K)	
	Min	Max	Min	Max	Min	Max
Ar	5.0	100.0	1053.233	1495.712	90.0	187.7662
N_2	3.5	90.0	604.0069	917.1604	70.0	158.0081
O_2	5.0	80.0	845.5365	1338.650	60.0	176.0196
CH_4	5.0	80.0	323.9083	469.7829	100.0	209.8933
CO_2	7.0	100.0	914.2519	1253.424	220.0	328.1373
H_2O	0.1	900.0	967.4033	1220.401	280.0	402.2188

Table 5. Points with initial values in supercritical gaseous phase (Algorithms 3.1.1 and 3.1.2).

	p (MPa)			T (K)
	Min	Max	Step	
Ar	0.50	5.0	0.50	160.0
N_2	0.35	3.5	0.35	140.0
O_2	0.50	5.0	0.50	170.0
CH_4	0.50	5.0	0.50	200.0
CO_2	0.70	7.0	0.70	320.0
H_2O	2.20	22.0	2.20	660.0

Table 6. Points with initial values in supercritical gaseous phase (Algorithms 3.2.1 and 3.2.2).

	T (K)			ρ (kg·m^{-3})
	Min	Max	Step	
Ar	160.0	260.0	10.0	243.2643
N_2	140.0	240.0	10.0	120.9870
O_2	170.0	270.0	10.0	162.6782
CH_4	200.0	300.0	10.0	87.76400
CO_2	320.0	420.0	10.0	178.7401
H_2O	660.0	760.0	10.0	141.9413

Table 7. Points with initial values in transcritical gaseous phase (Algorithms 3.1.1 and 3.1.2).

	p (MPa)			T (K)
	Min	Max	Step	
Ar	0.1	1.0	0.1	120.0
N_2	0.1	1.0	0.1	110.0
O_2	0.1	1.0	0.1	125.0
CH_4	0.1	1.0	0.1	155.0
CO_2	0.1	1.0	0.1	240.0
H_2O	0.1	1.0	0.1	460.0

Table 8. Points with initial values in liquid phase (Algorithm 3.3.1).

	T (K)			p (MPa)
	Min	Max	Step	
Ar	90.0	135.0	5.0	5.0
N_2	70.0	115.0	5.0	3.5
O_2	60.0	140.0	10.0	5.0
CH_4	100.0	170.0	10.0	5.0
CO_2	220.0	280.0	10.0	7.0
H_2O	280.0	360.0	10.0	0.1

Table 9. Average absolute deviation in supercritical gaseous phase (Algorithm 3.1.1).

	AAD (%)			
	ρ	p	c_p	c_v
Ar	0.0006	0.0011	0.0080	0.0061
N_2	0.0094	0.0131	0.0709	0.0575
O_2	0.0051	0.0075	0.0516	0.0374
CH_4	0.0057	0.0112	0.0961	0.0671
CO_2	0.0031	0.0041	0.0270	0.0177
H_2O	0.0059	0.0068	0.0629	0.0340

Table 10. Average absolute deviation in supercritical gaseous phase (Algorithm 3.1.2).

	AAD (%)			
	ρ	p	c_p	c_v
Ar	0.0230	0.0431	0.2729	0.1857
N_2	0.0253	0.0383	0.3050	0.2174
O_2	0.0239	0.0352	0.2440	0.1682
CH_4	0.1194	0.1865	1.3816	1.0070
CO_2	0.0275	0.0371	0.2824	0.2234
H_2O	0.0320	0.0399	0.4339	0.3562

Table 11. Average absolute deviation in supercritical gaseous phase (Algorithm 3.2.1).

	AAD (%)			
	p	T	c_p	c_v
Ar	0.0010	0.0033	0.2979	0.1558
N_2	0.0004	0.0014	0.0798	0.0524
O_2	0.0001	0.0004	0.0288	0.0189
CH_4	0.0011	0.0031	0.1798	0.0923
CO_2	0.0002	0.0004	0.0438	0.0299
H_2O	0.0004	0.0010	0.2117	0.1118

Table 12. Average absolute deviation in supercritical gaseous phase (Algorithm 3.2.2).

	AAD (%)			
	p	T	c_p	c_v
Ar	0.0004	0.0010	0.0490	0.0246
N_2	0.0003	0.0012	0.0658	0.0457
O_2	0.0002	0.0011	0.0616	0.0426
CH_4	0.0006	0.0011	0.0780	0.0467
CO_2	0.0003	0.0007	0.0666	0.0463
H_2O	0.0005	0.0011	0.2469	0.1302

Table 13. Average absolute deviation in transcritical gaseous phase (Algorithm 3.1.1).

	AAD (%)			
	ρ	p	c_p	c_v
Ar	0.0071	0.0116	0.0960	0.0663
N_2	0.0031	0.0050	0.0480	0.0306
O_2	0.0138	0.0191	0.1352	0.1030
CH_4	0.0213	0.0285	0.1243	0.0995
CO_2	0.0083	0.0101	0.0739	0.0596
H_2O	0.0016	0.0018	0.0227	0.0212

Table 14. Average absolute deviation in transcritical gaseous phase (Algorithm 3.1.2).

	AAD (%)			
	ρ	p	c_p	c_v
Ar	0.0119	0.0178	0.1032	0.0767
N_2	0.0440	0.0618	0.3475	0.2813
O_2	0.0331	0.0456	0.2994	0.2440
CH_4	0.1575	0.2003	1.0555	0.9065
CO_2	0.0149	0.0175	0.1382	0.1157
H_2O	0.0014	0.0016	0.0128	0.0108

Table 15. Average absolute deviation in liquid phase (Algorithm 3.3.1).

	AAD (%)			
	ρ	T	c_p	c_v
Ar	0.0001	0.0008	0.0603	0.0256
N_2	0.0001	0.0011	0.0839	0.0418
O_2	0.0010	0.0023	0.0759	0.0479
CH_4	0.0002	0.0011	0.0908	0.0507
CO_2	0.0003	0.0019	0.2212	0.1032
H_2O	0.0004	0.0013	0.0229	0.0186

Table 16. p–ρ–T ranges covered in supercritical gaseous phase (Algorithm 3.3.2).

	p (MPa)		ρ (kg·m^{-3})		T (K)	
	Min	Max	Min	Max	Min	Max
Ar	5.0	15.0	63.37348	293.2735	180.0	589.5826
N_2	3.5	14.0	32.52045	204.8415	160.0	535.9944
O_2	5.0	15.0	49.37306	247.1161	190.0	528.8307
CH_4	5.0	15.0	23.28734	122.3224	220.0	521.7476
CO_2	7.0	17.0	70.81165	278.1599	340.0	640.0213
H_2O	22.0	32.0	60.44128	151.0565	680.0	956.5035

Table 17. Points with initial values in supercritical gaseous phase (Algorithm 3.3.2).

	T (K)			p (MPa)
	Min	Max	Step	
Ar	180.0	380.0	20.0	5.0
N_2	160.0	360.0	20.0	3.5
O_2	190.0	390.0	20.0	5.0
CH_4	220.0	420.0	20.0	5.0
CO_2	340.0	540.0	20.0	7.0
H_2O	680.0	880.0	20.0	22.0

Table 18. AAD and number of iterations taken in supercritical gaseous phase (Algorithm 3.3.2).

	Iterations taken	AAD (%)			
		ρ	T	c_p	c_v
Ar	445	0.0007	0.0033	0.1202	0.0847
N_2	334	0.0026	0.0098	0.2915	0.2311
O_2	445	0.0011	0.0032	0.1399	0.1089
CH_4	445	0.0010	0.0015	0.0466	0.0350
CO_2	445	0.0005	0.0018	0.1001	0.0695
H_2O	556	0.0120	0.0133	0.9247	0.2586

Table 19. p–ρ–T ranges covered in supercritical gaseous phase (Algorithm 3.1.1).

	p (MPa)		ρ (kg·m⁻³)		T (K)	
	Min	Max	Min	Max	Min	Max
Ar	0.1	16.5101	3.0975	227.9245	156.08	350.0

Table 20. p–ρ–T ranges covered in transcritical gaseous phase (Algorithm 3.1.1).

	p (MPa)		ρ (kg·m⁻³)		T (K)	
	Min	Max	Min	Max	Min	Max
CO_2	0.5	14.4634	11.0975	198.7124	250.0	450.0

Table 21. Points with initial values in supercritical gaseous phase (Algorithms 3.1.1).

	p (MPa)			T (K)
	Min	Max	Step	
Ar	0.1	2.1	0.2	156.08

Table 22. Points with initial values in transcritical gaseous phase (Algorithms 3.1.1).

	p (MPa)			T (K)
	Min	Max	Step	
CO_2	0.5	1.2	0.1	250.0

Table 23. Average absolute deviation in supercritical gaseous phase (Algorithm 3.1.1).

	AAD (%) using measured speed of sound			
	ρ	p	c_p	c_v
Ar	0.0325	0.0356	0.1198	0.1760
	AAD (%) using EOS generated speed of sound			
Ar	0.0319	0.0351	0.1202	0.1761

Table 24. Average absolute deviation in transcritical gaseous phase (Algorithm 3.1.1).

	AAD (%) using measured speed of sound			
	ρ	p	c_p	c_v
CO_2	0.0845	0.0932	0.5893	0.5254
	AAD (%) using EOS generated speed of sound			
CO_2	0.0340	0.0403	0.3323	0.2874

Chebyshev polynomials in two variables

$$T = \ln\left(T_{i,j}\right)$$

$$P = \ln\left(P_{i,j}\right)$$

$$X_{i,j} = \ln\left(T_{i,j}^{PR}\right)$$

$$Y_{i,j} = \ln\left(P_{i,j}^{PR}\right)$$

$$X = \frac{2T - X_{1,1} - X_{N,N}}{X_{N,N} - X_{1,1}}$$

$$Y = \frac{2P - Y_{1,1} - Y_{N,N}}{Y_{N,N} - Y_{1,1}}$$

$$X_0 = 1$$

$$X_1 = X$$

$$X_2 = 2X^2 - 1$$

$$X_3 = 4X^3 - 3X$$

$$X_4 = 8X^4 - 8X^2 + 1$$

$$X_5 = 16X^5 - 20X^3 + 5X$$

$$X_6 = 32X^6 - 48X^4 + 18X^2 - 1$$

$$X_7 = 64X^7 - 112X^5 + 56X^3 - 7X$$

$$X_8 = 128X^8 - 256X^6 + 160X^4 - 32X^2 + 1$$

$$X_9 = 256X^9 - 576X^7 + 432X^5 - 120X^3 + 9X$$

$$X_{10} = 512X^{10} - 1280X^8 + 1120X^6 - 400X^4 + 50X^2 - 1$$

$$Y_0 = 1$$

$$Y_1 = Y$$

$$Y_2 = 2Y^2 - 1$$

$$Y_3 = 4Y^3 - 3Y$$

$$Y_4 = 8Y^4 - 8Y^2 + 1$$

$$Y_5 = 16Y^5 - 20Y^3 + 5Y$$

$$Y_6 = 32Y^6 - 48Y^4 + 18Y^2 - 1$$

$$Y_7 = 64Y^7 - 112Y^5 + 56Y^3 - 7Y$$

$$Y_8 = 128Y^8 - 256Y^6 + 160Y^4 - 32Y^2 + 1$$

$$Y_9 = 256Y^9 - 576Y^7 + 432Y^5 - 120Y^3 + 9Y$$

$$Y_{10} = 512Y^{10} - 1280Y^8 + 1120Y^6 - 400Y^4 + 50Y^2 - 1$$

$$\begin{aligned}
U = &\; C_1 + C_2 X_1 + C_3 Y_1 + C_4 X_2 + C_5 X_1 Y_1 + C_6 Y_2 + C_7 X_3 \\
&+ C_8 X_2 Y_1 + C_9 X_1 Y_2 + C_{10} Y_3 + C_{11} X_4 + C_{12} X_3 Y_1 \\
&+ C_{13} X_2 Y_2 + C_{14} X_1 Y_3 + C_{15} Y_4 + C_{16} X_5 + C_{17} X_4 Y_1 \\
&+ C_{18} X_3 Y_2 + C_{19} X_2 Y_3 + C_{20} X_1 Y_4 + C_{21} Y_5 + C_{22} X_6 \\
&+ C_{23} X_5 Y_1 + C_{24} X_4 Y_2 + C_{25} X_3 Y_3 + C_{26} X_2 Y_4 \\
&+ C_{27} X_1 Y_5 + C_{28} Y_6 + C_{29} X_7 + C_{30} X_6 Y_1 + C_{31} X_5 Y_2 \\
&+ C_{32} X_4 Y_3 + C_{33} X_3 Y_4 + C_{34} X_2 Y_5 + C_{35} X_1 Y_6 \\
&+ C_{36} Y_7 + C_{37} X_8 + C_{38} X_7 Y_1 + C_{39} X_6 Y_2 + C_{40} X_5 Y_3 \\
&+ C_{41} X_4 Y_4 + C_{42} X_3 Y_5 + C_{43} X_2 Y_6 + C_{44} X_1 Y_7 \\
&+ C_{45} Y_8 + C_{46} X_9 + C_{47} X_8 Y_1 + C_{48} X_7 Y_2 + C_{49} X_6 Y_3 \\
&+ C_{50} X_5 Y_4 + C_{51} X_4 Y_5 + C_{52} X_3 Y_6 + C_{53} X_2 Y_7 \\
&+ C_{54} X_1 Y_8 + C_{55} Y_9 + C_{56} X_{10} + C_{57} X_9 Y_1 + C_{58} X_8 Y_2 \\
&+ C_{59} X_7 Y_3 + C_{60} X_6 Y_4 + C_{61} X_5 Y_5 + C_{62} X_4 Y_6 \\
&+ C_{63} X_3 Y_7 + C_{64} X_2 Y_8 + C_{65} X_1 Y_9 + C_{66} Y_{10}
\end{aligned}$$

$T_{i,j}$	calculated temp. at i-th isochore and j-th isentrope
$P_{i,j}$	calculated pressure at i-th isochore and j-th isentrope
$T_{i,j}^{PR}$	temp. at P-R i-th isochore and P-R j-th isentrope
$P_{i,j}^{PR}$	pressure at P-R i-th isochore and P-R j-th isentrope
U	speed of sound at $T_{i,j}$ and $P_{i,j}$
C_i	coefficients of the Chebyshev polynomial

References:

[1] M. Bijedić, N. Neimarlija, "Thermodynamic Properties of Gases from Speed-of-Sound Measurements," *Int. J. Thermophys.*, *28*, 268-278, 2007.

[2] M. Bijedić, N. Neimarlija, "Thermodynamic Properties of Carbon Dioxide Derived from the Speed of Sound," *J. Iran. Chem. Soc.*, *5*, 286-295, 2008.

[3] Estrada-Alexanders, A. F. (1996). *Thermodynamic Properties of Gases from Measurements of the Speed of Sound* (Doctoral dissertation), Imperial College, London, UK.

[4] M. Bijedić, N. Neimarlija, "Speed of Sound as a Source of Accurate Thermodynamic Properties of Gases," *Lat. Am. Appl. Res.*, *43*, 393-398, 2013.

[5] M. Bijedić, S. Begić, "Thermodynamic Properties of Vapors from Speed of Sound," *J. Thermodyn.*, *2014*, 1-5, 2014.

[6] M. Bijedić, N. Neimarlija, "Thermodynamic Properties of Liquids from Speed of Sound Measurements," *Int. J. Thermodyn.*, *15*, 61-68, 2012.

[7] M. Bijedić, S. Begić, "Density and Heat Capacity of Liquids from Speed of Sound," *J. Thermodyn.*, *2016*, 1-8, 2016.

[8] A. F. Estrada-Alexanders, Justo, D., "New Method for Deriving Accurate Thermodynamic Properties from Speed-of-Sound," *J. Chem. Thermodyn.*, *36*, 419-429, 2004.

[9] M. Bijedić, S. Begić, "Solution of the Adiabatic Sound Wave Equation as a Nonlinear Least Squares Problem," *Int. J. Thermophys.*, *40*, 1-36, 2019.

[10] M. J. Moran, H. N. Shapiro, *Fundamentals of Engineering Thermodynamics, 5th Ed.* Chichester: John Wiley & Sons, 2006.

[11] W. Chenney, D. Kincaid, *Numerical Mathematics and Computing, 6th Ed.* Belmont: Thomson Brooks/Cole, 2008.

[12] C. de Boor, *A Practical Guide to Splines.* New York: Springer, 1978.

[13] G. H. Golub, C. F. Van Loan, *Matrix Computations.* Baltimore: Johns Hopkins University Press, 1983.

[14] T. E. Hull, W. H. Enright, and K. R. Jackson, *User's Guide for DVERK – A Subroutine for Solving Non-Stiff ODEs.* University of Toronto, 1976.

[15] K. Levenberg, "A Method for the Solution of Certain Non-Linear Problems in Least Squares," *Q. Appl. Math.*, *2*, 164-168, 1944.

[16] D. Marquardt, "An Algorithm for Least-Squares Estimation of Nonlinear Parameters," *SIAM J. Appl. Math.*, *11*, 431-441, 1963.

[17] J.J. Moré, B.S. Garbow, and K.E. Hillstrom, *User Guide for MINPACK-1.* Argonne National Laboratory Report ANL-80-74, 1980.

[18] C. Tegeler, R. Span, and W. Wagner, "A New Equation of State for Argon Covering the Fluid Region for Temperature from the Melting Line to 700 K at Pressures up to 1000 MPa," *J. Phys. Chem. Ref. Data*, *28*, 779-850, 1999.

[19] R. Span, E. W. Lemmon, R. T. Jacobsen, W. Wagner, and A. Yokozeki, "A Reference Equation of State for the Thermodynamic Properties of Nitrogen Covering the Fluid Region for Temperatures from 63.151 to 1000 K and Pressures to 2200 MPa," *J. Phys. Chem. Ref. Data*, *29*, 1361-1433, 2000.

[20] R. Schmidt, W. Wagner, "A New Form of the Equation of State for Pure Substances and Its Application to Oxygen," *Fluid Phase Equilibria*, *19*, 175-200, 1985.

[21] R. B. Stewart, R. T. Jacobsen, and W. Wagner, "Thermodynamic Properties of Oxygen from the Triple Point to 300 K with Pressures to 80 MPa," *J. Phys. Chem. Ref. Data*, *20*, 917-1021, 1991.

[22] U. Setzmann, W. Wagner, "A New Equation of State and Tables of Thermodynamic Properties for Methane Covering the Range from the Melting Line to 625 K and Pressures up to 1000 MPa," *J. Phys. Chem. Ref. Data*, *20*, 1061-1125, 1991.

[23] R. Span, W. Wagner, "A New Equation of State for Carbon Dioxide Covering the Fluid Region for Temperature from the Triple-Point Temperature to 1100 K at Pressures up to 800 MPa," *J. Phys. Chem. Ref. Data*, *25*, 1509-1596, 1996.

[24] W. Wagner, A. Pruss, "The IAPWS Formulation 1995 for the Thermodynamic Properties of Ordinary Water Substance for General and Scientific Use," *J. Phys. Chem. Ref. Data*, *31*, 387-535, 2002.

[25] D. Y. Peng, D. B. Robinson, "A New Two-Constant Equation of State," *Ind. Eng. Chem. Fund.*, *15*, 59-64, 1976.

[26] S. Lago, P. A. Giuliano Albo, "A Recursive Equation Method for the Determination of Density and Heat Capacity: Comparison Between Isentropic and Isothermal Integration Paths," *J. Chem. Thermodyn.*, *42*, 462-465, 2010.

A Two-Stage ORC Integration to an Existing Fluidized Bed Sewage Sludge Incineration Plant for Power Production in the Scope of Waste-to-Energy

A. Abusoglu[1*], A. Tozlu[2], A. Anvari-Moghaddam[3,4]

[1]Istanbul Technical University /Mechanical Engineering Department, Istanbul, 34437, Turkey
[2]Bayburt University/Mechanical Engineering Department, Bayburt, 69000, Turkey
[3]Aalborg University/Department of Energy Technology, Integrated Energy Systems Laboratory, Aalborg, 9220, Denmark
[4]University of Tabriz/Faculty of Electrical and Computer Engineering, Tabriz, 5166616471, Iran
E-mails: abusoglu@itu.edu.tr, alperentozlu@bayburt.edu.tr, aam@et.aau.dk

Abstract:

This paper presents the design, evaluation, and optimization of an electricity generation system based on the two-stage organic Rankine cycle (TS-ORC), which utilizes the waste heat of an existing fluidized bed sewage sludge incineration (FBSSI) facility. The facility incinerates an average of 300 tons per day of sewage sludge with a dry matter content of 22%. After the drying process, the sewage sludge is burned in a fluidized bed combustor, and exhaust gas at a temperature of about 850-900ºC is released due to the combustion. The system provides the energy required to dry the sludge from this exhaust gas. In this study, a TS-ORC is designed to be coupled to the exhaust gas flowlines discharged to the atmosphere at two different points in the FBSSI plant. The exergy efficiency of the FBSSI facility is found to be 70.5%. Three different working fluids are selected to examine the variations of thermodynamic and thermoeconomic performance parameters of the designed TS-ORC system. The highest power generation in the TS-ORC system (183.40 kW) is achieved using R1234yf as working fluid. R1234yf is also the most expensive fluid for electricity generation among the other working fluids (10.57 $/h). The least electricity generation in the TS-ORC (142.70 kW) occurs at the thermoeconomically most affordable cost with R245fa (9.35 $/h).

Keywords: *Fluidized bed sewage sludge incineration, ORC, thermodynamic, thermoeconomy, waste to energy, multi-objective optimization*

1. Introduction

After successive treatment and stabilization processes in a wastewater treatment plant (WWTP), sewage sludge is kept in tightly closed, airless tanks for a specific retention period and at a certain temperature range to produce biogas by anaerobic digestion. Finally, the sewage sludge, which is subjected to a dewatering process before discharging it from the facility and whose dry matter content is increased to about 20%, becomes ready for the disposal process. Sewage sludge incineration is one of the well-established disposal methods for municipal sewage sludge, and many researchers have conducted theoretical and experimental research on this issue since the 1980s [1-3]. In these early studies, it was reported that sewage sludge, which was discharged mostly to the seas or oceans in the 1970s, was disposed of by laying on agricultural lands in the 1980s or filling empty fields near cities. In developed countries, such as the USA, Canada, the EU, and Japan, sewage sludge was stored in landfills following strict environmental standards to prevent groundwater contamination [1-2]. In the 1990s, it began to be emphasized that incineration of treatment sludge was the most appropriate solution in big cities and metropolises. Besides, the waste heat of incineration plants was proposed to be used in the small and medium-sized cogeneration plants to be established on the plant site [4]. However, one of the essential advantages of sewage sludge incineration plants in those years, as it is today, was the process of drying the

sludge with the waste heat before burning to increase its dry matter content and achieve more efficient combustion.

Within the framework of the waste-to-energy (WtE) that started to develop in the early 2000s, it became increasingly important to use the sewage sludge as a sustainable fuel. Thus, systematic investigations were started to reveal the thermal value of sewage sludge for efficient energy recovery [5]. Utilizing sewage sludge as a fuel in the cement industry was reported as a promising approach [6] because ash with heavy metal content sourced by the combustion process was bound to the clinker matrix during the reaction taking place higher than 1300ºC, which prevents the formation of another type of waste through this process [7]. To clarify the combustion characteristics of sewage sludge, a new type of pressurized fluidized bed incinerator coupled with a turbocharger was compared to a conventional type of incinerator. It was reported that at a daily incineration capacity of 100 tons, an energy savings of 50% were achieved with the pressurized fluidized bed incinerator compared to the conventional incineration. Also, the amount of fuel supply was reduced by 25% because of pressurization [8]. A separate simulation study supporting this result also showed that heat and mass transfers are enhanced, and consequently, incineration mechanisms are accelerated in fluidized bed incineration [9]. A large proportion of the previously published works available in the literature focused on energy recovery from sewage sludge during its

disposal. Werther and Ogada [10] investigated the different burning methods of sewage sludge in the broadest sense. These methods include burning the sludge with pulverized coal as replenishment fuel and burning it with municipal solid waste. They also carried out detailed studies on the drying of the sewage sludge to increase its dry matter content to a certain volumetric percentage for more efficient combustion. In many pre-published studies, it was underlined that if sufficient scientific and technical infrastructure is established to incinerate sewage sludge with other wastes without any fossil fuel supply, incineration is a unique energy recovery method, highlighting the positive aspects for the environment [11-14]. Direct incineration of dried sewage sludge for use along with any fossil fuel in a power production plant or cement production as an auxiliary fuel was recently investigated by many scientists. Among these works, there are local/regional case studies in which energy is generated by drying and burning sewage sludge by various methods [15-18] and review studies on countries' energy recovery potentials by extensively investigating and revealing their sewage sludge inventories [19-21].

1.1 Electricity Production with an ORC Coupled to the Fluidized Bed Sewage Sludge Incineration (FBSSI) Plant

The principle of sewage sludge incineration in a fluidized bed boiler is based on moving the sludge particles whose dry matter ratio is increased to 40-60%, upward direction into the air or gas stream in the boiler. Thus, the sludge particles suspended in the air stream in the boiler behave like a fluid, making the combustion process homogeneous and efficient. The combustion process takes place at low combustion temperatures in the fluidized bed (FB). The exhaust gas energy is first used to dry the sewage sludge until it reaches certain dryness range for efficient combustion. The incineration of sewage sludge in the fluidized bed incineration (FBI) systems enabled the energy required to dry the sludge and use the remaining energy in both district heating (DH) and low-temperature electricity generation [22-27]. Considering these energy recovery possibilities results from the FBI's low thermal efficiency, the accumulation of sewage sludge at the bottom of the FB, and high emissions. The solutions were proposed to overcome the above problems using the energy obtained due to incineration in an environmentally beneficial recovery process for an effective sewage sludge disposal [28-31].

The organic Rankine cycle (ORC) usually generates electricity with low-temperature sources ($\geq$ 80ºC). However, there are applications where ORCs are used with medium (200-450ºC) and high-temperature (450ºC and above) sources [32]. The heat of the combustion gas obtained in a fluidized bed sewage sludge incineration (FBSSI) unit is first transferred to the heat transfer oil for drying the sludge. The exhaust gas, whose temperature drops after this process, is a candidate for a unique, medium-temperature, and sustainable heat source for the ORC. The evaluation of the exhaust gas released due to the combustion of sewage sludge in the FBSSIs for electricity generation with the ORC was discussed partly in only a few published papers in the open literature [33-35]. On the other hand, waste heat obtained from WWTP or MSWP integrated into an ORC was extensively studied [36-40].

In this study, an ORC system is designed, which utilizes the exhaust gas sourced from an existing FBSSI plant. First, the incineration facility is introduced, then a detailed thermodynamic analysis and evaluation are presented using the facility's actual operating data. Then, a two-stage ORC system compatible with the existing facility's operating conditions is designed. Three different working fluids are selected to examine the variations of thermodynamic and thermoeconomic performance parameters of the designed ORC system. Finally, multi-objective optimization of the designed system is performed in MATLAB using the non-dominated sorting genetic algorithm (NSGA-II) method. Considering the previously published works in the open literature, there are very few studies found on energy recovery based on sewage sludge incineration. In addition to the systematic analysis and optimization work performed in the presented study, using actual operating data based on an existing FBSSI facility constitutes the main motivation behind this study.

2. Material and Method
2.1. Description of a Two-Stage ORC System Integrated to the Existing FBSSI Plant (TS-ORC)

GASKI FBSSI plant is Turkey's first sewage sludge incineration facility, and considering the infrastructure needs of the city of Gaziantep, it was commissioned in 2012 for the incineration of a total of 300 tons of sludge per day with a dry matter content of 22%. Sewage sludge collected from the three advanced biological WWTP of the city is first dried in the furnace and then burned in the FB incinerator resulting in ash. In the facility, first, thermal drying is applied to the sewage sludge, and the amount of dry matter in its content is increased to 40-50%. It was reported by the facility management that the combustion efficiency reaches its highest value when the dry matter content of the sludge is between 50-60%. After the drying process, the sewage sludge is burned in a fluidized bed boiler, and 10-12 tons of ash is produced per day while a temperature of about 850-900ºC of exhaust gas is released (state 17) due to the combustion. The system provides the energy required to dry the sludge from this exhaust gas. Natural gas is used as auxiliary fuel in the facility until the boiler temperature reaches 650ºC during the combustion; then, when the temperature reaches 850-900ºC, it is possible to burn the sludge without the need for additional fuel. A flue gas purification system is used to prevent combustion gases from harming the environment (state 24 to 29). The result of the sludge incineration process is ash with a dry matter content of 99%, in which the harmful pathogens inside are destroyed by burning the sludge cake while its volume is reduced by 90% and is entirely harmless to the environment. Ash produced as a result of the combustion in the facility is buried in the municipal solid waste land and eliminated (state 29). Similarly, the dust in the exhaust gas is eliminated by the filtration system (state 27).

In this study, a two-stage ORC system (TS-ORC) is designed to be coupled to the exhaust gas flowlines discharged to the atmosphere at two different points in the FBSSI plant. The first exhaust gas stream (state 1) enters the TS-ORC system at a temperature of 279.95ºC, a pressure of 1.013 bar and a mass flow rate of 5.268 kg/s while the second stream (at state 11) enters the system at a temperature of 196.29ºC, a pressure of 1.077 bar, and a mass flow rate of 4.460 kg/s. The aim here is to generate electricity by using the thermal energy of the exhaust gas by providing a secondary benefit, apart from the main function of the FBSSI plant, where the sludge is first dried and then burned and thus completely disposed of. The flow schematic of the TS-ORC system integrated to FBSSI plant is given in Figure. 1.
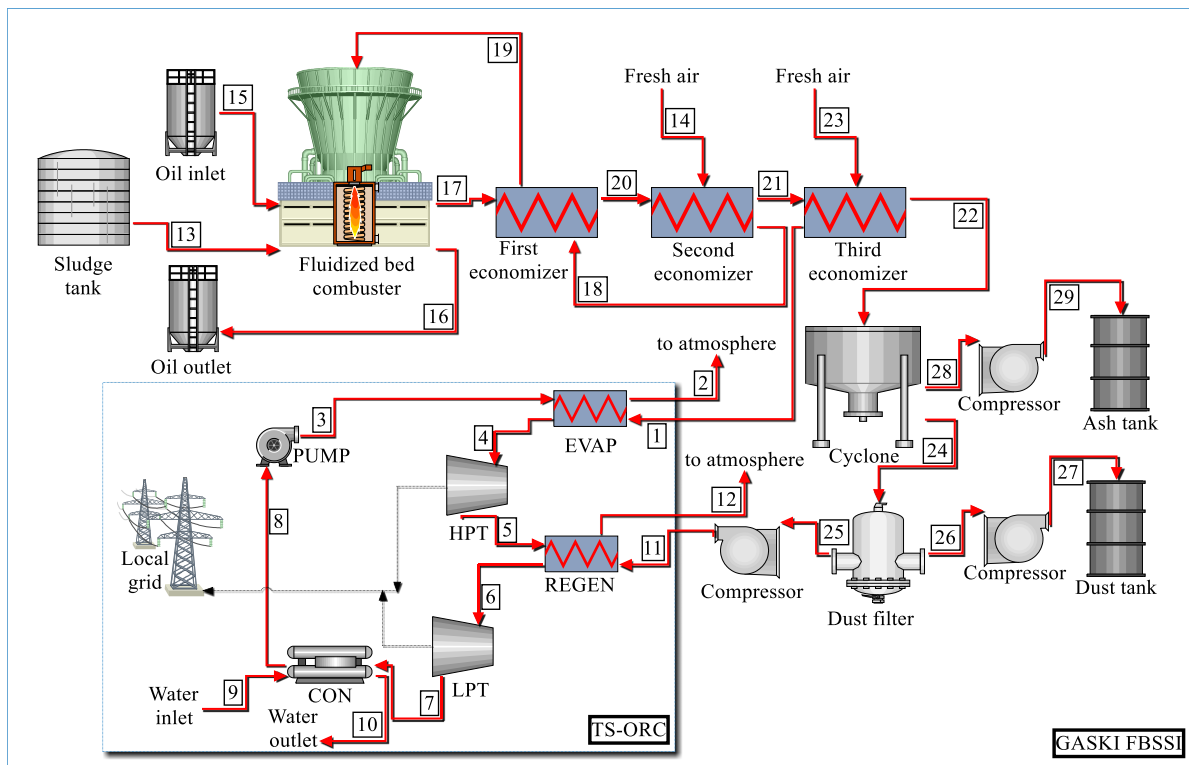
Figure 1. The flow schematic of the TS-ORC system integrated to an existing FBSSI plant

To use these different exhaust flows in the facility more efficiently together, the TS-ORC system is designed to include a two-stage turbine system. The TS-ORC system consists of an evaporator (EVAP), a high-pressure turbine (HPT), a regenerator (REGEN), a low-pressure turbine (LPT), a condenser (CON), and a pump (PUMP) (see Figure.1). As seen in Figure. 1, exhaust gas at a high temperature (280ºC) enters the evaporator (state 1), where it is discharged into the atmosphere immediately after transferring its heat to the working fluid (state 2). On the other hand, exhaust gas at a low temperature (196.3°C) enters the regenerator (state 11), where it transfers its heat to the working fluid exiting the HPT and then discharges into the atmosphere (state 12). The pressurized working fluid in a superheated steam phase provides the first power generation in HPT. Then, it enters REGEN and exchanges heat with the low-temperature exhaust gas before entering the LPT. The working fluid enters the LPT at the same temperature as it previously entered the HPT but at a lower pressure. After the final power generation occurs in LPT, the working fluid becomes condensed by transferring heat to water in CON, then enters PUMP to be pressurized again. Thus, the cycle is complete. The TS-ORC system is designed so that the working fluid temperatures are the same at both turbine inlets. Also, the temperature values at which the exhaust gases leave the EVAP and REGEN are the same. In heat exchangers in the TS-ORC system, the difference between the outlet temperatures of hot fluids and the inlet temperatures of cold fluids is defined as T_x. This is because LMTD values are kept at reasonable levels and a suitable heat exchanger selection can be made. Design parameters for the TS-ORC are listed in Table 1.

Table 1. Design parameters of the TS-ORC [37]

Parameter	Symbol	Value
Inlet temperature of heat source 1 (ºC)	T_1	279.95
Outlet temperature of heat source 1 (ºC)	T_2	60
Mass flow rate of heat source 1 (kg/s)	$\dot{m}_{ex}$	5.268
Inlet temperature of heat source 2 (ºC)	T_1	196.29
Outlet temperature of heat source 2 (ºC)	T_2	60
Mass flow rate of heat source 2 (kg/s)	$\dot{m}_{ex}$	4.460
Pressure ratio of TS-ORC	PR	10
Temperature difference	T_X	15
Inlet temperature of HPT (ºC)	T_4	181.3
Exit temperature of HPT (ºC)	T_5	134.5
Inlet temperature of LPT (ºC)	T_6	181.3
Exit temperature of LPT (ºC)	T_7	165.4
Isentropic efficiency of pump	η_{PUMP}	0.85
Isentropic efficiency of turbines	η_T	0.85
Effectiveness of heat exchangers	εf_{HE}	0.85
Inlet temperature of cooling water (ºC)	T_7	20
Outlet temperature of cooling water (ºC)	T_8	42
Ambient temperature (ºC)	T_0	20

As explained previously in section 2.1, ORCs can be designed to use the medium (200-450ºC) and high-temperature (450ºC and above) sources. In this study, considering the average temperatures of two different exhaust gas flows of the FBSSI plant, that will be used as a heat source for the TS-ORC system, the system's thermal source temperature can be evaluated in the medium temperature range. For this, three different working fluids are chosen suitable for medium temperature sources. The properties of the selected working fluids are shown in Table 2.

Table 2. Properties of the selected working fluids for the TS-ORC

Fluid	Chemical formula	Mol. Weight (kg/kmol)	P_{crit} (MPa)	T_{crit} (^oC)
R245fa	$CF_3CH_2CHF_2$	134	3.651	154
R1234yf	$C_3H_2F_4$	114.04	3.382	94.7
R1234ze	$CHF=CHCF_3$(trans)	114.04	3.635	109.4

Thermodynamic relations		Thermoeconomic relations	
$\Sigma \dot{m}_i = \Sigma \dot{m}_e$	$\dot{m}$; mass flow rate i; inlet, e; exit	$\dot{Z} = (PEC * CRF * \phi)/(3600 * N)$	$\dot{Z}$; capital cost rate
$\dot{Q} - \dot{W} = \Sigma \dot{m}_e h_e - \Sigma \dot{m}_i h_i$	$\dot{Q}$; net heat transfer $\dot{W}$; net work transfer h; enthalpy	$CRF = \dfrac{i_r(1 + i_r)^n}{(1 + i_r)^n - 1}$ $\phi = 1.06$ $n = 15$ $N = 8040$ $i = 15\%$ $PEC_{EVAP} = 130(A_{EVAP}/0.093)^{0.78}$ $PEC_{REGEN} = 130(A_{REGEN}/0.093)^{0.78}$ $PEC_{CON} = 1773(\dot{m}_{wf})$ $PEC_{PUMP} = 3540(\dot{W}_{PUMP})^{0.71}$ $PEC_{HPT\&LPT} = 6000(\dot{W}_{net})^{0.7}$	CRF; capital recovery factor ϕ; maintenance factor n; total life time N; annual operation time i_r; interest rate PEC; Purchased equipment costs wf; working fluid
$\dot{E}x_{Heat} - \dot{W} = \Sigma \dot{m}_e \psi_e - \Sigma \dot{m}_i \psi_i + \dot{E}x_D$	$\dot{E}x_{Heat}$; net exergy transfer ψ; specific flow exergy		
$\psi = (h - h_0) - T_0(s - s_0)$	s; entropy T; Temperature 0; dead state	$\dot{Q}_k = U_k A_k LMTD$	$\dot{Q}_k$; heat exchanger load A_k; heat transfer area k; component
$\dot{E}x = \dot{m}\psi$	$\dot{E}x$; Exergy rate	$U = 0.7$	U; heat transfer coefficient
$\dot{W}_{net} = \dot{m}_{wf}[(h_{t,i} - h_{t,e}) - (h_{p,e} - h_{p,i})]$	$\dot{W}_{net}$; net power	$LMTD = \dfrac{((T_{H,i} - T_{C,e}) - (T_{H,e} - T_{C,i}))}{ln\dfrac{(T_{H,i} - T_{C,e})}{(T_{H,e} - T_{C,i})}}$	$LMTD$; logarithmic mean temperature difference H; hot, C; cold
$\dot{Q}_{in} = \dot{m}_{wf}(h_i - h_e)$	$\dot{Q}_{in}$; heat transferred to the working	$\dot{D}_{D,k} = c_{f,k} \dot{E}x_{D,k}$	$\dot{D}_{D,k}$; exergy destruction cost rate
$\eta = \left(\dfrac{energy\ in\ products}{total\ energy\ input}\right) = \dfrac{\dot{W}_{net}}{\dot{Q}_{in}}$	η; energy efficiency	$\varepsilon = \left(\dfrac{exergy\ in\ products}{total\ exergy\ input}\right) = \dfrac{\dot{W}_{net}}{\dot{m}_{wf}(\psi_i - \psi_e)}$ $\dot{E}x_F - \dot{E}x_P = \dot{E}x_D$	ε; exergy efficiency F; fuel, P; product, D; destruction

2.2. Thermodynamic and Thermoeconomic Relations

The governing thermodynamic and thermoeconomic relations, including economic assumptions used in the FBSSI plant and TS-ORC system analyses, are presented in Table 3 [37-39]. The following assumptions are made for the thermodynamic analysis:

- All subsystems in the FBSSI plant and TS-ORC system operate in the steady-state conditions.
- The values for the reference environment (dead state) temperature and pressure are taken as 20°C and 1.0 bar, respectively.
- The combustion reaction in the FB combustor is complete.
- The kinetic and potential energy changes are negligible.
- The pressure losses taking place in the flows of working fluids through the pipes and heat exchangers are negligible.
- The exhaust gas is assumed as air. The exhaust gas and the air are assumed to be handled with sufficient accuracy by the ideal gas model at all states considered in the analysis.
- The heat exchangers' effectiveness is assumed as 0.85, and the isentropic efficiencies of the turbines, compressors and pumps are 0.85 [37].

The Chemical engineering plant cost index (CEPCI) is an essential parameter calculated using the ratio between the cost index of the reference year and the current year and considered in the calculation of facility costs [37]. Correlations given for purchase cost are usually explained by a cost index that needs to be updated using the CEPCI factor. It is calculated by the ratio of the CEPCI values of the reference years. The reference years should be chosen as the commissioned date of the facility and the model design year [38]. In this study, the facility cost index is selected for the years 2012 and 2020 to make a reliable thermoeconomic analysis [40-42]. The reference year is chosen as the year 2012 when the FBSSI plant was commissioned. In this study, the CEPCI value is calculated as 0.901, and the components

are updated according to this value.

2.3. NSGA-II Optimization

Evolutionary multi-objective optimization (EMO) is an established method for optimizing two or more objectives simultaneously. In this study, multi-objective optimization is performed in MATLAB using the non-dominated sorting genetic algorithm (NSGA-II) method. In this method, total production cost and exergy efficiency are determined as the TS-ORC system's objective functions. The main purpose of selecting these two objectives is that the current economic analysis is based on the exergy cost. In this way, the optimization result makes it possible to increase the system's efficiency and reduce the total cost by improving the design parameters. Decision variables determined to perform multi-objective optimization are given as

- pressure ratio (PR),
- the difference between the outlet temperature of the hot fluid and the inlet temperature of the cold fluid at each heat exchanger (T_x),
- and the dead state temperature (T_0).

The population size, Pareto fraction, and the number of generations are 120, 0.8 and 1000, respectively. The flowchart of optimization in the TS-ORC system is shown in Figure. 2. The limits of the decision variables for optimization of objective functions are given in Table 4.

Table 4. The limits of the decision parameters for the TS-ORC system

Pressure ratio	PR	$5 \leq PR \leq 15$
Temperature difference	T_X	$10 \leq T_X \leq 20$
Dead state temperature	T_0	$15 \leq T_0 \leq 25$

3. Results and Discussion
3.1. Thermodynamic Analysis of FBSSI Plant

Energy and exergy analyses of the GASKI FBSSI plant are performed using an educational version of Cycle-Tempo
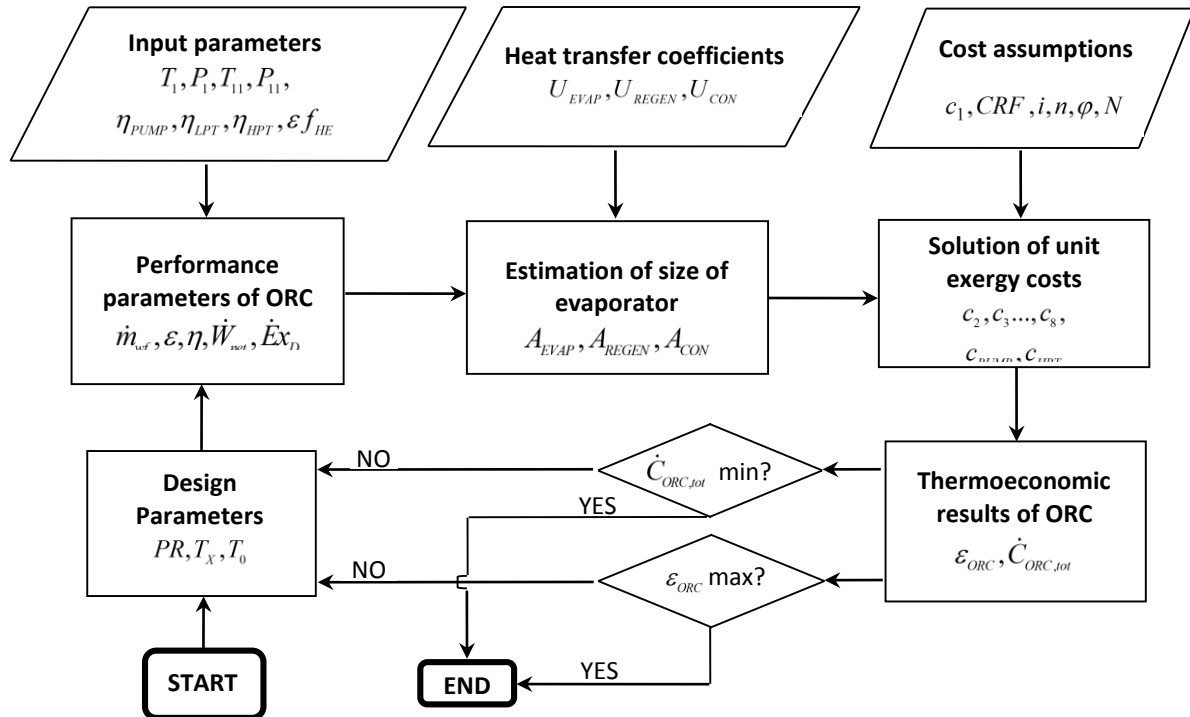
Figure 2. The flow chart for the optimization of the TS-ORC

software [43]. The temperature, pressure, and mass flow rate data and specific exergy values of the plant according to the nomenclature shown in Figure. 1 are presented in Table 5. Thermodynamic analysis results for the components of FBSSI plant is given in Table 6.

Table 5. Thermodynamic properties of the FBSSI plant with respect to state points in Figure.1

State	Fluid	P (bar)	T (°C)	$\dot{m}$ (kg/s)	Ψ (kj/kg)
1	Exhaust	1.013	280	5.268	76.78
2	Exhaust	1.013	60	5.268	3.57
11	Exhaust	1.077	196.3	4.460	45.15
12	Exhaust	1.077	60	4.460	8.72
13	Sludge	1.013	200.00	2.344	2942.09
14	Air	1.100	24.00	3.549	7.09
15	Oil	1.013	200.00	5.555	162.27
16	Oil	1.013	240.00	5.555	192.52
17	Flue gas	1.013	994.00	5.893	781.85
18	Air	1.095	538.00	3.549	245.10
19	Air	1.013	669.00	3.549	337.30
20	Flue gas	1.013	876.00	5.893	659.69
21	Flue gas	1.012	628.78	5.893	426.09
22	Flue gas	1.010	442.00	5.893	275.64
23	Air	1.013	24.00	5.268	0.25
24	Flue gas	1.003	222.00	5.186	126.82
25	Flue gas	1.003	186.00	4.460	111.00
26	Ash	1.006	154.00	0.726	99.36
27	Ash	1.041	158.56	0.726	104.00
28	Ash	1.003	154.00	0.707	96.76
29	Ash	1.041	158.56	0.707	101.27

Following Szargut et al. [44], the specific chemical exergy of a technical fuel such as sewage sludge containing a small amount of ash may be adopted as

$$\psi_{\text{sludge}}^{\text{CH}} = \left(LHV_{\text{sludge}} + \Box_{evap}z_{\text{water}}\right)\beta + \left(\psi_{\text{sulfur}}^{\text{CH}} - LHV_{\text{sulfur}}\right)z_{\text{sulfur}} + \psi_{\text{ash}}^{\text{CH}}z_{\text{ash}} + \psi_{\text{water}}^{\text{CH}}z_{\text{water}} \quad (1)$$

where LHV_{sludge} and LHV_{sulfur} are the lower heating values of sludge and sulfur respectively; h_{evap} is the enthalpy of water vaporization; $z_{\text{water}}, z_{\text{sulfur}}, z_{\text{ash}}$ are the mass fractions of water, sulfur and ash respectively; $\psi_{\text{sulfur}}^{\text{CH}}, \psi_{\text{ash}}^{\text{CH}}$, and $\psi_{\text{water}}^{\text{CH}}$ are the specific chemical exergies of sulfur, ash, and water respectively. β is a variable ratio which gives the atomic ratios in a mixture and does not depend on environmental parameters. It can be obtained for the sludge including the ratio of oxygen to carbon (*O/C*) less than 0.5 by the following relation:

$$\beta_{\text{sludge}} = 1.0437 + 0.0140\frac{H}{C} + 0.0968\frac{O}{C} + 0.0467\frac{N}{C} \quad (2)$$

where *H, C, O* and *N* are the percentage values of hydrogen, carbon, oxygen and nitrogen in the sludge, respectively. At the inlet of the FBSSI plant, the digested sewage sludge has a dry matter content of about 22% and its specific chemical

Table 6. Energy and exergy analysis results for the subsystems in the FBSSI plant.

Component	$\dot{Q}$ (kW)	$\dot{W}$ (kW)	$\dot{Ex}_F$ (kW)	$\dot{Ex}_P$ (kW)	$\dot{Ex}_D$ (kW)	ε (%)
FB Combustor	-28,128 +404.66 +7466.43	-	8994.75	5676.89	3317.86	63.11
First Economizer	-695.00 +467.00	-	719.89	327.22	392.67	45.46
Second Economizer	-1824.1 +1457.0	-	1376.60	844.70	531.90	61.36
Third Economizer	-1346.00 +1100.70	-	886.60	403.16	483.44	45.47
Cyclone	-1595.28	-	1520.00	726.41	793.60	47.79
Dust Filter	-241.20	-	657.70	567.20	90.50	86.24
Ash Tank Compressor	-	13.76	13.76	10.48	3.28	76.16
Dust Tank Compressor	-	14.15	14.15	10.78	3.37	76.18
Dust Filter Compressor	-	205.71	205.71	158.17	47.54	76.89
FBSSI	-28,128	-	9021.30	6359.40	2661.90	70.50

exergy becomes 2942.09 kJ/kg based on the specific exergy value of the dry sludge (see Table 5), which is obtained as 13,373 kJ/kg by Equation (1) and the data given in Table 7 [45]. The lower heating value (LHV) of the digested dry sludge is taken as 12,000 kJ/kg [46].

Table 7. The digested sewage sludge composition [45]

Content	Volumetric values (%)
Carbon (C)	50.0
Hydrogen (H)	2.5
Oxygen (O)	12.5
Nitrogen (N)	1.1
Sulfur (S)	0.4
Ash	10.0
Other	23.5

We note the followings from these results:

- The FB combustor has the highest exergy destruction at the FBSSI plant, with approximately 3317.86 kW. The exergy efficiency of this component is found to be 63.11%. The exergy destruction of the combustion process is mainly due to the irreversibilities associated with chemical reactions and heat transfer. Other causes of exergy destruction in the FB combustor are friction and mixing. Some of this destruction can be prevented by more effective preheating of the sludge and reducing the excess air. Note that the system for which thermodynamic analysis is made is a facility analyzed with real operating data. In this existing system, the exhaust gas transfers its heat to the air by entering a heat exchanger, and then heated air is blown onto the treatment sludge waiting in a sludge tank, unlike the scenario we developed by integrating the TS-ORC system. That is why sewage sludge enters the FB combustor at 200ºC (see state 13 in Table 5). Figure. 1 does not show this preheating process of the sludge by blowing hot air in the plant. Because in the WtE scenario developed in this study, all exhaust gas rejected from FB combustor provides heat to the TS-ORC system to generate electricity. Thus, if it is desired to evaluate the waste heat of an existing sludge incineration plant integrated with an ORC system as suggested in this study, the design conditions of the preheating system of sewage sludge should be reviewed. As understood from the thermodynamic analysis results of the existing system, preheating of the sludge has a remarkable effect on increasing the combustion efficiency.

- The second highest exergy destruction in the FBSSI plant is taken place in the cyclone. This device is used to separate ashes from the flue gas. The cyclone has an exergy destruction amount of 794 kW. While ash is separating from flue gas, heat transfer to the surroundings is always accompanied by exergy transfer.

- The third largest share of the total exergy destruction of the overall plant originates from the first economizer, which has the exergy destruction of about 532 kW, and its exergy efficiency is found to be approximately 61%. Exergy destruction in a heat exchanger is mostly caused by the temperature and mass flow rate differences between the material flow and phase difference. Exergy destruction in the first economizer is caused by the relatively high mean temperature difference of about 250ºC. As a result, the temperature difference of the fluids should be minimized to reduce exergy destruction. Two measures can achieve this: increase of

the heat transfer area and decreased airflow. The other air preheaters, the second and third economizers have high amounts of exergy destructions in the FBSSI plant, and their exergy destructions are found to be 393 and 483.3 kW, respectively. These destructions are mainly due to the relatively high-temperature differences of the fluids.

- Contrary to the components described above, the facility's product conditioning components play a minor role in exergy analysis. It is because they do not serve for energy conversion but for material separation. Exergy destruction in these components is mainly due to friction.

The exergy efficiency for the FBSSI plant can be calculated using the equation in the following (state numbers refer to Figure. 1 and Table 5),

$$\varepsilon_{FBSSI} = \frac{\sum \dot{E}x_P}{\sum \dot{E}x_F}$$
$$= \frac{\dot{E}x_1 + \dot{E}x_{11} + \dot{E}x_{16} + \dot{E}x_{17} + \dot{E}x_{29}}{\dot{E}x_{13}^{C\square emical} + \dot{E}x_{14} + \dot{E}x_{15} + \dot{E}x_{19} + \dot{E}x_{23}} \quad (3)$$

Using Equation (3), the exergy efficiency of the facility is found to be 70.5% which proves that exergy transfer by heat is inevitably degraded mostly due to the high-temperature differences between systems' boundary and the environment. It is possible to increase the exergy efficiency of the existing FBSSI facility by using the waste heat source (exhaust gas) in the system more efficiently by developing a TS-ORC scenario to be integrated into the FBSSI facility.

3.2. Thermodynamic and Thermoeconomic Analyses of TS-ORC

In this study, considering three working fluids listed in Table 2, detailed thermodynamic and thermoeconomic analyses of the TS-ORC system are performed comparatively using the governing equations given in Table 3. The thermodynamic and thermoeconomic analyses results obtained are presented in Table 9 using the design parameters listed in Table 1 and the thermodynamic properties given in Table 8.

The thermodynamic and thermoeconomic analysis results of the TS-ORC system using the working fluids listed in Table 2 are shown in Table 10. The analysis results listed in Table 10 can be evaluated as follows:

- The highest power generation in the TS-ORC system (183.40 kW) is achieved using R1234yf as working fluid. However, considering the economic viability, which is one of the most important issues to be taken into account for all engineering systems, it is seen that R1234yf is also the most expensive fluid for electricity generation among the fluids listed in Table 10 (10.57 $/h).

- On the other hand, the least electricity generation (142.70 kW) occurs at the thermoeconomically most affordable cost with R245fa (9.35 $/h). It is clearly seen that there is an inverse proportion between thermodynamic and thermoeconomic performances of the working fluids. Considering the governing equations given in Table 3 used to obtain the sub-components PEC values in each designed TS-ORC system based on the type of working fluid, the reason for this inverse ratio becomes apparent. Since the system's equipment costs with high power generation increase, then the power

Table 8. Thermodynamic properties of the TS-ORC with respect to state points in Figure.1

	State	Fluid	T (°C)	P (bar)	ṁ (kg/s)	h (kJ/kg)	s (kJ/kg.K)	Ψ (kJ/kg)
R245fa	1	Exhaust	280	1.013	5.268	558.3	6.323	76.78
	2	Exhaust	60	1.013	5.268	333.8	5.807	3.567
	3	R245fa	45	26.46	3.364	259.9	1.196	6.746
	4	R245fa	181.3	26.46	3.364	558.7	1.961	81.5
	5	R245fa	134.5	5.291	3.364	527.2	1.974	45.9
	6	R245fa	181.3	5.291	3.364	579.7	2.096	62.7
	7	R245fa	165.4	2.646	3.364	564	2.103	45.05
	8	R245fa	41.78	2.646	3.364	255	1.187	4.674
	9	Water	20	1	9.602	83.93	0.2962	0
	10	Water	42	1	9.602	175.9	0.5989	3.289
	11	Exhaust	196.3	1.077	4.46	472	6.137	45.15
	12	Exhaust	60	1.077	4.46	333.8	5.79	8.722
R1234ze	1	Exhaust	280	1.013	5.268	558.3	6.323	76.78
	2	Exhaust	60	1.013	5.268	333.8	5.807	3.567
	3	R1234ze	45	80.48	4.282	263.1	1.192	37.01
	4	R1234ze	181.3	80.48	4.282	497.9	1.798	94.05
	5	R1234ze	106.5	16.1	4.282	470.1	1.811	62.49
	6	R1234ze	181.3	16.1	4.282	556.1	2.017	87.85
	7	R1234ze	160.3	8.048	4.282	538.4	2.025	68.03
	8	R1234ze	41.78	8.048	4.282	258.3	1.197	30.68
	9	Water	20	1	11.08	83.93	0.2962	0
	10	Water	42	1	11.08	175.9	0.5989	3.289
	11	Exhaust	196.3	1.077	4.46	472	6.137	45.15
	12	Exhaust	60	1.077	4.46	333.8	5.79	8.722
R1234yf	1	Exhaust	280	1.013	5.268	558.3	6.323	76.78
	2	Exhaust	60	1.013	5.268	333.8	5.807	3.567
	3	R1234yf	45	106.5	4.701	261	1.178	45.08
	4	R1234yf	181.3	106.5	4.701	474.9	1.731	96.66
	5	R1234yf	107.5	21.3	4.701	448.6	1.743	66.79
	6	R1234yf	181.3	21.3	4.701	538.6	1.959	93.42
	7	R1234yf	160.3	10.65	4.701	521.2	1.967	73.94
	8	R1234yf	41.78	10.65	4.701	256.4	1.191	36.33
	9	Water	20	1	11.5	83.93	0.2962	0
	10	Water	42	1	11.5	175.9	0.5989	3.289
	11	Exhaust	196.3	1.077	4.46	472	6.137	45.15
	12	Exhaust	60	1.077	4.46	333.8	5.79	8.722

Table 9. Exergy and cost flow rates of the TS-ORC with respect to state points in Figure.1

State	R245fa		R1234ze		R1234yf	
	Ėx (kW)	Ċ ($/h)	Ėx (kW)	Ċ ($/h)	Ėx (kW)	Ċ ($/h)
1	404.48	1.456	404.48	1.456	404.48	1.456
2	18.79	0.06764	18.79	0.06764	18.79	0.06764
3	22.69	2.85	158.48	1.567	211.92	1.481
4	274.17	5.442	402.72	4.16	454.40	4.087
5	154.41	3.065	267.58	2.764	313.98	2.815
6	210.92	4.187	376.17	3.886	439.17	3.937
7	151.55	3.408	291.30	3.349	347.59	3.447
8	15.72	1.339	131.37	0.03134	170.79	0.1561
9	0.00	0	0.00	0	0.00	0
10	31.58	2.204	36.44	3.551	37.82	3.791
11	201.37	0.7249	201.37	0.7249	201.37	0.7249
12	38.90	0.14	38.90	0.14	38.90	0.14

production cost is expected to increase. For this reason, it is revealed that optimization is critical to find the most suitable conditions for a system.

- In the assessment of the WtE systems, the cost associated with the thermodynamically optimal cases are sometimes significantly higher. Accordingly, studies focusing only on the thermodynamically optimal performance to improve an existing system can lead to gross misevaluations and skewed decision making. On the other hand, qualitative analysis of energy, which is the basis of a rational cost assessment, offers a realistic perspective in improving systems. In the following section, the proposed system scenario's performative optimization steps with an optimization strategy based on effective exergetic cost analysis are presented.

The overall exergy efficiency for the FBSSI+TS-ORC system can be calculated using the equation in the following (state numbers refer to Figure. 1 and Tables 5 and 10),

$$\varepsilon_{FBSSI+TS-ORC} = \frac{\sum \dot{E}x_P}{\sum \dot{E}x_F}$$
$$= \frac{\dot{E}x_{16} + \dot{E}x_{17} + \dot{E}x_{29} + \dot{W}_{net,TS-ORC}}{\dot{E}x_{13}^{C\square emical} + \dot{E}x_{19}} \quad (4)$$

Table 10. Thermodynamic and thermoeconomic analysis results of the TS-ORC

Working fluid	η (%)	ε (%)	Ẇ (kW)	ĊORC,tot ($/h)	ŻORC,tot ($/h)
R245fa	2.83	23.55	142.70	9.35	7.38
R1234ze	3.45	28.70	173.90	10.29	8.32
R1234yf	3.63	30.30	183.40	10.57	8.59

The FBSSI + TS-ORC system's overall exergy efficiencies are found to be 72.8%, 73.2%, and 73.3% using Equation (4) for the selected working fluids R245fa, R1234ze, R1234yf, respectively. It is observed that the contribution of the TS-ORC system to an effective exergy
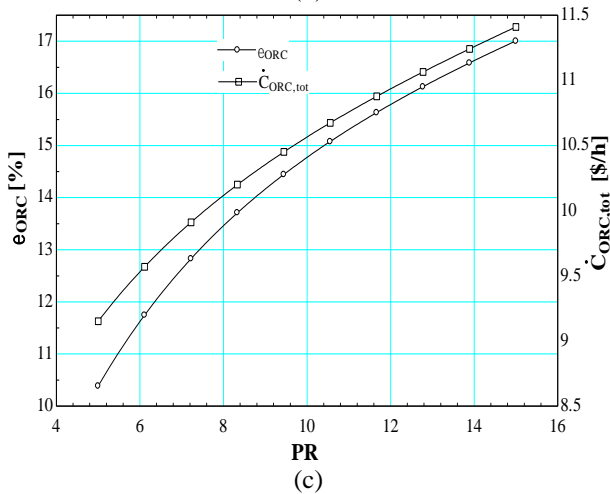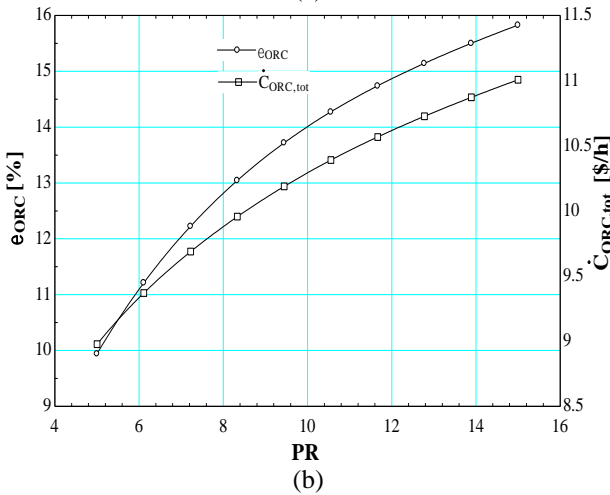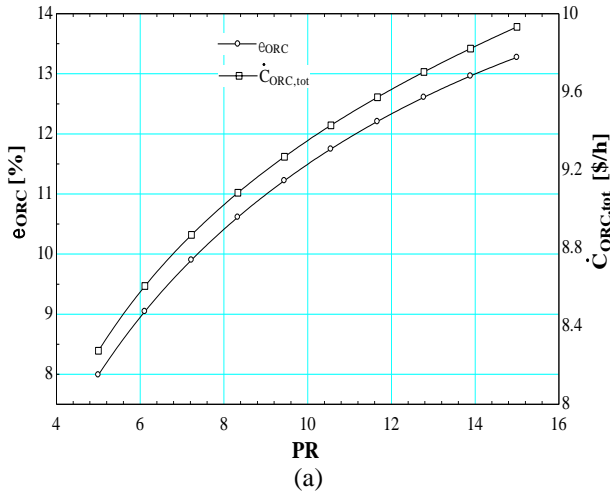
Figure 3. The effect of the pressure ratio (PR) on the exergy efficiency and total exergetic cost rate of the TS-ORC for (a) R245fa, (b) R1234ze, (c) R1234yf

as an economically not so feasible attempt with little benefit and high investment. However, if we consider the current global energy and environmental problems as our bottlenecks, we should not hesitate to offer innovative approaches to evaluate even the lowest heat source. Another solution can be district heating implication, and this will be taken into consideration in another research study; that is why the district heating scenario is excluded in this presented paper.
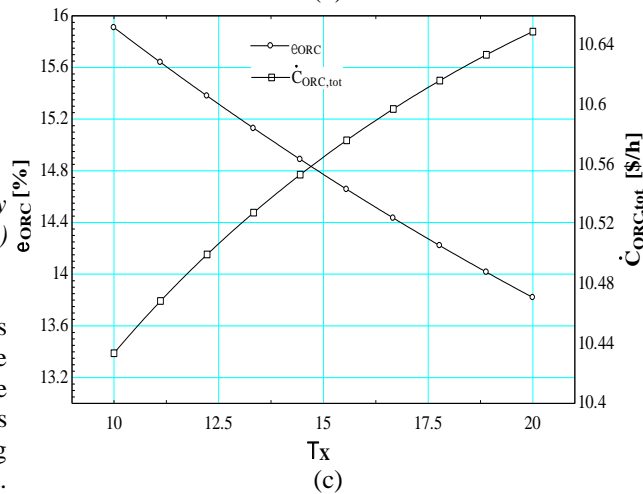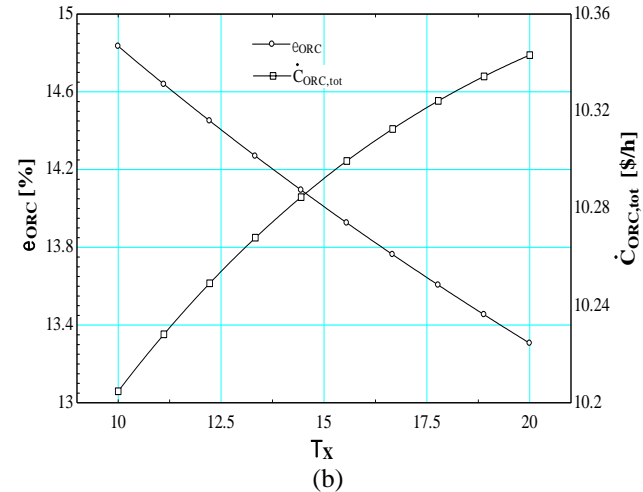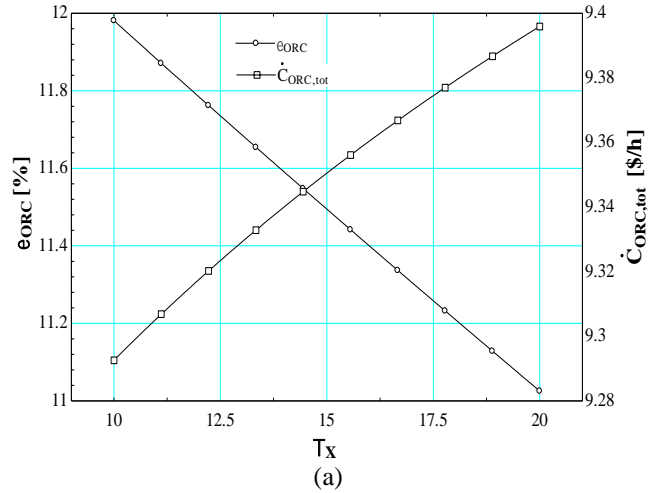

Figure 4. The effect of the temperature difference between the hot stream exit temperature and the cold stream inlet temperature in heat exchangers (Tx) on the exergy efficiency and total exergetic cost rate of the TS-ORC for (a) R245fa, (b) R1234ze, (c) R1234yf.

usage of the waste heat discharged by exhaust gases at states 1 and 11 (see Figure. 1) is relatively low than expected. One reason for that we have to use a low-to-medium temperature heat source for the designed TS-ORC. The exhaust gas temperature gradually decreases off through the drying applications and auxiliary processes in the FBSSI plant. Correspondingly, the exergy of the combustion gases is mostly destructed through these mandatory processes in the FBSSI plant. This is the inevitable result since the main purpose of incineration in the FBSSI plant is to dry the sewage sludge by increasing its dry matter content to 50-60%. As a final solution, developing an ORC system scenario in the scope of WtE for this case study may be seen

(a)

(b)

(c)

Figure 5. The effect of the dead state temperature (T0) on the exergy efficiency and total exergetic cost rate of the TS-ORC for (a) R245fa, (b) R1234ze, (c) R1234yf

In this study, various parametric studies are carried out using selected decision variables (PR, T_x, and T_0; see section 2.4) to evaluate the thermodynamic and thermoeconomic performances of the TS-ORC system. These parametric studies reveal the effects of the decision parameters' variations on the exergy efficiency and electricity production cost of the system. Figure. 3 shows the effect of the pressure ratio (PR) on the exergy efficiency and total exergetic cost rate of the TS-ORC for each working fluid. As seen, both the exergy efficiency and total exergetic cost rate increase with increasing the pressure ratio of the TS-ORC system for each working fluid. As the pressure ratio increases, the working fluid at a higher pressure enters the turbines and leaves at a

lower pressure. Thus, the net power output and exergy efficiency of the system increase. On the other hand, as the costs of the power production and consumption units of the system will increase with the increasing power generation, it is expected that the total production cost will also increase.
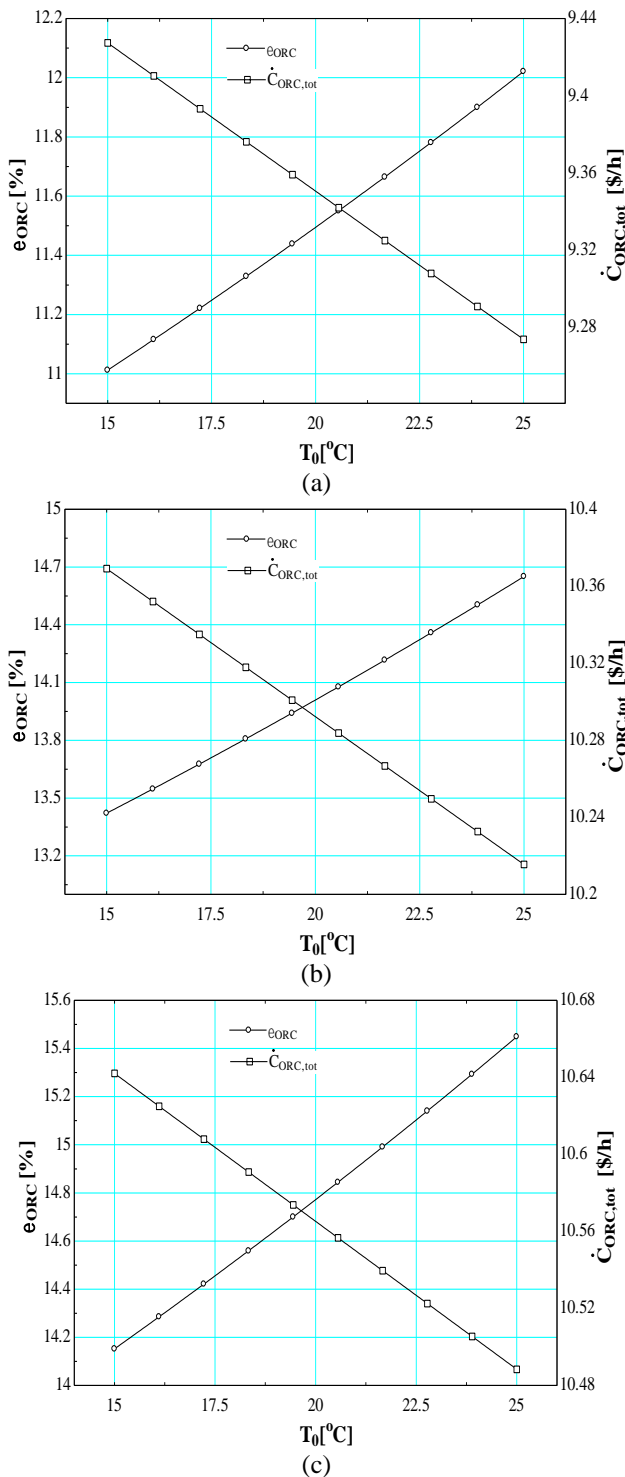
Figure. 4 shows the effect of the difference between the hot fluid's outlet temperature and cold fluid's inlet temperature of a heat exchanger on the system's exergy efficiency and total production cost. As understood, the increase in the temperature difference has a negative effect on both the exergy efficiency and total production cost of the TS-ORC system. Considering the TS-ORC system's design, the increase in temperature difference in the heat exchanger directly causes a decrease in the working fluid temperature at the turbine inlet. As a result, power generation in the turbine decreases, and power consumption in the pump increases due to the increasing load. This directly causes the reduction of the exergy efficiency of the TS-ORC. The total production cost can be expected to decrease considering the lower equipment costs due to reduced power generation. In this case, the costs required for both high-pressure and low-pressure turbines (PEC) are reduced. However, as the pump cost increases more than the cost of both turbines, the total production cost also increases. Thus, as the temperature difference (T_x) increases in the heat exchanger, the TS-ORC system's exergy efficiency decreases, whereas the total production cost of the system increases.

Figure. 5 shows the effect of the dead state temperature on the exergy efficiency and total production cost of the TS-ORC for each working fluid. It is observed in Figure 5 that the increase in the dead-state temperature has a positive effect on both the exergy efficiency and total production cost. This is because exergy losses are reduced with the increasing environmental temperature while the net power generation in the system remains constant. Thus, while the exergy efficiency increases, the total production cost decreases with the increasing dead state temperature. Considering Figures 3 through 5 on the whole, it is seen that the most effective parameter in the TS-ORC system is the pressure ratio. As the pressure ratio changes, inlet and outlet pressures of the turbine change, and thus the net power output value changes accordingly. Seeing Figure.3, the exergy efficiency and total production cost change in percentage are more than Figures 4 and 5. However, a change at the same rate is not observed in the temperature difference or the dead state temperature change. This result reveals that pressure is a relatively more effective parameter in the TS-ORC design than temperature.

3. Thermodynamic and Thermoeconomic Optimization of the TS-ORC

In this study, each working fluid's Pareto frontier is created by using a multi-objective function solution according to both the best exergy efficiency and electricity generation cost. Note that each optimization solution evaluated can be considered as the best solution according to the decision stage. However, in this study, the most compromise solution is considered and emphasized as the best solution to compare the optimization and decision stage results. In making this choice, the results of the solutions obtained during the design phase are considered. Pareto frontier images corresponding to each working fluid are given in Figures 6 to 8. Exergy efficiency and total production cost values calculated at the TS-ORC system's design stage are determined as constraints and indicated with dashed lines on the Figures. In the Pareto frontier, the closest

value of the optimum results between these dashed lines to the intersection is determined as "the best solution." Then, the decision parameters (PR, T_x, T_0) of this point are determined, and the optimum exergy efficiency and total production cost values of the TS-ORC system are calculated.
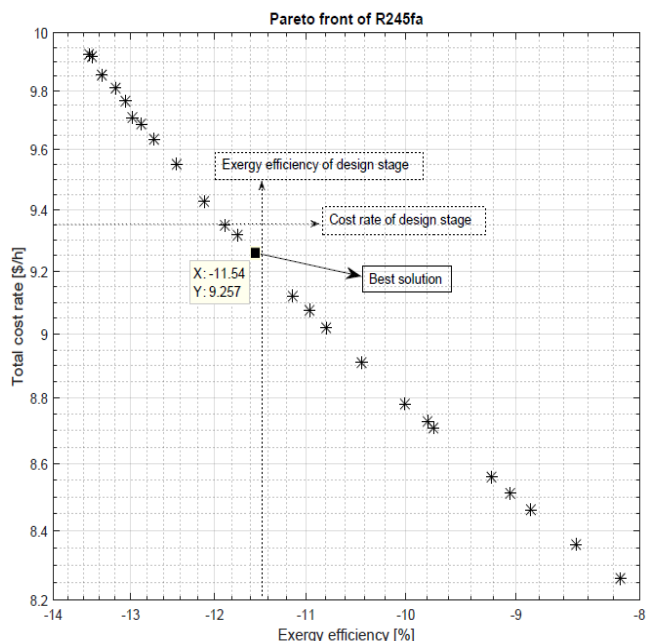

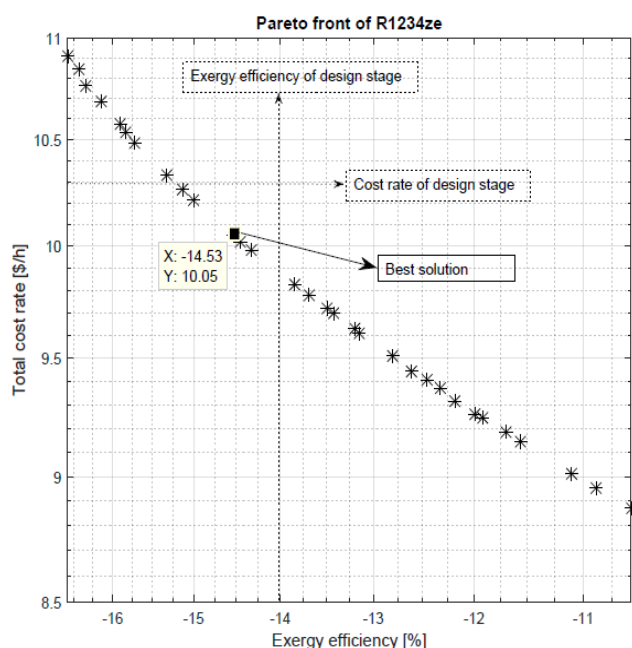Figure 6. Pareto frontier of the R245fa in the TS-ORC

Figure 7. Pareto frontier of the R1234ze in the TS-ORC

Optimum design values depending on the decision parameters of each working fluid are shown in Table 11. These values are found with NSGA-II optimization. The variations in the optimum design values are determined during the design stages. The results determining the thermodynamic and thermoeconomic performance parameters of the TS-ORC system using each decision variable's optimum results are shown in Table 12. As seen, improvements are made for each fluid, and both thermodynamic and thermoeconomic performance improvements are observed. According to these results, the most suitable working fluid for the designed TS-ORC system cannot be indicated. Because as the power generation

increases according to the working fluid selected, the system's total cost increases due to the increased equipment cost. Thus, it is necessary to consider more than one factor to make a suitable working fluid proposition for the TS-ORC system. Herein, the investor's budget plays a major role in choosing the working fluid. The electricity demand to be met by the designed TS-ORC system is relatively secondary since it is related to the investor's budget. As a result of the optimization, the highest increase in thermodynamic performance is achieved using R1234yf with a net power increase of 5%. On the other hand, if the R1234ze is selected, a decrease of about %2.8 will be observed in the total production cost of the TS-ORC system.
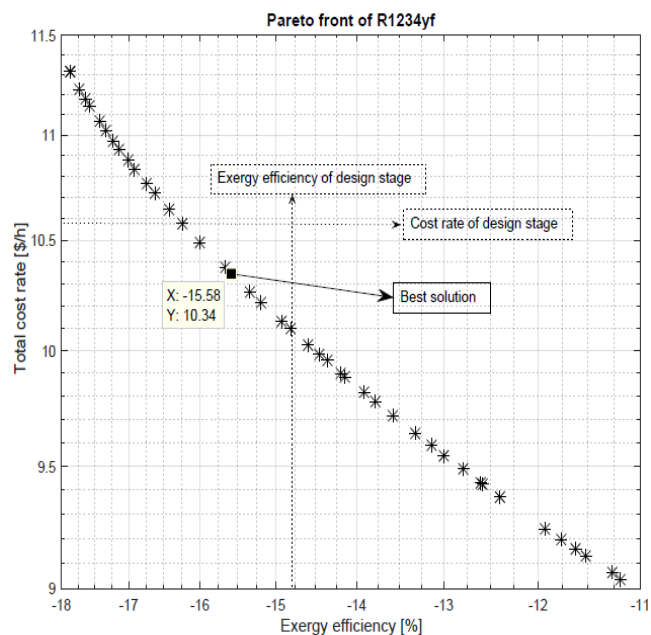

Figure 8. Pareto frontier of the R1234yf in the TS-ORC

Table 11. Optimum design values depending on the decision parameters for each working fluid using NSGA-II

Decision parameters	Decision stage	Optimum design of decision parameters for working fluids		
		R245fa	R1234ze	R1234yf
PR	10	9.55	9.26	9.52
T_x	15	10.71	10.11	10.37
T_0	20	18.46	20.98	20.50

Table 12. NSGA-II results for the TS-ORC

Performance parameters	R245fa		R1234ze		R1234yf	
	Design	NSGA	Design	NSGA	Design	NSGA
$\dot{W}$ (kW)	142.70	145.20	173.90	178.80	183.40	192.60
η (%)	7.93	8.07	9.67	9.94	10.19	10.71
ε (%)	11.49	11.54	14.01	14.53	14.77	15.58
$\dot{C}_{ORC,tot}$ ($/h)	9.35	9.26	10.29	10.05	10.57	10.34
$\dot{Z}_{ORC,tot}$ ($/h)	7.38	7.26	8.32	8.09	8.59	8.37

The decision-makers responsible for waste management in local municipalities should keep in mind that the exhaust gas sourced from the FBSSI facility is a unique and sustainable energy source in terms of waste-to-energy. Therefore, in a sewage sludge incineration facility, power generation should be envisaged depending on the incinerator's waste heat capacity rather than meeting a predetermined electricity requirement. Once this system is designed, it is necessary to ensure that the TS-ORC system operates under thermodynamically and thermo-economically best circumstances. In this study, a systematic

method is proposed and developed, and applied to provide the designed system's optimum working conditions. The use of sewage sludge as a sustainable resource within the scope of waste-to-energy can be encouraged by local governments to implement the study results.

According to the data received from TUIK [47], by the end of 2019, approximately 300,000 tons of municipal sewage sludge were produced in Turkey and the corresponding dry matter content of it was reported as nearly 60,000 tons. However, only 31.4% of the digested sewage sludge is being burned in FBSSI systems for disposal purposes. As seen, it is imperative that treatment sludge be disposed of in a sustainable manner by minimizing the damage to the environment. This study reveals the possibilities of a sustainable WtE approach for an effective design.

4. Conclusion

In this paper, a TS-ORC system is designed using the waste heat (exhaust gas) of a real FBSSI plant as a source. The TS-ORC design is built by the actual operating conditions of the FBSSI facility. Thermodynamic and thermoeconomic procedures and formulations are developed and expanded, considering the characteristics and structures of both the FBSSI plant and the designed TS-ORC system. TS-ORC system is analyzed and evaluated both thermodynamically and thermoeconomically according to the effects of three different working fluids on the performance parameters. Finally, the TS-ORC system's multi-objective optimization is performed in MATLAB using the non-dominated sorting genetic algorithm (NSGA-II) method. In the following some concluding remarks are given:

- The FB combustor's exergy efficiency is 63.11%, which corresponds to the exergy destruction of approximately 3317.86 kW. The second highest exergy destruction in the FBSSI plant is taken place in the cyclone as 794 kW. The third-largest share of the total exergy destruction of the overall FBSSI plant originates from the first economizer, which has the exergy destruction of about 532 kW, and its exergy efficiency is found to be approximately 61%. The second and third economizers have high amounts of exergy destructions in the FBSSI plant, and their exergy destructions are found to be 393 and 483.3 kW, respectively. The exergy efficiency of the FBSSI plant is found to be 70.5% which proves that exergy transfer by heat is inevitably degraded mostly due to the high-temperature differences between systems' boundary and the environment.
- The highest power generation in the TS-ORC system (183.40 kW) is achieved using R1234yf as working fluid. R1234yf is also the most expensive fluid for electricity generation among the other working fluids (10.57 $/h).
- The least electricity generation in the TS-ORC (142.70 kW) occurs at the thermoeconomically most affordable cost with R245fa (9.35 $/h).
- The FBSSI + TS-ORC system's overall exergy efficiencies are found to be 72.8%, 73.2%, and 73.3% for the selected working fluids R245fa, R1234ze, R1234yf, respectively.
- Both the exergy efficiency and total exergetic cost rate increase with increasing the PR of the TS-ORC system for each working fluid.
- As the temperature difference (T_x) increases in the heat exchanger, the TS-ORC system's exergy efficiency decreases, whereas the total production cost of the system increases.
- The increase in the dead-state temperature has a positive effect on both the exergy efficiency and total production cost. Thus, while the exergy efficiency increases, the total production cost decreases with the increasing dead state temperature.
- According to the optimization results, the most suitable working fluid for the designed TS-ORC system cannot be indicated. Because as the power generation increases according to the working fluid selected, the system's total cost increases due to the increased equipment cost. Thus, it is necessary to consider more than one factor to make a suitable working fluid proposition for the TS-ORC system, such as investor's budget, the electricity demand, etc.

Nomenclature

A	heat transfer area, m^2
$\dot{C}$	cost rate, $/h
c	cost per exergy unit, $/GJ
c_f	unit exergy cost of fuel, $/GJ
c_p	unit exergy cost of fuel, $/GJ
$\dot{D}$	cost rate of exergy destruction, $/h
$\dot{Ex}$	exergy rate, kW
$\square$	specific enthalpy, kJ/kg
i	interest rate
$\dot{m}$	mass flow rate, kg/s
n	total life time
N	annual operation time
P	pressure, bar
PR	pressure ratio of TS-ORC
$\dot{Q}$	heat addition, kW
s	specific entropy, kJ/kg-K
T	temperature, ^{o}C
U	heat transfer coefficient, kW/m^2-K
$\dot{W}$	work flow rate-power, kW
$\dot{Z}$	capital cost rate, $/h

Subscripts and Abbreviations

0	dead state
a	actual
CEPCI	chemical engineering plant cost index
CON	condenser
CRF	capital recovery factor
crit	critical point
D	destruction
EMO	evolutionary multi-objective optimization
EVAP	evaporator
exh	exhaust
FBSSI	fluidized bed sewage sludge incineration
HPT	high-pressure turbine
ORC	organic Rankine cycle
OT	ORC turbine
k	component

LMTD	logarithmic mean temperature difference
LPT	low-pressure turbine
NSGA-II	non-dominated sorting genetic algorithm
PEC	purchased equipment cost
PUMP	ORC pump
REGEN regenerator	
s	isentropic
tot	total
wat	water
wf	working fluid

Greek symbols

ε	exergy efficiency
εf_{HE}	effectiveness
η	energy efficiency
η_{PUMP}	ORC pump isentropic efficiency
η_T	ORC turbine isentropic efficiency
ϕ	maintenance factor
ψ	specific flow exergy, kJ/kg

References

[1] W. J. Ludikhuize, Special report: Research on new thermal treatment processes for domestic refuse in the Netherlands, Resour Recov Conserv, 5 (1980) 267-274.

[2] H. Wall, E. Waltz, A. Verdouw, Fuel savings in sewage sludge incineration, Waste Manage Res, 2 (1984) 205-225.

[3] S. Sakai, M. Hiraoka, N. Takeda, I. Ohhama, System design and full-scale plant study on a drying-incineration system for sewage sludge, Water Sci Technol, 21 (1989) 1453-1466.

[4] M. Hassebrauck, G. Ermel, Two examples of thermal drying of sewage sludge, Water Sci Technol, 33 (1996) 235-242.

[5] P. Thipkhunthod, V. Meeyoo, P. Rangsunvigit, B. Kitiyanan, K. Siemanond, T. Rirksomboon, Predicting the heating value of sewage sludges in Thailand from proximate and ultimate analyses, Fuel, 84 (2005) 849-857.

[6] P. Stasta, J. Boran, L. Bebar, P. Stehlik, J. Oral, Thermal processing of sewage sludge, Appl Therm Eng, 26 (2006) 1420-1426.

[7] T. Taruya, N. Okuno, K. Kanaya, Reuse of sewage sludge as raw material of Portland cement in Japan, Water Sci Technol, 46 (2002) 255-258.

[8] T. Murakami, Y. Suzuki, H. Nagasawa, T. Yamamoto, T. Koseki, H. Hirose, S. Okamoto, Combustion characteristics of sewage sludge in an incineration plant for energy recovery, Fuel Process Technol, 90 (2009) 778-783.

[9] B. Khiari, F. Marias, J. Vaxelaire, F. Zagrouba, Incineration of a small particle of wet sewage sludge: A numerical comparison between two states of the surrounding atmosphere, J Hazard Mater, 147 (2007) 871-882.

[10] J. Werther, T. Ogada, Sewage sludge combustion, Prog Energy Combust Sci, 25 (1999) 55-116.

[11] P. L. Chem, J. A. Hudson, Incineration – Is there a case? Water Environ J, 19 (2005) 286-295.

[12] S. Werle, R. K. Wilk, A review of methods for the thermal utilization of sewage sludge: Polish perspective, Renewable Energy, 35 (2010) 1914-1919.

[13] Y. Cao, A. Pawlowski, Sewage sludge-to-energy approaches based on anaerobic digestion and pyrolysis: Brief overview and energy efficiency assessment, Renew Sust Energ Rev, 16 (2012) 1657-1665.

[14] M. Horttanainen, J. Kaiko, R. Bergman, M. Pasila-Lehtinen, J. Nerg, Performance analysis of power generating sludge combustion plant and comparison against other sludge treatment technologies, Appl Therm Eng, 30 (2010) 110-118.

[15] S. Li, Y. Li, Q. Lu, J. Zhu, Y. Yao, S. Bao, Integrated drying and incineration of wet sludge in combined bubbling and circulating fluidized bed units, Waste Manage, 34 (2014) 2561-2566.

[16] J Zhou, Y. Yao, Q. Lu, M. Gao, Z. Ouyang, Experimental investigation of gasification and incineration characteristics of dried sewage sludge in a circulating fluidized bed, Fuel, 150 (2015) 441-447.

[17] M. C. Samolada, A. A. Zabaniotou, Comparative assessment of municipal sewage sludge incineration, gasification, and pyrolysis for a sustainable sludge-to-energy management in Greece, Waste Manage, 34 (2014) 411-420.

[18] H. Ahn, D. Kim, Y. Lee, Combustion characteristics of sewage sludge solid fuels produced by drying and hydrothermal carbonization in a fluidized bed, Renewable Energy, 147 (2020) 957-968.

[19] M. Schnell, T. Horst, P. Quicker, Thermal treatment of sewage sludge in Germany: A review, J Environ Manage, 263 (2020) 110367.

[20] A. Abusoglu, A. Anvari-Moghaddam, J. M. Guerrero, Producing bio-electricity and bio-heat from urban sewage sludge in Turkey using a two-stage process, 5th International Conference on Power Generation Systems and Renewable Energy Technologies (PGSRET 2019), August 26-27, 2019, Istanbul, Turkey. DOI:10.1109/PGSRET.2019.8882699

[21] N. Gao, K. Kamran, C. Quan, P. T. Williams, Thermochemical conversion of sewage sludge: A critical review, Prog Energy Combust Sci, 79 (2020) 100843.

[22] D.K. Sarkar, Thermal Power Plant: Design and Operation, ISBN: 978-0-12-801575-9, Elsevier Inc, 2015.

[23] F. Scala, Fluidized bed technologies for near-zero emission combustion and gasification, ISBN: 978-0-85709-880-1, Woodhead Publishing Ltd, 2013.

[24] M. R. Taib, J. Swithenbank, V. S. Nasserzadeh, M. Ward, D. Cottam, Investigation of sludge waste incineration in a novel rotating fluidized bed incinerator, Process Saf Environ Prot, 77 (1999) 298-304.

[25] W. Y. Wong, Y. Lu, V. S. Nasserzadeh, J. Swithenbank, T. Shaw, M. Madden, Experimental investigation into the incineration of wool scouring sludges in a novel rotating fluidized bed, J Hazard Mater, 73 (1999) 143-160.

[26] J. V. Caneghem, A. Brems, P. Lievens, C. Block, P. Billen, I. Vermeulen, R. Dewil, J. Baeyens, C. Vandecasteele, Fluidized bed waste incinerators: Design operational and environmental issues, Prog Energy Combust Sci, 38 (2012) 551-582.

[27] A. Shukrie, S. Anuar, A. Alias, Heat transfer of alumina sands in a fluidized bed combustor with novel circular edge

segments air distributor, Energy Procedia, 75 (2015) 1752-1757.

[28] R. Yan, T. D. Liang, L. Tsen, Case studies – Problem solving in fluidized bed waste fuel incineration, Energ Convers Manage, 46 (2005) 1165-1178.

[29] W. A. W. A. K. Ghani, A. B. Alias, R. M. Savory, K. R. Cliffe, Co-combustion of agricultural residues with coal in a fluidized bed combustor, Waste Manage, 29 (2009) 767-773.

[30] F. Burgess, P. D. W. Lloyd, P. S. Fennell, A. N. Hayhrust, Combustion of polymer pellets in a bubbling fluidized bed, Combust Flame, 158 (2011) 1638-1645.

[31] B. Liu, X. Yang, W. Song, W. G. Lin, Process simulation of formation and emission of NO and N_2O during decoupling combustion in a circulating fluidized bed combustor using Aspen Plus, Chem Eng Sci, 71 (2012) 375-391.

[32] Y. Koç, H. Yağlı, A. Koç, Exergy analysis and performance improvement of a subcritical/supercritical organic Rankine cycle (ORC) for exhaust gas waste heat recovery in a biogas fuelled combined heat and power (CHP) engine through the use of regeneration, Energies, 12 (2019) 1-22.

[33] S. Safa, K. Mobini, M. H. Khoshgoftar Manesh, Thermal and Exergetic Study of the Integrated "Multi-Effect Desalination"- "Solar Rankine Cycle" System for the Iranian Southern Coastal Regions, Int J of Thermodynamics, 24 (1) (2021) 31-52.

[34] G. Eksi, F. Karaosmanoglu, Combined bioheat and biopower: A technology review and an assessment for Turkey, Renew Sust Energ Rev, 73 (2017) 1313-1332.

[35] R. Strzalka, D. Schneider, U. Eicker, Current status of bioenergy technologies in Germany, Renew Sust Energ Rev, 72 (2017) 801-820.

[36] A. Abusoglu, A. Tozlu, A. Anvari-Moghaddam, District heating and electricity production based on biogas produced from municipal WWTPs in Turkey: A comprehensive case study, Energy, 223 (2021) 1-18. https://doi.org/10.1016/j.energy.2021.119904

[37] E. Ozahi, A. Tozlu, A. Abusoglu, Thermoeconomic multi-objective optimization of an organic Rankine cycle (ORC) adapted to an existing solid waste power plant, Energy Convers Manage, 168 (2018) 308-319.

[38] E. Ozahi, A. Abusoglu, A. Tozlu, A comparative thermoeconomic analysis and optimization of two different combined cycles by utilizing waste heat source of an MSWPP, Energy Convers Manage, 228 (2021) 113583.

[39] Çengel, Y. A., & Boles, M. A. Thermodynamics: An engineering approach. Boston: McGraw-Hill (2001).

[40] D. Mignard, Correlating the chemical engineering plant cost index with macro-economic indicators, Chem. Eng. Res. and Des., 92 (2014) 285-294.

[41] M. Jradi, S. B. Rıffat, Comparative thermodynamic and techno-economic assessment of green methanol production from biomass through direct chemical looping processes, J of Clean. Prod., 321 (2021) 129023.

[42] D. Baruah, D. C. Baruah, Decision support system based planning of biomass gasification system for decentralised energy generation, Renew. Energy Focus, 38 (2021) 22-35.

[43] http://www. http://www.asimptote.nl/software/cycle-tempo/cycle-tempo-model-examples/

[44] J. Szargut, D. R. Morris, F. R. Steward, Exergy analyses of thermal, chemical and metallurgical processes, California: Hemisphere Publishing Co., (1988).

[45] E. Cartmell, P. Gostelow, D. Riddell-Black, N. Simms, J. Oakey, J. Morris, Biosolids – A fuel or a waste? An integrated appraisal of five co-combustion scenarios with policy analysis, Environ Sci Technol, 40 (2006) 649-658.

[46] P. Stasta, J. Boran, L. Bebar, P. Stehlik, J. Oral, Thermal processing of sewage sludge. Appl Therm Eng 26 (2006) 1420-1426.

[47] https://data.tuik.gov.tr/Bulten/Index?p=Belediye-Atiksu-Istatistikleri-2018-30667

Book review: Thermal Analysis and Thermodynamic Properties of Solids (2nd Edition) by Jaroslav Šesták, Elsevier 2021, ISBN: 9780323855372

Robert Černý[*]

Department of Materials Engineering and Chemistry, Faculty of Civil Engineering, Czech Technical University in Prague
Thákurova 7, 16629 Prague 6, Czech Republic
E-mail: cernyr@fsv.cvut.cz

The book covers foundational principles and recent updates in the field of thermal science, presenting an authoritative overview of theoretical knowledge and practical applications across several fields. Since the first edition of this book was published in 2005, great progress has been made in the theoretical understanding - and subsequent ability to assess and apply - of the principles of thermal analysis, especially in thermodynamic intention with emphasis on temperature conditions. Features twenty-chapter contributions on 660 color pages provides an up-to-date cutting-edge themes involving the thermal analysis, thermotics, thermodynamics, thermal and applied solid-state physics, macro- and micro- dimensional approach to selected materials and their thermal properties.

The book provides the latest and most exceptional look at theoretical thermal analysis performed with processes out of thermal equilibrium (non-isothermal) and should become an essential part of all libraries of institutions with a similar material approach. It contains significant chapters featured in the book in two parts. Basics, such as

1. Thermophysical examinations, experimental set-ups, sample and temperature control
2. Understanding of temperature, heat, gradients and related thermodynamics
3. Phenomenological approach to the caloric theory of heat: An alternative thermodynamics
4. Thermostatics as textbook thermodynamics
5. Equilibrium background and its importance for temperature and particle size
6. Thermodynamics: Processes dynamics under constant heating
7. Thermotics: Theoretical thermal analysis, thermometry and calorimetry
8. Rationality of creating kinetic models: how to mold a reaction path in solid-state
9. Facilitated reaction kinetics by thermal analysis
10. Thermokinetics in DTA experiments
11. Physical thermokinetics of reversible thermal decomposition by thermogravimetry
12. Exploiting fractals, tackle thermal processes and truer non-isothermal kinetics,
1. and practical applications comprising of
13. Constrained states of glasses, exploitation of transition temperatures, glass -forming coefficients and concepts of fragility
14. Explanation of crystallization kinetics of both glasses during heating and melts on cooling while indicating the incorrectness of Kissinger method
15. Kinetic phase diagrams as an enforced consequence of rapid changing temperature or diminishing particle size
16. Thermodynamic description of mobile components behavior in non-stoichiometric partially open ceramic systems and superconductor model
17. Thermodynamics of periodic processes, dendrite self-similarity, self-organization and stimulated quantum diffusion
18. Non-bridging oxygen in silica bio-compatible ceramics, poly-sialates and geo-polymers
19. Thermodynamics and social behavior, econophysics and ecosystems applied in relation of laws against feelings
20. Thermal analysis scheme aimed at better understanding of the Earth's climate changes due to the alternating irradiation.

See: https://www.elsevier.com/books/thermal-analysis-and-thermodynamic-properties-of-solids/sestak/978-0-323-85537-2

In addition, it contains very convincing introductory matter such as "Anniversary of the half-century development and formation of a new field of thermal analysis" providing detailed description of the early development and "Glossary of terms, definition and symbols" giving an important overview of the meanings further elaborated in the text. Important is the section "Literature", which is concentrated on 71 separate pages containing almost two thousand multiple citations, including the titles of articles covering practically everything available on individual topics. The book will become an important tool for advanced undergraduates, graduate students, postdoctoral fellows, researchers, and lecturers working in the field of thermodynamic studies and thermophysical measurements, who will find this collection invaluable, as were the books once available at the beginning of 1960s of the field emergence.

The author Prof J. Šesták is a multi-award-winning scientist, educator, photographer and mountaineer, awarded for his life achievements in solid-state chemistry and physics by Dr.h.c. in 2010 and by the highest Czech honor given by the President in 2017. He has worked around the world, including positions at the Nuclear Centre in Studsvik, (Sweden), University of Missouri at Rola (USA), Kyoto University (Japan), Norwegian University of Science and Technology (Trondheim), Taiwan National University (Taipei), Institute of Physics, Charles University, Czech Technical University in Prague, University of West Bohemia in Pilsen and University of New York in Prague (Czech Republic).

*Corresponding Author

Comparative Energetic, Exergetic, Environmental and Enviroeconomic Analysis of Vapour Compression Refrigeration Systems Using R515B as Substitute for R134a

Ragıp Yıldırım[1]*, Arzu Şencan Şahin[2], Erkan Dikmen[2]

[1]Deparment of Electrical and Energy, Bucak Emin Gülmez Vocational School of Technical Sciences, Burdur Mehmet Akif Ersoy University, 15300, Burdur, Turkey
[2]Department of Mechanical Engineering, Faculty of Technology, Isparta University of Applied Sciences, 32200, Isparta, Turkey
E-mail: [1]*ryildirim@mehmetakif.edu.tr

Abstract

In this study, hydrofluoroolefin R515B was used rather than hydrofluorocarbon R134a to perform energetic, exergetic, environmental and enviroeconomic analyses on vapor-compression refrigeration systems with internal heat exchangers. The exergy efficiency, exergy destruction, and coefficient of performance for cooling mode (COP) were studied. EES (Engineering Equation Solver) program was employed for thermodynamic analysis. The impact on the COP, exergy destruction, and exergy efficiency of the system was investigated at various evaporator and condenser temperatures. Performance analysis shows that the COP of R515B refrigerant is like that of R134a. It has been found that the exergetic efficiency of R515B was slightly lower (about 1.40%) than that of R134a. It has also been found that at higher evaporation temperatures, the total exergy destruction increases. The most important exergy destruction occurs in the compressor. The environmental and enviroeconomic indexes of R515B refrigerant were like those of R134a. The results demonstrated that R515B may be a good alternative to R134a in the vapour-compression refrigeration systems with internal heat exchangers.

Keywords: Vapor compression refrigeration; energy; exergy, global warming; new generation refrigerants.

1. Introduction

Concrete alternatives to the burning of fossil fuels have yet to be found. In the meantime, more and more greenhouse gases are being emitted daily for generating electricity and heat (industries, the transportation sector etc.). An increase in the atmospheric concentrations of greenhouse gases produces several undesirable environmental problems. People widely use heating, ventilation, air conditioning, and cooling systems (HVAC-R) to provide their needs and comfort in their daily lives. The energy consumed by HVAC-R is substantial. HVAC-R systems negatively affect the environment due to their energy consumption and refrigerant leaks. The refrigerant's ozone depletion potential (ODP) and global warming potential (GWP) used in HVAC-R are commonly used to evaluate the effects of refrigerants on the environment.

R134a of the HFCs group is widely used in vapor-compression systems owing to its perfect thermodynamic properties. Nevertheless, the GWP rate of R134a is very high. Therefore, R134a refrigerants are listed as controlled greenhouse gases by the Kyoto protocol (1997). With the Montreal protocol - Kigali amendment (2016), it was decided to phase out the use of R134a refrigerant [1]. Developed as an alternative to HFCs, hydrofluoroolefins (HFOs), also known as fourth-generation refrigerants, have not been extensively studied in a variety of applications. Manufacturers of refrigerants have been trying to develop HFOs, a new generation of refrigerants that has a lower

GWP and can be used as an alternative to existing HFCs. It is therefore important to find alternative refrigerants with a lower GWP that can be used instead of R134a.

The choice of refrigerant for vapor-compression refrigeration systems depends on some criteria such as thermodynamic properties, safety (flammability and toxicity), cheapness, availability, zero ODP, and lower global potential. The current alternative refrigerants fall in two categories: (I) pure refrigerants and (II) refrigerant mixtures. In general, mixed refrigerants are preferred as alternative refrigerants due to theirs lower GWP rates. In the selection of refrigerants, good thermophysical properties, its safety (toxicity and flammability), economy, environmental protection, and cycle performance parameters must be sought [2], [3].

Possible working fluid alternatives are given in Table 1. GWP value and flammability of R1234yf and R1234ze(E) are very low (A2L by ASHRAE). The non-flammable mixtures of R450A and R513A show promising results, but their GWP values are both about 550. Although the GWP rates of R450A and R513A are quite low compared to R134a, these rates are still high. The R515B refrigerant with low GWP (299) is a mixture of R1234ze(E)/R-227ea (91.1/8.9). It is also included in the non-flammable group by the ASHRAE classification (A1). The use of R515B instead of R134a in vapor compression systems hasn't been extensively studied yet. Therefore, R515B refrigerant is used as an alternative to R134a in this study.

Table 1. Main characteristics of some refrigerants that may be alternatives to R134a [4], [5]

Refrigerants	Mass of molar (kg/kmol)	Boiling Point (°C)	Critical Point (°C)	Critical Pressure (MPa)	Security Group *	ODP	GWP
R134a	102	-26.10	101.06	4.06	A1	0	1300
R1234yf	114	−29.49	94.70	3.38	A2L	0	< 1
R1234ze(E)	114	−18.97	109.36	3.64	A2L	0	< 1
R516A	102	-29.40	96.80	3.62	A2L	0	131
R513A	108	-28.30	97.70	3.70	A1	0	573
R515B	117	-18.89	108.70	3.56	A1	0	299
R450A	108	-23.35	104.47	3.82	A1	0	547

* Security group:
(a) A: Low Toxicity, B: High Toxicity;
(b) 1: Not flammable, 2: low flammability, 3: highly flammable.

Over the years a pretty good number of articles have been published in the literature on cooling systems that use refrigerants as substitutes for R134a. Ahmed et al. (2012) [6] studied the energetic and exergetic analyses of household refrigerators usage of natural isobutane and butane. They compared the performance of mixture of butane and isobutane with that of R134a in a refrigeration the system. They found that the COP of the mixture was equal to that of R134a. They also compared exergy efficiency of isobutane and R134a, and they stated that butane has higher exergy efficiency. Wantha (2019) [7] investigated the characteristics of the heat transfer of inner tube heat exchanger theoretically and experimentally using R1234yf and R134a refrigerants. He found that the coefficient of heat transfer of R134a is higher than that of R1234yf. The effectiveness of the interior heat exchanger on the exergetic efficiency was also investigated in his study. It was noted that the usage of an inner heat exchanger in a cooling system increases the energy efficiency of both refrigerants. Matu-Royo et al. (2021) [8] have examined R1234ze(E) and R515B refrigerants with lower GWP instead of R134a in the heat pump system. They found that the energy and environmental performance of R1234ze(E) and R515B are almost the same as that of R134a and the lack of flammability of R515B is an important advantage in terms of safety. Kumar (2018) [9] examined the energetic and exergetic analyses of R134a, R1234ze(E), R1234yf and its mixtures in the vapor-compression system. It has been found that R134a /R1234yf /R1234ze(E) (%40/%22/%38) mixture showed the best performance instead of R134a in his study. Prabakaran et al. (2020) [10] studied the performance and environmental analyses of mobile air conditioning systems which using R1234yf as a substitute for R134a. Also, compressor velocity on the energetic and exergetic efficiency of the system was investigated. They found that the R1234yf system has better COP and exergetic efficiency according to the R134a system. Bellman-Flores et al. (2017) [11] conducted energetic and exergetic study of R1234yf as a direct substitute for R134a in household refrigeration systems. They also noted that for both R134a and R1234yf, the irreversibilities are most intensed in the compressor. Jemaa et al. (2017) [12] have examined the energetic and exergetic analyses of the use of R1234ze(E) and R134a refrigerants in a vapor-compression cooling system. The energetic and exergetic efficiency of R134a and R1234ze are very similar. Saravanakumar and Selladurai (2014) [1] used a mixture of refrigerant R290/R600a as a substitute for R134a, and conducted an exergy analysis of household refrigerators. In general, the experimental household refrigeration system using R600a/R290 mixed refrigerant has better performance than using R134a as the refrigerant. Yatagambaba et al. (2015) [13] performed exergetic analyses of R1234ze(E) and R1234yf replace to R134a in a vapor-compression cooling system which has a double evaporator. In their studies, the effects of condenser and evaporator temperature on exergy loss and system exergy efficiency were examined. Gil et al (2018) [14] have investigated the exergetic analysis of the use of refrigerants R450A and R134a in a cooling system. In the study, they stated that under the same conditions, R450A refrigerant gave better results than R134a. Shaik et al. (2020) [15] examined the energetic and exergetic analyses on R1234yf and R152a refrigerants instead of R134a in a hausehold refrigerators. They have stated that 152a and R1234yf refrigerants may well replace R134a refrigerants without any modification. Paula et al. (2020) [16] performed energetic, exergetic and environmental analyses of the use of R290, R1234yf and R744 refrigerants instead of R134a refrigerant in a vapor-compression cooling cycle. Mota-Babiloni et al. (2017) [17] provided literature information to review some curious aspects regarding the useage of new pure synthetic refrigerants and hybrid synthetic refrigerants to replace HFCs, which have a greater impact on the environment. Perez-Garcia et al. (2017) [18] carried out the exergy analysis of MAC (mobile air-conditioning) system that use inner heat exchangers (IHX) and R134a instead of refrigerants. It was also found that when R1234ze refrigerant is used, the operating efficiency of the system is the highest. Gorzari et al. (2017) [19] compared the performance of the R134a refrigerant with that of the R1234yf refrigerant in a automobile refrigeration system. Compared with R134a, the use of R1234yf as an air-conditioning refrigerant can bring out a higher exergy efficiency.

As can be seen from the studies in the literature, energy, exergy, and optimization works relative to the use of different refrigerants with lower GWP ratios than R134a in systems operating with the vapor-compression cycles have been carried out by a lot of researchers. Nevertheless, there is a lack of studies on the examination of vapor-compression systems using the new mixture refrigerant R515B in the literature. As R134a is about to be phased out in favor of R515B or any other suitable alternative.

This study aims to perform an energetic, exergetic, environmental and enviroeconomic analyzes and comparison of the use of R134a and R515B with an internal heat exchanger in a refrigeration system.

2. Analysis of Energy and Exergy

Figure 1 schematically shows the components of the vapour compression refrigeration system (VCR) which has an internal heat exchanger (IHX).
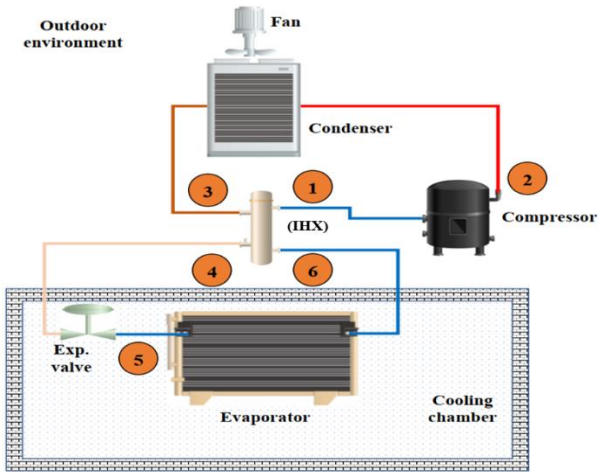

Figure 1. The vapor-compression refrigeration system diagram.

To effectively compare the application ranges of R515B and R134a, the P-T (pressure-temperature) and P-h (pressure-enthalpy) diagrams are given in Figure 2 and Figure 3, respectively. The saturation temperatures corresponding to the working pressures of the alternative refrigerants should be the same as or close to the refrigerant to be used instead. As seen in Figure 2, while the saturation pressures of R134a and R515B at low temperatures are very close, the saturation pressure of R134a at high temperatures is slightly higher than R515B.
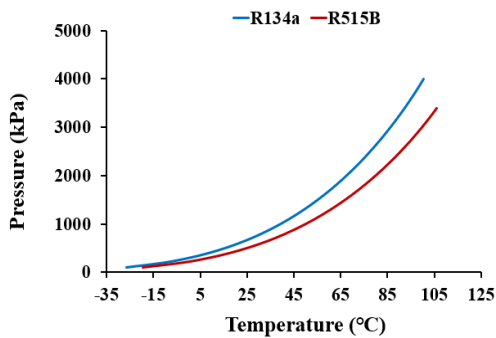

Figure 2. P – T diagram of R134a and R515B

The refrigerating effect (evaporator inlet and outlet enthalpy difference) affects the cooling capacity. The refrigerating effect of R134a at a pressure of 200, 400, 600, and 800 kPa is 206.02 kJ/kg, 191.61 kJ/kg, 180.89 kJ/kg, and 171.81 kJ/kg, respectively. For the same pressure values, the refrigerating effect of R515B is 179.77 kJ/kg, 166.63 kJ/kg, 156.73 kJ/kg, and 148.28 kJ/kg, respectively. The refrigerating effect of R515B is lower about %15.50 than that of R134a.

A computational model of vapor-compression cooling system with inner heat exchanger (IHX) has been developed to perform the thermodynamics and environmental analyses. The assumptions made to carry out this study are listed in Table 2. The REFPROP 9.1 [20] was used to obtain the refrigerant's properties.
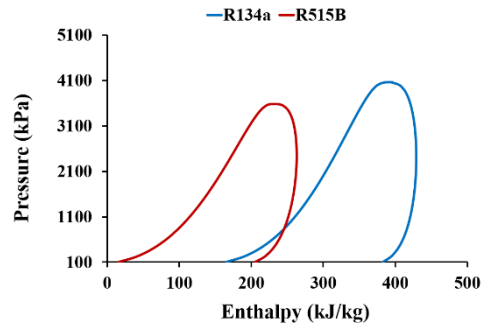

Figure 3. P-h diagram of R134a and R515B.

Table 2. Some acceptances for the analyses.

Parameter	Value
Temperature of evaporator (T_e)	(-20 ℃, 5 ℃) at steps of 5 ℃
Temperature of condenser (T_c)	40 ℃ and 45 ℃
Temperature of superheating ($\Delta T_{superheat}$)	5 ℃
Temperature of subcooling ($\Delta T_{subcooling}$)	5 ℃
Temperature difference between condenser and heat sink ($\Delta T_{heat,sink}$)	10 ℃
Temperature difference between evaporator and heat source ($\Delta T_{heat,source}$)	10 ℃
Compressor isentropic efficiency (η_{isen})	0.70
Compressor sweep volume	26.11 cm³/rev
Dead-state pressure (P_0) and temperature (T_0)	101.325 kPa and 25 ℃

The equations used in energy and exergy analyses are reproduced from the law of preservation of mass and energy. The compressor energy consumption can be calculated by the following Eqs. (1) – (5):

$$\dot{W}_{comp} = \dot{m}_r \, (h_2 - h_1) \tag{1}$$

$$h_2 = h_1 + \frac{(h_{2s} - h_1)}{\eta_{isen}} \tag{2}$$

The cooling capacity is calculated as follows:

$$\dot{Q}_{evap} = \dot{m}_r \, (h_6 - h_5) \tag{3}$$

The coefficient of performance for the cooling mode (COP) is written as:

$$COP = \frac{\text{Cooling capacity}}{\text{Compressor power consumption}} = \frac{\dot{m}_r \, (h_6 - h_5)}{\dot{m}_r \, (h_2 - h_1)} \tag{4}$$

The refrigerant mass flow rate ($\dot{m}_r$) is be calculated by:

$$\dot{m}_r = V_s \, \rho_1 \, RPM \, \frac{\eta_{vol}}{60} \tag{5}$$

Exergy analysis provides a quantitative measure of the inefficiency of cooling systems and information about exergy destruction. Assuming that the variation in the potential energy and kinetic energy can be ignored, the specific exergy is written as:

$$ex_i = (h_i - h_0) - T_0 \, (s_i - s_0) \tag{6}$$

at the ambient temperature (dead-state), T_0.

The total exergy balance equation of the compressor is given by:

$$\sum(\dot{m} \, ex)_{in} + \dot{W}_{comp} = \sum(\dot{m} \, ex)_{out} + \dot{Ex}_{dest,comp} \tag{7}$$

$$\dot{E}_1 - \dot{E}_2 + \dot{W}_{comp} - \dot{Ex}_{dest,comp} = 0 \tag{8}$$

$$\dot{Ex}_{dest,\ comp} = \dot{m}_r\left[(h_1 - h_2) - T_0(s_1 - s_2)\right] + \dot{W}_{comp} \tag{9}$$

Where $\dot{Ex}_{dest,comp}$ is the exergy destruction rate of the compressor. The general exergy balance equation of the condenser is given by Eq. (10).

$$\sum(\dot{m}\ ex)_{in} = \sum(\dot{m}\ ex)_{out} + \dot{Ex}_{th,cond} + \dot{Ex}_{dest,cond} \tag{10}$$

Where $\dot{Ex}_{th,cond}$ is the thermal exergy ratio of condenser. Calculation of thermal exergy is carried out by Equation (11).

$$\dot{Ex}_{th,cond} = \left(1 - \frac{T_0}{T_H}\right)\dot{Q}_{cond} \tag{11}$$

$$\dot{E}_2 - \dot{E}_3 + \left(1 - \frac{T_0}{T_H}\right)\dot{Q}_{cond} - \dot{Ex}_{dest,cond} = 0 \tag{12}$$

$$\dot{Ex}_{dest,cond} = \dot{m}_r[(h_2 - h_3) - T_0(s_2 - s_3)] - \left(1 - \frac{T_0}{T_H}\right)\dot{Q}_{cond} \tag{13}$$

Where $\dot{Ex}_{dest,cond}$ is the exergy destruction of the condenser. For the evaporator, the overall exergy balance equation is written as:

$$\sum(\dot{m}\ ex)_{in} + \dot{Ex}_{th,evap} = \sum(\dot{m}\ ex)_{out} + \dot{Ex}_{dest,evap} \tag{14}$$

Where $\dot{Ex}_{th,evap}$ represents the thermal exergy of evaporator. The thermal exergy is be calculated by Eq. (15) as follows:

$$\dot{Ex}_{th,evap} = \left(1 - \frac{T_0}{T_L}\right)\dot{Q}_{evap} \tag{15}$$

$$\dot{E}_5 - \dot{E}_6 + \left(1 - \frac{T_0}{T_L}\right)\dot{Q}_{evap} - \dot{Ex}_{dest,evap} = 0 \tag{16}$$

$$\dot{Ex}_{dest,evap} = \dot{m}_r\left[(h_5 - h_6) - T_0(s_5 - s_6)\right] + \left(1 - \frac{T_0}{T_L}\right)\dot{Q}_{evap} \tag{17}$$

Where $\dot{Ex}_{dest,evap}$ is the exergy destruction of the evaporator. For the expansion valve the total exergy balance equation is written as:

$$\sum(\dot{m}\ ex)_{in} = \sum(\dot{m}\ ex)_{out} + \dot{Ex}_{dest,exp} \tag{18}$$

$$\dot{E}_4 - \dot{E}_5 - \dot{Ex}_{dest,exp} = 0 \tag{19}$$

$$\dot{Ex}_{dest,exp} = \dot{m}_r[T_0(s_5 - s_4)] \tag{20}$$

Where $\dot{Ex}_{dest,exp}$ shows off the expansion valve's exergy destruction. Adding up the exergy destruction of whole the components of the cooling system, the total exergy destruction is as follows:

$$\dot{Ex}_{dest,total} = \dot{Ex}_{dest,comp} + \dot{Ex}_{dest,cond} + \dot{Ex}_{dest,evap} + \dot{Ex}_{dest,exp} \tag{21}$$

For the cooling system, the total exergetic efficiency (η_{ex}) can be calculated by Eq. (22).

$$\eta_{ex} = \frac{\dot{E}_{out}}{\dot{E}_{in}} = 1 - \frac{\dot{Ex}_{dest,total}}{\dot{E}_{in}} = 1 - \frac{\dot{Ex}_{dest,total}}{\dot{W}_{comp}} \tag{22}$$

3. Environmental and Enviroeconomic Analyses

Environmental analysis gives the emission of a system as "kgCO2/time" in a certain time period depending on the energy consumption of a system. Here, the production emission ($kgCO_2$/kWh) of the electrical energy consumed by the system is important. Environmental analysis can be calculated by Eq. (23) [21], [22].

$$X_{CO_2} = EM\ \dot{E}_{in}t_{working} \tag{23}$$

X_{CO_2} represents the greenhouse gas emission ($kgCO_2$/time) released for a certain period of time, the emission value of the energy source option used in EM electricity generation ($kgCO_2$/kWh), the energy consumption of the $\dot{E}_{in}$ system (kW) and the $t_{working}$ in a period of time (hour/time). It shows the operating time (hour/time) of the system.

Carbon pricing is one of the effective methods used to evaluate the greenhouse gas emissions caused by a system. Enviroeconomic analysis is based on environmental analysis ($kgCO_2$/time) and greenhouse gas emission price ($/kgCO_2$). Enviroeconomic analysis can be calculated with Eq. (24) [21], [22].

$$C_{CO_2} = c_{CO_2}X_{CO_2} \tag{24}$$

X_{CO_2} shows the environmental analysis result ($kgCO_2$/time), c_{CO_2} the price of greenhouse gas emission ($/kgCO_2$) and C_{CO_2} the result of enviroeconomic analysis ($/time). In Table 3, some assumptions made for environmental and enviroeconomic analyses are dedicated.

Table 3. Assumptions for environmental and enviroeconomic analyses.

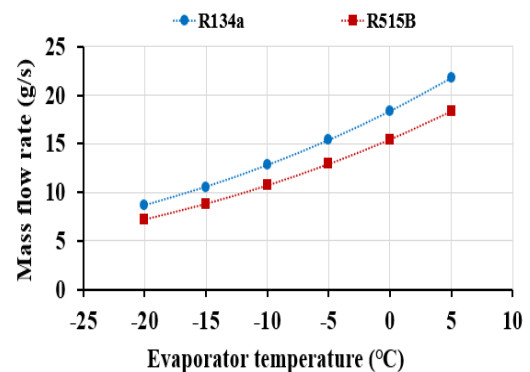| Description	Value
Cooling capacity	5 kW
$t_{working}$	12 h/day
c_{CO_2}	0.0145 $/kgCO_2$ [21], [22]
EM	0.523 $kgCO_2$/kWh [23]

4. Results and Discussions

Figure 4. Evaporator temperature-dependent changing of mass flow rate of R134a and R515B.

VCR with an inner heat exchanger was used to evaluate the performances of R134a and R515B. The comparison of the mass flow rates of R134a and R515B is given in Figure 4. The mass flow rates of R134a and R515B increased as the evaporator temperature increased: from 8.65 g/s to 21.79 g/s for R134a and from 7.21 g/s to 18.35 g/s for R515B. The mass flow rate of R515B is lower than that of R134a. It is due to the fact that R515B in the suction line has a lower vapor density than R134a. For both refrigerants, the mass flow rate is not affected by the condenser temperature.

Using R134a and R515B refrigerants in the refrigeration system, the effect of the temperature of the evaporator on compressor energy consumption is presented in Figure 5. While the condenser temperature is 40 °C, the compressor power consumption of R134a varies from 538.42 W to 709.66 W, while the compressor power consumption of R515B from 392.42 W to 529.84 W. While the condenser temperature is 45 °C, the compressor power consumption of R134a varies between 574.48 W and 797.69 W, while the compressor power consumption of R515B varies between 417.96 W and 594.63 W. The compressor specific compression work and the mass flow rates of the refrigerants affect the energy consumption of the compressor. The specific compression work and mass flow rate of R134a are higher compared to R515B. That's why as seen in Figure 5, the compressor energy consumption of R134a is higher than that of R515B. Because the mass flow rates increases as the temperature of the evaporator rises, the refrigeration system's power consumption rises.
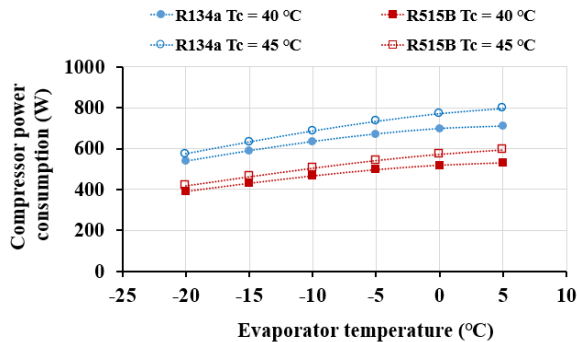

Figure 5. Evaporator temperature-dependent changing of compressor power consumption of R134a and R515B.

The compressor capacity is greatly affected by the cooling capacity. The cooling effect (the difference in enthalpy of the refrigerant entering and leaving the evaporator) and the mass flow rate of the refrigerant affect the cooling capacity. Figure 6 gives the cooling capacity variation to different evaporator temperatures for R134a and R515B at two condenser temperatures (40°C and 45°C). R134a refrigerant has a higher cooling capacity than R515B. Because both the cooling effect and the refrigerant mass flow rate of R134a are higher than that of R515B. When the condenser temperature is 40 °C, the cooling capacity of R134a varies from 1224.89 W to 3422.58 W, while the cooling capacity of R515B varies from 879.21 W to 2554.31 W. When the condenser temperature is 45 °C, the cooling capacity of R134a varies from 1160.98 W to 3261.56 W, while cooling capacity of R515B varies from 828.28 W to 2424.76 W. It has been observed that the cooling capacity of both refrigerants decreases when the condenser temperature increases. Because when the condenser temperature increases, the enthalpy of the refrigerant

entering the evaporator increases, so that the cooling effect decreases.
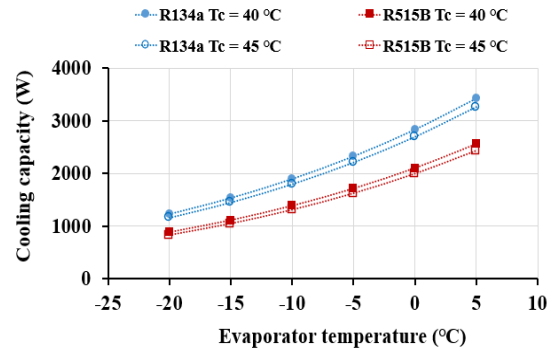

Figure 6. Evaporator temperature-dependent changing of cooling capacity of R134a and R515B

Figure 7 shows the COP of R134a and R515B refrigerants depending on the evaporator temperature at condenser temperatures of 40°C and 45°C. While the condenser temperature is 40 °C, the COP of R134a varies from 2.27 to 4.82, while the COP of R515B from 2.24 to 4.82 W. While the condenser temperature is 45 °C, the COP of R134a varies between 2.02 and 4.09, while the COP of R515B varies between 1.98 and 4.08. It is found that the COP obtained by using R515B refrigerant is nearly equal to the COP obtained by using R134a. This is because although the cooling capacity of R515B refrigerant is less than that of R134a refrigerant, the compressor power consumption of R515B refrigerant is lower than that of R134a refrigerant. The COP value of both refrigerants decreases as the temperature of the condenser rises.

Figure 7. Column chart of COPs of R134a and R515B
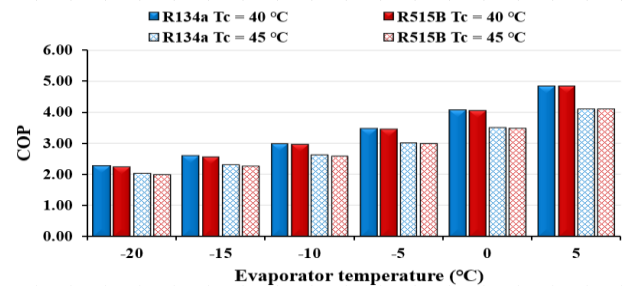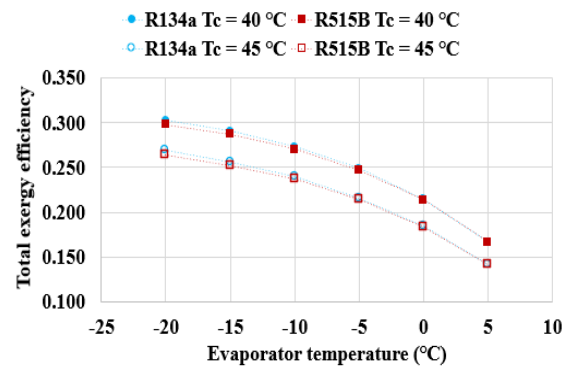

Figure 8. Evaporator temperature-dependent changing of total exergy efficiency of R134a and R515B

The changing of the total exergy efficiencies of R134a and R515B at different evaporator and condenser temperatures is demonstrated in Figure 8. As the evaporator temperature increases, the irreversibilities of the cooling system compenents increase, and consequently the exergy

efficiency of the cooling system decreases. The total exergy efficiency of R134a refrigerant at low evaporator temperature is slightly higher (about 1.40%) than that of R515B refrigerant, the total exergy efficiency of R134a is the same as that of R515B refrigerant at high evaporator temperature.
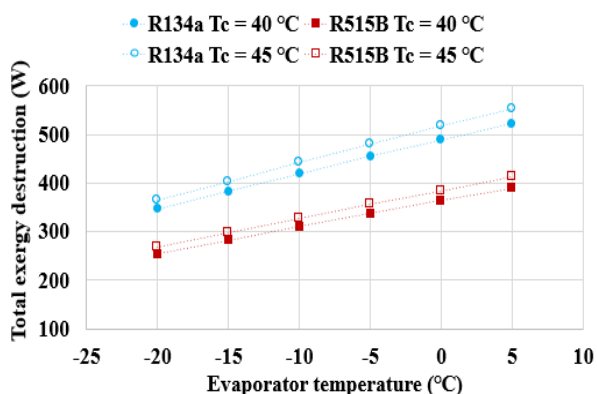

Figure 9. Evaporator temperature-dependent change in total exergy destructions of R134a and R515B

The change in total exergy destruction in case of using refrigerants R134a and R515B in the refrigeration system at different evaporator and condenser temperatures is shown in Figure 9. At a condenser temperature of 40 ºC, the total exergy destruction of the refrigeration system using R134a in the refrigeration system varies from 346.42 W to 522.73 W, while the total exergy destruction of the refrigeration system using R515B in the refrigeration system varies from 254.51 W to 390.33 W. At a condenser temperature of 45 ºC, the total exergy destruction of the refrigeration system using R134a in the refrigeration system varies from 363.75 W to 552.77 W, while the total exergy destruction of the refrigeration system using R515B in the refrigeration system varies from 267.36 W to 412.49 W. When R134a is used in the refrigeration system, the total exergy destruction is about 26% higher than when R515B is used in the refrigeration system. Also, the total exergy destruction of the system increases due to the increase in irreversibilities, as the condenser temperature increases.

In the case where refrigerants R134a and R515B are used in the refrigeration system, the exergy destruction of all components is shown in Figure 10. As can be seen in Figure 10, for both refrigerants the exergy destruction takes place mainly in the compressor. For both refrigerants, the component with the least exergy destruction at low evaporator temperatures is the evaporator, while the component with the least exergy destruction at high evaporator temperatures is the expansion valve. As the expansion valve is only affected by the entropy change between the evaporator and condenser pressure, there is generally lower exergy destruction in expansion valve. As the evaporator temperature increases in the expansion valve, the entropy production decreases. therefore, the exergy destruction of the expansion valve is reduced. As the evaporator temperature decreases, the exergy destruction of the expansion valve increases. Therefore, at low evaporator temperatures the minimum exergy destruction occurred in evaporator.

The comparison of compressor exergy destruction in the case of using R134a and R515B refrigerants in the cooling system is shown in Figure 11. The exergy destruction of the compressor for both refrigerant increase as the evaporator temperature increases. This is because as the evaporator temperature rises, the mass flow rate increases, and the compressor uses higher exergy. It was seen that the compressor exergy destruction of R515B refrigerant is lower (about 24%) than that of R134a refrigerant. Due to the thermal properties of R515B, the entropy generation in the compressor during compression is lower than that of R134a.

The comparison of the condenser exergy destruction of the cooling system for R134a and R515B is presented in Figure 12. It was explained above that the mass flow rates of the refrigerants increase with increasing evaporator temperature increases. Consequently, the exergy destruction of the condenser also increases with increasingevaporator temperature. When refrigerant R515B is used in the refrigeration system, the exergy destruction of the condenser is about 32.50% lower than that of R134a . This is since the condenser entropy difference of R134a is higher than that of R515B.
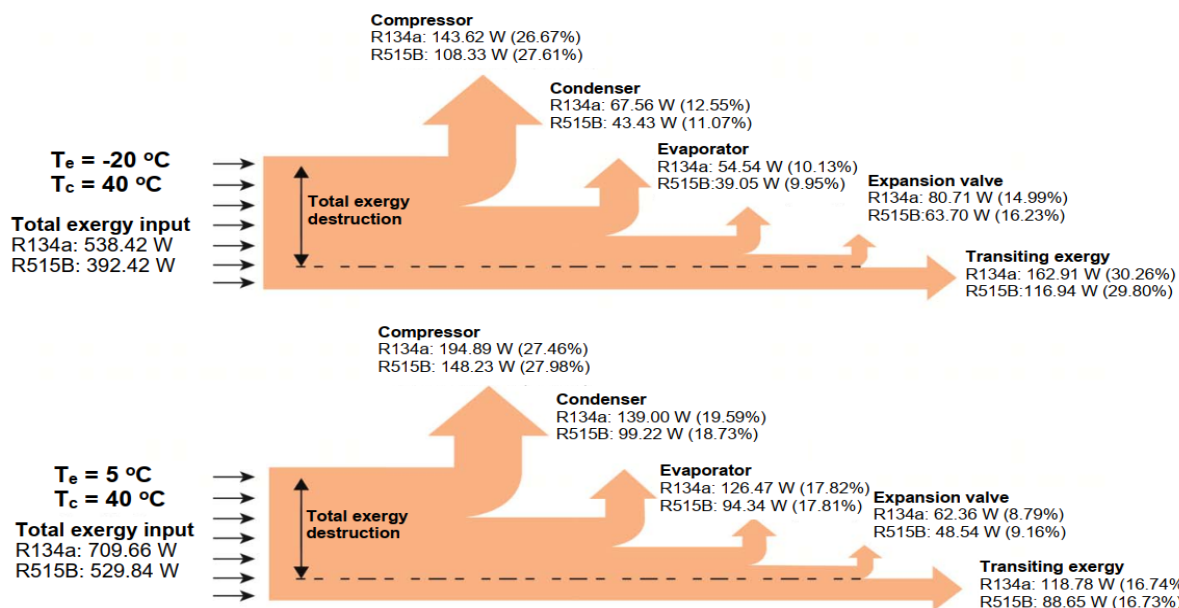

Figure 10. Graphical representation of all components's the exergy destruction for the refrigerants R134a and R515B.
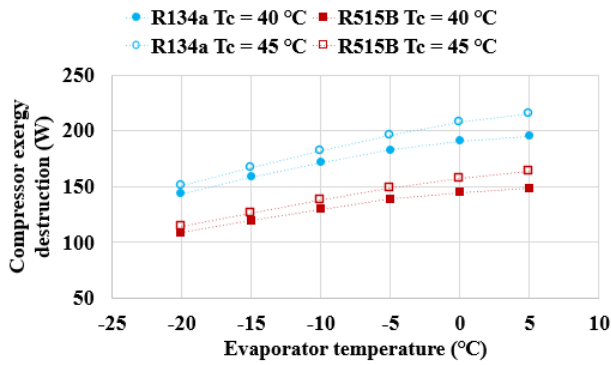
Figure 11. Evaporator temperature-dependent changing of compressor exergy destruction of R134a and R515B.
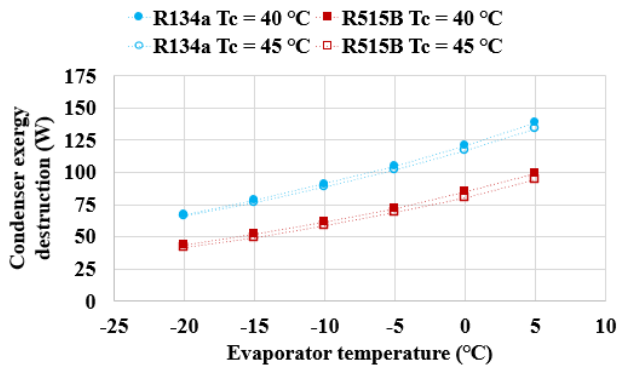

Figure 12. Evaporator temperature-dependent changing of condenser exergy destruction of R134a and R515B.

The comparison of the expansion valve exergy destruction of the cooling system for R134a and R515B is presented in Figure 13. The exergy destruction in the expansion valve decreases while the evaporator temperature rises. Because as the evaporator temperature rises in the expansion valve, the entropy production decreases. Therefore, the exergy destruction of the expansion valve reduces. It was found that the exergy destruction of the expansion valve was lower (about 21.50%) for the refrigerant R515B than for the refrigerant R134a. This is because when R515B is used in the refrigeration system, the entropy difference of the expansion valve and the mass flow rate of the refrigerant are lower compared to R134a.
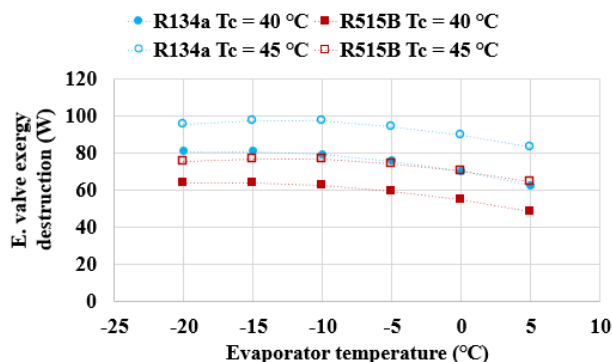
Figure 13. Evaporator temperature-dependent changing of expansion valve exergy destruction of R134a and R515B.

In Figure 14, comparing of the evaporator exergy destruction of refrigerants is given. When the evaporator temperature increases, the entropy generation in the evaporator increases. Therefore, as the evaporator temperature increases, the exergy destruction of the

evaporator also increases. When using the refrigerant R515B in the cooling system, the exergy destruction of the evaporator is about 27% lower than with R134a. Because both the mass flow rate and entropy production of R515B are lower compared to R134a.
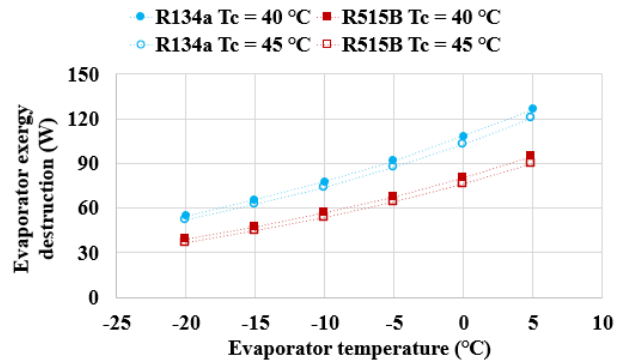
Figure 14. Evaporator temperature-dependent changing of evaporator exergy destruction of R134a and R515B.

The environmental analysis results of the refrigeration system with the evaporator temperature is given in Figure 15. When the evaporator temperature for both refrigerants increases, the COP value of the refrigeration system increases and consequently the environmental analysis results decrease. It can be seen that the results of the environmental analysis of R134a and R515B are very close in Figure 15. When the condenser temperature increases for both refrigerants, the energy consumption of the refrigeration system compressor increases. Therefore, the environmental analysis results increase.

Figure. 15. Evaporator temperature-dependent changing of results obtained from environmental analysis.

Figure. 16. Evaporator temperature-dependent changing of results obtained from enviroeconomic analysis.

The results of the environmental economic analysis depending on the evaporator and condenser temperatures

are shown in Figure 16. As the evaporator temperature increases, the energy efficiency of the refrigeration system increases, and consequentl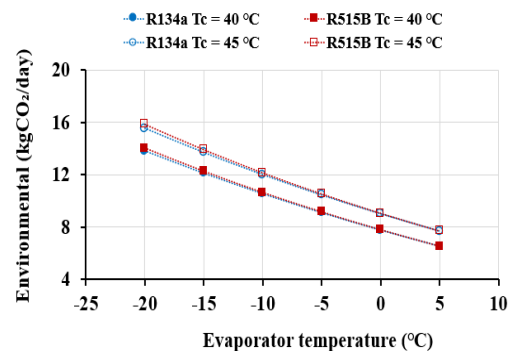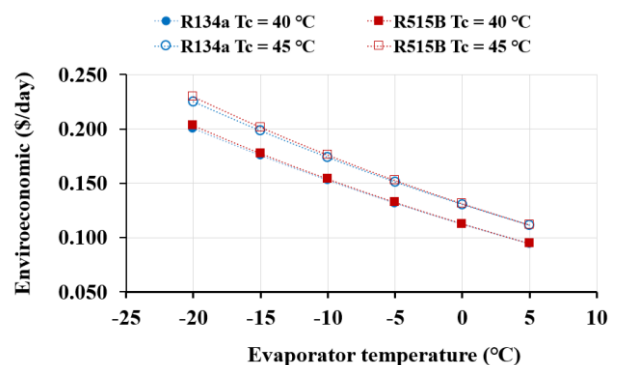y, the energy consumption of the refrigeration system compressor decreases. Therefore, the results of the enviroeconomic analysis decrease as the evaporator temperature increases. It is seen that results obtained from the enviroeconomic analysis of R134a and R515B are very close to each other. Moreover, as the condenser temperature increases, the results of the enviroeconomic analysis increase similarly to the results of the environmental analysis, because the energy consumption of the cooling system increases.

5. Conclusions

In this work, the analysis of the R515B with lower GWP as replacements for R134a in a VCR system that has an IHX was made. Based on the energy, exergy, **environmental and enviroeconomic** analyses the main results obtained from the study are given below:

- R515B has lower mass flow rate, compressor energy consumption, and cooling capacity than that of R134a.
- In the refrigerating system, the COP obtained by using R515B refrigerant is nearly equal to the COP obtained by using R134a.
- Most exergy destruction occurs in the compressor of the refrigeration system.
- The compressor exergy destruction of the refrigeration system using R515B refrigerant is approximately 24% lower than that of R134a. The expansion valve exergy destruction of the refrigeration system using R515B refrigerant is approximately 21.50 % lower than that of R134a.
- The condenser exergy destruction of the refrigeration system using R515B is about 32.50% lower than that of R134a.
- The exergy destruction of the evaporator of the refrigeration system using R515B is nearly 27% lower than that of R134a.
- Variation of evaporator and condenser temperatures greatly affects exergy destruction and exergy efficiency.
- It is found that the total exergy efficiency of the VCR system using R515B is slightly lower than that of R134a (about 1.40%).
- The results of environmental and enviroeconomic evaluation based on energy analysis showed that R515B refrigerant was slightly higher than R134a refrigerant.

Finally, R134a and R515B are slightly different in energy, exergy performance, environmental and enviroeconomic analysis. However, R515B has significant advantages in terms of installation safety requirements (no flammability (A1)) refrigerant). As a result, it has been shown that R515B can be a good alternative to R134a in VCR systems with an internal heat exchanger.

Nomenclature

$\dot{W}_{comp}$	Compressor power consumption [kW]
$\dot{m}_r$	Refrigerant mass flow rate [kg s^{-1}]
$\dot{Q}_{evap}$	Cooling capacity [kW]
$\dot{Q}_{con}$	Heating capacity [kW]
η_{isen}	Compressor isentropic efficiency [-]
η_{vol}	Compressor volumetric efficiency [-]
h	Enthalpy [kJ kg^{-1}]
s	Entropy [kJ kg^{-1} K^{-1}]
ρ	Density [kg m^{-3}]
T	Temperature [^{o}C or K]
P	Pressure [kPa or bar]
COP	Coefficient of performance for cooling mode [-]
$\dot{Ex}$	Exergy [kW]
$\dot{E}$	Energy [kW]
η_{ex}	Exergy efficiency [-]
COP$_{HP}$	Heat pump coefficient of performance [-]
$t_{working}$	Operation time (hour/time)
X_{CO_2}	Environmental analysis [kgCO$_2$ time^{-1}]
EM	Electricity energy production emission value [kgCO$_2$ kWh^{-1}]
C_{CO_2}	Environmentaleconomic analysis [kgCO$_2$ day^{-1}]
c_{CO_2}	Greenhouse gas emission price [\$ kgCO$_2$$^{-1}$]
RPM	Revolutions per minute [Rev min^{-1}]

References:

[1] R. Saravanakumar and V. Selladurai, "Exergy analysis of a domestic refrigerator using eco-friendly R290/R600a refrigerant mixture as an alternative to R134a," *J. Therm. Anal. Calorim. 2013 1151*, vol. 115, no. 1, pp. 933–940, June 2013.

[2] F. Molés, J. Navarro-Esbrí, B. Peris, A. Mota-Babiloni, and Á. Barragán-Cervera, "Theoretical energy performance evaluation of different single stage vapour compression refrigeration configurations using R1234yf and R1234ze(E) as working fluids," *Int. J. Refrig.*, vol. 44, pp. 141–150, August 2014.

[3] Z. Yang *et al.*, "Analysis of lower GWP and flammable alternative refrigerants," *Int. J. Refrig.*, vol. 126, pp. 12–22, Jun. 2021.

[4] P. Makhnatch, A. Mota-Babiloni, A. López-Belchí, and R. Khodabandeh, "R450A and R513A as lower GWP mixtures for high ambient temperature countries: Experimental comparison with R134a," *Energy*, vol. 166, pp. 223–235, January 2019.

[5] G. Li, "Performance evaluation of low global warming potential working fluids as R134a alternatives for two-stage centrifugal chiller applications," *Korean J. Chem. Eng*, vol. 38, no. 7, pp. 1438–1451, 2021.

[6] J. U. Ahamed, R. Saidur, H. H. Masjuki, and M. A. Sattar, "An Analysis of Energy, Exergy, and Sustainable Development of a Vapor Compression Refrigeration System Using Hydrocarbon," *http://dx.doi.org/10.1080/15435075.2011.621491*, vol. 9, no. 7, pp. 702–717, October 2012.

[7] C. Wantha, "Analysis of heat transfer characteristics of tube-in-tube internal heat exchangers for HFO-1234yf and HFC-134a refrigeration systems," *Appl. Therm. Eng.*, vol. 157, p. 113747, July 2019.

[8] C. Mateu-Royo, A. Mota-Babiloni, J. Navarro-Esbrí, and Á. Barragán-Cervera, "Comparative analysis of HFO-1234ze(E) and R-515B as low GWP alternatives to HFC-134a in moderately high temperature heat pumps," *Int. J. Refrig.*, vol. 124, pp. 197–206, April 2021.

[9] Gaurav and R. Kumar, "Computational energy and exergy analysis of R134a, R1234yf, R1234ze and their

mixtures in vapour compression system," *Ain Shams Eng. J.*, vol. 9, no. 4, pp. 3229–3237, December 2018.

[10]   R. Prabakaran, D. Mohan Lal, S. Devotta, and S. Devotta-Former Director, "Effect of thermostatic expansion valve tuning on the performance enhancement and environmental impact of a mobile air conditioning system," *J. Therm. Anal. Calorim.*, vol. 143, pp. 335–350, 2021.

[11]   J. M. Belman-Flores, V. H. Rangel-Hernández, S. Usón, and C. Rubio-Maya, "Energy and exergy analysis of R1234yf as drop-in replacement for R134a in a domestic refrigeration system," *Energy*, vol. 132, pp. 116–125, August 2017.

[12]   R. Ben Jemaa, R. Mansouri, I. Boukholda, and A. Bellagi, "Energy and exergy investigation of R1234ze as R134a replacement in vapor compression chillers," *Int. J. Hydrogen Energy*, vol. 42, no. 17, pp. 12877–12887, April 2017.

[13]   A. Yataganbaba, A. Kilicarslan, and I. Kurtbaş, "Exergy analysis of R1234yf and R1234ze as R134a replacements in a two evaporator vapour compression refrigeration system," *Int. J. Refrig.*, vol. 60, pp. 26–37, December 2015.

[14]   J. Gill, J. Singh, O. S. Ohunakin, and D. S. Adelekan, "Exergy analysis of vapor compression refrigeration system using R450A as a replacement of R134a," *J. Therm. Anal. Calorim. 2018 1362*, vol. 136, no. 2, pp. 857–872, August 2018.

[15]   M. H. Shaik, S. Kolla, and B. P. Katuru, "Exergy and energy analysis of low GWP refrigerants in the perspective of replacement of HFC-134a in a home refrigerator," *https://doi.org/10.1080/01430750.2020.1730960*, 2020.

[16]   C. H. de Paula, W. M. Duarte, T. T. M. Rocha, R. N. de Oliveira, and A. A. T. Maia, "Optimal design and environmental, energy and exergy analysis of a vapor compression refrigeration system using R290, R1234yf, and R744 as alternatives to replace R134a," *Int. J. Refrig.*, vol. 113, pp. 10–20, May 2020.

[17]   A. Mota-Babiloni, P. Makhnatch, and R. Khodabandeh, "Recent investigations in HFCs substitution with lower GWP synthetic alternatives: Focus on energetic performance and environmental impact," *Int. J. Refrig.*, vol. 82, pp. 288–301, October 2017.

[18]   V. Pérez-García, J. M. Belman-Flores, J. L. Rodríguez-Muñoz, V. H. Rangel-Hernández, and A. Gallegos-Muñoz, "Second Law Analysis of a Mobile Air Conditioning System with Internal Heat Exchanger Using Low GWP Refrigerants," *Entropy 2017, Vol. 19, Page 175*, vol. 19, no. 4, p. 175, April 2017.

[19]   S. Golzari, A. Kasaeian, S. Daviran, O. Mahian, S. Wongwises, and A. Z. Sahin, "Second law analysis of an automotive air conditioning system using HFO-1234yf, an environmentally friendly refrigerant," *Int. J. Refrig.*, vol. 73, pp. 134–143, January 2017.

[20]   E. W. Lemmon, M. L. Huber, and M. O. McLinden, "NIST Standard Reference Database 23: Reference Fluid Thermodynamic and Transport Properties-REFPROP, Version 9.1." .

[21]   H. Caliskan, "Energy, exergy, environmental, enviroeconomic, exergoenvironmental (EXEN) and exergoenviroeconomic (EXENEC) analyses of solar collectors," *Renewable and Sustainable Energy Reviews*, vol. 69. Elsevier Ltd, pp. 488–492, 1 March 2017.

[22]   H. Caliskan, "Novel approaches to exergy and economy based enhanced environmental analyses for energy systems," *Energy Convers. Manag.*, vol. 89, pp. 156–161, January 2015.

[23]   B. Atilgan and A. Azapagic, "Assessing the Environmental Sustainability of Electricity Generation in Turkey on a Life Cycle Basis," *Energies*, vol. 9, no. 1, p. 31, January 2016.

Excess Molar Volumes, Apparent Molar Volumes, Partial Molar Volumes of Methionine, An Amino Acid, in Water + Ethanol And Water + Methanol Solutions at 298.15 K

Ufuk Sancar Vural*[1], Saban Uysal[2],

*[1]Pasabayır Mh. Mehmetcik Cd. 77/16, Bandirma, Balikesir, Turkey
[2]Karabuk University, Faculty of Science, Department of Chemistry, Karabuk, Turkey
E-mail: [1]usvural@gmail.com, [2]sabanuysal@karabuk.edu.tr

Abstract

Methionine is an amino acid that is extremely important for human health. To better understand the biochemical events occurring in the human body, the excess molar properties of methionine and aqueous ethanol and aqueous methanol mixtures were determined at 298.15 K. Interactions between components in solutions are explained. Negative deviations from the ideal state have been observed in methionine solutions due to hydrogen bonds, dipole interactions, charge-transfer interactions.

Keywords: Methionine; excess molar volume; excess partial molar volume; apparent molar volume

1. Introduction

Methionine is an amino acid found in many proteins present in our bodies and food (Figure 1). It is not just a building block for proteins but contains some unique properties. The most important of these properties is its ability to be converted into sulfur-containing molecules [1]. Sulfur-containing molecules play an important role in protecting tissues, modifying DNA, and maintaining the proper functioning of cells [2,3,4[. Of the amino acids used to make protein in the body, only methionine and cysteine contain sulfur. Methionine also plays a critical role in initiating the process of making new proteins in cells. It occurs continuously as old proteins break down [5]. For example, it helps muscles produce new proteins after a muscle-damaging workout [6,7].
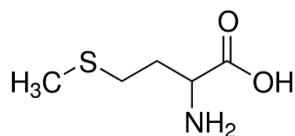

Figure 1. Methionine structure

Zhang et al. (2016) observed that the solubility of methionine in water is higher than in organic solvents, and the solubility decreases in water + acetone < water + ethanol < water + methanol in water + organic solvent mixtures [8]. According to the like dissolves like principle, they stated that the solubility of the amino acid, which has a polar structure, increases due to the increase in the polarity of organic solvents. Tyunina et al. (2020) reported that electrostatic interactions and the formation of hydrogen bonds were effective on the volumetric properties of methionine aqueous solutions [9]. El-Dossoki (2018) observed that the molal

solubility of methionine decreases as the mole fraction of methanol and ethanol increases due to the salt effect [10]. He also determined that the apparent molar volume of DL-methionine in water and methanol-water and ethanol-water solutions increased as the mole fraction of methanol and ethanol increased. He pointed out the inverse proportion between volume and density as the reason for this.

The excess molecular properties of amino acid solutions are very useful for understanding the conformational stability and unfolding behaviour of protein molecules. Some researchers have used thermodynamic methods to investigate the interactions of amino acids with organic molecules or salts in aqueous solutions [11,12].

Excess properties can be defined as the difference between the ideal volumetric properties of the mixture and the observed volumetric properties as a result of the molecular interactions between the components that make up the mixture and in the solution [13]. The excess volumes (V^E) are defined as the difference of volume of real solutions and volume of pure components (ideal solution).

Excess thermodynamic properties, which can also be understood as deviations from ideal thermodynamic behaviours, provide a better understanding of the behaviour of components in chemical and biochemical events, and their roles in production and application processes. In general, the excess properties result from three types of interactions between the constituent molecules of liquid mixtures [14-15].

(a) Positive effects: Physical interactions consisting of dispersion forces or weak dipole-dipole interaction,
(b) negative effects: chemical or specific interactions, including charge transfer, H-bonds, and other complex formation interactions,

(c) Structural effects: These are the structural contributions arising from the differences in the size and shape of the component molecules in the mixture depending on the structure of their molecules.

In this study, excess molar volumes, apparent molar volumes, partial molar volumes and excess partial molar volumes of the binary mixture of methionine + methanol and methionine + ethanol in water at 298.15 K, which is one of the most important building blocks of proteins, were investigated.

2 Materials

Amino acids; methionine of 99.5% purity, methanol and ethanol of 99% purity were obtained from Merck Company. Some physicochemical properties of the components are given in Table 1.

Using twice-distilled water with a conductivity of 0.038 μS/cm, 10 cm^3 of alcohol solutions were prepared between 0-1 mole fractions by increasing the volume by 0.5 cm^3. To alcohol solutions, amino acid was added until saturation. The sample tubes were mixed with a magnetic stirrer overnight in a thermostatic water bath at 298.15±0.1 K by closing the mouth with a Teflon cap. Then, the solution was left to rest overnight and the supernatant was separated by filtration. The filtered solutions were kept in a thermostatic water bath at 298.15±0.1 K and their densities were measured by Anton Paar DMA 4500 Denismeter. Experiments were performed in 4 repetitions.

Table 1 Molecular weight and densities of pure components in mixtures

Component	M, g/mol	Density, 298.15 K
Methionine	149.21	Powder
Methanol	32.04	0.7048
Ethanol	46.07	0.7875
Water	18.02	0.9968

3 Methodology
3.1 Excess Molar Properties

The excess molar volume of a liquid solution is defined by the following equation [16-17].

$$V^E = V - \sum_{i=0} x_i V_i^0 \tag{1}$$

where V is the molar volume of the solution, xi is the mole fractions of components, and V_i^0 is the molar volumes of pure components, respectively. Eq. (1) can be written in terms of density as Eq. (2). The excess molar volumes, calculated from the density data in Eq. (4), are listed in Table 3 and plotted in Figure 3.

$$V^E = \sum_{i=1} X_i M_i \left(\frac{1}{\rho} - \frac{1}{\rho_i}\right) \tag{2}$$

in which M_i is the molar masses of components, ρ is the density of the mixture, and ρ_i represent the densities of pure components, respectively.

The excess molar properties (V^E) can be correlated using the Redlich–Kister equation [16-20]:

$$V^E = X_i(1 - X_i) \sum_{i=1} A_i (2X_i - 1)^i \tag{3}$$

The values of the coefficients A_i were calculated by the method of least squares along with the standard deviation

$\sigma(V^E)$. The coefficients A_i are adjustable parameters for a better fit of the excess functions.

$$\sigma(V^E) = \left[\frac{\sum_{i=1}^{i=n}(V_{cal,i}^E - V_{exp,i}^E)}{n}\right]^{1/2} \tag{4}$$

where n is the number of parameters, V_{expt} and V_{cal} are the experimental and calculated parameters, respectively.

3.2 Partial Volume and Excess Partial Volume

To have more knowledge about interactions solute and solvent, the values of partial molar volumes of binary mixtures have been calculated using the following equations [18-20]:

$$V_i = \left(\frac{\partial V}{\partial n_i}\right)_{P,T,n_j} \tag{5}$$

Differentiation of Eq. (3) and combination with Eq. (5), gives the following equations for the partial molar volume of pure components

$$V_1 = V^E + V_1^0 + (1 - X_1)(\partial V^E/\partial X_1)_{T,P} \tag{6}$$

$$V_2 = V^E + V_2^0 - X_1(\partial V^E/\partial X_1)_{T,P} \tag{7}$$

where V_1^0 and V_2^0 are the molar volume of the pure component. Combination of Eqs. (3), (6) and (7) leads to Eqs. (8) and (9).

$$V_1 = V_1^0 + (1 - x)^2 \sum_{i=0} A_i(1 - 2x)^i - 2x(1 - x)^2 \sum_{i=1} A_i i(1 - 2x)^{i-1} \tag{8}$$

$$V_2 = V_2^0 + x^2 \sum_{i=0} A_i(1 - 2x)^i + 2x^2(1 - x) \sum_{i=1} A_i i(1 - 2x)^{i-1} \tag{9}$$

Values of the partial molar volumes at infinite dilution, V_i^∞, were obtained by the linear extrapolation of corresponding partial molar volumes using Eq. (8) and Eq. (9). Extrapolation of V_i to $x_i = 0$ results in V_i^∞. The excess partial molar volumes at infinite dilution, V_i^E, were calculated using the following relations [18-20]:

$$V_i^E = V_i - V_i^0 \tag{10}$$

The partial properties at infinite dilution are of interest since, at the limit of infinite dilution, the (solute + solute) interactions disappear. The values of the partial molar volume at infinite dilution provide information about (solute + solvent) interaction, independent of the composition effect. Setting ($x = 0$) in Eq. (8) and ($x = 1$) in Eq. (9) leads to Eq. (11) and Eq. (12). Eq. (11) and (12) give V_1^∞ and V_2^∞ (the partial molar volumes at infinite dilution) for the component (1) and (2), respectively [18-20].

$$V_1^\infty = V_1^0 + \sum_{i=0} A_i(-1)^i \tag{11}$$

$$V_2^\infty = V_2^0 + \sum_{i=0} A_i \tag{12}$$

Rearrangement of Eqs. (11) and (12) leads to Eqs. (13) and (14) for the excess partial molar volumes of components at infinite dilution,

$$V_1^{E,\infty} = \sum_{i=0} A_i(-1)^i \qquad (13)$$

$$V_2^{E,\infty} = \sum_{i=0} A_i \qquad (14)$$

Eq. (13) and Eq. (14) represent the partial molar volumes of components in solutions at infinite dilution, respectively.

3.3 Apparent Molar Volume

The apparent molar volume (V_φ) is a very useful parameter to understand the interactions between ion-solvent, ion-ion and solvent-solvent (structural) molecules that occur in mixtures. The Redlich–Kister equation and its derivatives do not always provide the best representation of properties of either component at infinite dilution in the other component. Instead of using the Redlich–Kister equation, we have also considered another approach, which may be more convenient and accurate, by calculating the partial molar volume at infinite dilution through apparent molar volumes. Apparent molar volumes of components, $V\phi$, were calculated from experimental data using the following relations [18-20].

$$V_{\emptyset 1} = \frac{(V - x_2 V_2^0)}{x_1} = \frac{M_1}{\rho} + \frac{(\rho_2 - \rho)x_2 M_2}{x_1 \rho \rho_2} \qquad (15)$$

$$V_{\emptyset 2} = \frac{(V - x_1 V_1^0)}{1 - x_1} = \frac{M_2}{\rho} + \frac{(\rho_1 - \rho)x_1 M_1}{x_2 \rho \rho_1} \qquad (16)$$

where M_i, m, ρ_i and ρ_i^0 are molecular weight, molality, densities of components and pure components, respectively. Extrapolation of $V_{\emptyset i}$ to $x_i = 0$ give the values of the limiting apparent molar volume ($V_{\emptyset,i}^0$). The excess apparent molar volumes at infinite dilution, $V_{\emptyset,i}^E$, were also calculated by equations similar to Eqs. (10). The apparent molar volumes of $V_{\phi 1}$ and $V_{\phi 2}$ can be calculated from Eq. (17) and Eq. (18).

$$V_{\emptyset 1} = \frac{V - (1-x)V_2^0}{x} \qquad (17)$$

$$V_{\emptyset 2} = \frac{V - xV_1^0}{1 - x} \qquad (18)$$

where V_1^0 and V_2^0 are the molar volumes determined from the experimental densities by M_i/ρ_i, and V is the molar volume of the solution determined by the following equation:

$$V = V^E + (x_1 V_1^0 + x_2 V_2^0) \qquad (19)$$

The combination of Eq. (1), Eq. (17), and Eq. (18) lead to:

$$V_{\emptyset 1} = V_1^0 - \frac{V^E}{x} \qquad (20)$$

$$V_{\emptyset 2} = V_2^0 - \frac{V^E}{1 - x} \qquad (21)$$

Simple graphical or analytical extrapolation of $V_{\phi 1}$ to $x = 0$ and $V_{\phi 2}$ to $x = 1$ leads to the partial molar volumes at infinite dilution, V_1^∞ and V_2^∞, respectively. Further, the limiting partial molar volume is expressed as $V_i^\infty = V_i^{E,\infty} + V_i^0$ from which the $V_i^{E,\infty}$ can be derived. It can be observed that the procedures of obtaining $V_i^{E,\infty}$ values by Eq. (13) and (14) or from the extrapolated $V_{\phi 1}$ values of Eq. (20) and Eq. (21) lead to comparable magnitudes of V_i^∞ values.

Partial molar volumes were calculated at infinite dilution from excess molar volumes using a method based on extrapolation of reduced volume. This method was obtained by rearrangement of Eq. (20) and division by *(1-x)*.

$$\frac{V^E}{x(1-x)} = \frac{V_{\emptyset i} - V_i^0}{1 - x} \qquad (22)$$

Linear extrapolation of the "reduced volume" represented by $V^E/x(1-x)$ to $x = 0$ and $x = 1$ leads to the desired V_1^∞ and V_2^∞, respectively. Thus, the methods of obtaining V_1^∞ and V_2^∞ by way of Eqs. (14) and (15), extrapolation of $V_{\phi i}$ to $x = 0$ or $V^E/x(1-x)$ to $x = 0$ are all satisfactory, giving equally approximately equal values of partial molar volumes at infinite dilution.

4. Result and Discussion

In this study, the densities, apparent molar volumes, partial molar volumes and excess molar properties of saturated solutions of methionine in aqueous solutions of different concentrations of methanol and ethanol at a constant temperature of 298.15 K were investigated. The densities of aqueous mixtures of amino acid over the entire range of compositions at 298.15 are shown in Table 2 and Figure 2.

Table 2. Densities and Excess Molar Volumes of Methionine + Ethanol + Water) and (Methanol + Water) Solutions at 298.15 K.

|	Densities, (g/cm³)		V^E, (cm³/mol)	
	Methanol	Ethanol	Methanol	Ethanol
x	+ Water	+ Water	+ Water	+ Water
0.00	0.9964	0.9983	0.0000	0.0000
0.05	1.0079	0.9951	-0.6118	-0.6359
0.10	1.0141	0.9901	-1.1343	-1.2238
0.15	1.0143	0.9837	-1.5474	-1.7660
0.20	1.0085	0.9765	-1.8410	-2.2658
0.25	0.9973	0.9687	-2.0135	-2.7269
0.30	0.9818	0.9606	-2.0715	-3.1528
0.35	0.9635	0.9524	-2.0306	-3.5466
0.40	0.9438	0.9442	-1.9161	-3.9098
0.45	0.9245	0.9359	-1.7630	-4.2420
0.50	0.9070	0.9276	-1.6136	-4.5397
0.55	0.8925	0.9190	-1.5135	-4.7954
0.60	0.8819	0.9100	-1.5035	-4.9969
0.65	0.8755	0.9002	-1.6096	-5.1255
0.70	0.8728	0.8892	-1.8329	-5.1549
0.75	0.8726	0.8766	-2.1397	-5.0486
0.80	0.8727	0.8617	-2.4549	-4.7577
0.85	0.8696	0.8440	-2.6535	-4.2159
0.90	0.8587	0.8227	-2.5449	-3.3335
0.95	0.8340	0.7970	-1.8311	-1.9866
1.00	0.7877	0.7661	0.0000	0.0000
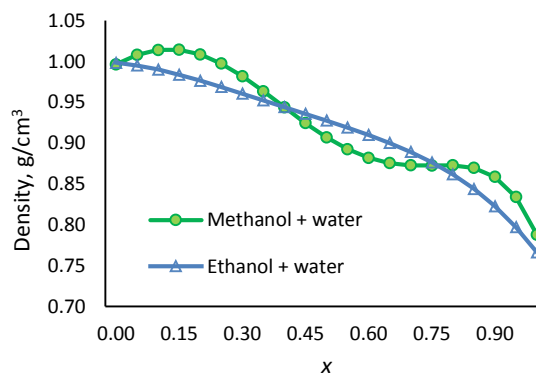
Figure 2. Densities of solutions of methionine + (ethanol +water) and (methanol + water) at 298.15 K.

As can be seen from Table 2, the solubility of amino acids decreases as the alcohol concentration decreases. Therefore, densities of binary mixtures of methionine and alcohol decrease as methanol and ethanol mole fraction increase. The density of the ethanol solution decreases slightly more than the methanol solution. However, the densities of the binary mixtures were found to be close to each other due to the strong interaction between functional groups in the side chain of the polar methionine and both alcohols.

The excess molar properties of methionine in aqueous alcohol solutions deviate from the ideal state. Chemical, physical, structural interactions between solvent-solute and components are the cause of this deviation. As can be seen in Table 2 and Figure 3, the excess molar volume of the binary mixture of methionine with ethanol and methanol showed a negative deviation. Negative deviation in excess molar property is in the direction of increasing alcohol fraction. The negative deviation of excess molar volume in ethanol solution is greater and more regular because ethanol is more polar than methanol and forms stronger H-bonds. The excess molar volume in methanol solutions shows irregularly negative deviations. The tendency of methionine to dissolve in the more polar water is deactivated as the mole fraction of methanol increases. Negative deviations in the excess molar volume of a binary mixture of methionine and both alcohol solutions indicate a strong hydrogen bond and chemical effects between the solvent and solute. Thus, it was understood that chemical interactions including charge transfer, H-bonds are effective in binary mixtures of methionine and alcohol solutions.

Partial molar volumes of components for all compositions can be calculated by using the Redlich-Kister coefficients in Eq. (3) at 298.15 K, and the results are shown in Table 3. The parameters A_i in Eq. (3) are reported in Table 4 along with standard deviations, σ, calculated by using Eq. (4). The partial molar volumes at infinite dilution show a good agreement between the calculation method, Eq. (11) and Eq. (12), and the linear extrapolation method of Eq. (8) and (9). As can be seen in Table 3, partial molar volumes in ethanol + water and methanol + water mixtures were calculated as close to each other. From these values, it is understood that there are stronger hydrogen bonds and dipole interactions between the sulfur in the structure of the amino acid and water molecules.
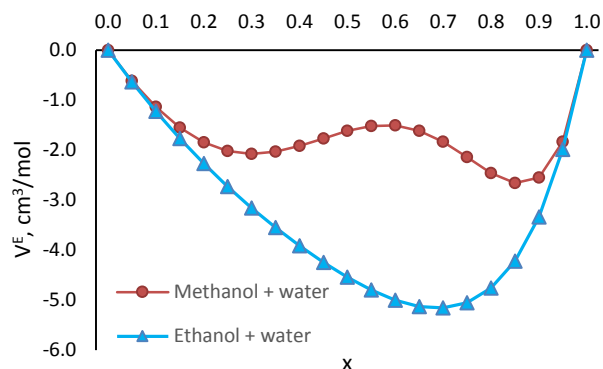

Figure 3. L-Excess molar volumes of methionine + (ethanol+water) and methionine + (methanol + water) solutions at 298.15 K.

From Eq. (13) and Eq. (14), excess apparent molar volumes values of methanol + water (1) and ethanol + water (2) solutions of methionine in infinitely dilute solutions were found V_1^∞=149.73 cm^3/mol and V_2^∞=149.50 cm^3/mol at 298.15 K, respectively. Similarly, it was found to be V_1^∞=144.74 cm^3/mol and V_2^∞=149.50 cm^3/mol from the linear extrapolation of Eq. (20) and Eq. (21). However, it can be said that the value found by interpolation is more reliable.

The change in volumetric properties of a binary mixture of methionine + alcohol can be explained by chemical interactions that occur in the form of charge-transfer interactions, hydrogen bonds and dipole-dipole interactions. Charge transfer bonds are formed between the electron donor amine group and the electron acceptor sulfur and carboxyl groups in the methionine structure. Strong hydrogen bonds and dipole-dipole interactions occur between the N, S atoms in the side chain molecules of methionine and the -OH group of the water molecule. Dipole-dipole interactions occur due to the dipole moment difference. The dipole moments of water, ethanol and methanol molecules are 1.85 D, 1.67 D and 1.69 D, respectively [21,22].

Table 3. Apparent Molar Volumes and Partial Molar Volumes of Methionine + (Ethanol + Water) and (Methanol + Water) Solutions at 298.15 K.

	Apparent molar volumes, V_ϕ, (cm^3/mol)				Partial Molar Volume, V_i (cm^3/mol)		Excess partial Molar Volume, V_i^E (cm^3/mol)	
x	Methanol + Water[a]	Ethanol + Water[b]	Methanol + Water[c]	Ethanol + Water[d]	Methanol + Water	Ethanol + Water	Methanol + Water	Ethanol + Water
0.00	147.97	147.43	149.75	149.46	149.73	149.46	-0.01	0.00
0.05	146.18	147.93	115.58	147.87	149.74	149.47	1.70	-0.47
0.10	145.23	148.72	123.59	146.40	149.74	149.47	2.61	-1.23
0.15	145.20	149.74	132.12	145.01	149.75	149.47	2.64	-2.20
0.20	146.09	150.91	140.77	143.64	149.75	149.47	1.80	-3.33
0.25	147.82	152.20	149.20	142.23	149.75	149.46	0.14	-4.56
0.30	150.29	153.55	157.16	140.71	149.75	149.46	-2.22	-5.86
0.35	153.31	154.95	164.37	139.02	149.75	149.46	-5.12	-7.20
0.40	156.68	156.38	170.60	137.10	149.75	149.46	-8.34	-8.57
0.45	160.14	157.84	175.63	134.88	149.75	149.46	-11.65	-9.96
0.50	163.40	159.33	179.28	132.29	149.75	149.46	-14.77	-11.39
0.55	166.18	160.90	181.44	129.27	149.75	149.46	-17.43	-12.89
0.60	168.28	162.58	182.15	125.78	149.75	149.46	-19.44	-14.50
0.65	169.57	164.45	181.56	121.80	149.75	149.46	-20.68	-16.29
0.70	170.12	166.59	180.04	117.35	149.75	149.46	-21.20	-18.34
0.75	170.16	169.12	178.07	112.62	149.75	149.46	-21.24	-20.76
0.80	170.15	172.19	176.29	108.09	149.75	149.46	-21.23	-23.69
0.85	170.78	175.98	175.44	105.20	149.75	149.46	-21.84	-27.33
0.90	173.06	180.76	176.43	108.82	149.75	149.47	-24.01	-31.90
0.95	178.45	186.87	180.45	145.04	149.75	149.46	-29.17	-37.75
1.00	189.42	194.77	189.42	194.77	149.75	149.53	-39.68	-45.24

[a] (Eq. 15), [b] (Eq. 16), [c] (Eq. 20), [d] (Eq. 21)

Tablo 4. The Values of Redlich-Kister Coefficients for The Studied Binary Mixtures of at 298.15 K and at Under The Atmospheric Pressure

Mixture	Metanol + Water	Ethanol + Water
A_0	0,5908	0,1995
A_1	-0,5940	-0,0924
A_2	-0,0172	-0,2116
A_3	0,0064	0,0415
A_4	-0,0005	-0,0027
A_5	0,0000	0,0001
σ	7,7400	15,07

5. Conclusion

In this study, the intermolecular interactions of methionine in aqueous alcohol solutions at 298.15 K were tried to be understood from the density, apparent molar volume, partial molar volume and excess molar properties. Since methionine, which has a strong polar structure, has strong functional groups such as sulfur, carboxyl, amine, and strong interactions between water molecules, the effect of increasing alcohol concentration on these interactions was weak. As the ethanol concentration increases, the volumetric changes are slightly more pronounced compared to methanol. Hydrogen bonds, dipole interactions and charge transfer complexes are stronger than structural interactions in the molecular behaviour of amino acids in solutions.

The volumetric properties of amino acids in water and alcohol are extremely important for understanding their interactions with the structures surrounding the proteins. Understanding the solvent-soluble, solute-soluble interactions of amino acids, which are the building blocks of proteins, is important in terms of understanding the behaviour of amino acids in biochemical reactions. As it can be understood from the volumetric properties of methionine, depending on the chemical structure of biological systems, interactions deviating from the ideal state occur with the amino acid due to physical and chemical effects such as hydrogen bonds, dipole interactions, charge-transfer interactions. These interactions, which occur due to these chemical and physical effects, can trigger biological events depending on the environment. For this reason, volumetric properties will give an idea for a better understanding of the behavior of compounds such as methionine, which have an important role in biological events, in solutions.

Nomenclature

A_i Redlich–Kister equation Coefficients
M_i Molar masses of components,
ρ_i Densities of pure components
ρ Density of the mixture,
$\sigma(V^E)$ Standart deviation
V Molar volume of the solution
V_ϕ Apparent molar volume
$V_{\phi,i}^E$ Excess apparent molar volumes at infinite dilution,
V_i^0 Molar volumes of pure components
V_i^E Excess partial molar volume,
V_i^∞ Partial molar volumes at infinite dilution
V_i^0 Molar volume of the pure component
V_{exp}^E Experimental excess molar volume
V_{cal}^E Calculated excess molar volume
x_i Mole fractions of components
x Mole fractions of the mixture

References

[1] J. T. Brosnan, M. E. Brosnan, R. F.P. Bertolo and J. A. Brunton, "Methionine: A metabolically unique amino acid," *Livestock Science*, 112(1-2): 2-7, 2007.

[2] G. Wu, Y. Z. Fang, S. Yang, J. R. Lupton and N. D. Turner, "Glutathione metabolism and its implications for health," *J Nutr.* 134(3): 489-92, 2004.

[3] M. H. Stipanuk and I. Ueki, " Dealing with methionine/homocysteine sulfur: cysteine metabolism to taurine and inorganic sulfur," *Journal of inherited metabolic disease*, *34*(1): 17–32, 2011.

[4] J. C. Heiby, B. Goretzki, and C. M. Johnson *et al.* "Methionine in a protein hydrophobic core drives tight interactions required for assembly of spider silk," *Nat Commun* 10, 4378, 2019.

[5] S. Ravanel, B. Gakière, D. Job and R. Douce, "The specific features of methionine biosynthesis and metabolism in plants," *Proc. Natl. Acad. Sci.* 95(13): 7805–7812, 1998.

[6] S. M. Phillips, "A brief review of critical processes in exercise-induced muscular hypertrophy," *Sports Med.* 44(1): 71-77, 2014.

[7] J. T. Brosnan and M. E. Brosnan, "The Sulfur-Containing Amino Acids: An Overview," *The Journal of Nutrition*, 136(6): 1636S-640S, 2006.

[8] T. Zhang, Z. Li, Y. Wang, C. Li, B. Yu, X. Zheng, L. Jiang, J. Gong, "Determination and correlation of solubility and thermodynamic properties of l-methionine in binary solvents of water+(methanol, ethanol, acetone)," *The Journal of Chemical Thermodynamics*, 96: 82-92, 2016.

[9] E. Yu. Tyunina, V. I. Smirnov and G. N. Tarasova, "Thermodynamic Properties of L-Methionine and Nicotinic Acid in an Aqueous Buffer Solution", *Russian Journal of Physical Chemistry A*, 94(11): 2238–2243, 2020.

[10] F. I. El-Dossoki, "Phase Diagrams, Molal Volumes and Polarizabilities of (Lysine, Methionine Amino Acids-Alcohol-Water) Tri-Component Systems," *International Research Journal of Pure & Applied Chemistry*, 16(2): 1-11, 2018

[11] F. I. El-Dossoki, "Phase Diagrams, Molal Volumes and Polarizabilities of (Lysine, Methionine Amino Acids-Alcohol-Water)Tri-Component Systems,"*International Research Journal of Pure & Applied Chemistry,* 16(2): 1-11, 2018.

[12] M. Mokhtarpour and H. Shekaari, "Measurement and correlation of thermophysical properties in aqueous solutions of some novel bio-based deep eutectic solvents (lactic acid/amino acids) at T = (298.15 to 313.15) K," *J. Chem. Thermodynamics,* 144, 106051, 2020.

[13] A. Shalmashi and F. Amani, "Densıtıes And Excess Molar Volumes For Bınary Solutıon Of Water + Ethanol, + Methanol And + Propanol From (283.15 To 313.15) K," *Latin American Applied Research*, 44: 163-166, 2014.

[14] A. Ali, A. K. Nain, V. K. Sharma and S. Ahmad, "Molecular interactions in binary mixtures of tetrahydrofuran with alkanols (C6, C8, C10): an ultrasonic and volumetric study," *Indian J Pure Appl Phys*, 42: 666-673, 2004.

[15] H. Iloukhani, M. Rezaei-Sameti and J. Basiri-Parsa, "Excess molar volumes and dynamic viscosities for binary mixtures of toluene ? n-alkanes (C5–C10) at T = 298.15 K, comparison with Prigogine-Flory-Patterson theory. J Chem Thermodyn. 38: 975-982, 2006.

[16] U. S. Vural, "Excess molar volumes and viscosities of binary mixtures of epichlorohydrine and alcohols," *Russian Journal of Physical Chemistry A,* 79: 1096-1101, 2005.

[17] U. S. Vural, V. Muradoglu and S. Vural, "Excess molar volumes, and refractive index of binary mixtures of glycerol + methanol and glycerol + water at 298.15 K and 303.15 K," *Bulletin of the Chemical Society of Ethiopia,* 25: 111, 2011

[18] W. A. A. Ddamba, "Excess and Partial Molar Volumes for [Difurylmethane+Acetonitrile] Binary Mixtures in the Temperature Range: 288.15–323.15 K," Asian Journal of Chemistry, 21(4): 3057-3067, 2009.

[19] F. Allal, A. Dahmani, B. Saidat, "Volumetric Properties of Binary Mixtures of 1-Ethyl-3-methylimidazolium ethyl phosphonate + Methanol or 2-Propanol," International Journal of Thermodynamics (IJoT), 22(3): 128-136, 2019.

[20] H. Iloukhani and H. Bahrami, "Excess Molar Volumes and Partial Molar Volumes For Binary Mıxtures of Water with 1,2-Ethanediol, 1,2-Propanediol, and 1,2-Butanediol at 293.15, 303.15 and 313.15 K," Phys. Chem. Liq., 38: 103-111, 2004.

[21] T. Zhu and T. V. Voorhis, **"**Understanding the Dipole Moment of Liquid Water from a Self-Attractive Hartree Decomposition**,"** *The Journal of Physical Chemistry Letters, 12* (1)**:** 6-12**,** 2021.

[22] F. C Frank, "Dipole Induction and the Solvent Effect in Dipole Moment Measurements," *Proceedings of the Royal Society of London. Series A, Mathematical and Physical Sciences*, 152 (875): 171-196, 1935.

Novel Design and Thermodynamic Analyses of Cascade Refrigeration System at Ultra-Low Temperature

Hüsamettin Tan[1*], Ali Erişen[2]

[1*] Mechanical Engineering, Kırıkkale University, Yahşihan/Kırıkkale, 71450, Turkey
[2] Institute of Scientific, Kırıkkale University, Yahşihan/Kırıkkale, 71450, Turkey
E-mail: [1*]husamettintan@hotmail.com

Abstract

In this study, a cascade refrigeration system comprising gas and vapor compression cycles operating at ultra-low temperature was designed. In the thermodynamic analyses, R744, R404A, and R410A refrigerants in the high temperature cycle (HTC), and R1150, R170, and R23 in the low temperature cycle (LTC) were used. Thermodynamic analyses were carried out using the Engineering Equation Solver package program. Outputs considered were: system performance(COP), compression ratio, mass flow ratio and HTC cascade outlet temperature. Results show that, at different LTC condenser temperature values, R404A/R23 has the highest COP value, in the LTC, R23 has the highest compression ratio, while R1150 has the lowest one, in the HTC, R404A has the highest compression ratio, while R744 has the lowest one, the performance of the system increased with the decrease of the mass flow ratio.

Keywords: Ultra-low temperature; COP; cascade refrigeration; thermodynamic analyses; gas cycle; vapor compression cycle

1. Introduction

In refrigeration systems, energy consumption and the negative impact of the refrigerants on the environment are critical issues that need to be addressed. Refrigeration systems represent almost 17% of the global electrical energy consumption [1]. Considering that the available energy resources worldwide are limited and gradually decreasing, in the last 50 years, the improvement of refrigeration systems has become increasingly important. Moreover, environmental consciousness requires the evaluation of refrigerants in terms of ozone layer depletion (ODP) and global warming potential (GWP). The European Commission has introduced restrictions by approving the F-gas regulation for refrigerants [2]. The F-gas regulation restricts the implementation of hydrofluorocarbon (HFC) refrigerants based on their high GWP value. Since 2020, refrigerants having a GWP value of higher than 2500 have been generally restricted by F-gas regulation. However, these restrictions do not apply to military equipment and systems that function at temperatures below −50 °C [3].

Refrigeration systems vary based on the application area and the required ambient temperature [4]–[9]. In applications such as in the petroleum, medical, or food industries, as well as for air conditioning systems, the ambient temperatures vary between −150 °C and 5 °C. Vapor compression refrigeration cycles have been widely used in refrigeration systems for many years [10]. When using single-stage vapor compression systems, low temperatures are difficult to obtain because of the system elements restriction. In addition, due to the low coefficient of performance (COP), single-stage vapor compression systems are not economically viable because of their high energy consumption. In industrial applications, the lowest ambient

temperature that is possible to obtain is approximately −40 °C when using single-stage vapor compression systems [11]. Cascade refrigeration systems operating with two or more cycles provide ultra-low temperatures and a high COP. They comprise independent cycles that allow the use of different operating designs and refrigerants [12]–[18]. This studies on cascade refrigeration systems are aimed at increasing the COP. To achieve this, there are two different possible working areas: the use of alternative cycles and the use of an alternative refrigerant or refrigerant mixtures.

There are mainly four different cascade refrigeration system designs in the literature for the use of alternative cycles. These designs are two-stage vapor compression cascade refrigeration system (CCRS), vapor compression and absorption cascade refrigeration system (CACRS), two-stage absorption cascade refrigeration system (CARS), and auto-cascade refrigeration system (ACRS)[19].

The studies conducted on the CCRS have mostly used the R717 / R744 refrigerant pair [20]–[27]. These studies have shown that high COP is obtained when using the R744 refrigerant in the low-temperature cycle (LTC) and the R717 refrigerant in the high-temperature cycle (HTC). In addition to these two refrigerants, thermodynamic analyses for hydrocarbon and HFC group refrigerants in the HTC, such as, R1270 [15], [28], [29], R600 [4], R290 [15], [29], [30], and R404A [29], [31], [32], and in the LTC, such as R41 [33], R170 [28], [34], R1150 [28], R23 [31], and N_2O [28],[35] have already been conducted.

In all studies, pure refrigerants were used. Research has also been conducted using an ejector as an innovative design for two-stage vapor compression cycles for increasing the COP [5], [36]–[39].

---

*Corresponding Author

Two-stage CARSs are systems in which NH_3/H_2O and $LiBr/H_2O$ pairs are used to obtain low temperatures down to −40 °C [19]. The use of LiBr is not suitable at ultra-low temperatures because it crystallizes. The use of CARS is preferred to reduce energy consumption. Limited research has been conducted on CARS because of their low COP. Researches are available in the literature for LiBr, LiCl, NH_3, and H_2O refrigerants [40]–[42]. Although low ambient temperatures are obtained using two-stage vapor compression cascade refrigeration systems, they are ineffective because they consume large amounts of electrical energy. In this case, CARS in the HTC and CCRS in the LTC are used. Previous studies analyzed CARS using LiBr, NH_3, and H_2O refrigerants [42] and CCRS using R1234yf, R1234ze, CO_2, NH_3, R410A, and R134a [42]–[48]. The operation and maintenance of cascade refrigeration system is high. Therefore, in recent years, Auto-cascade refrigerant system with mixed refrigerants driven by single compressor that has lower capital cost are widely used. There have been many researches to improve system performance(COP) in ACRS, including optimization of system parameters, selection of refrigerant and efficient cycle modification [49]–[56].

When analyzing the refrigeration cycles used in cascade refrigeration systems, the primary aim is to reach the desired ambient temperature with an effective COP. In this study, a cascade refrigeration system operating at ultra-low temperature using gas (high temperature) and vapor compression (low temperature) refrigeration cycles is designed, which has not yet been discussed in previous studies. The gas refrigeration cycle in cascade systems has never been investigated before. In all cases, the refrigerant is in a single phase state in the gas cycle. The gas refrigeration cycle in cascade systems has never been investigated before. In all cases, the refrigerant is in a single phase state in the gas cycle. The objectives of the study are to make a new system design contribution to the literature in terms of the refrigerant cycles used and the reduction of net energy consumption with the energy produced by the expansion element in the gas cycle. In the designed system, thermodynamic analyses were performed using R410A, R404A, and R744 refrigerants in the HTC and R23, R1150, and R170 refrigerants in the LTC. For the different refrigerant couples, coefficient of performances, compression ratio and mass flow ratio were investigated in the new designed system.

2. Material and Method
2.1 System Design

Figure 1 illustrates the cascade refrigeration system wherein the designed gas and vapor compression cycles work together. Gas refrigeration cycle in the HTC and vapor compression refrigeration cycle in the LTC are used. These two cycles are connected via a cascade heat exchanger.

In the LTC, the saturated vapor phase refrigerant (# 4) at the evaporator outlet enters the cascade heat exchanger by increasing its temperature and pressure with the LTC compressor (# 1). In the cascade heat exchanger, heat is transferred from the LTC to the HTC at constant pressure, and the refrigerant enters the expansion valve (# 2) as a saturated liquid, expanding at constant enthalpy and entering the evaporator as a saturated liquid–vapor mixture (# 3). In the HTC, the pressure and temperature of the refrigerant at the cascade heat exchanger outlet (# 8) is increased by the HTC compressor, and the refrigerant enters the cooler (# 5). In the HTC gas cooler, the refrigerant, whose temperature

decreases with the release of heat at constant pressure (# 6), enters the cascade heat exchanger, and its pressure and temperature are reduced by the expander element (# 7). There is a two-phase flow in the LTC and a single-phase flow in the HTC.
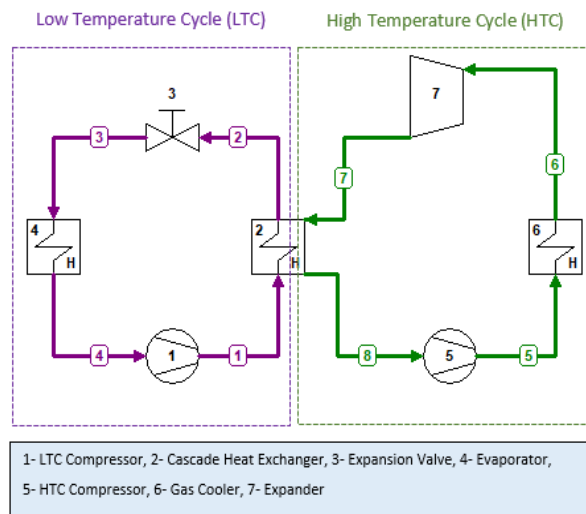

Figure 1. Schematic of cascade refrigeration system.

2.2 Modeling and Thermodynamic Analysis of the Cascade Refrigeration Cycle

In the theoretical analyses of the designed system in terms of energy, the following assumptions have been made:

- All components are assumed to be in steady-state and steady-flow process;
- The potential and kinetic energy changes are negligible;
- Pressure losses in fittings and heat exchangers are negligible;
- In the LTC, the evaporator outlet is considered to be saturated vapor (# 4) and the condenser outlet is considered to be saturated liquid (# 2);
- The isentropic efficiency for both compressors and expander was fixed as 80%; based on recommended values by [40];
- The expansion valves are isenthalpic devices;
- The evaporator working pressure is higher than the atmospheric pressure;
- In the thermodynamic analysis, the refrigeration capacity of the system is 1 kW, the LTC evaporator temperature is −80 °C (T_4) and HTC expander outlet temperature is -42 ºC (T_7);
- LTC condenser temperature is in intervals of 1 °C ranging from -35 ºC to -30 ºC (T_2), HTC cascade heat exchanger outlet temperature is changed according to getting the best COP (T_8), HTC gas cooler outlet temperature 20 ºC (T_6).

According to the balance of mass and energy, the thermodynamic analyzes of system are carried out for steady-state process. Energy analyzes are made for all system elements based on Equations (1) and (2). As a result of energy analyzes, the equations of the system elements are given in the below.

Mass balance;
$$\sum \dot{m}_g = \sum \dot{m}_\varsigma \tag{1}$$

Energy balance;
$$\sum \dot{Q}_{net} + \sum W_{net} + \sum \dot{m}(h_g - h_\varsigma) = 0 \tag{2}$$

Cycle	Refrigerant	Boiling Point, ºC	Critical Temperature, ºC	Critical Pressure, bar	GWP
HTC	R744 (HC)	-78.464	30.978	73.77	1
	R404A (HFC)	-46.5	72	37.29	3260
	R410A (HFC)	-51.5	71.8	49.01	2088
LTC	R23 (HFC)	-81.87	26.29	48.32	14800
	R170 (HC)	-88.584	32.172	48.72	6
	R1150 (HC)	-103.77	9.2	50.41	4

Energy balance across the evaporator is given by:

$$\dot{Q}_{evap} = \dot{m}_{LTC}.(h_4 - h_3) \tag{3}$$

The isentropic efficiency for LTC compressor is given by:

$$\eta_{C\_LTC} = \frac{h_{1s} - h_4}{h_1 - h_4} \tag{4}$$

The power input to the LTC compressor is given by:

$$\dot{W}_{LTC} = \dot{m}_{LTC}.(h_1 - h_4) \tag{5}$$

The energy balance across the cascade heat exchanger is given by:

$$\dot{m}_{LTC}.(h_1 - h_2) = \dot{m}_{HTC}.(h_8 - h_7) \tag{6}$$

The isentropic efficiency for HTC compressor is given by:

$$\eta_{C\_HTC} = \frac{h_{5s} - h_8}{h_5 - h_8} \tag{7}$$

The power input to the HTC compressor is given by:

$$\dot{W}_{HTC} = \dot{m}_{HTC}.(h_5 - h_8) \tag{8}$$

The energy balance across the gas cooler is given by:

$$\dot{Q}_{gas} = \dot{m}_{HTC}.(h_6 - h_5) \tag{9}$$

The isentropic efficiency for expander is given by:

$$\eta_{EXP} = \frac{h_6 - h_7}{h_{6s} - h_7} \tag{10}$$

The power output to the expander is given by:

$$\dot{W}_{EXP} = \dot{m}_{HTC}.(h_6 - h_7) \tag{11}$$

The COP of the system, which is the main parameter to be calculated for the energy analysis, is obtained using Equation 12. Here, $\dot{Q}_{evap}$ is the evaporator refrigeration capacity in the LTC, $\dot{W}_{LTC}$ is the compressor power in the LTC, $\dot{W}_{HTC}$ is the compressor power in the HTC, $\dot{W}_{EXP}$ is the power generated during expansion in the HTC.

$$COP_{system} = \frac{\dot{Q}_{evap}}{\dot{W}_{LTC} + \dot{W}_{HTC} - \dot{W}_{EXP}} \tag{12}$$

The COP was calculated using the Engineering Equation Solver (EES) package program using the energy equations[58]. EES provides many built-in mathematical and thermophysical property functions useful for engineering calculations. Many researchers used the EES for thermodynamic modeling of refrigeration systems [12], [20], [21], [25], [43], [59]–[63]. In the thermodynamic analysis, R744, R404A, and R410A refrigerants in the high temperature cycle (HTC), and R1150, R170, and R23 in the low temperature cycle (LTC) were used. In the selection of refrigerants, R23, R1150 and R170 were selected when their boiling point temperatures were considered in order to provide -80ºC refrigerant temperature in the low temperature cycle. Refrigerants selections in the high temperature cycle are environmentally friendly and widely used, so R744. Since R404A and R410A are widely used, it has also been observed that the boiling temperature decreases to -42 ºC at 1 atm pressure. Otherwise, a situation below atmospheric pressure is not be desired in the system. The thermodynamic properties of the refrigerants used from the library in the EES. The main properties of the selected refrigerants are presented in Table 1.

3. Results and Discussion

Under the assumptions, thermodynamic analyses were conducted for refrigerant couples in the cascade refrigeration system. COPs of refrigerant couples, compression ratio of compressors and net energy consumption values of system were determined. According to these parameters, the best refrigerant couple among them selected.

Figure 2 shows the change in the COPs of refrigerant couples with respect to the LTC condenser temperature. In this figure, LTC evaporator, HTC gas cooler outlet and HTC expander outlet temperature are kept constant at -80 ºC, 20 º and -42ºC, respectively. At different LTC condenser temperature values, HTC cascade heat exchanger outlet temperature has been determined to maximize system performance (COP). COPs for refrigerant couples increases with increasing LTC condenser temperature as shown in Figure 2. In the determined LTC condenser temperature range, R404A/R23 has the highest COP value, while R744/R170 has the lowest one. R404A/R1150 can be considered as an alternative for R404A/R23 because the COP of R404A/R1150 is very close that of R404A/R23.

Figure 3a shows the change in the compression ratio of refrigerant in LTC with respect to the LTC condenser temperature. In this figure, HTC compression ratio is kept constant at 3.6 for R744 in HTC. Among the different fluids in the low temperature cycle, R23 has the highest compression ratio, while R1150 has the lowest one. Figure 3b shows the compression ratio of HTC refrigerants. In this figure, HTC expander outlet and gas cooler outlet temperature are kept at constant at -42ºC and 20ºC, respectively. Therefore, compression ratio of HTC is

constant for all LTC refrigerants. Among the different fluids in the HTC, R404A has the highest compression ratio, while R744 has the lowest one.
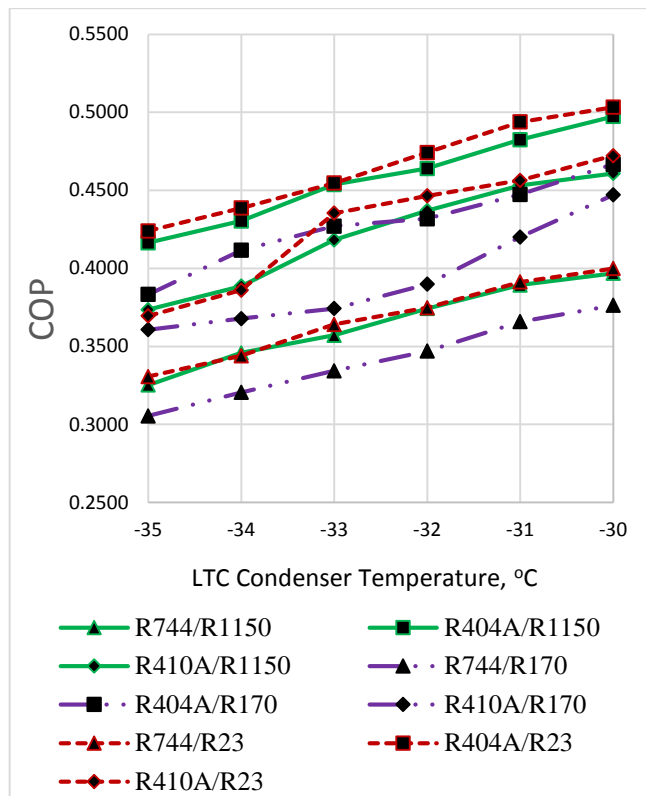

Figure 2. COPs of refrigerant couples as a function of LTC condenser temperature.

The relation between HTC cascade heat exchanger and LTC compressor outlet temperatures is presented in Table 2, Table 3 and Table 4 for all refrigerant couples. Increasing the LTC compressor outlet temperature allows the HTC cascade heat exchanger outlet temperature to increase. As the HTC cascade heat exchanger outlet temperature increases, the mass flow ratio decreases between LTC and HTC. The performance of the system increased with the decrease of the mass flow ratio. Because, energy consumption value of the compressor in the high temperature cycle has decreased.
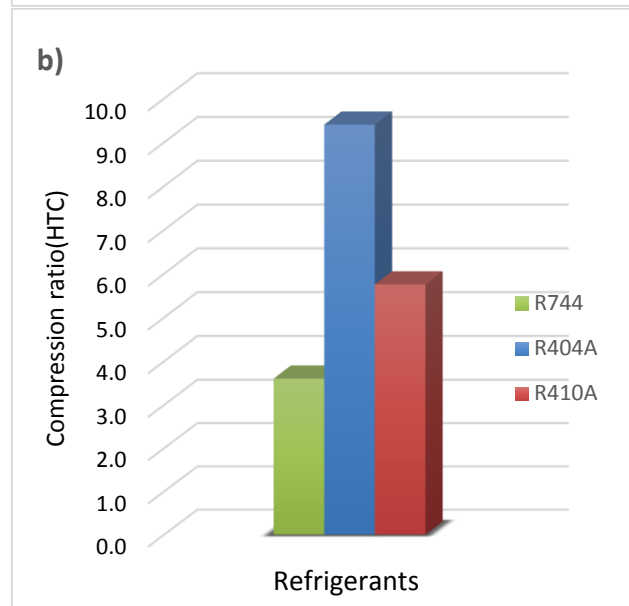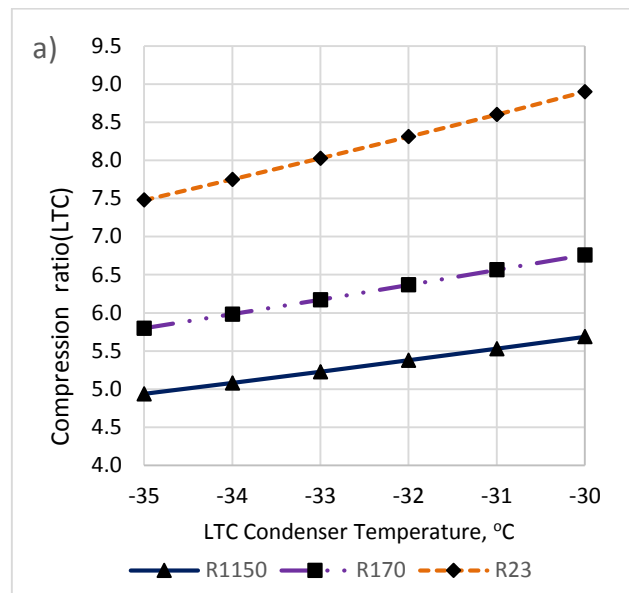

Figure 3. Compression ratio a) LTC refrigerants b) HTC refrigerants.

Table 2. Relation between HTC cascade heat exchanger outlet and LTC compressor outlet temperature for R1150 in LTC.

Refrigerant Couples	LTC Condenser Temperature	HTC Cascade Heat Ex. Outlet Temperature	LTC Compressor Outlet Temperature	Mass Flow Ratio (LTC/HTC)	COP
R744/R1150	-30	-3	32,65	13,94	0,3969
R404A/R1150	-30	-3	32,65	14,09	0,4974
R410A/R1150	-30	-4	32,65	14,55	0,4609
R744/R1150	-31	-5	30,66	14,75	0,3894
R404A/R1150	-31	-6	30,66	15,38	0,4825
R410A/R1150	-31	-6	30,66	15,40	0,4532
R744/R1150	-32	-8	28,65	15,93	0,3743
R404A/R1150	-32	-9	28,65	16,65	0,464
R410A/R1150	-32	-9	28,65	16,66	0,437
R744/R1150	-33	-11	26,63	17,31	0,3571
R404A/R1150	-33	-11	26,63	18,12	0,4538
R410A/R1150	-33	-12	26,63	18,74	0,4183
R744/R1150	-34	-13	24,61	18,93	0,3459
R404A/R1150	-34	-14	24,61	19,96	0,4304
R410A/R1150	-34	-16	24,61	21,38	0,3886
R744/R1150	-35	-16	22,57	20,93	0,3253
R404A/R1150	-35	-16	22,57	21,48	0,4165
R410A/R1150	-35	-18	22,57	22,93	0,3736

Table 3. Relation between HTC cascade heat exchanger outlet and LTC compressor outlet temperature for R170 in LTC.

Refrigerant Couples	LTC Condenser Temperature	HTC Cascade Heat Ex. Outlet Temperature	LTC Compressor Outlet Temperature	Mass Flow Ratio (LTC/HTC)	COP
R744/R170	-30	-8	22,29	17.50	0,3763
R404A/R170	-30	-9	22,29	18,30	0,4667
R410A/R170	-30	-8	22,29	17,77	0,4471
R744/R170	-31	-10	20,53	18,44	0,3659
R404A/R170	-31	-12	20,53	19,96	0,4474
R410A/R170	-31	-12	20,53	19,97	0,4202
R744/R170	-32	-13	18,76	20,20	0,347
R404A/R170	-32	-14	18,76	21,27	0,4318
R410A/R170	-32	-16	18,76	22,79	0,3899
R744/R170	-33	-15	16,98	22,28	0,3344
R404A/R170	-33	-15	16,98	22,67	0,4271
R410A/R170	-33	-18	16,98	25,36	0,3743
R744/R170	-34	-17	15,19	23,89	0,3205
R404A/R170	-34	-17	15,19	24,29	0,4117
R410A/R170	-34	-19	15,19	26,25	0,3678
R744/R170	-35	-19	13,38	25,75	0,3055
R404A/R170	-35	-20	13,38	27,36	0,3833
R410A/R170	-35	-20	13,38	27,21	0,3608

Table 4. Relation between HTC cascade heat exchanger outlet and LTC compressor outlet temperature for R23 in LTC.

Refrigerant Couples	LTC Condenser Temperature	HTC Cascade Heat Ex. Outlet Temperature	LTC Compressor Outlet Temperature	Mass Flow Ratio (LTC/HTC)	COP
R744/R23	-30	-4	36,45	7,84	0,399
R404A/R23	-30	-4	36,45	7,92	0,5033
R410A/R23	-30	-4	36,45	7,97	0,4722
R744/R23	-31	-6	34,42	8,24	0,3913
R404A/R23	-31	-6	34,42	8,34	0,4939
R410A/R23	-31	-7	34,42	8,60	0,4564
R744/R23	-32	-9	32,39	9,07	0,3748
R404A/R23	-32	-9	32,39	9,21	0,4743
R410A/R23	-32	-9	32,39	9,21	0,4465
R744/R23	-33	-11	30,35	9,58	0,3642
R404A/R23	-33	-12	30,35	10,04	0,4547
R410A/R23	-33	-11	30,35	9,72	0,4354
R744/R23	-34	-14	28,29	10,71	0,344
R404A/R23	-34	-14	28,29	10,91	0,4387
R410A/R23	-34	-17	28,29	12,14	0,3861
R744/R23	-35	-16	26,22	11,44	0,3308
R404A/R23	-35	-16	26,22	11,64	0,424
R410A/R23	-35	-19	26,22	13,07	0,3696

4. Conclusions

In this study, a new cascade system was designed for a refrigeration system operating at ultra-low temperatures, consisting of two cycles, namely HTC by gas and LTC by vapor compression. Thermodynamic analysis of the system in terms of the energy performance was performed. In order to determine the best refrigerant couples in terms of the COP, R1150, R170, and R23 refrigerants in the LTC and R404A, R410A, and R744 refrigerants in the HTC were analyzed. LTC condenser temperature was considered as a variable parameter in the system. HTC cascade heat exchanger inlet temperature is constant and the outlet temperature is changed in each condition. The primary results of the study are listed below:

- Among the different refrigerants analyzed, the R404A / R23 refrigerant couple has the best result in terms of the COP while R744/R170 has the lowest one. (Figure 2):
- R23 has high vapor density and low condensing pressure at design temperatures in the LTC. These properties reduce the compressor energy consumption in the LTC. The high temperature value at the compressor outlet increases the HTC outlet temperature in the cascade heat exchanger. Increasing the enthalpy difference between the inlet and outlet of the HTC cascade heat exchanger

reduces the mass flow rate. The decrease in HTC mass flow rate increases the system performance by reducing HTC net energy consumption. Among the refrigerants (R744, R410A), R404A has the highest vapor density at operating conditions in HTC. In this case, the HTC compressor has the lowest specific volume at its inlet, thereby increasing the system performance by reducing energy consumption.

- R744 has low vapor density at design temperature. In this case, the high specific volume at the compressor inlet increases the energy consumption value. The vapor density of R170 is low at design temperature. Again, this situation increases the energy consumption value due to the high specific volume of compressor inlet. In addition, when compared to other refrigerants at the compressor outlet in the low-temperature cycle, the low-temperature value reduces the outlet temperature in the high-temperature cycle cascade heat exchanger. The decrease in the HTC cascade heat exchanger outlet temperature increased the HTC mass flow rate. For this reason, HTC net energy consumption value increased and decreased the system performance.

- Compression ratios of refrigerants vary according to the lower and upper pressure values at operating

temperatures. Among the operating temperatures for the low temperature cycle, the upper and lower pressure ratio is highest for R23 and lowest for R1150. For high temperature cycle, between -42°C and 20°C, the upper and lower pressure ratio is the highest for R404A and the lowest for R744.

- With the increase of LTC condenser temperature, system performance (COP) values increased for all refrigerant couples.
- As the HTC cascade heat exchanger outlet temperature increases, the mass flow ratio decreases between LTC and HTC and the performance of the system increased. It is an important parameter for the best value of system performance (COP).
- The higher the mass flow ratio between the gas and vapor compression cycles, the lower the temperature difference between the HTC cascade heat exchanger inlet and outlet. In this case, the high mass flow rate on the gas cycle increases the energy consumption and has a negative effect on the system performance (COP).
- The energy consumption value of the HTC compressor is more effective than the energy consumption of the LTC compressor in determining the system performance.

It is seen that the system performance (COP) values are not at a satisfactory level according to the results in the literature. It is necessary to take into account the negative situations that arise as a result of using gas and vapor compression cycles together. In the study, a novel design idea has contributed to the literature in terms of cascade systems designs. In future studies, the results of the thermodynamic analysis of the design will give an idea to the researchers. Before making this design experimentally, it has been determined that theoretical studies should be carried out in order to eliminate the problems that cause the system performance to be low in thermodynamic analyzes.

Nomenclature
$\dot{m}$ Mass flow rate (kg/s)
h   Enthalpy (kJ/kg)
$\dot{W}$ Energy consumption (kW)
$\dot{Q}$ Heat rate (kW)

Greek Letters
η   Isentropic efficiency (-)

Subscripts
gas   gas cooler
EXP   expander
evap   evaporator

Abbreviations
LTC   Low temperature cycle
HTC   High temperature cycle
COP   Coefficient of performance
EES   Engineering Equation Solver
ODP   Ozone layer depletion
GWP   Global warming potential
HFC   Hydrofluorocarbon
CCRS   Two-stage vapor compression cascade refrigeration system
CACRS   Vapor compression and absorption cascade refrigeration system
CARS   Two-stage absorption cascade refrigeration system
ACRS   Auto-cascade refrigeration system

References:

[1] IIR, "The Role of Refrigeration in the Global Economy," 2015.[Online].Available:https://www.scribd.com/document/452307076/NoteTech-29-EN-2-pdf.

[2] European Commission, "Regulation (EU) No 517/2014 of The European Parliament and of the council of 16 April 2014 on fluorinated greenhouse gases and repealing Regulation (EC) No 842/2006," 2014.

[3] A.Mota-Babiloni *et al.*, "Ultralow-temperature refrigeration systems: Configurations and refrigerants to reduce the environmental impact,"*Int.J.Refrig.*, vol.111,pp.147–158,Mar.2020,doi: 10.1016/J.IJREFRIG.2019.11.016.

[4] H. Yamaguchi, X.-D. Niu, K. Sekimoto, and P. Nekså, "Investigation of dry ice blockage in an ultra-low temperature cascade refrigeration system using CO2 as a working fluid," *Int. J. Refrig.*, vol. 34, no. 2, pp. 466–475, Mar. 2011, doi: 10.1016/J.IJREFRIG.2010.11.001.

[5] K. Megdouli, B. M. Tashtoush, E. Nahdi, M. Elakhdar, L. Kairouani, and A. Mhimid, "Thermodynamic analysis of a novel ejector-cascade refrigeration cycles for freezing process applications and air-conditioning," *Int. J. Refrig.*, vol. 70, pp. 108–118, Oct. 2016, doi: 10.1016/J.IJREFRIG.2016.06.029.

[6] J. Lee, C. Lee, S. Baek, and S. Jeong, "Investigation of ejector-equipped Joule–Thomson refrigerator operating below 77 K," *Int. J. Refrig.*, vol. 78, pp. 93–107, Jun. 2017, doi: 10.1016/J.IJREFRIG.2017.03.016.

[7] H. C. Wang, G. F. Chen, X. Q. Dong, Y. X. Zhao, H. Guo, and M. Q. Gong, "Performance comparison of single-stage mixed-refrigerant Joule–Thomson cycle and pure-gas reverse Brayton cycle at fixed-temperatures from 80 to 180 K," *Int. J. Refrig.*, vol. 80, pp. 77–91, Aug. 2017, doi: 10.1016/J.IJREFRIG.2017.05.011.

[8] A. Biglia *et al.*, "Reversed Brayton cycle for food freezing at very low temperatures: Energy performance and optimisation," *Int. J. Refrig.*, vol. 81, pp. 82–95, Sep. 2017, doi: 10.1016/J.IJREFRIG.2017.05.022.

[9] Z. Hongli, H. Yu, and C. Liang, "Experimental study on a small Brayton air refrigerator under −120 °C," *Appl. Therm. Eng.*, vol. 29, no. 8–9, pp. 1702–1706, Jun. 2009, doi: 10.1016/J.APPLTHERMALENG.2008.07.028.

[10] L. H. P. Massuchetto, R. B. C. do Nascimento, S. M. R. de Carvalho, H. V. de Araújo, and J. V. H. d'Angelo, "Thermodynamic performance evaluation of a cascade refrigeration system with mixed refrigerants: R744/R1270, R744/R717 and R744/RE170," *Int. J. Refrig.*, vol. 106, pp. 201–212, Oct. 2019, doi: 10.1016/J.IJREFRIG.2019.07.005.

[11] D. Yılmaz, Ü. Sınar, A. Özyurt, B. Yılmaz, and E. Mancuhan, "Numerical Investigation of Performance Effects of Excessive Cooling and Heating in a Two-Stage Cooling System Operating at Ultra Low Temperatures," *Afyon Kocatepe Univ. J. Sci. Eng.*, vol. 17, pp. 1172–1180, 2017, doi: 10.5578/fmbd.66304.

[12] A. M. Dubey, S. Kumar, and G. Das Agrawal, "Thermodynamic analysis of a transcritical CO2/propylene (R744-R1270) cascade system for cooling and heating applications," *Energy Convers.*

Manag., vol. 86, pp. 774–783, 2014, doi: 10.1016/j.enconman.2014.05.105.

[13] P. Bansal, "A review - Status of CO 2 as a low temperature refrigerant: Fundamentals and R&D opportunities," *Appl. Therm. Eng.*, vol. 41, pp. 18–29, 2012, doi: 10.1016/j.applthermaleng.2011.12.006.

[14] B. Niu and Y. Zhang, "Experimental study of the refrigeration cycle performance for the R744/R290 mixtures," *Int. J. Refrig.*, vol. 30, no. 1, pp. 37–42, Jan. 2007, doi: 10.1016/J.IJREFRIG.2006.06.002.

[15] K. K. Singh, R. Kumar, and A. Gupta, "Multi-objective Optimization of Thermodynamic and Economic Performances of Natural Refrigerants for Cascade Refrigeration," *Arab. J. Sci. Eng.*, vol. 46, no. 12, pp. 12235–12252, 2021, doi: 10.1007/s13369-021-05924-w.

[16] Y. D. Zhu, Z. R. Peng, G. B. Wang, and X. R. Zhang, "Thermodynamic analysis of a novel multi-target-temperature cascade cycle for refrigeration," *Energy Convers. Manag.*, vol. 243, no. March, p. 114380, 2021, doi: 10.1016/j.enconman.2021.114380.

[17] V. Adebayo, M. Abid, M. Adedeji, M. Dagbasi, and O. Bamisile, "Comparative thermodynamic performance analysis of a cascade refrigeration system with new refrigerants paired with CO2," *Appl. Therm. Eng.*, vol. 184, p. 116286, 2021, doi: 10.1016/j.applthermaleng.2020.116286.

[18] K. Golbaten Mofrad, S. Zandi, G. Salehi, and M. H. Khoshgoftar Manesh, "4E analyses and multi-objective optimization of cascade refrigeration cycles with heat recovery system," *Therm. Sci. Eng. Prog.*, vol. 19, p. 100613, 2020, doi: 10.1016/j.tsep.2020.100613.

[19] M. Pan, H. Zhao, D. Liang, Y. Zhu, Y. Liang, and G. Bao, "A review of the cascade refrigeration system," *Energies*, vol. 13, no. 9, 2020, doi: 10.3390/en13092254.

[20] E. Gholamian, P. Hanafizadeh, and P. Ahmadi, "Advanced exergy analysis of a carbon dioxide ammonia cascade refrigeration system," *Appl. Therm. Eng.*, vol. 137, no. October 2017, pp. 689–699, 2018, doi: 10.1016/j.applthermaleng.2018.03.055.

[21] A. H. Mosaffa, L. G. Farshi, C. A. Infante Ferreira, and M. A. Rosen, "Exergoeconomic and environmental analyses of CO2/NH3 cascade refrigeration systems equipped with different types of flash tank intercoolers," *Energy Convers. Manag.*, vol. 117, pp. 442–453, 2016, doi: 10.1016/j.enconman.2016.03.053.

[22] M. Aminyavari, B. Najafi, A. Shirazi, and F. Rinaldi, "Exergetic, economic and environmental (3E) analyses, and multi-objective optimization of a CO2/NH3 cascade refrigeration system," *Appl. Therm. Eng.*, vol. 65, no. 1–2, pp. 42–50, 2014, doi: 10.1016/j.applthermaleng.2013.12.075.

[23] J. Alberto Dopazo, J. Fernández-Seara, J. Sieres, and F. J. Uhía, "Theoretical analysis of a CO2-NH3 cascade refrigeration system for cooling applications at low temperatures," *Appl. Therm. Eng.*, vol. 29, no. 8–9, pp. 1577–1583, 2009, doi: 10.1016/j.applthermaleng.2008.07.006.

[24] W. Bingming, W. Huagen, L. Jianfeng, and X. Ziwen, "Experimental investigation on the performance of NH3/CO2 cascade refrigeration system with twin-screw compressor," *Int. J. Refrig.*, vol. 32, no. 6, pp. 1358–1365, 2009, doi: 10.1016/j.ijrefrig.2009.03.008.

[25] H. M. Getu and P. K. Bansal, "Thermodynamic analysis of an R744-R717 cascade refrigeration system," *Int. J. Refrig.*, vol. 31, no. 1, pp. 45–54, 2008, doi: 10.1016/j.ijrefrig.2007.06.014.

[26] T. S. Lee, C. H. Liu, and T. W. Chen, "Thermodynamic analysis of optimal condensing temperature of cascade-condenser in CO2/NH3 cascade refrigeration systems," *Int. J. Refrig.*, vol. 29, no. 7, pp. 1100–1108, 2006, doi: 10.1016/j.ijrefrig.2006.03.003.

[27] G. Di Nicola, G. Giuliani, F. Polonara, and R. Stryjek, "Blends of carbon dioxide and HFCs as working fluids for the low-temperature circuit in cascade refrigerating systems," *Int. J. Refrig.*, vol. 28, no. 2, pp. 130–140, 2005, doi: 10.1016/j.ijrefrig.2004.06.014.

[28] J. Sarkar, S. Bhattacharyya, and A. Lal, "Performance comparison of natural refrigerants based cascade systems for ultra-low-temperature applications," *Int. J. Sustain. Energy*, vol. 32, no. 5, pp. 406–420, 2013, doi: 10.1080/14786451.2013.765426.

[29] G. Sachdeva, V. Jain, and S. S. Kachhwaha, "Performance Study of Cascade Refrigeration System Using Alternative Refrigerants," *Int. J. Mech. Aerospace, Ind. Mechatron. Manuf. Eng.*, vol. 8, no. 3, p. 7, 2014, [Online]. Available: http://waset.org/publications/9997619/performance-study-of-cascade-refrigeration-system-using-alternative-refrigerants.

[30] Nasruddin, S. Sholahudin, N. Giannetti, and Arnas, "Optimization of a cascade refrigeration system using refrigerant C3H8 in high temperature circuits (HTC) and a mixture of C2H6/CO2 in low temperature circuits (LTC)," *Appl. Therm. Eng.*, vol. 104, pp. 96–103, 2016, doi: 10.1016/j.applthermaleng.2016.05.059.

[31] A. Kilicarslan and M. Hosoz, "Energy and irreversibility analysis of a cascade refrigeration system for various refrigerant couples," *Energy Convers. Manag.*, vol. 51, no. 12, pp. 2947–2954, 2010, doi: 10.1016/j.enconman.2010.06.037.

[32] R. Roy and B. K. Mandal, "Thermo-economic analysis and multi-objective optimization of vapour cascade refrigeration system using different refrigerant combinations: A comparative study," *J. Therm. Anal. Calorim.*, vol. 139, no. 5, pp. 3247–3261, 2020, doi: 10.1007/s10973-019-08710-x.

[33] M. Deymi-Dashtebayaz, A. Sulin, T. Ryabova, I. Sankina, M. Farahnak, and R. Nazeri, "Energy, exergoeconomic and environmental optimization of a cascade refrigeration system using different low GWP refrigerants," *J. Environ. Chem. Eng.*, vol. 9, no. 6, p. 106473, 2021, doi: 10.1016/j.jece.2021.106473.

[34] M. Gong, Z. Sun, J. Wu, Y. Zhang, C. Meng, and Y. Zhou, "Performance of R170 mixtures as refrigerants for refrigeration at -80 °C temperature range," *Int. J. Refrig.*, vol. 32, no. 5, pp. 892–900, 2009, doi: 10.1016/j.ijrefrig.2008.11.007.

[35] S. Bhattacharyya, A. Garai, and J. Sarkar,

"Thermodynamic analysis and optimization of a novel N2O-CO2 cascade system for refrigeration and heating," *Int. J. Refrig.*, vol. 32, no. 5, pp. 1077–1084, 2009, doi: 10.1016/j.ijrefrig.2008.09.008.

[36] HAN XINGWANG, "Super low temperature transcritical cascade refrigeration system and refrigeration method," CN110887266A, 2020.

[37] G. Chen, V. Ierin, O. Volovyk, and K. Shestopalov, "An improved cascade mechanical compression–ejector cooling cycle," *Energy*, vol. 170, pp. 459–470, Mar. 2019, doi: 10.1016/J.ENERGY.2018.12.107.

[38] R. Ben Mansour, M. Ouzzane, and Z. Aidoun, "Numerical evaluation of ejector-assisted mechanical compression systems for refrigeration applications," *Int. J. Refrig.*, vol. 43, pp. 36–49, Jul. 2014, doi: 10.1016/J.IJREFRIG.2014.04.010.

[39] T. K. Nguyen and C. H. Le, "Thermodynamic analysis of an ejector–vapour compressor cascade refrigeration system," *J. Therm. Anal. Calorim.*, vol. 141, no. 6, pp. 2189–2200, 2020, doi: 10.1007/s10973-020-09635-6.

[40] X. She, Y. Yin, M. Xu, and X. Zhang, "A novel low-grade heat-driven absorption refrigeration system with LiCl-H2O and LiBr-H2O working pairs," *Int. J. Refrig.*, vol. 58, pp. 219–234, 2015, doi: 10.1016/j.ijrefrig.2015.06.016.

[41] A. K. Songara, M. Fatouh, and S. Srinivasa Murthy, "Thermodynamic studies on HFC134a-DMA double effect and cascaded absorption refrigeration systems," *Int. J. Energy Res.*, vol. 22, no. 7, pp. 603–614, 1998, doi: 10.1002/(SICI)1099-114X(19980610)22:7<603::AID-ER379>3.0.CO;2-9.

[42] P. Cui, M. Yu, Z. Liu, Z. Zhu, and S. Yang, "Energy, exergy, and economic (3E) analyses and multi-objective optimization of a cascade absorption refrigeration system for low-grade waste heat recovery," *Energy Convers. Manag.*, vol. 184, no. January, pp. 249–261, 2019, doi: 10.1016/j.enconman.2019.01.047.

[43] V. Jain, S. S. Kachhwaha, and G. Sachdeva, "Thermodynamic performance analysis of a vapor compression-absorption cascaded refrigeration system," *Energy Convers. Manag.*, vol. 75, pp. 685–700, 2013, doi: 10.1016/j.enconman.2013.08.024.

[44] Y. Xu, F. S. Chen, Q. Wang, X. Han, D. Li, and G. Chen, "A novel low-temperature absorption-compression cascade refrigeration system," *Appl. Therm. Eng.*, vol. 75, pp. 504–512, 2015, doi: 10.1016/j.applthermaleng.2014.10.043.

[45] H. He, L. Wang, J. Yuan, Z. Wang, W. Fu, and K. Liang, "Performance evaluation of solar absorption-compression cascade refrigeration system with an integrated air-cooled compression cycle," *Energy Convers. Manag.*, vol. 201, no. September, p. 112153, 2019, doi: 10.1016/j.enconman.2019.112153.

[46] Z. Sun, C. Wang, Y. Liang, H. Sun, S. Liu, and B. Dai, "Theoretical study on a novel CO2 Two-stage compression refrigeration system with parallel compression and solar absorption partial cascade refrigeration system," *Energy Convers. Manag.*, vol. 204, no. August 2019, p. 112278, 2020, doi:

10.1016/j.enconman.2019.112278.

[47] J. Fernández-Seara, J. Sieres, and M. Vázquez, "Compression-absorption cascade refrigeration system," *Appl. Therm. Eng.*, vol. 26, no. 5–6, pp. 502–512, 2006, doi: 10.1016/j.applthermaleng.2005.07.015.

[48] Y. Xu, G. Chen, Q. Wang, X. Han, N. Jiang, and S. Deng, "Performance study on a low-temperature absorption-compression cascade refrigeration system driven by low-grade heat," *Energy Convers. Manag.*, vol. 119, pp. 379–388, 2016, doi: 10.1016/j.enconman.2016.04.061.

[49] J. Liu, Y. Liu, J. Yu, and G. Yan, "Thermodynamic analysis of a novel ejector-enhanced auto-cascade refrigeration cycle," *Appl. Therm. Eng.*, vol. 200, no. October 2021, p. 117636, 2022, doi: 10.1016/j.applthermaleng.2021.117636.

[50] T. Bai, G. Yan, and J. Yu, "Experimental investigation on the concentration distribution behaviors of mixture in an ejector enhanced auto-cascade refrigeration system," *Int. J. Refrig.*, vol. 99, pp. 145–152, Mar. 2019, doi: 10.1016/J.IJREFRIG.2018.11.024.

[51] G. Yan, C. He, and J. Yu, "Theoretical investigation on the performance of a modified refrigeration cycle using binary zeotropic hydrocarbon mixture R170/R290," *Int. J. Refrig.*, vol. 94, pp. 111–117, 2018, doi: 10.1016/j.ijrefrig.2018.07.023.

[52] T. Bai, G. Yan, and J. Yu, "Experimental investigation of an ejector-enhanced auto-cascade refrigeration system," *Appl. Therm. Eng.*, vol. 129, pp. 792–801, Jan. 2018, doi: 10.1016/J.APPLTHERMALENG.2017.10.053.

[53] X. Hao, L. Wang, Z. Wang, Y. Tan, and X. Yan, "Hybrid auto-cascade refrigeration system coupled with a heat-driven ejector cooling cycle," *Energy*, vol. 161, pp. 988–998, Oct. 2018, doi: 10.1016/J.ENERGY.2018.07.201.

[54] Y. Tan, L. Wang, and K. Liang, "Thermodynamic performance of an auto-cascade ejector refrigeration cycle with mixed refrigerant R32 + R236fa," *Appl. Therm. Eng.*, vol. 84, pp. 268–275, Jun. 2015, doi: 10.1016/J.APPLTHERMALENG.2015.03.047.

[55] K. Du, S. Zhang, W. Xu, and X. Niu, "A study on the cycle characteristics of an auto-cascade refrigeration system," *Exp. Therm. Fluid Sci.*, vol. 33, no. 2, pp. 240–245, 2009, doi: 10.1016/j.expthermflusci.2008.08.006.

[56] S. G. Kim and M. S. Kim, "Experiment and simulation on the performance of an autocascade refrigeration system using carbon dioxide as a refrigerant," *Int. J. Refrig.*, vol. 25, no. 8, pp. 1093–1101, 2002, doi: 10.1016/S0140-7007(01)00110-4.

[57] J. S. Oh, M. Binns, S. Park, and J. K. Kim, "Improving the energy efficiency of industrial refrigeration systems," *Energy*, vol. 112, pp. 826–835, 2016, doi: 10.1016/j.energy.2016.06.119.

[58] S. A. Klein, "Engineering Equaiton Solver(EES)." F-Chart Software, p. 9.0, 2012.

[59] Q. Jiang *et al.*, "Experimental study on the thermal hydraulic performance of plate-fin heat exchangers for

cryogenic applications," *Cryogenics (Guildf).*, vol. 91, pp. 58–67, Apr. 2018, doi: 10.1016/J.CRYOGENICS.2018.02.006.

[60] V. Jain, A. Singhal, G. Sachdeva, and S. S. Kachhwaha, "Advanced exergy analysis and risk estimation of novel NH3-H2O and H2O-LiBr integrated vapor absorption refrigeration system," *Energy Convers. Manag.*, vol. 224, no. June, p. 113348, 2020, doi: 10.1016/j.enconman.2020.113348.

[61] V. Jain, G. Sachdeva, and S. S. Kachhwaha, "Comparative performance study and advanced exergy analysis of novel vapor compression-absorption integrated refrigeration system," *Energy Convers. Manag.*, vol. 172, no. June, pp. 81–97, 2018, doi: 10.1016/j.enconman.2018.06.116.

[62] E. Mancuhan, "Comparative evaluation of a two-stage refrigeration system with flash intercooling using different refrigerants," *Therm. Sci.*, vol. 24, no. 2, pp. 815–830, 2020, doi: 10.2298/TSCI180921011M.

[63] T. A. Moreira, F. J. do Nascimento, and G. Ribatski, "An investigation of the effect of nanoparticle composition and dimension on the heat transfer coefficient during flow boiling of aqueous nanofluids in small diameter channels (1.1 mm)," *Exp. Therm. Fluid Sci.*, vol. 89, pp. 72–89, Dec. 2017, doi: 10.1016/J.EXPTHERMFLUSCI.2017.07.020.